

Thermal Infrared Characterization of Ground Targets and Backgrounds

Second Edition

Tutorial Texts Series

- *Thermal Infrared Characterization of Ground Targets and Backgrounds, Second Edition*, Pieter A. Jacobs, Vol. TT70
- *Introduction to Confocal Fluorescence Microscopy*, Michiel Müller, Vol. TT69
- *Artificial Neural Networks An Introduction*, Kevin L. Priddy and Paul E. Keller, Vol. TT68
- *Basics of Code Division Multiple Access (CDMA)*, Raghuvver Rao and Sohail Dianat, Vol. TT67
- *Optical Imaging in Projection Microlithography*, Alfred Kwok-Kit Wong, Vol. TT66
- *Metrics for High-Quality Specular Surfaces*, Lionel R. Baker, Vol. TT65
- *Field Mathematics for Electromagnetics, Photonics, and Materials Science*, Bernard Maxum, Vol. TT64
- *High-Fidelity Medical Imaging Displays*, Aldo Badano, Michael J. Flynn, and Jerzy Kanicki, Vol. TT63
- *Diffraction Optics—Design, Fabrication, and Test*, Donald C. O’Shea, Thomas J. Suleski, Alan D. Kathman, and Dennis W. Prather, Vol. TT62
- *Fourier-Transform Spectroscopy Instrumentation Engineering*, Vidi Saptari, Vol. TT61
- *The Power- and Energy-Handling Capability of Optical Materials, Components, and Systems*, Roger M. Wood, Vol. TT60
- *Hands-on Morphological Image Processing*, Edward R. Dougherty, Roberto A. Lotufo, Vol. TT59
- *Integrated Optomechanical Analysis*, Keith B. Doyle, Victor L. Genberg, Gregory J. Michels, Vol. TT58
- *Thin-Film Design Modulated Thickness and Other Stopband Design Methods*, Bruce Perilloux, Vol. TT57
- *Optische Grundlagen für Infrarotsysteme*, Max J. Riedl, Vol. TT56
- *An Engineering Introduction to Biotechnology*, J. Patrick Fitch, Vol. TT55
- *Image Performance in CRT Displays*, Kenneth Compton, Vol. TT54
- *Introduction to Laser Diode-Pumped Solid State Lasers*, Richard Scheps, Vol. TT53
- *Modulation Transfer Function in Optical and Electro-Optical Systems*, Glenn D. Boreman, Vol. TT52
- *Uncooled Thermal Imaging Arrays, Systems, and Applications*, Paul W. Kruse, Vol. TT51
- *Fundamentals of Antennas*, Christos G. Christodoulou and Parveen Wahid, Vol. TT50
- *Basics of Spectroscopy*, David W. Ball, Vol. TT49
- *Optical Design Fundamentals for Infrared Systems, Second Edition*, Max J. Riedl, Vol. TT48
- *Resolution Enhancement Techniques in Optical Lithography*, Alfred Kwok-Kit Wong, Vol. TT47
- *Copper Interconnect Technology*, Christoph Steinbrüchel and Barry L. Chin, Vol. TT46
- *Optical Design for Visual Systems*, Bruce H. Walker, Vol. TT45
- *Fundamentals of Contamination Control*, Alan C. Tribble, Vol. TT44
- *Evolutionary Computation Principles and Practice for Signal Processing*, David Fogel, Vol. TT43
- *Infrared Optics and Zoom Lenses*, Allen Mann, Vol. TT42
- *Introduction to Adaptive Optics*, Robert K. Tyson, Vol. TT41
- *Fractal and Wavelet Image Compression Techniques*, Stephen Welstead, Vol. TT40
- *Analysis of Sampled Imaging Systems*, R. H. Vollmerhausen and R. G. Driggers, Vol. TT39
- *Tissue Optics Light Scattering Methods and Instruments for Medical Diagnosis*, Valery Tuchin, Vol. TT38
- *Fundamentos de Electro-Óptica para Ingenieros*, Glenn D. Boreman, translated by Javier Alda, Vol. TT37
- *Infrared Design Examples*, William L. Wolfe, Vol. TT36
- *Sensor and Data Fusion Concepts and Applications, Second Edition*, L. A. Klein, Vol. TT35
- *Practical Applications of Infrared Thermal Sensing and Imaging Equipment, Second Edition*, Herbert Kaplan, Vol. TT34
- *Fundamentals of Machine Vision*, Harley R. Myler, Vol. TT33
- *Design and Mounting of Prisms and Small Mirrors in Optical Instruments*, Paul R. Yoder, Jr., Vol. TT32
- *Basic Electro-Optics for Electrical Engineers*, Glenn D. Boreman, Vol. TT31
- *Optical Engineering Fundamentals*, Bruce H. Walker, Vol. TT30
- *Introduction to Radiometry*, William L. Wolfe, Vol. TT29
- *Lithography Process Control*, Harry J. Levinson, Vol. TT28
- *An Introduction to Interpretation of Graphic Images*, Sergey Ablameyko, Vol. TT27

Thermal Infrared Characterization of Ground Targets and Backgrounds

Second Edition

Pieter A. Jacobs

Tutorial Texts in Optical Engineering
Volume TT70

SPIE
PRESS

Bellingham, Washington USA

The Library of Congress has catalogued the earlier edition as follows:

Library of Congress Cataloging-in-Publication Data

Jacobs, Pieter A.

Thermal infrared characterization of ground targets and backgrounds / Pieter A. Jacobs.

p. cm. — (Tutorial texts in optical engineering : v. TT 26)

Includes bibliographical references and index.

ISBN 0-8194-2180-4 (softcover)

1. Infrared detectors. 2. Target acquisition. 3. Heat—Radiation and absorption. I. Title. II. Series.

TA1570.J33 1996

621.36'72—dc20

96-10613

CIP

2nd Edition ISBN 0-8194-6082-6

Published by

SPIE—The International Society for Optical Engineering

P.O. Box 10

Bellingham, Washington 98227-0010 USA

Phone: +1 360 676 3290

Fax: +1 360 647 1445

Email: spie@spie.org

Web: <http://spie.org>

Copyright © 2006 The Society of Photo-Optical Instrumentation Engineers

All rights reserved. No part of this publication may be reproduced or distributed in any form or by any means without written permission of the publisher.

The content of this book reflects the work and thought of the author(s).

Every effort has been made to publish reliable and accurate information herein, but the publisher is not responsible for the validity of the information or for any outcomes resulting from reliance thereon.

Printed in the United States of America.



The International Society
for Optical Engineering

Introduction to the Series

Since its conception in 1989, the Tutorial Texts series has grown to more than 60 titles covering many diverse fields of science and engineering. When the series was started, the goal of the series was to provide a way to make the material presented in SPIE short courses available to those who could not attend, and to provide a reference text for those who could. Many of the texts in this series are generated from notes that were presented during these short courses. But as stand-alone documents, short course notes do not generally serve the student or reader well. Short course notes typically are developed on the assumption that supporting material will be presented verbally to complement the notes, which are generally written in summary form to highlight key technical topics and therefore are not intended as stand-alone documents. Additionally, the figures, tables, and other graphically formatted information accompanying the notes require the further explanation given during the instructor's lecture. Thus, by adding the appropriate detail presented during the lecture, the course material can be read and used independently in a tutorial fashion.

What separates the books in this series from other technical monographs and textbooks is the way in which the material is presented. To keep in line with the tutorial nature of the series, many of the topics presented in these texts are followed by detailed examples that further explain the concepts presented. Many pictures and illustrations are included with each text and, where appropriate, tabular reference data are also included.

The topics within the series have grown from the initial areas of geometrical optics, optical detectors, and image processing to include the emerging fields of nanotechnology, biomedical optics, and micromachining. When a proposal for a text is received, each proposal is evaluated to determine the relevance of the proposed topic. This initial reviewing process has been very helpful to authors in identifying, early in the writing process, the need for additional material or other changes in approach that would serve to strengthen the text. Once a manuscript is completed, it is peer reviewed to ensure that chapters communicate accurately the essential ingredients of the processes and technologies under discussion.

It is my goal to maintain the style and quality of books in the series, and to further expand the topic areas to include new emerging fields as they become of interest to our reading audience.

*Arthur R. Weeks, Jr.
University of Central Florida*

Contents

Introduction	ix
1 Sensor Systems	1
1.1 Active Sensor Systems	1
1.2 Passive Sensor Systems	3
1.3 Active Versus Passive Sensor Systems	5
References	6
2 Radiation Terminology and Units	7
2.1 Definitions and Spatial Relationships	7
2.1.1 Blackbody radiation	7
2.1.2 Blackbody spectral emittance: Planck's radiation law	8
2.1.3 Wein displacement law	9
2.1.4 Stefan-Boltzmann law	9
2.1.5 Gray bodies	10
2.2 Intrinsic Radiation Terms	10
2.3 Atmospheric Propagation	12
2.4 Range-Dependent Radiation Terms	13
2.5 Target-to-Background Contrast	14
References	15
3 Introduction to Target Detection	17
3.1 IR Detection Process	17
3.1.1 Target-to-background radiation contrast	17
3.1.2 Attenuation processes	18
3.1.3 IR systems	18
3.1.4 Detection system	21
3.2 Point Target Detection	22
3.3 Extended Target	23
3.4 Signature Variations	24
3.5 Thermal Contrast Considerations	27
References	28

4	Theory of Heat and Mass Transfer	29
4.1	Surface-Atmospheric Boundary Layer	29
4.2	Heat and Mass Transfer	31
4.3	The Heat-Balance Equation	35
4.3.1	Solar heating	36
4.3.1.1	Solar absorption coefficient α_s	36
4.3.1.2	Solar irradiance E_{sun}	41
4.3.2	Long-wave radiation exchange	44
4.3.2.1	Long-wave absorption coefficient α_l	44
4.3.2.2	Long-wave sky irradiance E_{sky}	45
4.3.3	Surface emittance E_s	47
4.3.4	Convective heat exchange Q_c	47
4.3.5	Heat exchange by evaporation/condensation Q_{ec}	51
4.4	First Principles Modeling	53
4.4.1	Model definition	54
4.4.2	Sensitivity analysis	57
4.4.3	Pros and cons	65
	References	66
5	Meteorological and Atmospheric Parameters	69
5.1	Meteorological Sensors and Measurements	69
5.2	SCORPIO Infrared Sky Radiance Distribution	72
	References	78
6	Infrared Calibration Procedures	79
6.1	Calibration Methodology	80
6.2	Calibration Parameters	83
6.3	Calibration Procedures Guidelines	86
6.3.1	Blackbodies and target in the same image	86
6.3.2	Blackbodies and target at different ranges	88
6.3.3	Blackbodies and target in different images	89
6.4	Practical Example	91
	References	97
7	Infrared Signature Characterization	99
7.1	Target Signatures	99
7.1.1	Field measurement of the long wave reflection coefficient	100
7.1.2	Measurement of thermal target signatures in the field	103
7.1.2.1	CHAR-II experiment	104
7.1.2.2	IRIS trials	108
7.1.2.3	Land mine detection experiments	111
7.1.3	IR target modeling	115
7.1.3.1	T62 tank	115
7.1.3.2	Land mines	119
7.2	IR Background Characterization	122
7.2.1	Field measurement of the shortwave reflection coefficient	125

7.2.2	Measurement of background apparent temperatures	128
7.2.2.1	CARABAS measurement system configuration	129
7.2.2.2	Practical examples	137
7.3	Background Temperature Statistics	138
7.3.1	Background temperature distributions	139
7.3.2	Statistical temperature differences between 3–5 μm and 8–12 μm	143
7.3.3	Background temperature curve fitting	145
7.3.3.1	Radiometer data	146
7.3.3.2	Images	153
7.3.4	Pros and cons	159
	References	159
8	Signature Management	161
8.1	Target and Background Signature Analysis	161
8.2	Thermal Signatures of Materials	166
8.3	Mobile Camouflage Systems	172
8.4	Thermal Camouflage of Personnel	174
	References	179
	Index	181

Introduction

A number of physical phenomena can be used to observe or, more generally, to detect an object in a background. Usually such a detection process has the following elements: target-to-background contrast (with or without camouflage), atmospheric attenuation, and sensor performance (detector and signal processing) (see Fig. 1). It is essential that there be a difference, i.e., a contrast, between at least one object and one background feature, such as a radiation contrast or a temperature contrast (difference). Furthermore, this contrast must generate a detector signal S that significantly differs from the noise N spectrum of the sensor system, thus $S/N > 1$. If this is the case, then detection in principle is possible. NATO operations of today are deployed worldwide, exposing man and machine to a wide variety of climatological and environmental conditions. Consequently, target-to-background contrasts vary accordingly, and may reach considerable values at some extreme locations.

Various imaging and nonimaging sensor systems have been developed to detect special features such as color, temperature, sound, smell, shape, and such.

Detection-system designers select features and system parameters to achieve the highest possible detection probability for a large variety of sensor-target-background scenarios under various weather conditions. On the other hand, military-equipment designers search for construction methods and materials that minimize the detection probability for such detection systems.

So, for both worlds it is of utmost importance to have detailed knowledge of target signatures under various target and environmental conditions.

Detection systems are subdivided into three categories:

(1) *Active* sensor systems.

This type of system needs an active source to create or enhance a feature difference in order to detect it. Sometimes source and detector (receiver) are integrated into one system, such as a laser range finder or a synthetic aperture radar (SAR) system. At other times they are separate, as in a situation in which a forward observer illuminates the target as a beacon for homing devices.

(2) *Passive* sensor systems.

In the same context, passive systems do not need an active source, but utilize the existence of natural features, such as a thermometer to

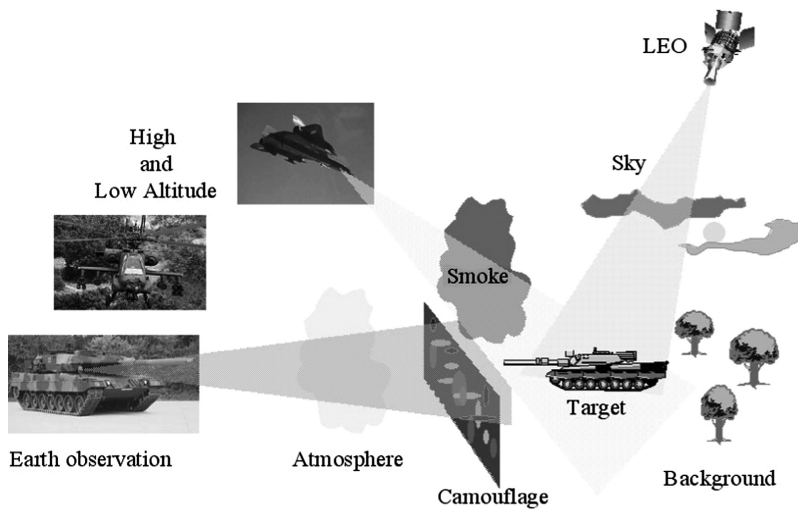


Figure 1 Detection scenario.

measure temperatures, or a thermal imager measuring emitted radiation of an object (the sun and moon are considered natural passive sources).

(3) *Semiactive* sensor systems.

Detecting alien, foreign active sources, such as radar (RWR), laser (LRF), and electronic support measures (ESM).

Some active sensors are considered passive when the detection principle is based on signals that exist in a background. A microphone would be considered passive when picking up the sound of a bird, which is an example of a passive natural sound. However, the microphone becomes active when picking up an artificial source such as a helicopter. Another example is the human eye. The human eye-brain system is the best known active sensor system and, in terms of performance, is probably the best system that exists today. It operates in a very small spectral region, the visible part of the electromagnetic (EM) spectrum, as shown in Fig. 2.* However, its practical use is limited to daytime and its performance decreases seriously under adverse weather conditions. Figure 2 shows that the EM spectrum offers many more frequency regions, which could be utilized in either a passive or active way.

Gradually, more and more parts of the EM spectrum have been used in imaging sensor systems, comprising the ultraviolet (UV), near-infrared (NIR), thermal infrared (TIR), and radar systems. Operational radar systems were introduced during World War II and contributed largely to the defeat of the German U-boat fleet. With the enormous revolution in technology during the post-war years, new detector materials became increasingly available, opening up more spectral bands to be used in sensor systems.

*Source: www.temple.edu/biomed/spectrum.gif.

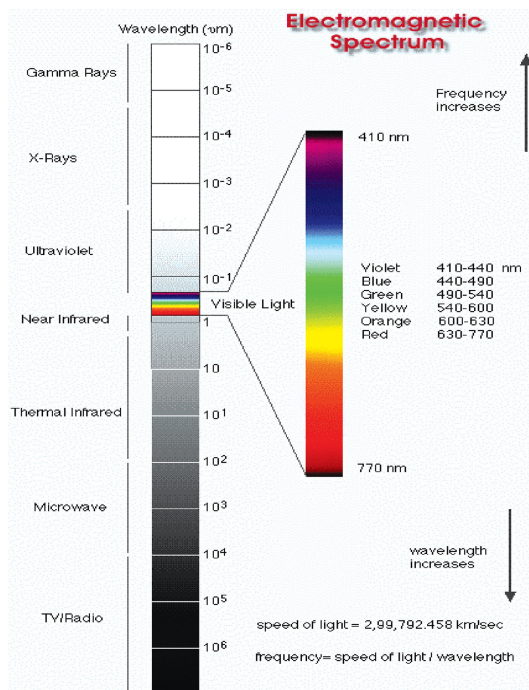


Figure 2 Electromagnetic spectrum.

Imaging sensor systems in the UV region, frequently used for missile (plume) detection, have become available. Especially, the spectral window from 0.25–0.39 μm is used for this purpose because the natural background does not contain solar UV radiation (solar blind window). Also, sensor systems have been developed in the NIR 1.1–3 μm , based on new sensor technology, such as quantum-well detectors. Although reflected natural NIR radiation can be used for detection, spotlights such as a NIR lamp or laser may be needed to enhance contrast during adverse weather conditions, as with laser detection and ranging (LADAR) systems.

One promising option was the TIR spectral region, ranging from 3–50 μm . Since all surfaces emit electromagnetic radiation in this spectral region, it can be used for passive detection. The explosive development of modern electronics and ongoing development of new detector materials have resulted in high-performance IR imaging systems. In this context, “high performance” means that the characteristic system parameters, such as NETD (noise equivalent temperature difference), IFOV (instantaneous field of view), MRTD (minimum resolvable temperature difference), etc. can be optimized, theoretically to take nearly any desired value for a given choice of hardware components. During the last few years, uncooled IR detector technology emerged, offering a cheaper alternative to cooled systems, but providing less performance.

Computer computational power also has grown enormously, offering powerful image-processing tools that can analyze imagery almost in real time. The conse-

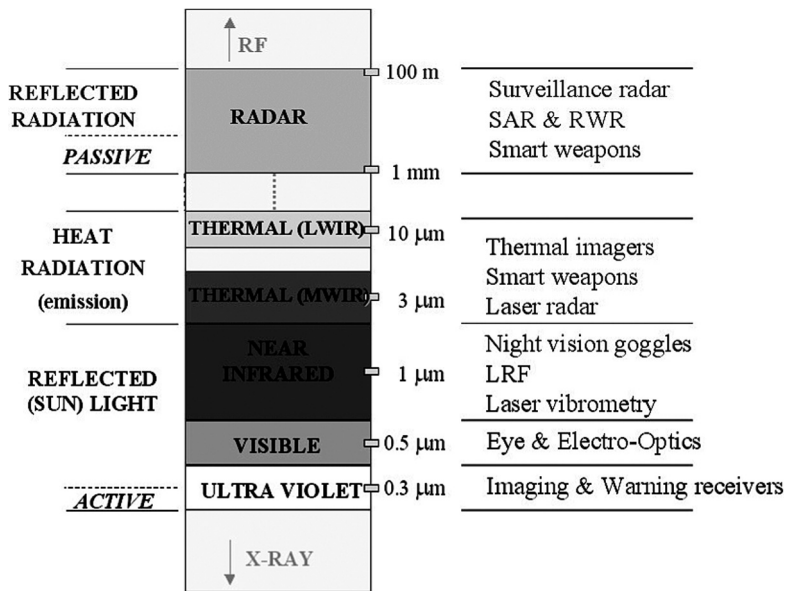


Figure 3 Overview of spectral ranges, in which modern detection systems operate.

quence is that in the detection process, more target and background features can be analyzed quickly and automatically, which makes targets even more vulnerable. Modern sensors use many parts of the EM spectrum to optimize their performance for specific applications. Figure 3 shows an overview of spectral ranges in which modern detection systems operate.

In addition to system hardware specifications, system performance should be expressed in terms of the system's ability to perform the task for which it was designed. This could be expressed thus: "With this system, it is possible to detect an armored personnel carrier parked in front of a tree line from a distance of 3 km, during the middle of a clear European night." The performance of that system is determined not only by its hardware specifications, but also by atmospheric propagation and, probably to the largest extent, the momentary IR contrast between the object and the local background. This is why *all* components, as given in Fig. 1, must be taken into account to accurately judge the detection performance of a given sensor system.

Analyses of atmospheric transmission enhance the understanding of atmospheric effects, such as aerosols, dust, and smoke particles, which have an impact on the propagation of IR radiation through the atmosphere. Many short- and long-range measurements have been conducted under various meteorological conditions. These efforts have culminated in a number of sophisticated semi-empirical models, such as MODTRAN and HITRAN. These models have been updated continuously over the last 15 years as new measurements and theory became available. Today, these models are reliable tools for calculating the atmospheric propagation and only require a small number of meteorological input

parameters. Other than the use of MODTRAN, atmospheric transmission is not be discussed in this text.

The next part of the observation scenario is the characterization of the IR contrast between the object and the background. For simple object geometry, IR signatures can be calculated by solving the heat balance equation for the different object facets. However, with increasing object complexity, calculations soon become unreliable because mathematical representations of some energy flows are not valid (or not known) for small, arbitrarily oriented object facets. Measurements are a good alternative because on many occasions object conditions can be controlled and the environmental conditions can more or less be selected (i.e., waited for). Databases exist comprising more than 10,000 images of military targets alone, taken at various target conditions and observation angles.

The characterization of background radiation is the most complex issue. This complexity is probably one reason it was (until recent years, when the lack of background information became the most limiting factor in the detection process) given more attention. In spite of this increase of effort, especially in the modeling area, little progress was made in the development of models that produced results accurate enough to be used in detection and recognition studies. This mainly is because, on the one hand, backgrounds are difficult to model as a result of their complex geometrical structure and, on the other hand, because the mathematical description for some transfer processes, such as those that exist in a vegetation layer, are not yet known accurately enough. The temporal variability of IR background radiation can be described satisfactorily with the aid of semi-empirical models. The characterization of the spatial distribution of IR background radiation is not discussed explicitly in this Tutorial Text.

The main part of this Tutorial Text deals with the characterization of the thermal infrared (3–12 μm) radiation contrast between ground targets and backgrounds. Sensor systems are discussed only as far as necessary to explain the topic under discussion. For more detailed information on sensor systems, the reader is referred to one of the many textbooks available on this topic,^{1–3} or to specific literature on IR detectors.⁴

Passive radar systems use differences in reflected cosmic radiation between target and background in the higher frequency bands. Generally, detection ranges are relatively short (a few kilometers) and strongly weather dependent. This topic is not further addressed. Not only is the EM spectrum used to gather information using active and passive detection, but acoustic, magnetic, and seismic phenomena can also be used. Systems based on these principles are not discussed any further here.

In summary, many sensor systems that can be used for detection purposes are available, offering a wide range of deployment options: active/passive, day/night, long-/short-range, good/bad weather, and such.

Chapter 1

Sensor Systems

1.1 Active Sensor Systems

Active systems in their simplest form are used in the typical setup shown in Fig. 1.1.

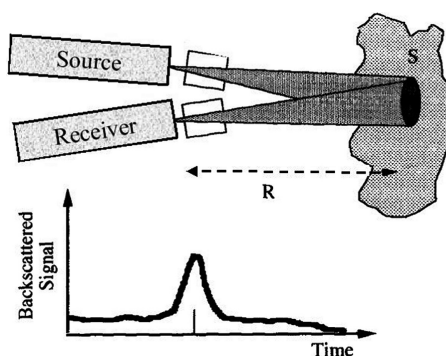


Figure 1.1 Active systems.

A source directly “illuminates” the target and the reflected radiation is detected. Although many kinds of active sources can be used, most active systems use a part of the EM spectrum, such as light sources (including lasers) and radar. Radar systems can be active or passive, and can be subdivided into the following operational spectral bands:

- 1–18 GHz \cong 30–2 cm
- 35 GHz \cong 1 cm
- 94 GHz \cong 0.3 cm

In a conventional active radar system, a beam is sent out and, when the receiver is opened after period of time (t_o) has elapsed, the incoming reflected beam will have traveled a distance $R = \frac{ct_o}{2}$ (c = speed of light). Depending on the characteristics of the source and receiver, other target features, such as target size, speed, and direction, can be determined. Radar surveillance systems operate in the lower fre-

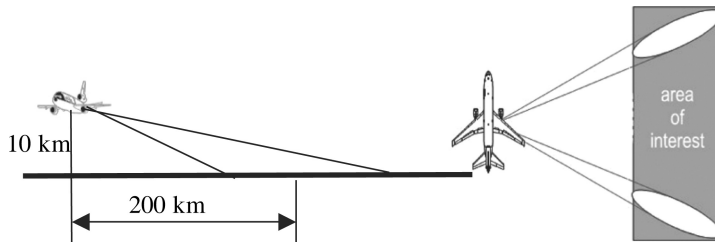


Figure 1.2 SAR system.

quency bands (1–18 GHz). For target acquisition (seekers), the higher frequencies (specifically 35 and 94 GHz, mm wave) are used, because the antenna diameter can be kept small. Normally the emitter (horn) and receiver (dish) are integrated into one system. Because of technological developments over the past few decades, mechanical scanning has been replaced by electronic beam steering (phased arrays). This has great advantages for target tracking.

A special radar application is used in a synthetic aperture radar (SAR). The beam of a normal operating radar scans the environment (Fig. 1.2), and when it hits a target the dwell time on the target is very short.

In a SAR system, the beam can be locked onto a desired object (target or background area) and consequently the dwell time is much longer, resulting in a higher S/N ratio. Therefore, SAR systems are very well suited as imaging devices.

Instead of a radar source, a laser source can be used to illuminate the target. The big advantage is the much higher geometrical resolution that can be obtained by the use of optical wavelengths (micrometer range) as opposed to radar wavelengths (cm and mm range). In a LIDAR system, a pulsed (frequency-modulated) laser is used and the receiver is synchronized with this frequency (Fig. 1.3). Range gating can be used in a manner similar to radar to acquire range-dependent information, but with a much higher-depth resolution. Each range gate can therefore be represented by a high-resolution image.

With laser vibrometry the mechanical vibration of a surface is determined by analyzing the modulation (i.e., measuring the Doppler shift) of the reflected laser beam by the surface (Fig. 1.4). By scanning the laser over the surface, a laser vibration image can be created. Figure 1.5 shows such an image of an idling tank.

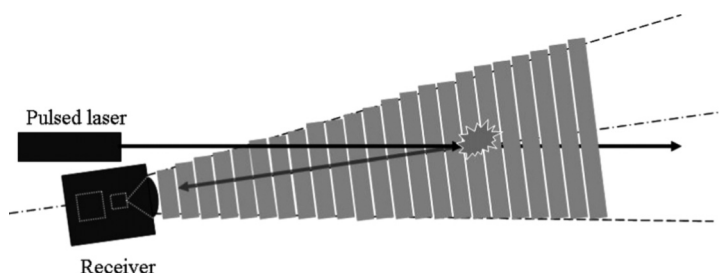


Figure 1.3 LIDAR principle.

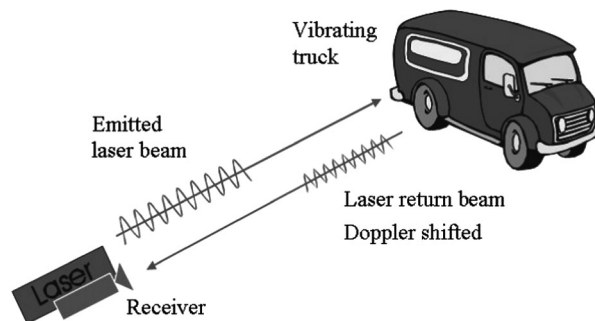


Figure 1.4 Laser vibrometry setup.

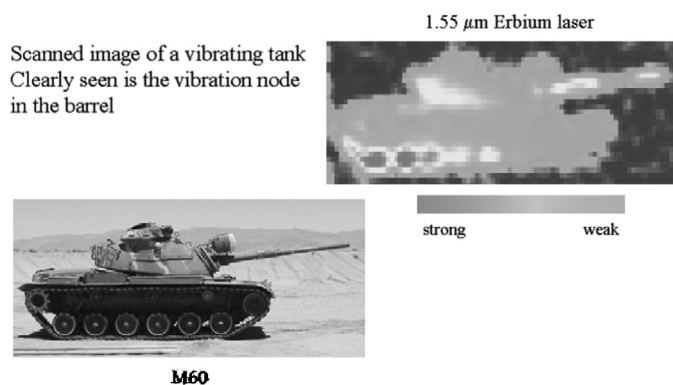


Figure 1.5 Laser vibration spectrum example.

1.2 Passive Sensor Systems

Passive sensor systems do not require an active source, but use the existence of “natural” sources (Fig. 1.6). Because of the limited use of the visible spectral region and the military preference for passive sensor systems over the past decades, attention was focused on passive (EM) sensor systems.

Passive systems can utilize a broad spectrum of features, but a majority of these systems operate in a specific part of the EM spectrum. Electro-optical sensor systems can be subdivided into the following operational spectral bands:

- Ultraviolet (UV): 0.250–0.410 μm
- Visible (VIS): 0.410–0.770 μm
- Near-infrared (NIR): 0.770–3.0 μm
- Thermal infrared (TIR): 3.0–15 μm
- Passive (radar) radiometry: >35 GHz

Radiation leaving a surface in the spectral range of 0.25–3 μm mainly consists of reflected environmental radiation. From 3–15 μm , the main component is emitted radiation. Passive radar fully depends on surface reflective properties.

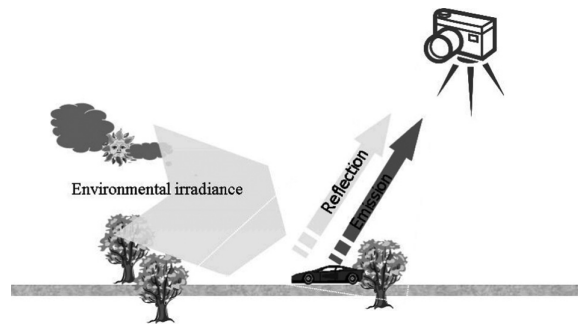


Figure 1.6 Passive detection.

Instead of using a single-band spectral filter, a variable filter (circumferential variable filter or CVF) or prism can be used to create a large number of narrow spectral bands, typically 256, each 20–40 nm wide. This principle is used in spectral (nonimaging) radiometers or in combination with an imaging device (Fig. 1.7).

In the latter case, each pixel in the image is resolved for each spectral band. The final output is a hyperspectral cube of 256 layers (images). Figure 1.8 shows the spectral reflectivity curves of a variety of surface land mines, recorded with a spectral radiometer.

Figures 1.9 and 1.10 show a comparison between the spectral reflectivity of a contiguous layer of snow of various flake sizes in comparison with the spectral reflectivity of up to three layers of white fabric (used for snow camouflage nets).

Figures 1.8 and 1.9 show the use of spectral reflectivity data with opposite interest. In order for mines to be detected, a maximum difference in reflectivity with the local environment is required. For camouflage purposes, just the opposite is required: a maximum spectral match with the local environment.

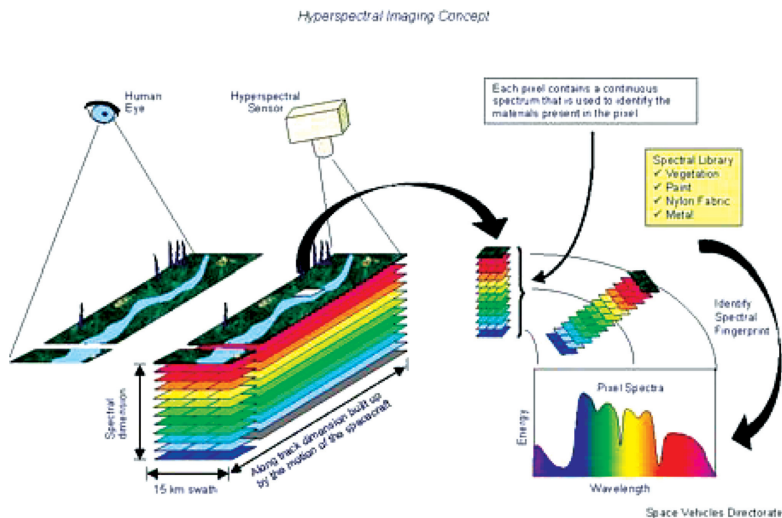




Figure 1.7 Hyperspectral imaging concept.

Table 1.1 Active versus passive sensor systems.

Active	Passive
<ul style="list-style-type: none"> • Range information • Velocity information (speed and direction) • Long range detection • Gated viewing (range resolution) • Signal modulation (source) (noise suppression) 	<ul style="list-style-type: none"> • No range information (except for stereo viewing) • No velocity information • Short to medium range detection • More weather dependent
 DETECTABLE	 NOT DETECTABLE

References

1. J.S. Accetta and D.L. Shumaker, executive eds., *The Infrared and Electro-Optical Systems Handbook*, Environmental Research Institute of Michigan, Ann Arbor, and SPIE: The International Society for Optical Engineering, Bellingham, Washington (1993).
2. J.M. Loyd, *Thermal Imaging Systems*, Plenum Press, New York (1975).
3. R. Siegel and J.R. Howell, *Thermal Radiation Heat Transfer*, Taylor & Francis (1995).
4. E.L. Dereniak and R.E. Sampson, eds., *Infrared Detectors and Focal Plane Arrays II*, SPIE Vol. 1685 (1992).

Chapter 2

Radiation Terminology and Units

This chapter discusses radiometric parameters, units, and terminology that are commonly used to describe radiation processes. The “Système International (SI)” will be used to define terms and units. Since it would be impractical to treat all parameters here, the list is limited to those definitions necessary to discuss the topics dealt with in the remaining chapters. For additional definitions of terms and units, the reader is referred to the many existing textbooks.^{1–3}

When quantities depend on wavelength, they are preceded by the adjective “spectral.” The symbol for that quantity is followed by the symbol for wavelength, λ , such as $L(\lambda)$ for the radiance.

2.1 Definitions and Spatial Relationships

The basic radiation parameter is the *radiant flux*, Φ , representing the amount of radiant energy (Joules) emitted, transmitted, or received per unit time (s), usually expressed in watts ($\text{W} = \text{J s}^{-1}$). The term *radiant flux density*, φ is the radiant flux per unit area in watts per square meter (W m^{-2}). The *irradiance*, E , is the radiant flux density *incident* at a surface.

2.1.1 Blackbody radiation

Kirchhoff investigated the relationship between absorbed and emitted radiation. He defined the *spectral absorptivity*, $\alpha(\lambda)$, of a surface as the fraction of incident radiation absorbed at the wavelength λ . He came to the important conclusion that $\alpha(\lambda, \vartheta, \varphi)$ is always equal to $\varepsilon(\lambda, \vartheta, \varphi)$ in each direction (ϑ, φ).

For an object completely absorbing radiation at wavelength λ , $\alpha(\lambda, \vartheta, \varphi) = \varepsilon(\lambda, \vartheta, \varphi) = 1$ and the emitted radiation is the maximum possible (“a good emitter is a good absorber”). In the special case where $\varepsilon = 1$ at all wavelengths, the emitting surface is called a blackbody.

A *blackbody* is an ideal body, which absorbs all incident energy and reflects none at all wavelengths and at all angles of incidence. In discussions the word “black” often is misunderstood, because it is associated with the

visual color black. But, for instance, fresh snow, although visually bright white, closely approximates a blackbody radiator. Blackbodies are often used as reference panels to calibrate IR sensors and images that are taken with spectral band filters.

The *spectral emissivity*, $\epsilon(\lambda)$, is the ratio of the actual spectral emittance of a body and the spectral emittance of a blackbody at the same temperature and wavelength λ .

2.1.2 Blackbody spectral emittance: Planck's radiation law

Planck showed that the spectral radiant exitance, $E_{bb}(\lambda, T)$, of a blackbody depends on the wavelength λ and the absolute surface temperature T of the object as

$$E_{bb}(\lambda, T) = c_1 \left\{ \lambda^5 \left[\exp\left(\frac{c_2}{\lambda T}\right) - 1 \right] \right\}^{-1} \quad (\text{W m}^{-2} \mu\text{m}^{-1}), \quad (2.1)$$

where c_1 and c_2 are radiation constants, given by

$$c_1 = 3.7418 \times 10^8 \quad (\text{W m}^{-2} \mu\text{m}^4)$$

$$c_2 = 1.4388 \times 10^4 \quad (\mu\text{m K}).$$

Figure 2.1 shows a graphical representation of Eq. (2.1) as a function of wavelength and temperature T .

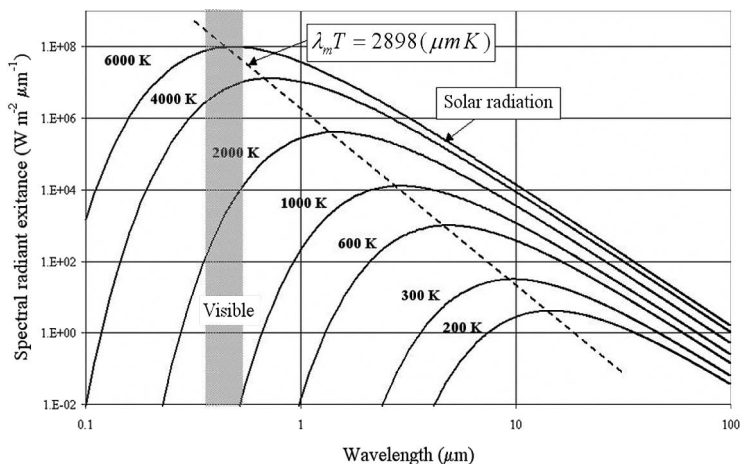


Figure 2.1 Spectral radiant exitance of a blackbody as a function of wavelength. The dashed line indicates the wavelength at which maximum exitance occurs.

2.1.3 Wien displacement law

An important characteristic of the spectral radiant exitance is that the peak in the curve (Fig. 2.1) shifts to shorter wavelengths with increasing temperature. The wavelength, λ_m , at which the peak occurs, is found by differentiating Eq. (2.1) with respect to λ and by setting the result to zero. The result is

$$\lambda_m T = 2898 \text{ (}\mu\text{m K)}, \tag{2.2}$$

where λ_m is the wavelength at which, at a given temperature T , the maximum energy is emitted. This is Wien's displacement law. Equation (2.2) is presented as a dashed line in Fig. 2.1 and shows the decrease of λ_m with increasing surface temperature T . This explains why hot matter starts emitting energy in the visible part of the electromagnetic spectrum (reddish light) and becomes more yellow as the temperature increases.

2.1.4 Stefan-Boltzmann law

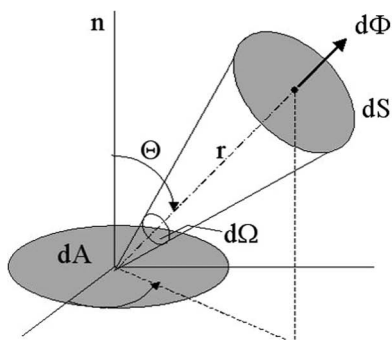
Integrating the spectral radiant exitance in Eq. (2.1) over all wavelengths results in the total *radiant exitance* or *emittance*, E_{bb} , of a blackbody. The result is known as the Stefan-Boltzmann equation and is given by

$$E_{bb} = \int_0^\infty E_{bb}(\lambda, T) d\lambda = \sigma T^4 \text{ (W m}^{-2}\text{)}, \tag{2.3}$$

with $\sigma = 5.67 \times 10^{-8}$ (Stefan-Boltzmann constant) (W m⁻² K⁻⁴).

Equation (2.3) shows that the magnitude of the total radiant exitance for a blackbody, at a temperature of typically $T = 300$ K, is approximately 460 W m⁻².

Several additional terms are needed to describe radiation dispersing in all directions from a point source or from a radiating surface. The *radiant intensity*, I , is defined as the flux per unit solid angle (Fig. 2.2), or $I = d\Phi/d\Omega$, expressed in watts per steradian (W sr⁻¹).



$$d\Omega = \frac{dS}{r^2}$$

$$dI = \frac{d\Phi}{d\Omega}$$

$$\text{radiance } L = \frac{dI}{dA} = \frac{dI}{dS \cos \Theta}$$

Figure 2.2 Spatial relationships of radiometric quantities.

Figure 2.2 also shows the definition of the *radiance*, L , as the ratio of the radiant intensity, dI , and the projected surface area at right angles to the direction of the beam, $dS \cos \Theta$. This quantity is expressed in watts per m^2 per steradian ($\text{W m}^{-2} \text{sr}^{-1}$). It can be shown that the irradiance E is found by multiplying the radiance L with the solid angle π , i.e., $E = \pi L$. The definition of the radiance is the basis for *Lambert's cosine law*, which states that when radiation of a blackbody is emitted at an angle Θ to the normal, the emitted flux per unit solid angle is proportional to $\cos \Theta$, i.e.,

$$I = I_n \cos \Theta \quad (I_n \text{ emitted flux at normal incidence}). \quad (2.4)$$

Many surfaces in nature exhibit such behavior and are called Lambertian radiators.

2.1.5 Gray bodies

So far only blackbodies (surfaces that emit maximum possible energy) have been considered, but in practice most surfaces are not black and are called gray bodies. On the contrary, it is very difficult to make a blackbody, for instance, for calibration purposes. Special surface treatments such as roughening and highly diffuse coatings are required to achieve the maximum emittance. The ability of a surface to emit radiation is determined by a surface property, the spectral emissivity $\varepsilon(\lambda)$.

Emission coefficient ε is the ratio of the actual emittance of a body to the emittance of a blackbody at the same temperature. The emission coefficient ε is calculated as a weighted mean value by integrating the spectral emissivity over the spectral region and surface temperature of interest, using Eq. (2.1) as a weight function. The result is

$$\varepsilon = \frac{\int_{\lambda_0} \varepsilon(\lambda) E(\lambda, T) d\lambda}{\int_{\lambda_0} E_{bb}(\lambda, T) d\lambda}, \quad (2.5)$$

where λ_0 : spectral region of interest,
 T : surface temperature.

Many manmade and natural materials can be approximated by a gray body for which the spectral emissivity is constant and independent of wavelength, e.g., $\varepsilon(\lambda) = \varepsilon$ constant ($\varepsilon < 1$). In Chapter 8, a variation of the emission coefficient of paints is used to generate infrared patterns.

2.2 Intrinsic Radiation Terms

In contrast to a blackbody, a gray surface also reflects a fraction of the incident long wave ($\lambda > 3 \mu\text{m}$) radiation, depending on the reflective properties of the surface.

Long wave spectral reflectivity $\rho_l(\lambda)$ is the ratio of the reflected spectral radiant flux and the incident spectral flux. For practical reasons, only diffuse reflection will be considered throughout this text.

Long wave reflection coefficient ρ_l is the ratio of the reflected radiant flux and the incident flux. ρ_l is found by integrating $\rho_l(\lambda)$ with respect to λ and using Eq. (2.1) as a weight function. The result is

$$\rho = \frac{\int_{\lambda_0} \rho(\lambda) E(\lambda, T) d\lambda}{\int_{\lambda_0} E_{bb}(\lambda, T) d\lambda}. \quad (2.6)$$

From the conservation of radiant energy, it can be shown that $\rho_l + \varepsilon + \tau_l = 1$, where τ_l is the long wave transmissivity of the material. Thus, for an opaque surface ($\tau_l = 0$) in equilibrium with the enclosure in which it is placed, $\rho_l + \varepsilon = 1$.

The radiation leaving a gray surface therefore is composed of emitted (self-emission) and reflected (environmental) radiation. Since it is not possible to discriminate between the two contributions, an IR sensor always measures the sum of the two. This measurement is considered as being *only* emitted radiation and is given the prefix “apparent,” while related parameters are given the index “ap.” The apparent emittance of a gray body consequently is written as

$$E_{ap} = \int_{\lambda_0} [\varepsilon(\lambda) E(\lambda, T_t) + \rho_l E(\lambda, T_{ae})] d\lambda, \quad (2.7)$$

where T_t : target temperature,

T_{ae} : apparent “environmental” temperature.

The environmental temperature T_{ae} is a vague term. For a horizontal surface, $E(\lambda, T_{ae})$ represents the spectral irradiance of the sky-hemisphere, $E(\lambda, T_{sky})$. The sky-hemisphere is taken as solid blackbody screen at close range and at some apparent temperature, T_{sky} . For a vertical surface, this is a mixture of spectral terrain and sky irradiance and is difficult (if not impossible) to determine. The importance of this contribution strongly depends on the spectral reflectivity of the surface and the radiation levels prevailing in the background. Many manmade and natural materials behave like gray bodies with a relatively low reflection coefficient $0.1 < \rho_l < 0.2$, which results in a low contribution to the total radiation leaving the surface under moderate environmental radiation conditions.

Because humans have developed a better feeling for temperature units than radiant units, often E_{ap} is converted to a corresponding *apparent temperature*, T_{ap} (in degrees Kelvin), which by definition is determined by

$$E_{ap} = \int_0^{\infty} [\varepsilon(\lambda) E(\lambda, T_t) + \rho_l E(\lambda, T_{ae})] d\lambda \xrightarrow{\text{Definition}} = \sigma T_{ap}^4. \quad (2.8)$$

Through this definition, it is thus assumed that the detected radiation E_{ap} is the emittance of a blackbody at temperature T_{ap} . Sometimes the apparent temperature is defined according to the spectral band in which the apparent emittance is measured (defined by the spectral response of the IR system). In that case, T_{ap}

is solved from the implicit equation

$$E_{ap} = \int_{\lambda_0} E(\lambda, T_{ap}) d\lambda.$$

The foregoing derivations of radiant parameters apply only if atmospheric effects are negligible; normally this is the case for very short object ranges. Parameters defined in the target plane have the prefix “intrinsic.”

2.3 Atmospheric Propagation

Combining the spectral properties of atmospheric propagation (Fig. 2.3) with the spectral performance characteristics of the most frequently used IR detectors leads to two classical spectral windows, 3–5 μm (I) and 8–12 μm (II). In the following discussions, reference is made to these two spectral bands.

It might be coincidence or a lucky characteristic of nature that the emittance of the earth’s surfaces, at an average temperature of $T = 290$ K, is at about $\lambda_m \cong 10$ μm , which is exactly in the middle of an atmospheric window (II). The other window is centered around $\lambda_m \cong 4$ μm , corresponding to a temperature of $T = 720$ K, and therefore is best suited to detect hot sources such as engines, power generators and hot combustion gases. These two windows, which span the thermal infrared, are generally used, but other, sometimes very narrow, spectral bands are used for special purposes.

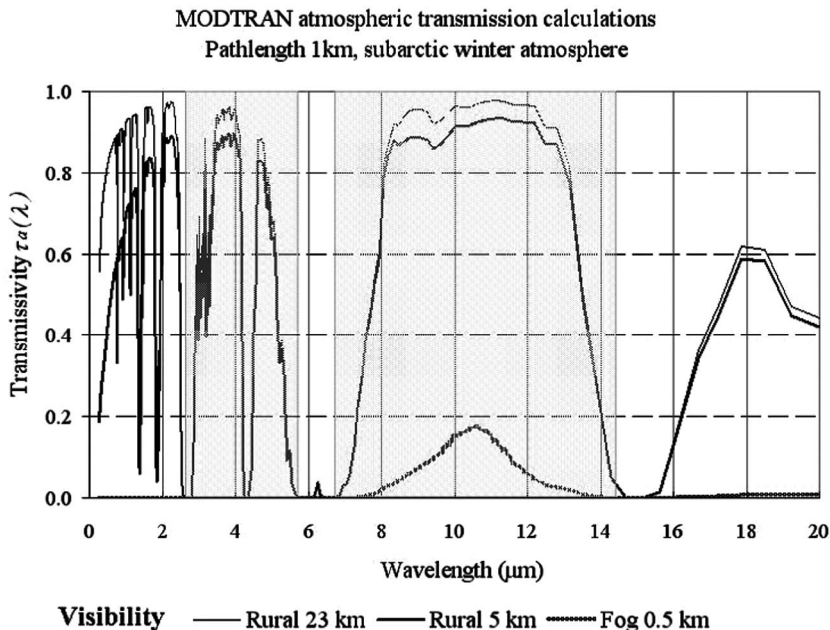


Figure 2.3 An example of the spectral atmospheric transmissivity $\tau_a(\lambda)$.

2.4 Range-Dependent Radiation Terms

For measurements at longer ranges, atmospheric effects have to be incorporated in order to convert measurements over long ranges to values in the object plane, i.e., the intrinsic values. The total blackbody radiation, which is incident on the aperture of the system at range r , i.e., the irradiance, E_{ap} , is then given by

$$E_{ap} = F(r) \int_{\lambda_0} \left\{ \tau_a(\lambda, r) E(\lambda, T_t) + [1 - \tau_a(\lambda, r)] E(\lambda, T_a) \right\} d\lambda, \quad (2.9)$$

with $F(r)$: range-dependent geometrical factor,
 $\tau_a(\lambda, r)$: spectral atmospheric transmissivity,
 T_a : air temperature (K),
 r : range of target to system's aperture (m).

The first term on the right-hand side of Eq. (2.9) represents the transmitted spectral emittance of the target, while the second term represents the atmospheric path irradiance. The term in square brackets represents the spectral atmospheric emissivity. For a gray body having an emission coefficient ε_t , the situation is a little more complicated because the target reflects environmental radiation into the optical path. The irradiance at the aperture in this situation is

$$E_{ap} = F(r) \int_{\lambda_0} \left[\tau_a(\lambda, r) \{ \varepsilon_t E(\lambda, T_t) + \rho_l E(\lambda, T_{ae}) \} + [1 - \tau_a(\lambda, r)] E(\lambda, T_a) \right] d\lambda. \quad (2.10)$$

The physical target temperature T_t can be derived only if the spectral atmospheric transmissivity, the spectral distribution of the environmental radiation, and the target emissivity are known. Setting $F(r) = 1$ for simplicity, Eq. (2.10) is rewritten as

$$\begin{aligned} E_{ap} &= \int_{\lambda_0} \left\{ [1 - \tau_a(\lambda, r)] E(\lambda, T_a) + \rho_l \tau_a(\lambda, r) E(\lambda, T_{ae}) \right\} d\lambda \\ &= \varepsilon_t \int_{\lambda_0} \tau_a(\lambda, r) E(\lambda, T_t) d\lambda. \end{aligned} \quad (2.11)$$

In principle, T_t can be solved iteratively (for a given range r) from this implicit equation. However, in many cases ε_t (and therefore ρ_l) and T_{ae} are unknown, and in that case only the apparent temperature T_{ap} can be found. The basic assumption is to consider the target as a blackbody. If it is further assumed that the atmospheric transmissivity $\tau_a(\lambda, r)$ is constant over the spectral band under consideration, then the intrinsic apparent target temperature T_{ap} can be solved from

$$E_{ap} - [1 - \tau_a(r)] \int_{\lambda_0} E(\lambda, T_a) d\lambda = \tau_a(r) \int_{\lambda_0} E(\lambda, T_{ap}) d\lambda. \quad (2.12)$$

2.5 Target-to-Background Contrast

For detection, the relevant scene parameter is the *apparent radiation contrast*, ΔE_{ap} , between the target and the local background, which is incident at the aperture of the IR system. ΔE_{ap} is found by applying Eq. (2.10) to the target, giving E_{apt} and subtracting E_{apb} , which is found by applying Eq. (2.10) to the local background. If it is assumed that the momentary atmospheric path irradiance is equal for both target and background (i.e., observed from the same bearing and range), this leads to

$$E_{apt} = F(r) \int_{\lambda_0} \left\{ \tau_a(\lambda, r) [\varepsilon_t E(\lambda, T_t) + \rho_{lt} E(\lambda, T_{ae})] + [1 - \tau_a(\lambda, r)] E(\lambda, T_a) \right\} d\lambda. \quad (2.13)$$

$$E_{apb} = F(r) \int_{\lambda_0} \left\{ \tau_a(\lambda, r) [\varepsilon_b E(\lambda, T_t) + \rho_{lb} E(\lambda, T_{ae})] + [1 - \tau_a(\lambda, r)] E(\lambda, T_a) \right\} d\lambda. \quad (2.14)$$

The indices t and b refer to target and background, respectively. Subtracting Eqs. (2.13) and (2.14) gives

$$\Delta E_{ap} = \int_{\lambda_0} \tau_a(\lambda, r) [E_{ap}(\lambda, T_t) - E_{ap}(\lambda, T_b)] d\lambda \quad (2.15)$$

The geometrical factor $F(r)$ is incorporated into $E_{ap}(\lambda, T_t)$ and $E_{ap}(\lambda, T_b)$. For a blackbody, Eq. (2.15) converts to

$$\Delta E_{ap} = \int_{\lambda_0} \tau_a(\lambda, r) [E(\lambda, T_t) - E(\lambda, T_b)] d\lambda. \quad (2.16)$$

Equations (2.15) and (2.16) contain all the basic elements that determine the detectability of a target. The equations show that the target emission coefficient and target surface temperature (both combined in the apparent emittance) are the *only* two physical target parameters that influence the radiation contrast. In the next chapter, the influence of ΔE_{ap} on the detection process is discussed for two of the most frequently occurring situations.

In general, however, detection is determined not only by the detected contrast between the target and the local background, but also by the way this contrast can be discriminated from a larger background area. If the image contains many areas with similar local contrasts spread throughout the image, the detection probability is greatly influenced by the spatial distribution and temporal thermal (temperature) behavior of these areas. This spatial and temporal distribution of local contrasts in the background often is referenced as thermal clutter. If spatial information is important, the field of view (FOV) of the system and the instantaneous field of view (geometrical resolution, IFOV) and target size must be incorporated in the analysis.

It is hardly possible to develop a purely theoretical model of land clutter because the spatial distribution of the various clutter elements in natural scenes (roads, grass, trees, sand, etc.) is determined by the randomness of Mother Nature.

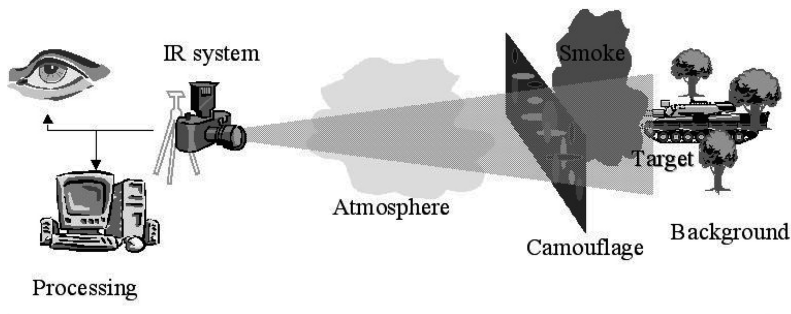
References

1. J.L. Monteith, *Principles of Environmental Physics*, Edward Arnold Ltd., London (1973).
2. W.L. Wolfe and G.J. Zissis, eds., *The Infrared Handbook*, Environmental Research Institute of Michigan, Ann Arbor (1993).
3. F. Grum and R.J. Becherer, *Optical Radiation Measurements* Vol. 1, Academic Press (1979).

Chapter 3

Introduction to Target Detection

Figure 3.1 shows the scenario taken as the starting point for discussing the influence of the various components in the IR observation (detection) process, such as the IR system, type of target, weather and environmental parameters, and countermeasures such as camouflage and smokescreens.



$$(S/N)_d \gg \int_{\lambda_0} R(\lambda) \times \tau_a \times \tau_c \times \Delta E_{ap}$$

Figure 3.1 Elements in the infrared observation process.

3.1 IR Detection Process

The detection process can be separated into four independent primary areas, which can be characterized as follows.

3.1.1 Target-to-background radiation contrast

In any detection process, it is essential that at least one target feature be different from the same feature in the background. Since infrared systems use radiation

emitted by the target and background, the transmitted radiation contrast between the target and its local background is the basic input parameter for detection.

As already mentioned, detection can occur only if a target feature can be discriminated from the background. This requires that a minimum of two criteria be fulfilled. First, the radiation contrast between target and background must generate a detector output voltage exceeding the system noise level. This is basically determined by system design and is dependent on (limited by) the performance of optical and electronic system components. Second, the radiation contrast must be discernible from the total observed scene. In other words, if more similar radiation levels exist in the observed scene (spatial radiation distribution, also called background clutter), detection is not unique. In a highly cluttered background, target discrimination is possible only if more target and/or background features are taken into account.

3.1.2 Attenuation processes

In the optical path between the target and the IR system, the radiation contrast can be influenced by environmental conditions. In the adopted scenario, the radiation contrast is attenuated by passive countermeasures (camouflage, smoke) and by atmospheric effects, caused by molecular absorption and emission (mainly water and carbon dioxide) and atmospheric scattering processes (aerosols). The MODTRAN model is a commonly accepted model with which to perform such atmospheric properties calculations.

3.1.3 IR systems

Next to a distinction between active and passive systems, as mentioned earlier, systems generally are differentiated as imaging and nonimaging. Active systems obviously have the disadvantage of needing an artificial source to operate, which makes them vulnerable to enemy detection. On the other hand, the contrast between target and background may be greatly enhanced, which gives an advantage under reduced “visibility” conditions. Active systems recently have become interesting again because of the development of new NIR eye-safe lasers. These systems also can be used in a gated viewing mode, similar to the LIDAR processing: the emitted laser pulses hit an object and are reflected back to the sensor system. By tuning the receiving detector electronics with the frequency of the emitted pulses, a range gate can be selected. Only the reflections that occur in this range gate will reach the detector, eliminating much of the stray radiation. The very narrow spectral bands at which these lasers operate also lower the probability of detection by enemy sensors. Either active or passive sensor systems may also use a series of narrow spectral bands (hyperspectral), especially in spectral bands where high radiation levels are expected and specific target features can be determined.

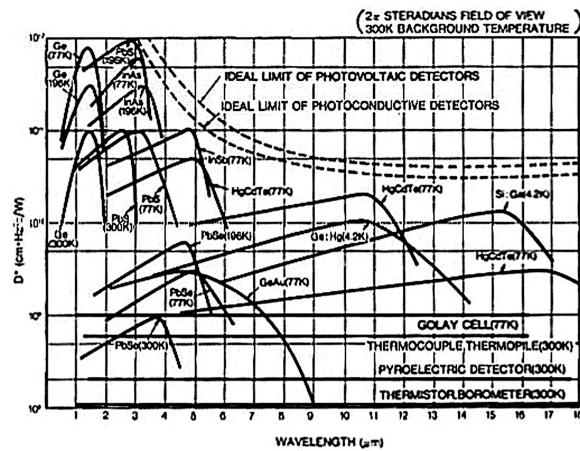


Figure 3.2 Overview of some relevant IR detector materials.

The heart of any IR system is the infrared detector. Because of the explosive development of modern electronics and developments in materials research, a large variety of IR detectors have become available (Fig. 3.2). Moreover, the single IR detector has been replaced gradually by detector arrays, leading to imagery of much higher resolution.

In its simplest form, IR radiation is measured with a radiometer. Such a device, in essence, consists of a spectral band filter, λ_o , to determine the spectral region of interest, and a single IR detector. Figure 3.3 shows a modern background measurement setup with a computer-controlled radiometer. The measured incoming radiation is converted



Figure 3.3 IR field radiometer.

to a corresponding apparent temperature, using internal calibration sources, with

$$E_{ap} = \int_{\lambda_o} E(\lambda, T_{ap})d\lambda \quad \text{or} \quad E_t = \bar{\epsilon}_t \int_{\lambda_o} E_{bb}(\lambda, T_t)d\lambda,$$

where the known target emissivity, $\bar{\epsilon}_t$, is set on the radiometer.

Imaging systems produce an image of the target, that is, a two-dimensional (2D) representation in some feature space of a three-dimensional (3D) object. For instance, a color photograph is a 2D representation of an object using color as a feature. A thermal image is a 2D representation of an object using thermal radiation as a feature. The quality of the image is determined by the geometrical detail (resolution elements, pixels) and the feature detail (color resolution, thermal resolution).

As will be explained in Section 3.3, the size of a resolution element in the target plane can be larger than the target size. In such a case, the target will only be represented by one pixel and in fact represents the situation of a nonimaging system. Figure 3.4 schematically shows how an image is built up by a modern focal plane array (FPA) IR imager. The focal plane is projected in space by the front optics, creating an imaginary 2D grid of detectors over the target. The size of the projected detector area (pixel) in the target plane depends on the size of the FPA (number of detectors), the IFOV, and the range to the target. The radiation incident at each detector depends on the irradiance of the projected detector area on the target, atmospheric attenuation (including countermeasures), and spectral filter and system optics.

The incident radiation on the detector is converted to a voltage output. The output of all detectors is connected to a display, which converts voltages to gray levels as is schematically shown in Fig. 3.5. As shown before, a surface emits radiation proportional to T^4 . Consequently, a hot surface generates a higher detector output voltage than a colder surface. Normally, a black-and-white image is created in which white corresponds to hot and black to cold.

In Chapter 6, a calibration procedure is outlined, using two blackbodies of known temperature within the image (generating two gray levels) to calibrate the entire image in terms of radiation or apparent temperatures.

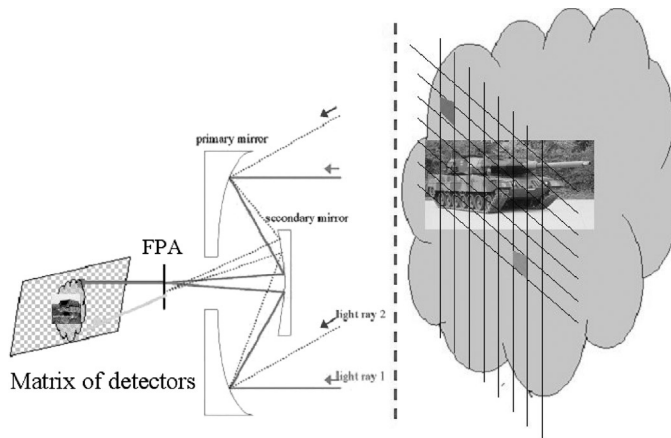


Figure 3.4 Image formation using a focal plane array (FPA).

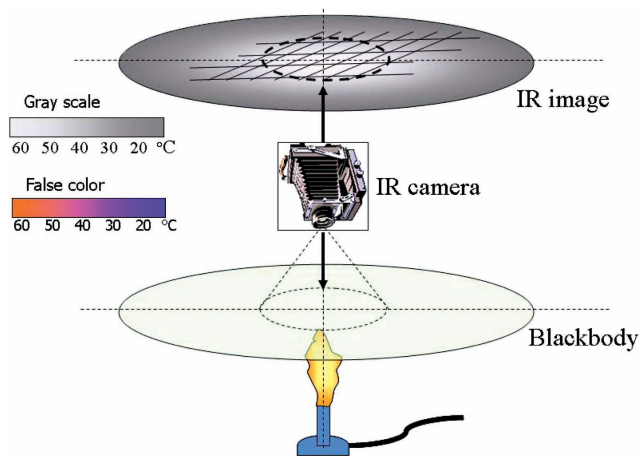


Figure 3.5 Converting detector output voltage to a gray (color) scale IR image.

3.1.4 Detection system

The incident radiation contrast is converted to an electrical output (voltage) from the IR detector. The performance of a system can be expressed by many parameters, but essentially it is the ability of the system to detect the lowest possible radiation contrast. The ultimate goal is to characterize ground targets and backgrounds in terms of radiation properties (or apparent temperatures). The main interest is to study the influence of the radiation contrast on the detection process. Therefore, in order to simplify the situation, background clutter is excluded from the detection model by placing the target against a background with a uniform, homogeneous radiation (temperature) distribution. With this assumption, the detection problem is reduced to the detection of the radiation contrast only. It is assumed that detection occurs if a preset detector threshold voltage is exceeded, i.e., if the incident radiation contrast on the detector, ΔE_{ap} , is large enough to generate a detector output signal S that significantly exceeds the detector noise level N . The significance (confidence) of detection is determined by the required detection task, k , i.e., the required probability of detection.

A threshold detection task can successfully be completed if the following inequality holds:

$$\Delta E_{ap} \geq k NEI,$$

where k : level of the detection task

NEI: noise equivalent irradiance (W m^{-2}).

The NEI of a system is the minimum detectable radiation (contrast), which is found for $S/N = 1$, and corresponds with the lowest possible level of detection.

Observed from a large distance, the target is completely confined to one resolution element (pixel) of the imaging system. In this case, the projected

detector area in the target plane is larger than the target dimensions, and the target cannot be resolved. In this situation the target is called a point target. As the imager closes in on the target, the target occupies more pixels and can gradually be resolved. In this situation, the target is called an extended target. The signal processor, which makes the final decision, is the concluding link in the detection process. This decision can be based on human-aided observation or made autonomously by a computer.

3.2 Point Target Detection

A point target, where the solid angle Ω_t is subtended by the target of area A_t , at range r is smaller than the sensor system instantaneous field of view Ω_s (Fig. 3.6).

The radiation incident on the detector, E_{apt} , from a target at a distance r is given by Eq. (2.10) as

$$E_{apt} = \frac{A_t}{\pi r^2} \int_{\lambda_0} \left\{ \tau_a(\lambda, r) [\varepsilon_t E(\lambda, T_t) + \rho_{lt} E(\lambda, T_{ae})] + [1 - \tau_a(\lambda, r)] E(\lambda, T_a) \right\} d\lambda. \quad (3.1)$$

Since the background completely fills the instantaneous field of view ($\Omega_t < \Omega_s$), the background radiation incident on the detector, E_{apb} , becomes range independent:

$$E_{apb} = \frac{\Omega_s}{\pi} \int_{\lambda_0} \left\{ \tau_a(\lambda, r) [\varepsilon_b E(\lambda, T_b) + \rho_{lb} E(\lambda, T_{ae})] + [1 - \tau_a(\lambda, r)] E(\lambda, T_a) \right\} d\lambda. \quad (3.2)$$

The path radiation terms cancel out only if the atmospheric transmission and the air temperature are the same for both optical lines of sight. The result is that the radiation contrast on the detector ΔE_{ap} varies with the inverse square of the

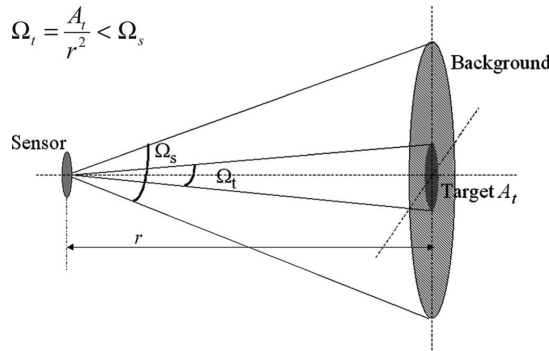


Figure 3.6

distance and with the range dependency through $\tau_a(\lambda, r)$, as

$$\Delta E_{ap} \approx \frac{1}{r^2} \int_{\lambda_0} \tau_a(\lambda, r) [E_{ap}(\lambda, T_t) - E_{ap}(\lambda, T_b)] d\lambda = \frac{1}{r^2} \int_{\lambda_0} \tau_a(\lambda, r) \Delta E_{ap}(\lambda) d\lambda.$$

Finally, the detection range R_d is solved by successive iteration from

$$\frac{1}{R_d^2} \int_{\lambda_0} \tau_a(\lambda, R_d) \Delta E_{ap}(\lambda) d\lambda = k \text{ NEI}. \quad (3.3)$$

$\tau_a(\lambda, R_d)$ can be calculated with a computer program, for instance, with MODTRAN 4.0.¹

In reality, the detection process is somewhat different. The radiation contrast between the target and background cannot be calculated from a measurement in one single pixel containing the point target and the background. This is because the target dimensions are not known. So, to arrive at the radiation contrast, the pixel containing the target is subtracted from, for instance, a neighboring pixel. This means that the term $A_t/\pi r^2$ in Eq. (3.1) in fact equals Ω_s/π in Eq. (3.2). If the background radiation is uniform within the two pixels, the subtraction gives the true difference between the target and background. Of course, when the target dimensions are known, the contrast could be calculated just from the one pixel containing the target.

3.3 Extended Target

For an extended target, the solid angle subtended by the target at range r is larger than the instantaneous field of view (see Fig. 3.7).

In this situation, the target completely fills the field of view. The contrast has to be determined with respect to another pixel. This can be another target pixel (detection clues on the target itself) or a background pixel. Here, the argument that the atmospheric transmission and the air temperature must be the same for both optical lines of sight becomes important if the target is highly resolved. For this situation, ΔE_{ap} is given by

$$\Delta E_{ap} = \int_{\lambda_0} \tau_a(\lambda, r) [E_{ap}(\lambda, T_t) - E_{ap}(\lambda, T_b)] d\lambda = \int_{\lambda_0} \tau_a(\lambda, r) \Delta E_{ap}(\lambda) d\lambda.$$

The range dependency is implicitly given through $\tau_a(\lambda, r)$, as

$$\int_{\lambda_0} \tau_a(\lambda, R_d) \Delta E_{ap}(\lambda) d\lambda = k \text{ NEI}. \quad (3.4)$$

In the detection process, where the range between the system and the target is decreasing continuously, at some point a transition from a point source to an extended target will take place.

Equations (3.3) and (3.4) only contain one system parameter, the NEI, and two scene parameters, τ_a and ΔE_{ap} . As already mentioned, system parameters only limit performance in today's modern systems to a very small extent. This

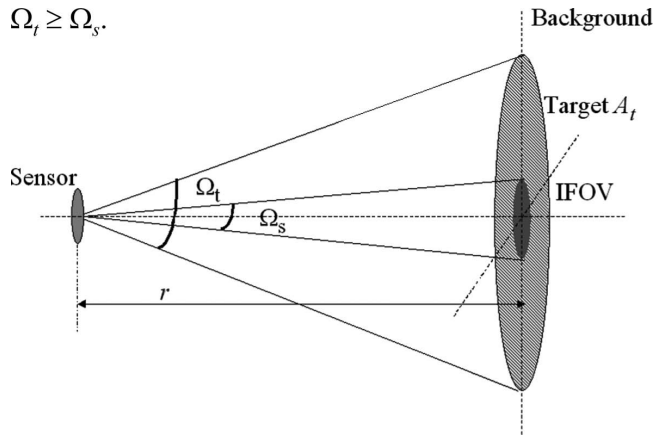


Figure 3.7

does not imply that system performance is not an issue anymore, but it does mean that improving system performance will result in longer detection ranges and, for instance, will not improve the possibility of discriminating a target from the background as such. Therefore, if the system is assumed to be adequate to execute the desired detection task, i.e., the geometrical and temperature (radiation) resolutions are high enough, detection is largely ruled by the atmospheric transmission τ_a and the apparent radiation contrast ΔE_{ap} between the target and the local background. Again, this does not include background clutter or the effects of countermeasures such as camouflage and smoke. Consequently, to be able to evaluate the detection possibilities of a target against a uniform background, the dynamic behavior of these two parameters must be studied under different target conditions in representative meteorological conditions (geographical locations).

3.4 Signature Variations

Signature variations are generated by:

- (1) Target conditions
 - Exhaust grid and gases
 - Crew compartment heating/cooling
 - Power generator
 - Material properties
 - Camouflage
 - Target location and orientation

Figure 3.8 shows several hot sources on a ship at sea. These are a mixture of hot and cold solid surfaces and hot exhaust gases.

- (2) Environmental variations
 - Induced weather (sun, clouds, rain, snow, etc.)
 - Atmospheric influences on transmission
 - Geographical location (moderate, desert climate, etc.)



Figure 3.8 Thermal image of a ship at sea, showing various hot sources.

Figure 3.9 shows a diagonal signature cycle of some “passive” stationary targets.

(3) Spectral diversity

Figure 3.10 shows signatures of a hovering helicopter in various spectral bands.

(4) Materials properties

Figure 3.11 shows a collection of different types of materials, deployed to three very different structures. This exercise was part of the TIREX trials² to measure the thermal signatures of a large number of materials and deployment techniques. Figure 3.12 shows a thermal image of these materials.

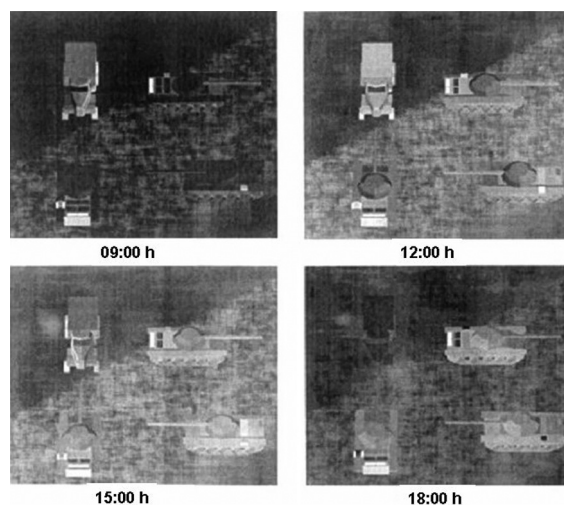


Figure 3.9 Impact of variable weather conditions on the signature of stationary targets.

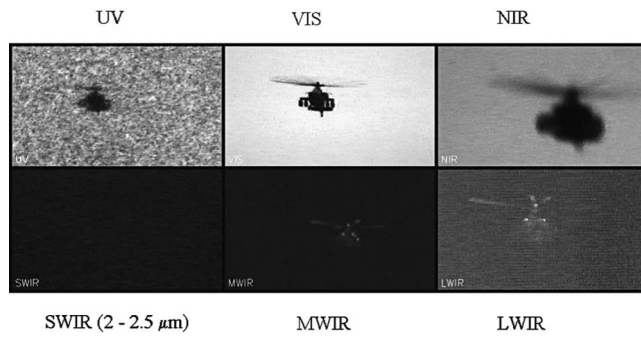


Figure 3.10 Signatures of a hovering helicopter in various spectral bands.

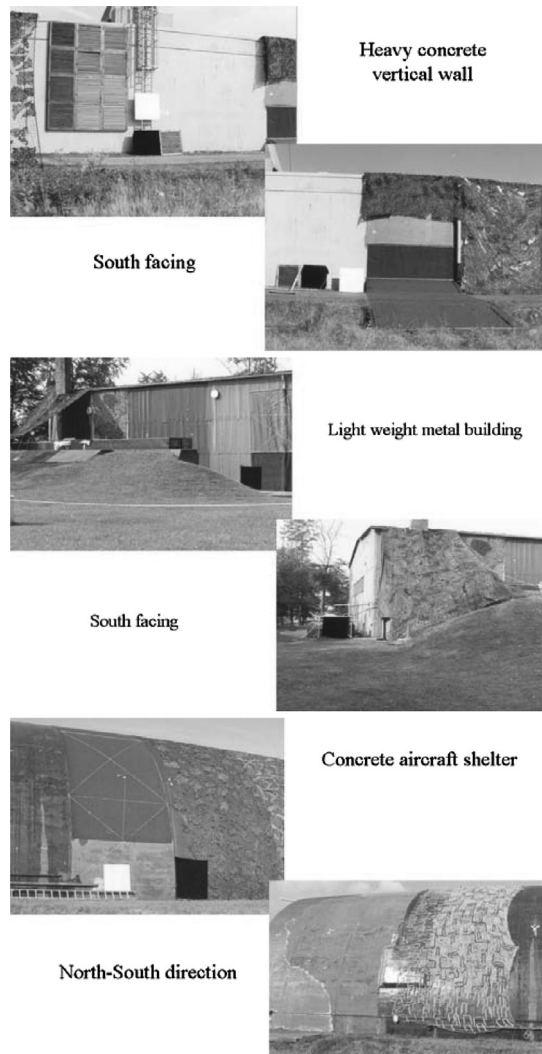


Figure 3.11 Various types of materials deployed to three different kinds of structures.

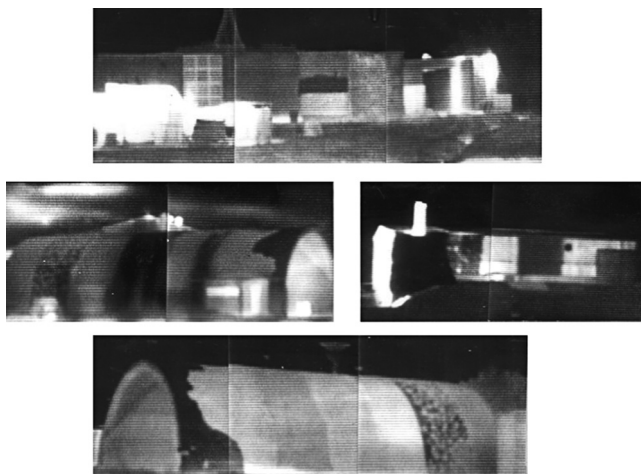


Figure 3.12 Thermal image of the materials shown in Fig. 3.11.

3.5 Thermal Contrast Considerations

To this point, the discussions have led to a single scene parameter: the apparent thermal contrast, ΔE_{ap} . Concerning the characterization of targets and backgrounds, this is the most essential parameter. To learn more about the influence of target, background, and environmental parameters on ΔE_{ap} , it is common to define a physical model in which these dependencies are defined. Important issues to consider concerning sensors and measurements include

- (1) the physical processes and their relevance in the formation of a thermal contrast;
- (2) optical and physical material properties of targets and backgrounds to be investigated;
- (3) sensors and measurement techniques to collect environmental, weather data, and material properties;
- (4) global geographical coverage; and
- (5) blackbodies for calibration purposes.

Concerning model definition and numerical solution, the following important issues are to be considered:

- (1) the mathematical representation of these physical processes and, most importantly, their applicability (validity) for the geometry under consideration;
- (2) numerical scheme and computational platform;
- (3) required input data (model parameter sensitivity);
- (4) model performance, such as accuracy, numerical stability, and computational time; and
- (5) model validation and model limitations.

For a simple geometry, a model approach as outlined above is quite feasible. For complex targets, an accurate description of the physical processes for the various facets becomes either complicated or very inaccurate. Efforts in the past have generated a number of practical and useful target models. Physical and optical properties of natural backgrounds, such as grass and trees, change almost continuously. Background models, therefore, are very complex and need an enormous array of input data, which make such models rather impractical. In such cases, semi-empirical background models may give better results. Today, there still is a poor understanding of the nature and thermal variability of natural backgrounds.

References

1. A. Berk et al., "Modtran 4.0.1," AFGL (1999).
2. P.A.M. Jacobs et al., "Thermal camouflage of fixed installations," *Project TIREX* Vol. I, II and III (classified) (1983).

Chapter 4

Theory of Heat and Mass Transfer

This chapter is devoted to the physical characterization of the various processes that determine the apparent emittance E_{ap} of targets and backgrounds. For this purpose, the problem is split into two parts:

- (1) the conduction of heat within the target, and
- (2) the heat exchange in the surface atmospheric boundary layer.

It is emphasized that parameters will not be discussed at full length. Discussion will be limited to the functional relations between parameters and the definition of practical usable expressions. Therefore, the origin of these parameters are only given limited attention. To be able to evaluate the behavior of ΔE_{ap} in a theoretical model for a given situation, it is necessary to determine:

- (1) the physical processes involved in creating a radiation contrast;
- (2) the parameterization of these processes;
- (3) the relative importance of these parameters (sensitivity analysis); and
- (4) the availability and required accuracy of these parameters for model input.

The latter has no particular meaning in a theoretical survey as such, but in the end it determines the practical usefulness (and validation possibilities) of the model.

4.1 Surface-Atmospheric Boundary Layer

If a target is exposed to outdoor environmental conditions, a number of heat and mass transfer (transport) mechanisms, $Q(i)$, take place inside the target and at the target-surface-atmospheric boundary (Fig. 4.1).

The contribution of each process to the total heat budget depends on the prevailing meteorological conditions and physical properties of the target. The exchange of energy can be broken down into the following processes:

- $Q(1)$: absorbed shortwave irradiance ($\lambda \leq 3 \mu\text{m}$);
- $Q(2)$: absorbed long wave irradiance ($\lambda > 3 \mu\text{m}$);
- $Q(3)$: convective heat exchange;

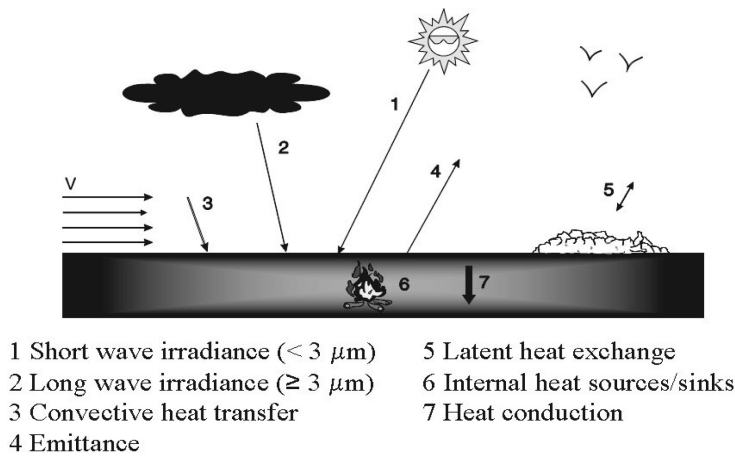


Figure 4.1 Energy transfer processes at the surface-atmospheric boundary layer.

$Q(4)$: target emittance;

$Q(5)$: latent heat exchange by condensation/evaporation;

$Q(6)$: internal heat sources and/or sinks; and

$Q(7)$: heat conduction in the target.

Applying the principle of energy conservation leads to the solution for the temperature distribution in the target and results in a solution for the surface temperature T :

$$\sum_{i=1}^7 Q(i) = 0 \implies \text{physical surface temperature } T. \quad (4.1)$$

The thermodynamic response of the target and, in particular, the surface-temperature change, is determined by the physical properties of the bulk material and surface characteristics. The internal or bottom boundary is often at constant temperature or a constant moisture content (groundwater level), and has only a small direct influence on the surface temperature. Next to conduction of heat through the bulk material, heat is transported by moisture and vapor flow.

Next to transport within the body, the transfer of heat and moisture (rain, condensation, evaporation) from and to the surface through the atmospheric-surface boundary layer is the other important transport mechanism. The net heat and moisture flow in the surface-atmospheric boundary layer is found from the heat- and moisture-balance equations, respectively. Rain is excluded from further analysis because it is a very specific situation in which the observed apparent temperature is mainly determined by the temperature of the rain and the thermal properties of the object, and therefore is very unpredictable.

Consequently, the analysis is limited to the transfer of heat and the transfer of latent heat by evaporation and condensation.

4.2 Heat and Mass Transfer

The transport of mass and heat within a body is given by the continuity equation and the energy equations, which can vary from quite simple for a solid material to very complex for a porous material, including the flow of moisture and transport of latent heat. In a mathematical model, the system of material and the atmosphere above it is divided into layers. The surface temperature of the material (of main interest in this context) is predicted by determining the transfer of energy and mass in, out, and through the body (considered to be a series of layers with constant properties).

A basic assumption that is often made is that the layers are horizontally uniform and the thickness of a layer is much smaller than its horizontal extent. These conditions imply that the most significant heat fluxes are vertical. Thus, the estimated temperature results from solving the one-dimensional (1D) equations for heat and mass transfer. For the heat flow in a solid material with constant properties, no transport of mass takes place and the model equations take a rather simple form that can be solved straightforwardly (numerically) without much difficulty.

The 1D equation for the transport of heat for this case is

$$\frac{\partial T(z, t)}{\partial t} = \kappa \frac{\partial^2 T(z, t)}{\partial z^2} + Q_{source}(z_1 \leq z \leq z_2), \quad (4.2)$$

where $\kappa = \frac{\lambda_c}{\rho C}$: the thermal diffusivity ($\text{m}^2 \text{s}^{-1}$),

and λ_c : thermal conductivity ($\text{W m}^{-1} \text{K}^{-1}$),

ρ : specific mass (kg m^{-3}),

C : specific heat ($\text{J kg}^{-1} \text{K}^{-1}$),

t : time (s),

z : axis \perp surface (m),

Q_{source} : internal heat source (K s^{-1}).

The boundary condition at the top (atmospheric side) of the solid, $z = z_1$, is given by the net heat flow into or from the solid, which is a result of the heat-transfer processes $Q(t)$ in the atmospheric-surface boundary layer. These processes are be discussed in more detail in Section 4.3.

The flow of heat at the top surface going into the solid (positive z -direction) is

$$-\lambda_c \left(\frac{\partial T}{\partial z} \right)_{z=z_1} = Q(t) \quad (\text{W m}^{-2}).$$

The other boundary condition at $z = z_2$ is defined at some depth in the solid, at which the temperature or heat flow is known. For instance, the boundary temperature T_o is constant in time. Another possibility is to assume a constant heat flux Φ_o over the boundary, for instance, an inside wall of a room kept at constant

temperature. In mathematical form,

$$T(z_2, t) = T_o \quad \text{or} \quad \pm \lambda_c = \left(\frac{\partial T}{\partial z} \right)_{z=z_2} = \Phi_o.$$

The initial ($t \leq t_o$) condition is a uniform, constant temperature distribution, T_c , in the system, that is

$$T(z, t) = T_c \quad (z_1 \leq z \leq z_2 \wedge t \leq t_o).$$

For many materials with constant physical properties, values for λ_c , ρ and C can be found in literature.¹ However, when consulting the literature, it is sometimes discouraging to find many different values for the same type of material, implying that detailed information about material constituents and their properties is required.

Several computer models are available for solving the equations for various geometrical configurations and different weather conditions.^{2,3}

For porous materials, like some soil types, insulating materials (glass-wool), etc., the transport of water and water vapor, associated with a transport of latent heat, must be considered. For such porous materials, the formulation of the mathematics in the model becomes more complex, taking the form of a system of two combined differential equations for moisture and heat flow with nonlinear coefficients.⁴ In this case, the equation for 1D moisture flow look like:

$$\frac{\partial \Theta}{\partial t} = \frac{\partial}{\partial z} \left(D_T \frac{\partial T}{\partial z} + D_\Theta \frac{\partial \Theta}{\partial z} + k_h \right) (z_1 \leq z \leq z_2),$$

and for heat flow,

$$C_v \frac{\partial T}{\partial t} = \frac{\partial}{\partial z} \left(K_T \frac{\partial T}{\partial z} + K_\Theta \frac{\partial \Theta}{\partial z} + k_h \rho_m h_m \right) (z_1 \leq z \leq z_2),$$

where Θ : moisture content ($\text{cm}^3 \text{cm}^{-3}$),

ρ_m : density of water (kg m^{-3}),

h_m : specific enthalpy of water (J kg^{-1}),

C_v : volume-averaged heat capacity ($\text{J K}^{-1} \text{m}^{-3}$),

k_h : hydraulic conductivity (m s^{-1}),

D_T, D_Θ and K_T, K_Θ : nonlinear transport coefficients.

The boundary condition at the top surface at $z = z_1$ for heat flow is

$$Q(z_1, t) = K_T \frac{\partial T}{\partial z} + K_\Theta \frac{\partial \Theta}{\partial z} + k_h \rho_m h_m,$$

and for moisture flow is,

$$e(z_1, t) = D_T \frac{\partial T}{\partial z} + D_\Theta \frac{\partial \Theta}{\partial z} + k_h.$$

The boundary condition at some depth (for instance, the groundwater level) where $z = z_2$ is

$$Q(z_1, t) = 0 \quad \text{and} \quad e(z_1, t) = 0 \text{ (no fluxes).}$$

The initial condition ($t \leq t_o$) is a uniform and constant temperature distribution, T_c , and moisture distribution, Θ_c , in the system:

$$\left. \begin{aligned} T(z, t) &= T_c \\ \Theta(z, t) &= \Theta_c \end{aligned} \right\} \quad (z_1 \leq z \leq z_2 \wedge t \leq t_o).$$

The major problem of this system of equations is embedded in the transport coefficients, which depend on material properties, moisture content, and temperature. The dependence of D_T and D_Θ , and the hydraulic conductivity k_h on moisture content for a sandy soil⁵ is shown in Fig. 4.2.

Values for K_T and K_Θ are related to D_T and D_Θ as

$$K_T = \rho_{ml} D_{Tl} \Theta_{ml} + \rho_{mv} D_{Tv} \Theta_{mv} + \lambda_c \quad (\text{W m}^{-1} \text{K}^{-1}),$$

$$K_\Theta = \rho_{ml} D_{\Theta l} \Theta_{ml} + \rho_{mv} D_{\Theta v} \Theta_{mv} \quad (\text{W m}^{-1}).$$

The subscripts l and v refer to liquid (water) and vapor phase, respectively.

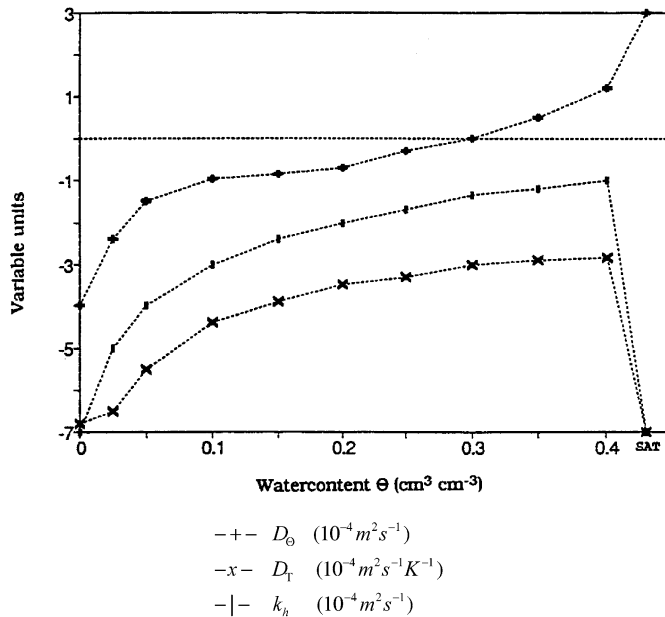


Figure 4.2 D_Θ , D_T , and k_h as a function of soil moisture content Θ .

One can imagine that it is a cumbersome task to determine these curves through measurements, preferably without disturbing the geometrical structure and moisture content of the soil.

Table 4.1 shows the calculated thermal conductivity⁶ for three soil types as a function of soil porosity and moisture content. As can be seen, the different substances that constitute a soil have widely different thermal properties, so it is important to have detailed knowledge of the soil under investigation. Figure 4.3 shows a comparison between the calculated and theoretical values of the thermal conductivity of quartz sand at 40°C and 75°C as a function of water content.

The previous models are two extremes, the first of which is simple and consequently has limited application. However, it is easy to use because the physical properties of most materials are readily known and the numerical scheme is simple. It also is a very useful tool for studying the general thermodynamics of solids and creating a feeling for the order of magnitude and time scales involved.

The second model is much more troublesome to solve. This is mainly because of the difficulty of finding adequate representations for the nonlinear and time-dependent coefficients. If measurements are missing, only very rough, generalized estimates can be made. Although the numerical scheme is complex, it does not present a serious problem. Probably the integral

Table 4.1 Properties of soils and their components.⁶

		Density ρ (10^3 kg m^{-3})	Specific heat C_v ($\text{J m}^{-3} \text{ K}^{-1}$)	Thermal conductivity λ_c ($\text{W m}^{-1} \text{ K}^{-1}$)	Thermal diffusivity κ ($10^{-6} \text{ m}^2 \text{ s}^{-1}$)
Soil components					
	Quartz	2.6	0.8	8.8	4.2
	Clay minerals	2.6	0.9	2.9	1.2
	Organic matter	1.3	1.9	0.3	1.0
	Water	1.0	4.2	0.6	0.1
Soils					
	Water content (Θ)				
	↓				
Sandy soil	0.0	1.6	0.8	0.3	0.3
40% pore space	0.2	1.8	1.2	1.8	0.9
	0.4	2.0	1.5	2.2	0.7
Clay soil	0.0	1.6	0.9	0.3	0.2
	0.2	1.8	1.3	1.2	0.5
80% pore space	0.4	2.0	1.6	1.6	0.5
	0.0	0.3	1.9	0.06	0.1
Peat soil	0.4	0.7	3.3	0.3	0.1
	0.8	1.1	3.7	0.5	0.1

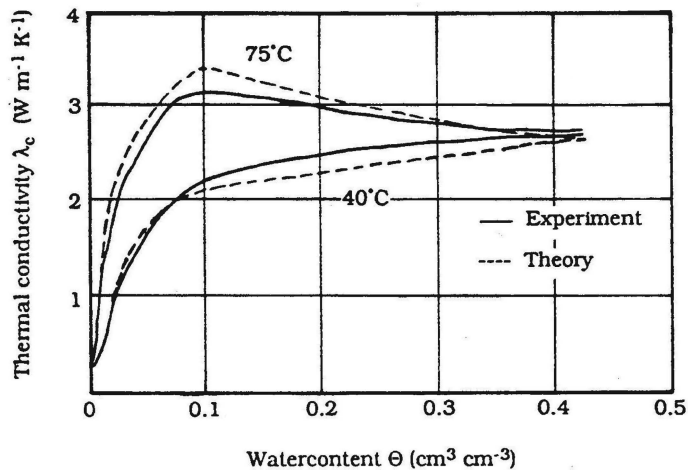


Figure 4.3 Thermal conductivity of quartz⁶ as a function of soil moisture content Θ .

complexity of the problem has prevented a wide application of this type of model until today.

4.3 The Heat-Balance Equation

In its most general form, the heat-balance equation at the surface-atmospheric boundary is given by

$$-\lambda_c \left(\frac{\partial T}{\partial z} \right)_{z=z_1} = \alpha_s E_{sun} + \alpha_l E_{sky} - \varepsilon \sigma T^4 \pm Q_c \pm Q_{ec}, \quad (4.3)$$

where $\alpha_s E_{sun}$: absorbed shortwave (solar) irradiance α_s solar absorption coefficient,
 $\alpha_l E_{sky}$: absorbed long wave (sky) irradiance α_l long wave absorption coefficient,
 $\varepsilon \sigma T^4$: surface emittance ε mean surface emission coefficient ($\varepsilon = \alpha_l$),
 Q_c : convective heat exchange,
 Q_{ec} : latent heat exchange.

Equation (4.3) looks treacherously simple, but depending on the type of surface and the meteorological conditions, it can become rather complex. In the next section, the various parameters in Eq. (4.3) are discussed and the required model input data addressed.

4.3.1 Solar heating

Solar radiation reaching the earth surface can be split into two components:

- (1) a direct component, i.e., sun-rays directly reaching the earth's surface without scattering in the atmosphere and therefore depending on the sun's altitude, and
- (2) a diffuse component, i.e., sun rays reaching the earth surface through multiple scattering in the atmosphere.

4.3.1.1 Solar absorption coefficient α_s

The solar absorption coefficient α_s is determined by the optical surface characteristics and is normally measured through the solar reflection coefficient ρ_s ($1 - \alpha_s$). Because solar radiation has a directional and diffuse component, the reflective properties of a surface are subdivided into a reflection coefficient for direct radiation, ρ_{sd} , and one for diffuse radiation, ρ_{sf} .

The reflection coefficient of flat, smooth surfaces (the dimension of the roughness elements is much smaller than the wavelength of the incident radiation, $d \ll \lambda$) shows a high specular (directional) component, while rougher surfaces ($d \approx \lambda$) show a more diffuse character. Generally, a mixture of both types is found for most surfaces. For solid materials with constant surface properties, such as color, roughness, etc., reproducible measurements can be carried out on sample surfaces and, therefore, mean values, which are found in the literature,¹ can be used. For porous materials like a soil^{7,8} and vegetation,⁹ the situation is different. Because of the varying physical and geometrical surface properties, ρ_s (in particular ρ_{sd}) changes continuously on a small time scale as well as over seasons, and the definition of a mean value becomes less meaningful. Figure 4.4 shows, as an example, the measured optical spectral properties of ears, stalks, and leaves of mature wheat⁹ and the underlying soil.

Theoretical derivations become mathematically complicated as soon as the geometrical structure of the surface, that is, the distribution of the roughness elements, becomes complex. In model calculations, these elements are given a certain spatial distribution and density, representing a specific stage during the growing process. Analytical models for calculating the optical characteristics of a canopy, based on a set of linear differential equations,^{10,11} produce satisfactory results for a number of situations. However, model performance completely depends on an accurate description of the geometrical structure and on the optical properties of the individual (roughness) elements that constitute the surface structure.

With stochastic models,¹² optical canopy characteristics can be calculated rather simply by using Monte Carlo or ray-tracing techniques. But again, detailed information on the roughness elements is required. The conversion from theoretical calculations to practical values is the final step, which is not an easy one to make.

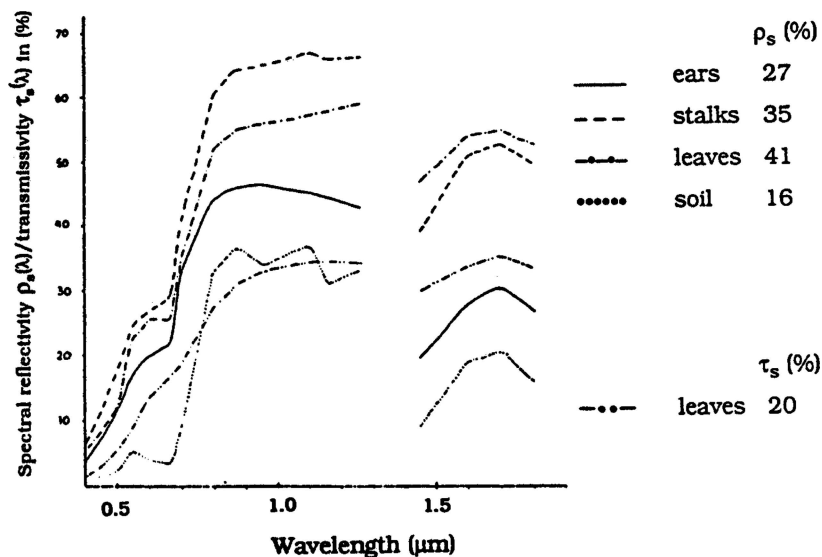


Figure 4.4 Optical spectral properties of mature wheat.⁹ Equation (4.4) was used to calculate ρ_s and τ_s .

The mean optical values are calculated by integrating the spectral reflectivity $\rho_s(\lambda)$, weighted by the distribution of radiation in the solar spectrum. This spectral distribution is close to the Planck's distribution of a blackbody at $T_{sun} = 6000$ K. This method can be used to determine average values for optical parameters, such as the reflection coefficient, ρ_s :

$$\rho_s = \int_0^3 \frac{\rho_s(\lambda)E(\lambda, T_{sun})}{E(\lambda, T_{sun})} d\lambda. \quad (4.4)$$

Furthermore, the reflection coefficient ρ_s strongly depends on the density of the foliage, that is, the optical depth (Fig. 4.5), vegetation height (Fig. 4.6), and soil moisture content (Fig. 4.7).

During the growing and maturing seasons, the leaf area density (LAD) of the canopy changes continuously and consistently. For wheat, for instance, the horizontal LAD decreases strongly because of the strong inclination of the leaves. Also, the chlorophyll absorption band at $0.665 \mu\text{m}$ disappears, while the steep rise in spectral reflectivity between $0.67 \mu\text{m}$ and $0.80 \mu\text{m}$ decreases considerably.

Figure 4.8 shows a comparison of the directional spectral reflectivity $\rho_s(\lambda)$ for wheat in May and August⁹ with comparable solar bearing and measuring position. Figure 4.9 shows a similar comparison for grass in August and October. The grass in August was freshly cut, a mixture of dry stubble and green leaves with a predominant vertical orientation leaving part of the soil unobscured; while in October the grass was much longer with a predominant horizontal orientation and completely covering the soil beneath.

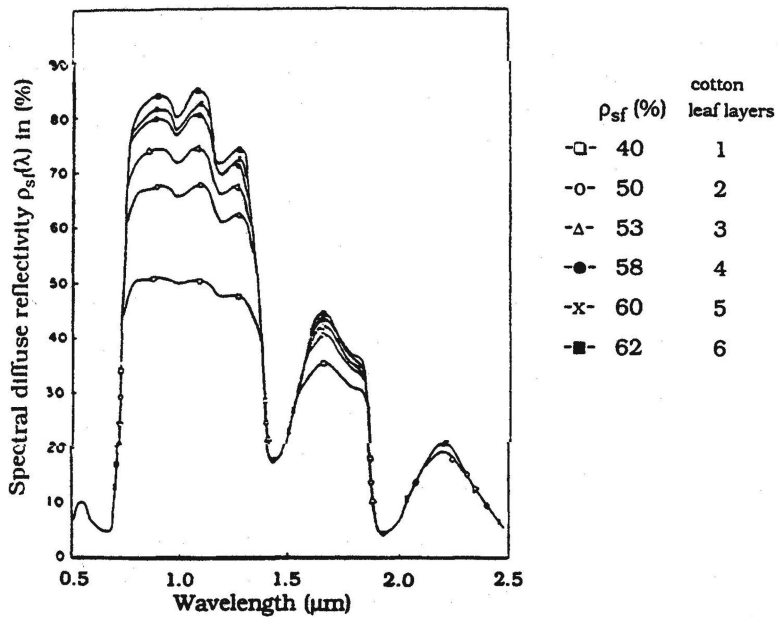


Figure 4.5 Diffuse spectral reflectivity $\rho_{sf}(\lambda)$ of six layers of stacked cotton leaves.⁹

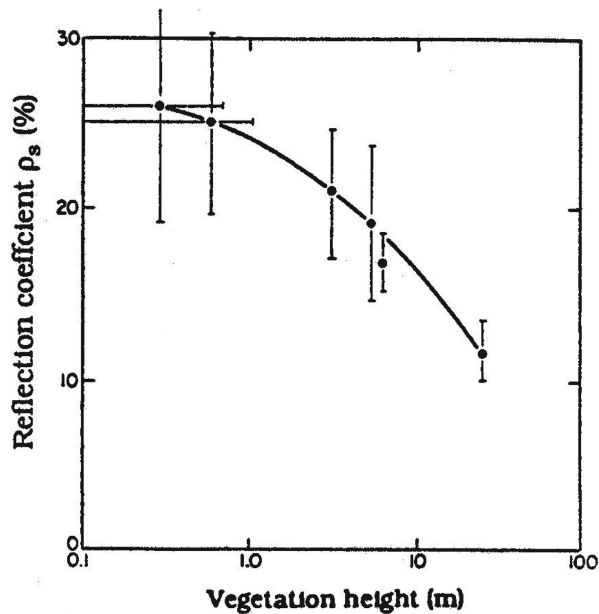


Figure 4.6 Relation between the vegetation height and the reflection coefficient ρ_s .⁸

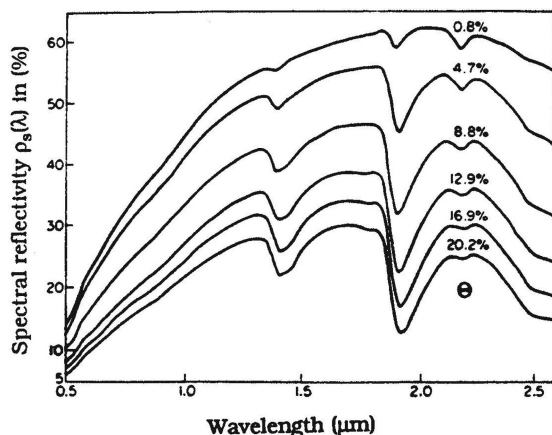


Figure 4.7 Spectral reflectivity $\rho_s(\lambda)$ of loam as a function of water content Θ .⁷

These figures clearly illustrate that seasonal average values for the reflection coefficient for this type of surface are not so meaningful, unless detailed information about the actual situation is available. For these complex surface structures, a direct measurement of ρ_s is the most satisfactory solution. But in

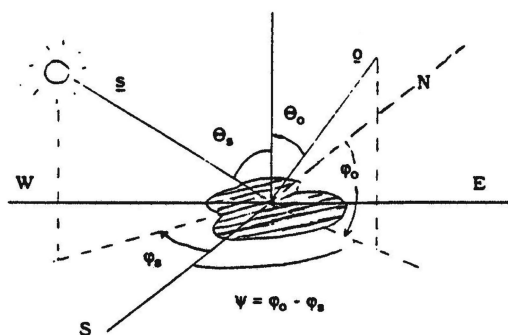
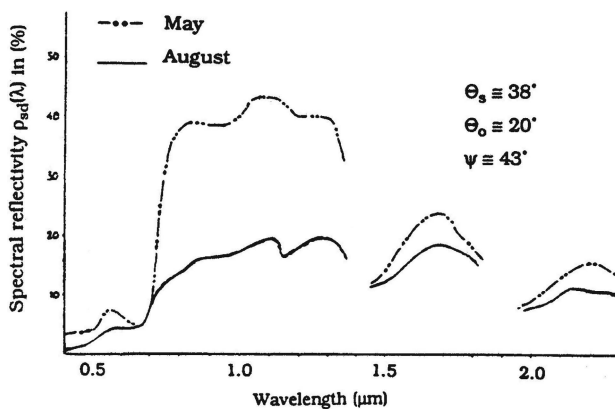


Figure 4.8 Comparison of the spectral reflectivity $\rho_{scf}(\lambda)$ for wheat in May and August.

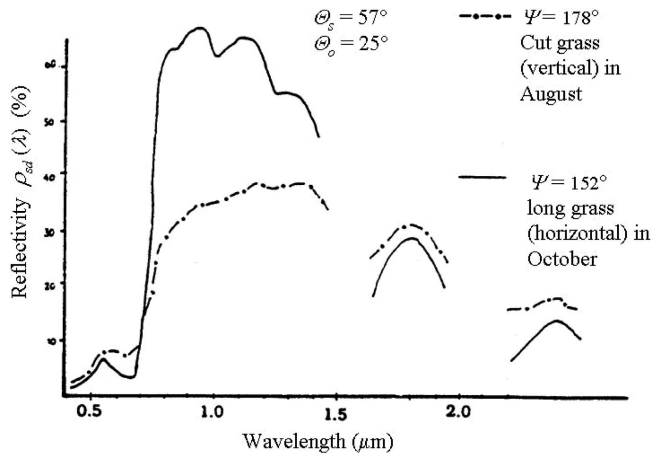


Figure 4.9 Comparison of the spectral reflectivity $\rho_{sc}(\lambda)$ for grass in August and October during a clear day.⁹

order not to disturb the actual surface conditions, samples cannot easily be taken away into the laboratory. Therefore troublesome measurements *in situ* (if suitable measurement systems exist) must be performed. Often, the sun is taken as the illuminating source (very much weather dependent), which presents various incident angles but limits the time available to perform a full measurement with constant solar bearing to a very small time window. Other systems use large, powerful artificial sources⁹ to obtain a good S/N ratio and a large target sampling area. This is especially important for very coarse and tall vegetation. Special optical components have to be used to obtain beam uniformity and have a good solar spectral match.

The conclusion is that a mean reflection coefficient has significance only for solid materials with constant surface properties. In all other cases, no more than a good guess can be made, depending on the availability of actual information. Published measurements of several crop types under various conditions⁹ can, to a limited extent, be used to estimate ρ_s .

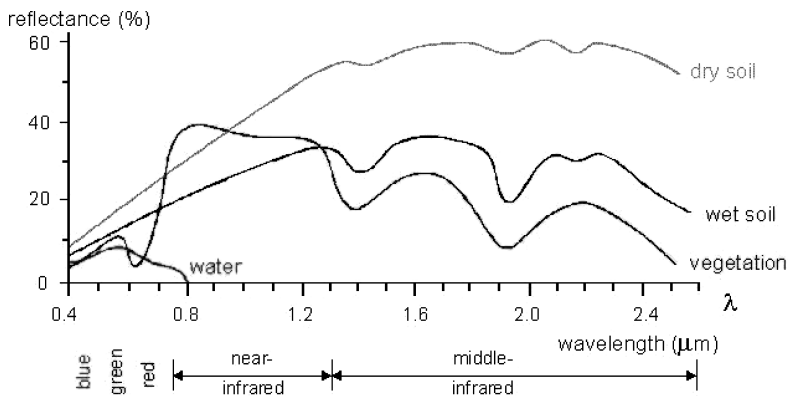


Figure 4.10 Reflectivity of some background elements.

4.3.1.2 Solar irradiance E_{sun}

Solar radiation reaching the earth's surface has a direct component, S , and a diffuse component, D , both depending on the azimuth and elevation angle of the sun. Since the absorption coefficient of a surface for direct and diffuse irradiance can differ, both solar components must be known separately. The radiation incident on a surface depends on the scattering and absorption processes in the atmosphere^{14,15} and on the shape and orientation of the surface.¹⁶

Atmospheric attenuation depends on the type of air (maritime, rural, urban) and therefore depends on the geographical location and local weather conditions. Consequently, theoretical expressions will always contain a number of empirical parameters that have to be measured locally. Direct measurement, not more complicated atmospheric-propagation measurement, is the most convenient and direct way to determine the solar irradiance at a surface. Generally, two instruments are sufficient to determine the irradiance: a pyrheliometer to measure the solar irradiance at normal incidence, S_n , and a solarimeter to measure the sum of direct and diffuse incident irradiance on a horizontal plane, i.e., the global irradiance, S_g . By using a shading ring on the solarimeter, the hemispherical diffuse solar irradiance is measured, because the ring blocks the direct solar irradiance.

For a clear day, the relation between S_n and the diffuse irradiance on a horizontal plane D_h can be represented¹⁹ by

$$D_h = \frac{(\zeta_s - S_n)\sin(\vartheta_s)}{3} \quad (\text{W m}^{-2}), \quad (4.5)$$

where ϑ_s : sun elevation angle and
 ζ_s : solar constant, given by

$$\zeta_s = 1353 \left\{ 1 + 0.0338 \cos \left[\frac{2\pi(n-3)}{365} \right] \right\} \quad (\text{W m}^{-2}),$$

and n : the Julian day.

The total absorbed radiation for a horizontal surface, Q_h^s is

$$Q_{sun}^h = \alpha_s E_{sun}^h = \alpha_{sd} S_n \sin(\vartheta_s) + \alpha_{sf} D_h.$$

The diffuse irradiance at a vertical plane D_v depends on the solar incident angle v_s , i.e., the angle between the normal of the surface and the solar bearing (Fig. 4.11), expressed as

$$\cos(v_s) = \cos(\vartheta_s) \cos(\varphi_s - \varphi),$$

where φ : azimuth angle between north and the surface azimuth, and
 φ_s : sun azimuth angle.

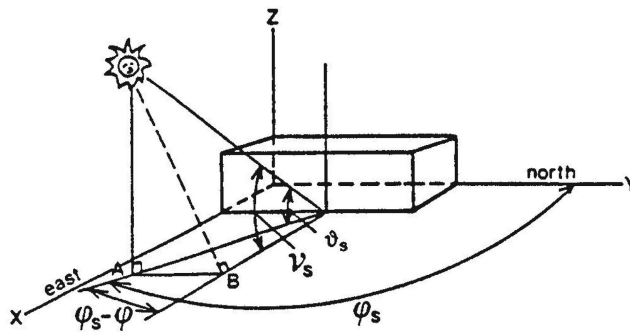


Figure 4.11 Surface and solar related angles.

Two situations are distinguished:

(a) $\cos(\nu_s) \geq -0.3$

$$D_v = D_h[0.56 + 0.436 \cos(\nu_s) + 0.35 \cos^2(\nu_s)],$$

(b) $\cos(\nu_s) < -0.3$

$$D_v = D_h[0.473 + 0.043 \cos(\nu_s)].$$

Figure 4.12, as an example, shows the calculated values for a horizontal surface and a south-facing vertical surface on a clear day in July.

Similarly, the total absorbed radiation for a vertical surface is

$$Q_{sun}^v = \alpha_s E_{sun}^v = \alpha_{sd} S_n \cos(\vartheta_s) + \alpha_{sf} D_v.$$

Since a pyrheliometer is usually not part of a weather station, in many situations the solar irradiance at normal incidence is not available. For clear skies,

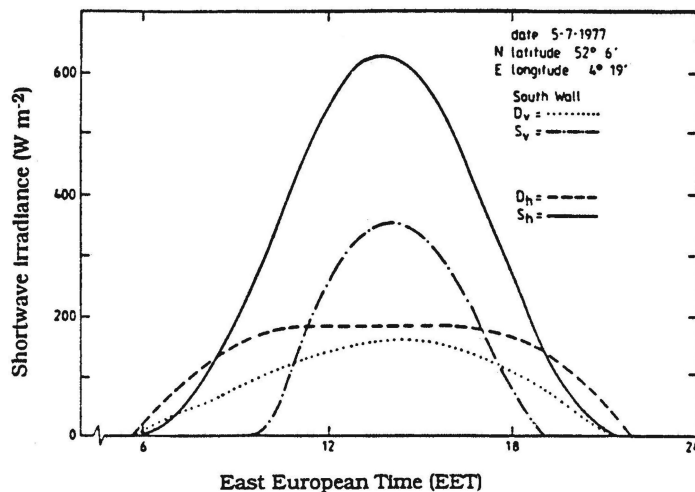


Figure 4.12 Calculated solar irradiance at various oriented surfaces.

this problem can be overcome by taking the global irradiance, S_g , as a starting point from which to calculate the various solar components on different oriented surfaces. In this case (i.e., clear-sky conditions) S_n can be calculated¹⁹ from Eq. (4.5) by putting $S_g = S_n \sin(\vartheta_s) + D_h$, and rewriting S_n explicitly as

$$S_n = \frac{3S_g - \zeta_s \sin(\vartheta_s)}{2 \sin(\vartheta_s)}$$

Some care must be taken when this method is used with low sun elevations (the nominator becomes very small).

The problem becomes more complicated if clouds are involved. In that case, for the surface energy budget, only two situations can occur: either the surface is sunlit or it is not. So, for the calculation of the direct component, a parameter like cloud cover is not particularly meaningful.

Although many measurements of cloud radiation for different types of clouds have been carried out,¹⁷ no simple, practical models yet exist. Models can describe the fundamental physics of radiative transfer in clouds,¹⁸ but again depend very much on empirical factors. Figure 4.13 shows some empirical relations¹⁶ between solar radiation and solar angle for different cloud types.

For the heat budget, it is important to know whether the sun shines through the clouds onto the surface or is obscured by a cloud. The heat balance for these two situations is completely different. This is the reason that, for an arbitrarily oriented surface under cloudy conditions, it is so difficult to calculate the diffuse solar component D , even if S_g and/or S_n are known. Even for clear skies this is difficult, because the half hemisphere to which the surface is exposed is composed of some part of the sky and some part of the terrestrial background.

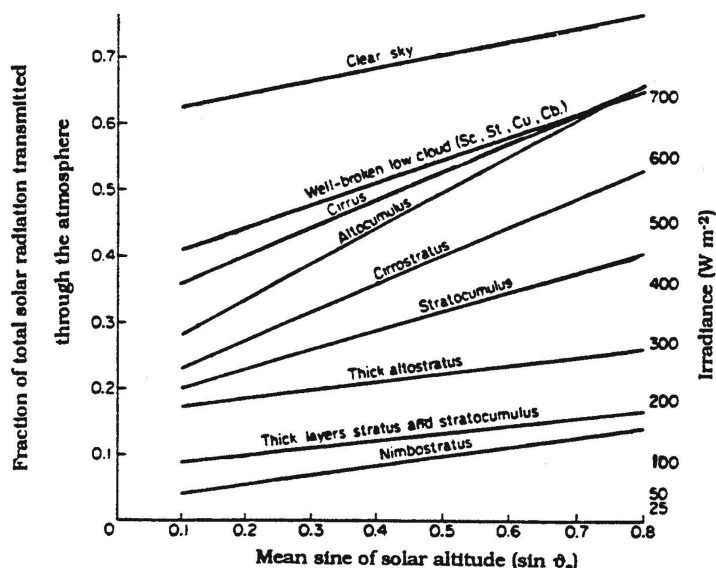


Figure 4.13 Empirical relation between solar radiation and solar angle for different cloud types (52 deg N, 20 deg W).²¹

To calculate the total irradiance at an arbitrarily oriented surface, information is needed about the solar radiance distribution over the sky-hemisphere.¹⁹ However, the problem of radiation reflected from the environment remains largely unsolved and can often only be roughly estimated.

4.3.2 Long-wave radiation exchange

The long-wave radiation exchange of a surface is derived from the balance between received environmental radiation (sky and background) and emitted radiation by the surface. For a nonhorizontal surface, the received radiation is a mixture of terrain and sky radiation. On many occasions, the sky-hemisphere and terrain backgrounds can be approximated by diffuse (black or graybody) radiators, and consequently only the diffuse long-wave properties of the surface must be considered. Moreover, many natural surfaces exhibit a diffuse reflective behavior. However, under very inhomogeneous cloud distributions, directional influences may have to be taken into account.

4.3.2.1 Long-wave absorption coefficient α_l

Since the emission coefficient ε and absorption coefficient α_l are equal (Kirchoff), they can be treated in the same way. For most natural surfaces, the emission coefficient has a predominant diffuse behavior and is, as in the case of the short-wave reflection coefficient, determined by the surface properties. Practical models for calculating the emission coefficient do not exist, and in this case measured values are the only available option left.²² For many manmade materials with constant surface properties, the mean emission coefficient has been measured this way and can be found in literature.²⁰

For materials of which a representative sample can be heated to a temperature T_s , the emission coefficient can be determined directly from

$$\varepsilon = \frac{\int_{\lambda_o} M(\lambda, T_{ap}) d\lambda}{\int_{\lambda_o} M(\lambda, T_s) d\lambda} \quad \text{or} \quad \varepsilon = \frac{\int_o^\infty M(\lambda, T_{ap}) d\lambda}{\int_o^\infty M(\lambda, T_s) d\lambda} = \left(\frac{T_{ap}}{T_s} \right)^4,$$

where T_{ap} is, for instance, measured with a hand-held radiometer (and neglecting reflected environmental radiation).

However, this technique only applies to a very limited number of materials, because either they cannot be heated to the required temperature without changing some of the material properties or representative samples cannot be taken without disturbing the original surface (and bulk) properties. In the latter case, measurements have to be performed *in situ*. This can be done indirectly, by measuring the reflection coefficient ρ_l and from that calculating the emission coefficient as $\varepsilon = 1 - \rho_l$. In Section 7.1.1, a portable system is described for performing this type of measurement quickly and easily (diffuse-diffuse emission coefficient).

4.3.2.2 Long-wave sky irradiance E_{sky}

If the atmosphere in a solid angle (φ, ϑ) has a mean emission coefficient $\varepsilon_a(\varphi, \vartheta, \lambda)$ and a mean air temperature $T_a(\varphi, \vartheta)$, the sky irradiance, E_{sky} , at the surface can be found from

$$E_{sky} = \int_0^{2\pi} d\varphi \int_0^{\pi/2} \int_{\lambda_0} g(\varphi, \vartheta) \varepsilon_a(\varphi, \vartheta, \lambda) M[\lambda, T_a(\varphi, \vartheta)] d\lambda d\vartheta, \quad (4.6)$$

where $g(\varphi, \vartheta)$ is a geometrical factor accounting for the orientation of the surface.

MODTRAN can solve this equation directly using either standard atmospheres (supplied with the computer program) or actual weather data.

Often Eq. (4.6) is simplified by assuming that the solid angle of atmosphere is a solid gray radiator [$\varepsilon_a(\varphi, \vartheta, \lambda) = \varepsilon_a(\varphi, \vartheta)$ independent of λ] at air temperature T_a , and having an emission coefficient $\varepsilon_a(\varphi, \vartheta)$, leading to

$$E_{sky} = \int_0^{2\pi} d\varphi \int_0^{\pi/2} g(\varphi, \vartheta) \varepsilon_a(\varphi, \vartheta) \int_{\lambda_0} M(\lambda, T_a) d\lambda d\vartheta. \quad (4.7)$$

Clear skies show hardly any dependence of the emission coefficient^{23,24} on the azimuth angle φ . A most commonly adopted description for $\varepsilon_a(\varphi, \vartheta)$ for this case is

$$\varepsilon_a(\vartheta) = a_1 + a_2 \sqrt{e} + a_3 \ln[\sin(\vartheta)], \quad (4.8)$$

where e : water vapor pressure (hPa), and

a_1, a_2, a_3 is determined by experiment.

Solving Eq. (4.7) for a horizontal surface and using Eq. (4.8) leads to a Brunt type formula,²⁷

$$E_{sky} = (a + b\sqrt{e})\sigma T_a^4 = \varepsilon_a \sigma T_a^4, \quad (4.9)$$

with a_1 and a_2 to be determined by experiment.

From several experiments at locations in England and the United States, Unsworth²³ determined values for the constants a_1 and a_2 , ranging from $0.51 < a_1 < 0.60$ to $0.059 < a_2 < 0.065$. Mean values are listed as $a_1 = 0.58$ and $a_2 = 0.061$. Measurements carried out by Wartena²⁶ over various seasons at Wageningen in the Netherlands resulted in values ranging between $0.60 < a_1 < 0.75$ and $0.017 < a_2 < 0.057$. Figure 4.14 shows the atmospheric emission coefficient as a function of elevation angle for these ranges of a_1 and a_2 .

Measurements of the empirical constants in Eqs. (4.8) and (4.9) in various parts of the world show a strong dependence on the geographical location, i.e., on the temporary composition of the local atmosphere. In most cases, however, the spread is not so critical, and with the use of the best choice leads to a 10–20% inaccuracy in the sky radiance contribution. However, if during circumstances in which E_{sky} is the major contributor (for example, a clear, calm night) to the total heat budget or is of the same order of magnitude as the other heat-transfer flows, then this may lead to quite erroneous temperature calculations.

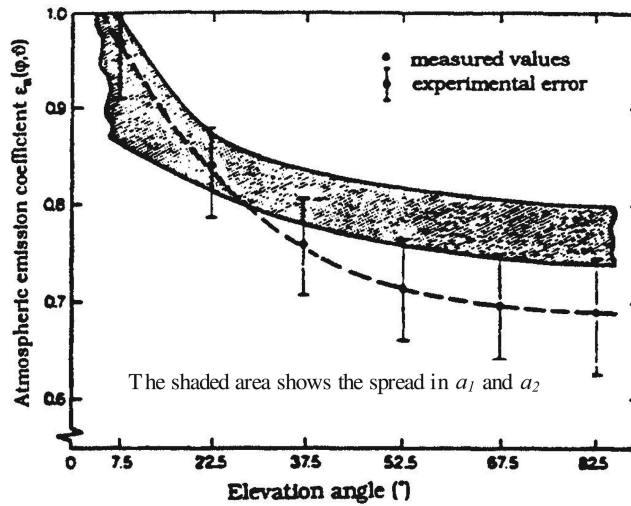


Figure 4.14 Atmospheric emission coefficient $\varepsilon_a(\vartheta)$ vs. ϑ on a clear night.¹⁹

To solve Eq. (4.6) for a clouded sky, the cloud type and cloud distribution must be known.²⁷ This will rarely be the case and therefore statistical theoretical expressions are derived from experimental data. This is most conveniently done through the emission coefficient $\varepsilon_a(c)$ of a cloud,^{16,23} taken as

$$\varepsilon_a(c) = \varepsilon_a(1 + nc^2) \quad \text{and} \quad E_{cl}(c) = \varepsilon_a(c)\sigma T_{cl}^4,$$

where c : degree of cloud cover,
 T_{cl} : cloud base temperature,
 E_{cl} : cloud emittance, and
 n : empirical factor, ranging from 0.2 to 0.04 for low and high clouds, respectively.

The total sky irradiance on a horizontal plane is the sum of the irradiance of the clouds and the clear sky:

$$E_{sky} = (1 - c)\varepsilon_a\sigma T_a^4 + \varepsilon_a(c)\sigma T_{cl}^4.$$

This equation again contains a number of parameters that hardly have a theoretical foundation and only can be roughly estimated.

At this point, it is important to realize that both radiation terms E_{sun} and E_{sky} are statistical correlations, implicating that they are accurate under average conditions but not accurate enough to describe short-term variations. In cases where micro-meteorological analyses on a small time scale (i.e., a few hours) are required, these equations do not apply.

4.3.3 Surface emittance E_s

The emission coefficient of a surface was discussed in Section 4.3.2.1, and there is no more to tell, other than that the temperature T_s is the dominant part in the equation for the surface emittance, $E_s = \varepsilon_s \sigma T_s^4$. Finally, the net result of incoming and outgoing long-wave radiation, E_l^{net} is

$$E_l^{net} = [pE_{sky} + (1 - p)E_{env}] - \varepsilon_s \sigma T_s^4,$$

where p : fraction of the sky viewed by the surface (view factor³²),
 E_{env} : radiation contribution of the environment.

The associated absorbed heat flux Q_l^{net} is

$$Q_l^{net} = \alpha_l [pE_{sky} + (1 - p)E_{env} - \sigma T_s^4].$$

4.3.4 Convective heat exchange Q_c

Convective heat exchange is the transport of heat from or toward a surface by motion of the surrounding fluid. This type of heat transfer depends on target geometry, fluid dynamics, and fluid properties (in this case, the transport medium is air). The flow can be either laminar or turbulent. The transition between the two flow types is governed by the Reynolds number, N_{Re} , a dimensionless flow parameter given by

$$N_{Re} = \frac{vd}{\nu},$$

where v : wind speed (m s^{-1}),
 d : target characteristic length (m),
 ν : kinematic viscosity ($\text{m}^2 \text{s}^{-1}$).

The heat-exchange mechanism can be either free or forced, governed by the ratio of buoyancy to inertial forces, i.e., the ratio of N_{Gr} over the squared N_{Re} . The Grashof number, N_{Gr} , another dimensionless flow parameter, is given by

$$N_{Gr} = \frac{\beta g d^3 (T_s - T_a)}{\nu^2},$$

where β : coefficient of thermal expansion of air (K^{-1}),
 g : acceleration of gravity (m s^{-2}).

In the situation of a flat surface in thermal equilibrium with air flowing over it, expressions for Q_c have been determined from wind-tunnel experiments for a

number of simple geometries and for laminar and turbulent flow.¹⁶ These expressions are represented by

$$Q_c = h_c \Delta T = \frac{\lambda_a}{d} \left\{ \begin{array}{l} a(N_{Re})^n \\ b(N_{Gr})^m \end{array} \right\} \Delta T \begin{array}{l} \longrightarrow \text{forced convection} \\ \longrightarrow \text{free convection} \end{array}, \quad (4.10)$$

where h_c : convective heat transfer coefficient ($\text{W m}^{-2} \text{K}^{-1}$),
 λ_a : thermal conductivity of air ($\text{W m}^{-1} \text{K}^{-1}$),
 ΔT : temperature difference between the surface and free air, while
 (a, b) and (m, n) depend on the geometry and flow type.

Experimental data for a 3D block obstacle were successfully fitted to equations,²⁸ such as the example shown in Fig. 4.15. The figure shows the dependence of the heat transfer coefficient h on the wind speed v . The straight lines represent a fit to $h_c = bv^m$ for a horizontal surface and the average for the combined vertical surfaces of a 3D block obstacle.

Orientation	b	m	Δh_c (rms)
Horizontal	10.5	0.57	2.1
Vertical, windward	7.9	0.57	1.6
leeward	7.9	0.30	1.8

Figure 4.16 shows the dependence of h_c on the wind direction Φ_v for the west-facing surface of the same 3D obstacle for wind speeds of 2 and 4 m s^{-1} .

So far, only limited studies have been carried out to investigate convective heat exchange of obstacles under outdoor atmospheric conditions. This might be the

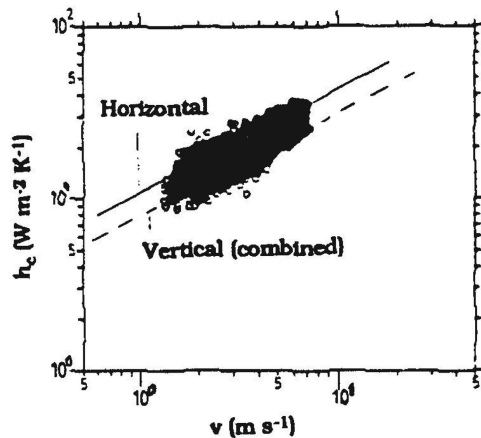


Figure 4.15 Convective heat transfer coefficient h_c as a function of wind speed v for a 3D obstacle.²⁸

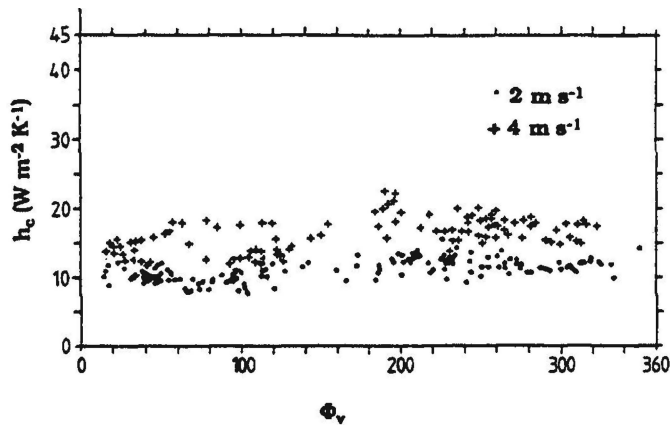


Figure 4.16 Convective heat-transfer coefficient h_c as a function of wind direction Φ_v for a west-facing surface.

reason that in many models convective heat exchange is still represented by equations (mostly derived in a wind tunnel) that may be quite erroneous under the given circumstances. A surface exposed to atmospheric conditions rarely is in thermal equilibrium with the air flowing over it, and turbulence within the boundary layer is the main transfer mechanism between the surface and the free atmosphere. Under these circumstances, equations such as those in Eq. (4.10) no longer apply.

Heat transfer by turbulence, described by the transfer coefficient K_H , is analogous to the process of turbulent momentum transfer described by the transfer coefficient, K_M . The relationship between these coefficients depends on atmospheric stability and many partly conflicting papers have been published on this topic. For simplicity, in many analyses K_M and K_H are assumed to be equal, which is a reasonable assumption in the case of a stable atmosphere (i.e., increasing temperature with height) and also during moderately unstable atmospheric conditions (for unstable conditions $K_M > K_H$).

Again, it is beyond the scope of this book to elaborate in detail on this problem, but the relevant results of the commonly accepted Monin-Obukhov similarity theory is presented to illustrate what kinds of equations and parameters are involved. In this theory, the atmospheric surface layer is described by an independent variable, the length scale, L , assuming horizontal homogeneity (for instance, a large area of grass) and steady-state conditions. The turbulent heat exchange, that is, the dissipation of energy by mechanical turbulence and the production of energy by buoyancy forces, is described by L and the Richardson number, N_{Ri} , a dimensionless flow parameter, which is a measure of atmospheric stability, given by

$$N_{Ri} = \frac{g \left(\frac{\partial T_a}{\partial z} \right)}{T_a \left(\frac{\partial v}{\partial z} \right)}.$$

The Monin-Obukhov length scale L is given by

$$L = -\frac{\rho_a C_p T_a u_*^3}{kgQ_c},$$

where ρ_a : density of air (kg m^{-3}),
 u_* : friction velocity (m s^{-1}),
 z : vertical coordinate (m),
 k : von Kármán constant,
 C_p : specific heat of air ($\text{J kg}^{-1} \text{K}^{-1}$).

The relation between N_{Ri} and L is simply given by

$$N_{Ri} = \frac{z}{L}.$$

The friction velocity u_* is determined from the wind profile, which is given by²⁹

$$v - n(z - d) \frac{g}{T_a} \left(\frac{\partial T_a}{\partial v} \right) = \frac{u_*}{k} \ln \left(\frac{z - d}{z_o} \right), \quad (4.11)$$

where n : experimental number ($n \cong 5$),
 h : vegetation height (m),
 z_o : roughness length ($z_o \cong 0.13 h^{0.997}$) (m),
 d : zero displacement level ($d \cong 0.7 h^{0.979}$) (m).

Figure 4.17 shows the change of d and z_o with u_* for maize¹⁶ and Fig. 4.18 illustrates the graphical solution of u_* from Eq. (4.11). Finally, Q_c is

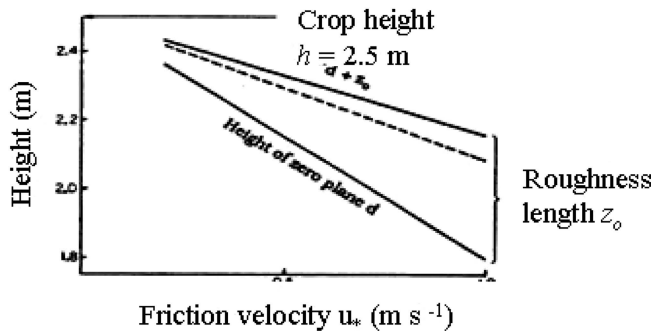


Figure 4.17 The change of d and z_o with u_* for maize.³²

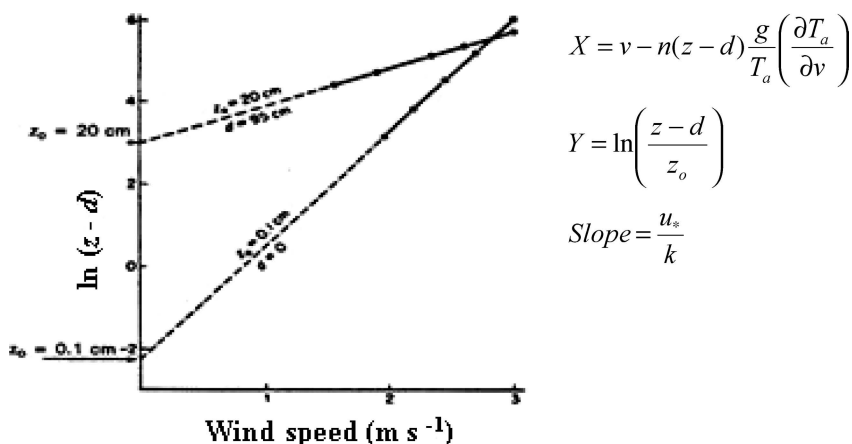


Figure 4.18 Graphical representation to solve u_* .¹⁶

calculated from

$$Q_c = -\rho_a C_p u_*^2 \frac{g \left(\frac{\partial T_a}{\partial z} \right)}{T_a \left(\frac{\partial v}{\partial z} \right)}. \quad (4.12)$$

From the previous set of equations, it is obvious that a large array of input variables is required. Special equipment and a large (uniform) measurement area are needed to collect data for just that one type of surface.

The outlined analyses can only be applied for steady-state conditions, i.e., in situations in which the various atmospheric profiles are well established. After having passed an obstacle (for instance, a tree line) with an aerodynamic height h , steady-flow conditions only reestablish after a distance of $100h$. This means that a large uniform area is required to perform undisturbed measurements. For instance, for a height of 15 m, the upstream obstacle-free distance must be 1.5 km! The required input data normally is not available and therefore, in many models with any practical significance, simplified versions must be used instead.

4.3.5 Heat exchange by evaporation/condensation Q_{ec}

Following the same aerodynamic method as was used for the convective heat exchange in the previous section, it can be shown that the transport of latent heat, Q_{ec} , is given by

$$Q_{ec} = -L_h u_*^2 \frac{\left(\frac{\partial \chi}{\partial z} \right)}{\left(\frac{\partial v}{\partial z} \right)}, \quad (4.13)$$

where L_h : latent heat of vaporization of water (4.2 J kg^{-1}),
 χ : absolute atmospheric humidity (g m^{-3}).

To incorporate this transport mechanism in the analysis, another atmospheric height profile (the absolute humidity or some related parameter, such as the atmospheric water vapor pressure e), has to be available. The relation between the water vapor pressure and the absolute humidity can be approximated by

$$e = \frac{\chi T_a}{217}$$

where T_a = kelvin.

The relative humidity, RH, is defined from

$$\text{RH}(\%) \cong \frac{\chi T_a}{e_s(T_a) 217} \times 100\%.$$

If the absolute humidity profile in Eq. (4.13) is positive with z , i.e., transport of vapor toward the surface, then condensation takes place only if the local air temperature drops below the dew-point temperature, T_d . In such a case, the amount of energy Q_{ec} (heat of condensation) is released to the environment, preventing the surface from cooling down further, e.g., condensation takes place under constant temperature.

The dew-point temperature, T_d , is found from

$$T_d = T_a \left\{ \frac{[e_s(T_a) - e(T_a)]}{\Delta} \right\},$$

where e_s : saturation vapor pressure (hPa),
 T_a : air temperature (K),

where

$$e_s(T_a) \cong 23.7910^{-3} T_a \exp[0.06(T_a - 273)],$$

and

$$\Delta = \frac{\partial e_s}{\partial T_a} \cong \frac{e_s(T_a)}{T_a} (1 + 0.06 T_a) \quad (\text{hPa K}^{-1});$$

Δ is called the saturation deficit.

For bodies with a large heat capacity, the energy transfer resulting from this transport mechanism is not taken into account because the energy involved is small compared to the heat flows normally involved in such heavy bodies. However, for materials with a small heat capacity, such as leaves and thin metals (as in a car), often condensation occurs. One important characteristic of dew is that it prevents the surface from cooling down further, which creates an extra temperature difference over surfaces without condensation. Especially, in the late evening on clear days, when condensation starts, this may enhance the contrast (in a positive sense) between a target and background. Also, the water layer changes the optical (infrared) surface properties, which also influences the observed apparent temperature.

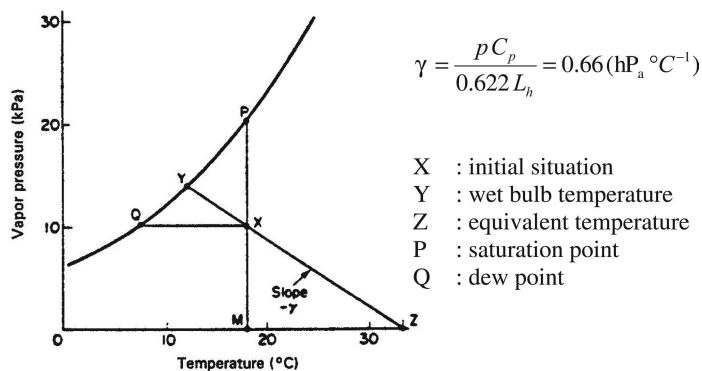


Figure 4.19 State diagram for humid air.¹⁶

For evaporation, the theory is similar but of opposite sign; that is, heat is used to evaporate the water, and consequently the temperature of the body does not increase further until the water is evaporated. Also, in this case, the temperature contrast with nonevaporating surfaces may be enhanced. Especially in the early morning after a cool, clear night, this may enhance the contrast (in a negative sense) between a target and background.

However, under normal outdoor conditions, the influence of both heat flows is of short duration, but could be critical. Figure 4.19 shows the state diagram for humid air. This diagram shows the equilibrium between the vapor and liquid water phase (the line YQP). Left of this line is the liquid phase. If X is the starting point, then increasing the humidity of the air sample at a constant temperature increases the water vapor pressure until point P is reached. Further increasing the humidity leads to condensation. Similarly, when the temperature is lowered at a constant vapor pressure, condensation begins at point Q.

4.4 First Principles Modeling

It is understood that the foregoing analysis is far from complete. However, it clearly demonstrates the large quantity of materials and atmospheric parameters that play a role in the thermodynamics of bodies in the atmospheric boundary layer. A complete picture of this problem area is given by Balick.² A major conclusion is that most modeled processes, in spite of the fact that they underlie some theory, are largely determined by empirical constants. Model performance in general is therefore limited by these empirical factors and not by theory or by numerical problems. Because of this strong dependence, the models cannot be extended easily to different surface types or geographical locations without considerable loss of realism. It might be clear that for accurate model predictions, many input parameters, depending on the local situation, have to be measured.

A second important conclusion is that models requiring many specific input parameters are not well suited to study infrared signatures in practice because

these input parameters are normally not available. But, as stated earlier, these models are most beneficial for determining the relative importance of parameters and, through that, to define measurement accuracies and find justified model simplifications.

In the next section, the limitations of theoretical first-principle models are discussed by varying the most relevant input parameters. For this purpose, the straightforward explicit finite difference numerical scheme is used, applied to the simple geometry of a horizontal slab of concrete, 15-cm thick and laid out over a sandy soil.

4.4.1 Model definition

The complicated nonlinear boundary conditions, as described in the previous sections, require that the equation for the conduction of heat (4.2) be solved numerically.³³ First-principle models were applied to simple geometries, such as a flat asphalt/concrete road or a brick wall²⁸ under clear or overcast conditions, and gave encouraging results. These models were extended to incorporate more difficult geometries and varying meteorological conditions, eventually becoming quite complex. To handle these complex situations, equations for the heat exchange processes are often simplified by, for instance, introducing empirical constants. Often, models are only validated for one vegetation type for a short period of time, i.e., one type of weather, because the effort is too demanding to afford a second one. It is therefore important to determine (1) the sensitivity of the model to the governing (input) parameters, and (2) whether these parameters are available or can be made available with the required accuracy.

In the following analyses, the discussions are limited to those parameters that are difficult to measure with high accuracy (being surface and time dependent) and that consequently can make a large contribution to model errors. A comprehensive parameter analysis is also given by Balick.² For reasons of simplicity, an explicit finite difference method is used here to solve a 2D model of a horizontal slab of concrete placed on a layer of sandy soil. It is furthermore assumed that the vertical dimensions are much smaller than the horizontal dimensions and, e.g., only vertical transports must be considered. This sandwichlike structure is divided into a number of layers, representing a medium of homogeneous and isotropic (constant) physical properties (Fig. 4.20).

On *each* layer n , a rectangle $[(z, t) | 0 \leq z \leq L_n \wedge 0 \leq t \leq t_{max}]$ of discrete net points (z_i, t_j) is placed (L_n is the layer thickness). These net points are subject to the constraints

$$\begin{aligned} z_1 &= 0, \quad z_{N_1} = L_n, \quad t_1 = 0, \quad t_M = t_{max}, \\ h &= z_{i+1} - z_i \{ \forall i \in [2, N_1 - 1] \cap |N \}, \\ k &= t_{j+1} - t_j \{ \forall j \in [2, M - 1] \cap |N \}. \end{aligned}$$

The implementation of a finite-difference method is based upon the division of the heat flow into discrete intervals in space, h and time, k . The temperature

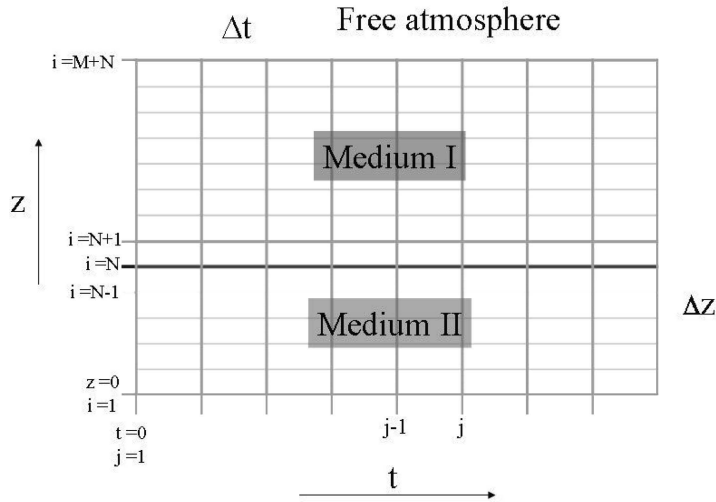


Figure 4.20 Rectangular grid of net points (z_i, t_j) .

change of all layers is computed and updated in these (discrete) intervals (grid net points). The top layer represents the surface, which is situated at the atmospheric-ground boundary layer. The partial differential equation (4.2) for the flow of heat is approximated by a finite-difference equation. The boundary conditions at the top and bottom of the sandwich structure are also evaluated in the net points.

Expressed in finite differences, the derivatives with respect to time and space take the form

$$\frac{\partial T(z, t)}{\partial z} = \frac{T_{i+1}^j - T_i^j}{h} \quad \text{and} \quad \frac{\partial T(z, t)}{\partial t} = \frac{T_i^{j+1} - T_i^j}{k}.$$

For the second-order derivative,

$$\frac{\partial^2 T(z, t)}{\partial z^2} = \frac{T_{i+1}^j - 2T_i^j + T_{i-1}^j}{h^2}.$$

Applied to the example of a concrete slab (medium I) on sand (medium II), the equation for the flow of heat in a solid Eq. (4.2) transforms to (Fig. 4.21):
Medium I,

$$T_i^{j+1} - T_i^j = \kappa_1 R(T_{i+1}^j - 2T_i^j + T_{i-1}^j),$$

where

$$\begin{aligned} i = N_1 &\equiv z = L_1, \\ i = N_1 + N_2 &\equiv z = L_1 + L_2, \\ \{\forall i \in [N_1 + 1, N_1 + N_2 - 1] \cap |N\}. \end{aligned}$$

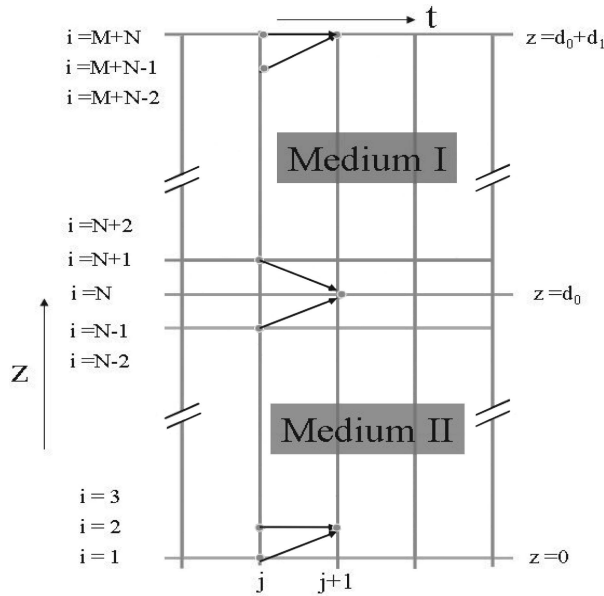


Figure 4.21 Finite-difference scheme in the net points (z, t) .

Medium II,

$$T_i^{j+1} - T_i^j = \kappa_2 R (T_{i+1}^j - 2T_i^j + T_{i-1}^j),$$

where

$$\begin{aligned} i = 1 &\equiv z = 0, \\ i = N_1 &\equiv z = L_1, \\ i = N_1 + N_2 &\equiv z = L_1 + L_2 \\ \{\forall i \in [2, N_1 - 1] \cap |N|\}, \end{aligned}$$

and

$$R = \frac{k}{h^2}.$$

The heat flow between both media (at $z = L_1$) is derived from the continuity equation, i.e., equalizing the heat flow at the boundary of both media, leading to the boundary temperature, T_{N_1} , determined from

$$\lambda_1 \left[\frac{\partial T(z, t)}{\partial z} \right]_{\uparrow z=L_1} = \lambda_2 \left[\frac{\partial T(z, t)}{\partial z} \right]_{\downarrow z=L_1},$$

or in discrete form,

$$T_{N_1}^{j+1} = \frac{\lambda_1 T_{N_1-1}^{j+1} + \lambda_2 T_{N_1}^{j+1}}{\lambda_1 + \lambda_2}.$$

The surface temperature $T_{N_1+N_2}$ (top layer in the concrete, at $z = L_1 + L_2$), is:

$$\lambda_1 \left[\frac{\partial T(z, t)}{\partial z} \right]_{z=L_1+L_2} = Q(t) \quad \text{or} \quad T_{N_1+N_2}^{j+1} - T_{N_1+N_2-1}^{j+1} = \frac{h}{\lambda_1} Q^{j+1},$$

where Q^{j+1} is determined by the heat balance equation given in Eq. (4.3).

Finally, the boundary condition in the sand (at $z = 0$) and the initial condition are derived as

$$T_0^{j+1} = T_{constant} \quad \text{and} \quad T_i = T_{initial} \quad \{\forall i \in [0, N_1 + N_2], \forall j \in [j \leq t_o] \cap \mathbb{N}\}.$$

One of the main disadvantages of the explicit finite-difference method is the conditional stability of the numerical scheme, in order to obtain a converging solution. This means that a free choice of combinations of the step size in space and time are limited and ruled by the stability criterion. This criterion combines the thermal diffusivity (κ_1 and κ_2) and numerical parameters (k and h) as

$$2R \leq \min\{\kappa_1^{-1}, \kappa_2^{-1}\}.$$

The condition implies that for a large time step, which is most practical, a small step-size in space is enforced. For many natural materials, the thermal diffusivity is of the order of 10^{-6} ($\text{m}^2 \text{s}$), leading to $h \cong 1$ cm and $k \cong 1$ min, which normally leads to acceptable computing times. Generally, a much finer grid has to be used for materials with a high thermal diffusivity (thermal conductors), and this can lead to unacceptably long computing times. The alternative implicit calculation method is unconditionally stable, but the numerical scheme is more complicated. For complex structures, finite-elements methods (FEM) are more suitable.

4.4.2 Sensitivity analysis

The temperature change of the surface of a material resulting from a change of a specific weather or material parameter is different for many materials and is determined by the interaction of parameters in the heat balance. To determine the sensitivity of the model, i.e., the sensitivity of the predicted temperature for a specific parameter, model calculations are performed repeatedly for various values. The outcome gives an indication of the required accuracy at which the parameter should be available in order to obtain an accurate temperature prediction. Calculations were performed on a concrete slab using a 1D numerical model, which was discussed in the previous sections.

At first, the model was tested against measurements to check its performance. These measurements were carried out on a concrete slab placed outside in Gilze Rijen Air Force base in the Netherlands (51 deg 34'N, 4 deg 56'E). The physical (real) temperature and apparent temperature were measured at intervals of 15 minutes. Temperature profiles in the concrete and the underlying soil were measured with thermocouples. A weather station was set up near the concrete, measuring a number of required model-input parameters. The measurements were carried out as a part of a large-scale exercise, which is described in more detail in Section 7.2.2.1.

The real temperature of the concrete surface was calculated using measured physical data combined with some “best guesses” for unknown parameters taken from existing literature (the solar absorption coefficient and some soil parameters). Calculations were performed for two more or less extreme weather situations: one cold, cloudy day in November and the other a warm, sunny day in August. Figures 4.22 and 4.23 show the weather data for both days, respectively. As explained earlier, real temperatures are less interesting than apparent temperatures when studying IR radiation properties. Therefore, the model was also used to calculate apparent temperatures. The apparent temperatures were calculated in the 7.8–12.0 μm spectral range using the spectral response curve of the CARABAS radiometer (Section 7.2.2.1).

Figure 4.24 shows the excellent agreement between calculations and measurements in August. It must be admitted that the unknown physical properties were optimized to get the best fit between measurements and calculations. The

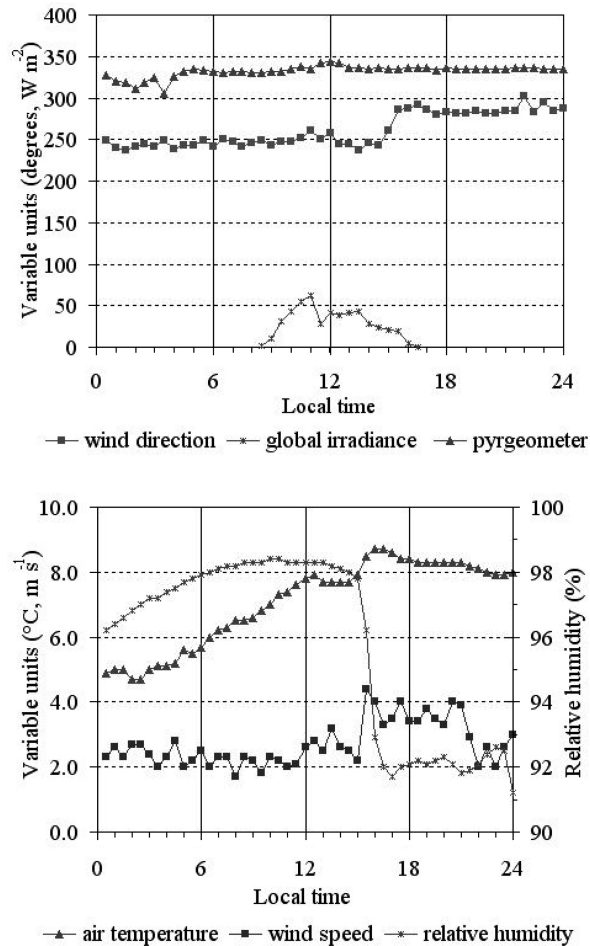


Figure 4.22 Weather data on 27 November 1989.

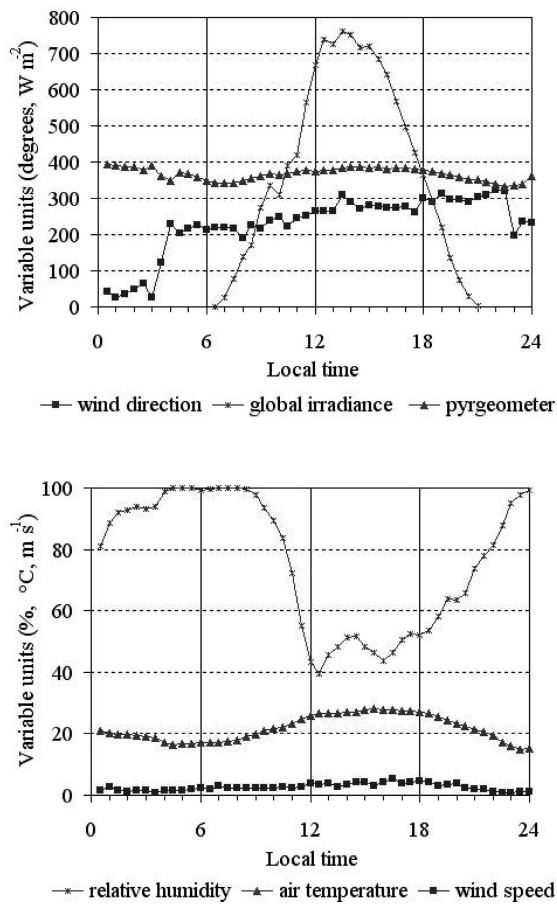


Figure 4.23 Weather data on 14 August 1990.

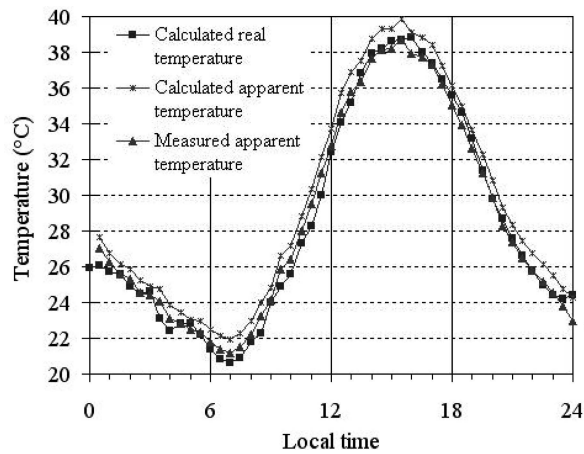


Figure 4.24 Comparison of the measured and calculated temperature of concrete.

calculated apparent temperatures for 14 August and 27 November are taken as the reference situation for the sensitivity-analysis study and have the subscript “ref.”

During a sensitivity analysis, the value of a particular parameter is varied, while all other parameters remain constant and set to their reference value. The resulting calculated temperatures have the subscript “calc.” Thus, for each value of the selected parameter, the corresponding real and apparent temperatures are calculated. The sensitivity of the model for a given parameter is expressed by the temperature difference, ΔT , between the calculated and reference temperature, i.e., $\Delta T = T_{calc} - T_{ref}$. For a given parameter setting, values of ΔT are calculated over a 24-hour period. The maximum and minimum temperature difference, ΔT_{max} and ΔT_{min} , respectively, that occur during this period are stored. This procedure is repeated for each new parameter value, eventually leading to a set of parameter values and corresponding values for ΔT_{max} and ΔT_{min} . Variation of the density and heat capacity did not show much variation and is not discussed.

The next series of figures shows the results of a sensitivity analysis for the following parameters: the solar absorption coefficient α_s (Fig. 4.25), the surface emission coefficient ϵ_s (Fig. 4.26), the thermal conductivity λ_c (Fig. 4.27), the convective heat transfer coefficient h_c (Fig. 4.28), the absorbed solar irradiance $\alpha_s E_{sun}$ (Fig. 4.29), and the absorbed sky irradiance $\epsilon_s E_{sky}$ (Fig. 4.30).

The figures show that the model sensitivity can vary considerably for the various input parameters. For the cold November day, the variations are much more moderate, mainly because of the low solar loading. In wintertime, the influence of clear sky conditions has a major effect on the apparent temperature.

The worst situation is found when all “errors” add up, i.e., when $\alpha_s E_{sun}$ and $\epsilon_s E_{sky}$ both have opposite sign from Q_c . The influence of the thermal conductivity shown in Fig. 4.27 can be negative as well as positive. This is also the case for the emission coefficient of the target and depends on the balance of the radiation terms, i.e., absorbed sky radiation compared to emitted radiation. This is determined by

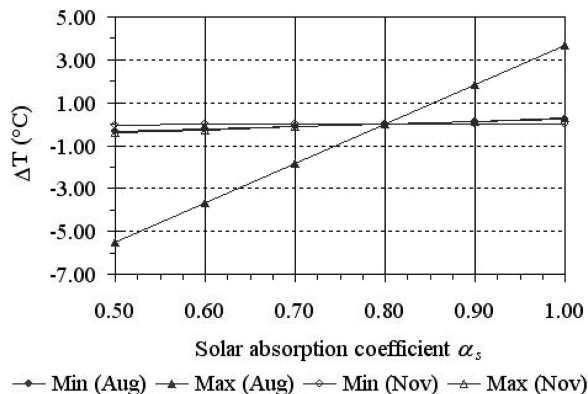


Figure 4.25 Variation of α_s .

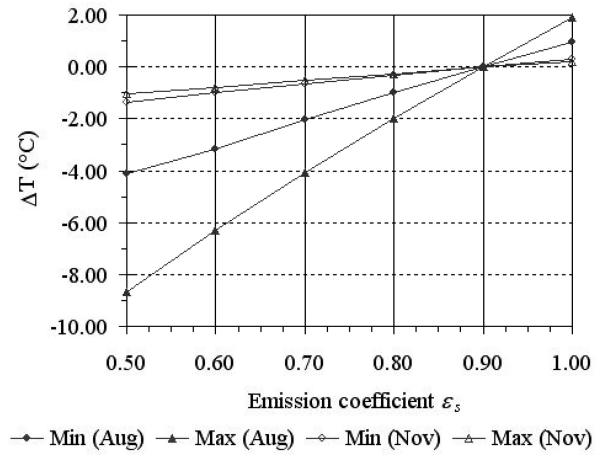


Figure 4.26 Variation of ϵ_s .

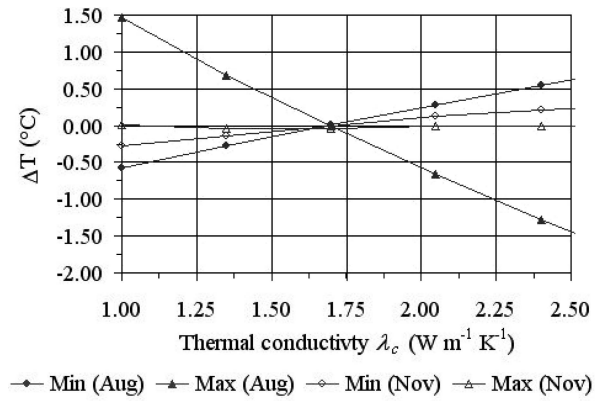


Figure 4.27 Variation of λ_c .

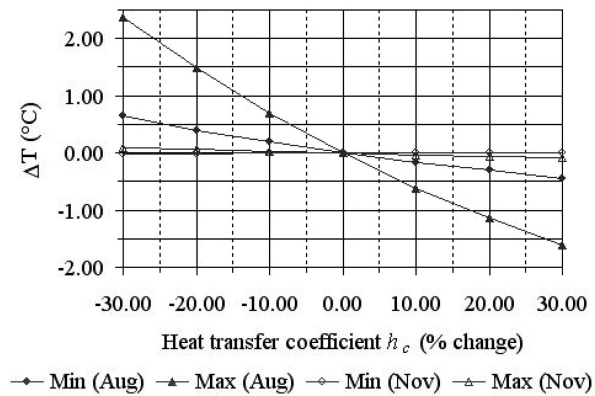


Figure 4.28 Variation of h_c .

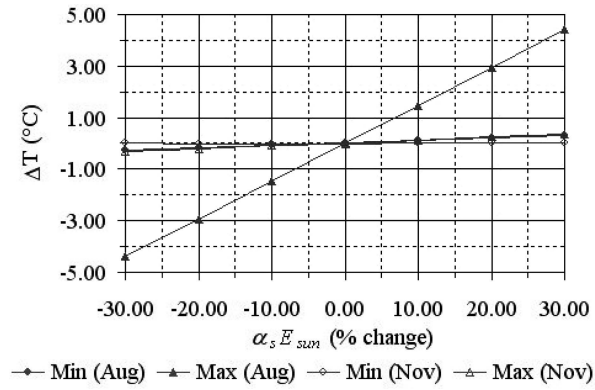


Figure 4.29 Variation of $\alpha_s E_{sun}$.

the weather situation (clouded vs. clear sky conditions). In general, these figures show a weak response to parameter variation under moderate weather conditions, like the conditions in November, occurring at this geographical location. As was to be expected, the surface temperature strongly depends on the solar absorption coefficient (Fig. 4.25) and on the absorbed solar irradiance (Fig. 4.29) during summer conditions. Figure 4.26 shows the strong dependency on the emission coefficient. This is caused by an increase of the reflected sky irradiance, which is incorporated in the apparent temperature and which resembles “cold” sky radiation.

For overcast situations, this effect is marginal because cloud base temperatures are much higher than clear-sky temperatures. Because both parameters, α_s and ϵ_s , are difficult to measure or reasonably estimate for heavy structured surfaces (such as trees, bushes, grass), large errors are likely to occur and consequently the calculation error increases dramatically.

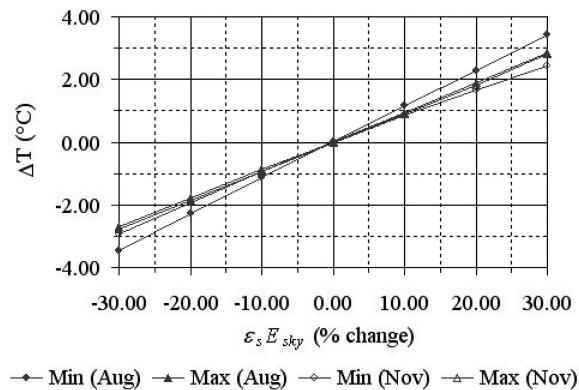


Figure 4.30 Variation of $\epsilon_s E_{sky}$.

Variation of the absorbed sky irradiance (Fig. 4.30) shows a similar response on both days. The parameters E_{sun} and E_{sky} can be measured quite accurately, so the problem again becomes securing an accurate measurement of α_s and ϵ_s .

The response on the variation of the thermal conductivity and the convective heat transfer coefficient is moderate, except for the maximum temperature during high solar loading in August.

Next to the influence of the individual parameters, the overall model sensitivity is of main importance. Figure 4.31 (top) shows that the cumulative error in the *apparent* temperature can rise to considerable values. Figure 4.31 (bottom) shows the comparison of the relative error (RE) in the real and apparent temperature in the same situation. These minimum and maximum relative errors are defined as

$$(RE)_{real}^{min} = \frac{\Delta T_{real}^{min}}{(T_{ref}^{min})_{real}} \times 100\%, \text{ respectively } (RE)_{real}^{max} = \frac{\Delta T_{real}^{max}}{(T_{ref}^{max})_{real}} \times 100\%,$$

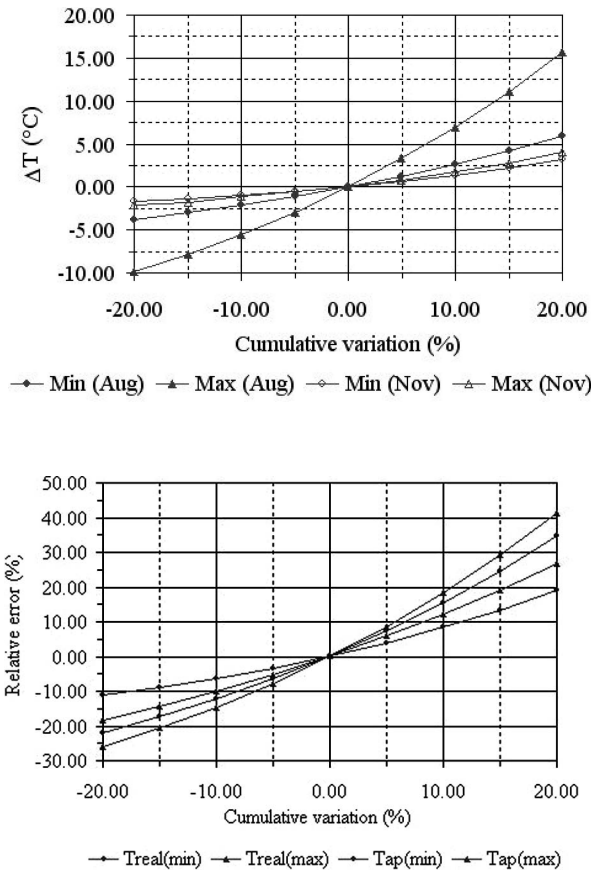


Figure 4.31 Cumulative errors.

with

$$\Delta T_{real}^{min} = (T_{calc}^{min})_{real} - (T_{ref}^{min})_{real}.$$

Similarly, the relative errors for the apparent temperatures are defined as $(RE)_{ap}^{min}$ and $(RE)_{ap}^{max}$.

The overall sensitivity is calculated, assuming that all errors work in the same direction (i.e., adding up), resulting in a maximum error and representing a worst-case situation. Figure 4.31 shows that even for moderate conditions, the errors reach unacceptably high values. It must be emphasized that the sensitivity of the model to specific parameters may change considerably if one material is replaced by another or the entire sandwich structure is changed by new materials. Therefore, model performance (validation) should always be checked before the model can be used to generate reliable output in other situations.

It is important to note that the relative errors for the calculated *real* temperatures are much smaller than for the calculated *apparent* temperatures. Therefore, if model performance is expressed in terms of a comparison between calculated and measured *real* temperatures, this could lead to a too-optimistic interpretation of model performance. Especially, if models are to be used for radiation studies, accuracy should be expressed in terms of apparent rather than real temperatures.

What is the consequence of these errors if such a model is used for IR-detection probability calculations?

To answer this question, take a situation with zero apparent temperature contrast between the target and background, $\Delta T_{ap} = 0$; that is, detection is not possible. Furthermore, suppose that because of inaccuracies in model parameters, the overall model error is 10%, then the calculated contrast is $\cong 5^\circ\text{C}$ (Fig 4.31, top) instead of zero. This is equivalent to an error in the intrinsic apparent contrast (in $7.8\text{--}12\ \mu\text{m}$), ΔE_{ap} , of $\cong 3\ \text{W m}^{-2}\ \text{sr}^{-1}$. Finally, assume the following (most common and reasonable) sensor system conditions.

System characteristics

- Detector sensitive area A_d : $50 \times 50\ \mu\text{m}$
- Focal length f : $50\ \text{mm}$
- IFOV : $1\ \text{mrad}$
- NEI : $1.3 \times 10^{-9}\ \text{W m}^{-2}$

Operational conditions

- Range r : $5\ \text{km}$
- Visibility: $25\ \text{km}$
- $T_a = 20^\circ\text{C}$ and $RH = 65\% \Rightarrow \tau_a = 0.4$ (MODTRAN)

Table 4.2 Model response for various input parameters.

Very sensitive	Moderately sensitive	Very insensitive
Air temperature	Relative humidity	Air pressure
Solar irradiance	Target height	Cloud cover (high level clouds)
Solar absorption coefficient	Wind speed	Time step
Emission coefficient	IR sky irradiance	Grid spacing
Top layer heat conductivity	Bottom boundary flux	
Cloud cover (middle level clouds)	24 hr repetitions	
Cloud type	Initial conditions	

Under these conditions, the apparent radiation contrast at the aperture of the sensor system, ΔE_{ap} , is given by Eq. (4.14),

$$\Delta E_{ap} = \frac{\tau_a \Delta E_{ap} A_d}{f^2} = 1.210^{-8} \gg NEI \quad (4.14)$$

↓

**ERRONEOUSLY PREDICTED
DETECTION!**

Table 4.2 summarizes more generally the relative response of the model to variation of various input parameters.

4.4.3 Pros and cons

In summary, pros and cons of first principles models can be formulated in general terms as follows:

Pros

- The functional relation between parameters is clearly visible and allows controlled study of the influence of the individual parameters.
- Easy to apply under different weather conditions and for different geographical locations.
- Numerical solution is not complicated and has a relatively fast (computational) response time.
- Good to predict trends or for comparisons, but less suited for absolute results.
- Time and cost saving.

Cons

- Application to complex (geometrical) structures is not very realistic.
- Detailed input of a large array of parameters, which is hard to obtain, is required.

- Mathematical formulation of some physical processes is too inaccurate.
- The absolute model accuracy frequently is not good enough for detection applications.

References

1. R.C. Weast, *Handbook of Chemistry and Physics*, CRC Press, Inc. (1974).
2. L.K. Balick et al., "Thermal modeling of terrain surface elements," *U.S. Army Engineer Waterways Experiment Station, Technical Report EL-81-2* (1981).
3. W. Reynolds, "Validation and accuracy assessment of the physically reasonable infrared signature model (PRISM)," *Proceedings of the TACOM/KRC Ground Vehicle Symposium, 27–28 August* (1988).
4. J.C. Slattery, *Momentum, Energy and Mass Transfer in Continua*, McGraw-Hill Book Company, New York (1981).
5. J.R. Philip and D.A. de Vries, "Moisture movement in porous materials under temperature gradients," *Trans. Am. Geo. Un.*, 38(2) (1957).
6. W.R. van Wijk and D.A. de Vries, "Periodic temperature variation," in *Physics of Plant Environment*, ed. W.R. van Wijk, North Holland Publishing Co., Amsterdam (1966).
7. E.F. Bowers and R.D. Hanks, "Reflection of radiant energy from soils," *Soil Sci.*, 100(130) (1965).
8. G. Stanhill, "Some results of helicopter measurements of albedo," *Sol. Energy*, 13(59) (1970).
9. N.J.J. Bunnik and W. Verhoef, "The spectral directional reflectance of agricultural crops," *NIWARS publication no. 23* (1974).
10. D.A. Kiner and J.A. Smith, "Simulation of solar radiation absorption in vegetation canopy," *Applied Optics*, 19 (August, 1980).
11. G.H. Suits, "The calculation of the directional reflectance of a vegetative canopy," *Remote Sensing of Env.* 2, pp. 117–125 (1972).
12. R.E. Oliver and J.A. Smith, "Vegetation canopy reflectance models," *Final Report, Colorado State University* (1973).
13. S.B. Idso et al., "The dependence of bare soil albedo on soil water content," *J. Appl. Meteorol.* 14, pp 109–113 (1975).
14. J.L. Threlkeld, *Thermal Environmental Engineering*, Prentice Hall (1977).
15. S.T. Henderson, *Daylight and Its Spectrum*, Adam Hilger Ltd, Bristol (1977).
16. J.L. Monteith, *Principles of Environmental Physics*, Edward Arnold Ltd., London (1973).
17. R.M. Welch et al., "Solar radiation and clouds," Vol 17(19), *American Meteorological Society*, Boston (1980).
18. M.P. Levesque, "Cloud simulation: proposed model," *Defense Research Establishment Valcartier (DREV)*, Canada (1988).
19. P.A.M. Jacobs, "The thermal behavior of a three-dimensional target placed in the open field," Thesis at the Agricultural University of Wageningen, Netherlands (1982).

20. F.E. Lumb, "The influence of cloud on hourly amounts of total solar radiation at the sea surface," *Q. J. R. Met. Soc.* 90, 43 (1964).
21. J.S. Accetta and D.L. Shumaker, eds., *The Infrared and Electro-Optical Systems Handbook*, Environmental Research Institute of Michigan, Ann Arbor (1993).
22. K.J.K. Buettner et al., "The determination of infrared emissivity of terrestrial surfaces," *J. Geo. Res.*, 70(6) (1965).
23. Q.J. Unsworth and J.L. Monteith, "Long wave radiation at the ground," *Q. J. R. Met. Soc.*, 101, pp. 13–34 (1975).
24. H.E. Bennet et al., "Distribution of infrared radiance over a clear sky," *J. Opt. Soc. Am.*, 50(100) (1960).
25. W.D. Sellers, *Physical Climatology*, University of Chicago, I11 (1965).
26. L. Wartena et al., "Checking of some formulae for the calculation of long wave radiation from clear skies," *Arch. Met. Geoph. Biocl., Ser. B*, 21, pp. 335–348 (1973).
27. J.M. Slingo, "The development and verification of a cloud prediction scheme for the ECMWF model," *Q. J. R. Met. Soc.*, 113, pp. 899–927 (1987).
28. P.A.M. Jacobs, "Convective heat exchange of a three-dimensional target placed in the open field," *Arch. Met. Geoph. Biocl., Ser. B*, 33, pp. 349–358 (1984).
29. N.J. Rosenberg, *Microclimate*, John Wiley and Sons, New York (1974).
30. P.A.M. Jacobs, "Simulation of the thermal behavior of a target and its nearby surroundings," *TNO publication PHL-1980-08* (1980).
31. W.A. Gray and R. Müller, *Engineering Calculations in Radiative Heat Transfer*, Pergamon Press (1974).
32. T. Maki, "On zero plane displacement and roughness length in the wind velocity profile over a corn canopy," *J. Agric. Met.*, 25(13), Tokyo, (1969).
33. F. Olsen and M. Gamborg, "Modelling the thermal signature of natural backgrounds," *FFI Rapport-2001/05324*.

Chapter 5

Meteorological and Atmospheric Parameters

As demonstrated in the previous chapter, prevailing weather conditions largely drive the thermodynamic behavior of objects. For targets, internal heat sources also may affect the exterior thermal signature. To understand the thermal behavior of objects and quantify the IR radiation exchange, a number of weather parameters have to be measured in the target area together with target signature data. Chapter 4 showed that sophisticated models need a large array of meteorological input parameters, and special measurement facilities are required to collect these. However, this array is too big to be practical, and the challenge is to choose a minimum set of parameters that give sufficient (complete) information to quantify thermal signatures. From a practical point of view, it would be beneficial to relate calculated as well as measured thermal signatures to a limited set of weather data that are readily available or easy to obtain.

For the characterization of IR signatures, this indeed is a difficult choice. It must be weighed against costs, time, and sensor availability. Unfortunately, the result often is a bad compromise, resulting in a poor and/or inadequate recording of the weather conditions.

5.1 Meteorological Sensors and Measurements

In the previous chapter, it was shown which meteorological and environmental parameters play a role in the energy (heat) budget of an object. Ideally, the following parameters are needed:

- Relative (absolute) humidity
- Wind speed
- Wind direction
- Solar radiation ($\lambda < 3 \mu\text{m}$)
 - Solarimeter
 - Pyrheliometer
- Sky radiation ($\lambda \geq 3 \mu\text{m}$)
 - Pyrgeometer
- Atmospheric pressure

- Rain rate
- 1 m standard height
- Height profiles

Information needed for:

- Atmospheric (radiation) properties
- Sensor performance modeling
- Calibration procedures
- Target and background modeling

All these parameters can be measured by sensors and are very well suited for automation. The weather data of a synoptic meteorological station could be a good starting point. These stations measure a standard set of parameters and are located in a rather dense network all over the world. However, the frequency at which the measurements are carried out, i.e., every hour, is not high enough to perform accurate model calculations. In many situations, a weather station is set up in the same area (Fig. 5.1) where the signature measurements are carried out. Cloud information of the nearest synoptic station can also be used.

Some details of a solarimeter and a pyrgeometer are shown in Fig. 5.2, while Fig. 5.3 shows details of a rain gauge and wind sensor (speed and direction).

A special problem is the calculation of the atmospheric transmission. Although models such as MODTRAN and EOSTAR¹ can do a good job, sometimes it may be useful to perform a direct measure of this property. A visibility sensor (Fig. 5.4) is such a device. It measures the scattered laser light of a volume of air, which relates to the atmospheric visibility (provided atmospheric conditions do not vary much over the ranges of interest).



Figure 5.1 Portable meteorological station set up in a coastal environment.

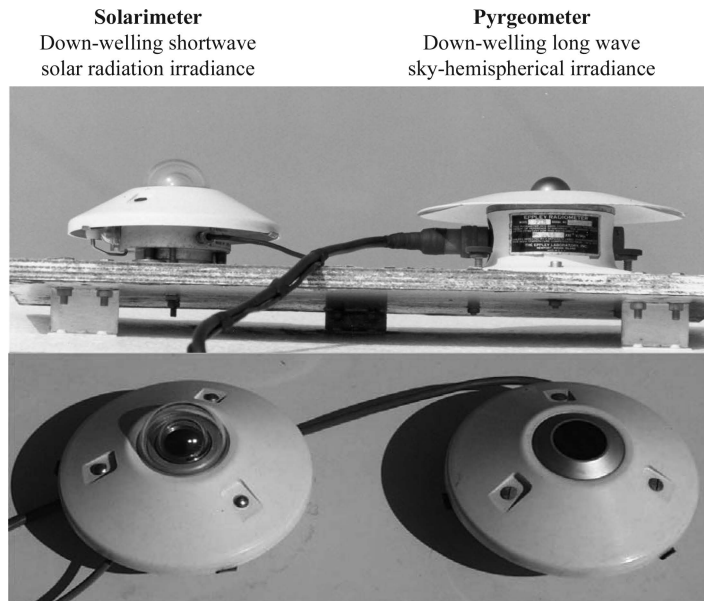


Figure 5.2 Details of a solarimeter and a pyrgeometer.

To solve the heat balance of a surface, the transfer of energy at the surface and, in particular for infrared studies, the radiation balance must be known.

A first step to obtain this kind of information is to incorporate a pyrgeometer. This device measures the total integrated down-welling long-wave irradiance on a horizontal plane (the infrared equivalent of a solarimeter) of the sky-hemisphere ($3 \leq \lambda < 50 \mu\text{m}$), but does not give the sky radiance distribution. It is, however, a useful and inexpensive instrument, simple to handle and readily available.

A pyrheliometer, which measures the direct solar irradiance at normal incidence, also is very useful and can be used in combination with the solarimeter



Figure 5.3 Details of a rain gauge and wind sensor.

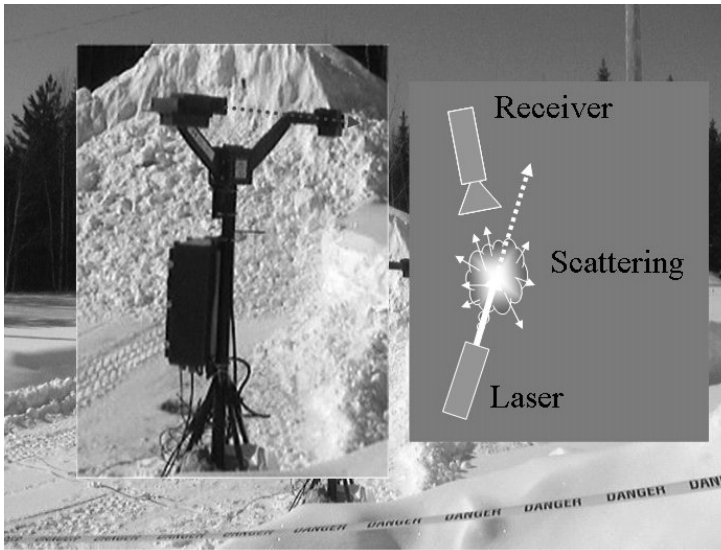


Figure 5.4 Visibility sensor.

(global irradiance) to resolve the solar irradiance at non-horizontal surfaces. Today, with onboard computing power, this instrument is more user friendly than it used to be and does not need so much maintenance anymore.

For surfaces that are not horizontal, the incident radiation is a combination of direct solar and sky irradiance and indirect reflected radiation from the surrounding terrain. Therefore, the incident radiation can only be determined if the shortwave and long wave radiance distribution² over the sky-hemisphere and the bidirectional optical properties of the terrain are known in both spectral bands.

In the next section, a special sensor, which provides very useful supplementary information for model input, is presented. The sensor was developed in-house and measures the infrared radiation of the upper sky-hemisphere with a very high geometrical resolution. Originally, the output was used to study the signatures of point targets near cloud edges. But it has a wider use, as will be demonstrated further on.

5.2 SCORPIO Infrared Sky Radiance Distribution

As previously illustrated, the sky irradiance E_{sky} at a horizontal surface is determined from

$$E_{sky} = \int_0^{2\pi} d\varphi \int_0^{\pi/2} \int_{\lambda_0} g(\varphi, \vartheta) E(\varphi, \vartheta, \lambda) d\lambda d\vartheta \quad (5.1)$$

or can be calculated from

$$E_{sky} = \int_0^{2\pi} d\varphi \int_0^{\pi/2} \int_{\lambda_0} g(\varphi, \vartheta) \varepsilon_a(\varphi, \vartheta) E(\lambda, T_a) d\lambda d\vartheta. \quad (5.2)$$

In Eq. (5.1), the term $E(\varphi, \vartheta, \lambda)$ represents the incident radiation from the entire atmospheric sector in the cone comprised by $(d\varphi, d\vartheta)$. In Eq. (5.2), the term $E(\lambda, T_a)$ describes the incident radiation from the same sector, but from a solid sphere segment at temperature T_a . The term $\varepsilon_a(\varphi, \vartheta)$ in Eq. (5.2) is the atmospheric emission coefficient of the sector in the cone comprised by $(d\varphi, d\vartheta)$. By the appropriate choice of angles φ and ϑ , both equations can be used to determine the sky irradiance at a surface of arbitrary orientation.

To solve both equations, in either case the distribution of $\varepsilon_a(\varphi, \vartheta)$ or $E(\varphi, \vartheta, \lambda)$ must be known. As part of a project to study the IR emittance of various cloud types, a high-resolution, 3D-scanning, imaging radiometer (3–5 and 8–12 μm) called SCORPIO was developed. Although such high resolution is not really needed to measure the sky radiation distribution [$E(\varphi, \vartheta, \lambda)$], SCORPIO was used anyway for this purpose. Figure 5.5 shows the schematic drawings of the SCORPIO system. The central part of the system is a high-speed rotating mirror (25 Hz), which is tilted 0.8 mrad with every revolution. Via a stationary mirror at the top of the overhead bar, radiation is reflected into the desired optical path, which can be selected manually. The detector signal is used to modulate the light output of a laser, which illuminates a film negative. An image is produced by scanning the laser spot over the film negative by a mirror, which is mechanically connected to the scanning mirror. Additionally, the digitized (12-bit) detector signal is stored on disk. The temperature of the overhead bar is controlled by the use of circulating warm water; the overhead bar is used to calibrate each scan line.

Figure 5.6 shows a photograph of the SCORPIO system. The technical specifications of the SCORPIO system follow.

Spectral sensitivity

3–5 and 8–12 μm (selectable), single detector ($0.1 \times 0.1 \text{ mm}$) and LN_2 cooled.

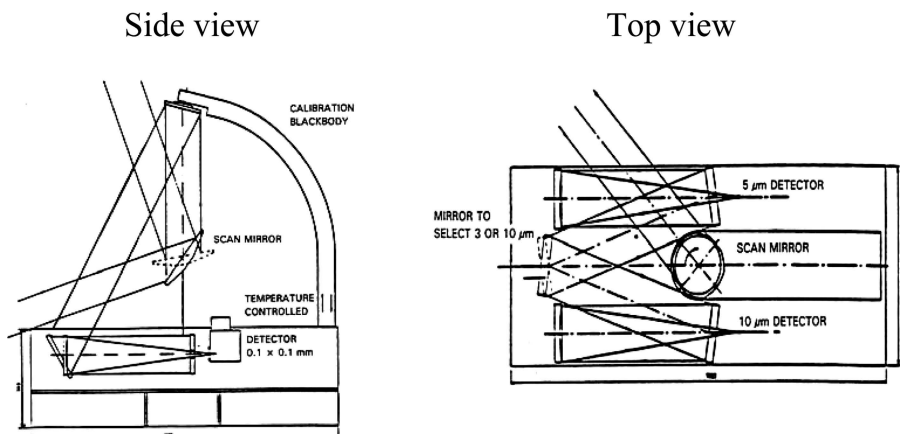


Figure 5.5 Schematic layout of the SCORPIO system.

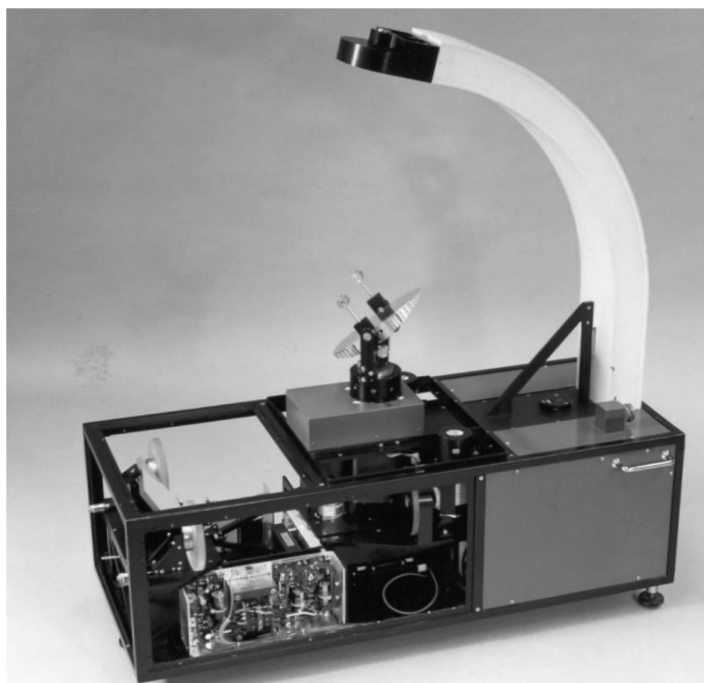


Figure 5.6 The SCORPIO scanner.

Field of view

Total angle coverage is 360 deg in azimuth and -18 deg to 72 deg in elevation, with an option to select a limited azimuth/elevation sector by electronic means.

Instantaneous field of view

$3-5 \mu\text{m}$: LSF (line spread function) is 0.80 mrad.

$8-12 \mu\text{m}$: LSF is 0.78 mrad.

Calibration

Calibration for every horizontal scan line, using the temperature-controlled overhead bar as a reference blackbody.

Temperature resolution

$3-5 \mu\text{m}$: NETD 0.3°C (noise equivalent temperature difference).

$8-12 \mu\text{m}$: NETD 0.1°C .

Image collection

2000 lines by 5600 pixels per image.

Recording time for one image in a given spectral band is 80 seconds.

Selection of the optical ($3-5$ or $8-12 \mu\text{m}$) channel is done manually.

Direct recording on film negative by a modulated laser and/or 12-bit digital recording on hard disk.

Figures 5.7 and 5.8 show two SCORPIO images (8–12 μm), taken from the yard of the TNO-FEL laboratory. The first image shows a cloudy sky with a rather homogeneous cloud distribution. At the circumference of the image, part of the FEL building and a radar tower are visible. The second image shows a band of clouds in the north (top right in the image). Both images were created directly on film negative by the modulated laser and recorded on hard disk. The black circle in the middle is the overhead mirror and the black cone-shaped area is the overhead calibration bar. The white center line in the middle of the bar is the exact calibration position. White parts in the sky are clouds (warm), while black parts result from clear skies (cold). The bright white spot in the upper-left part is the sun. It can be seen in the 8–12 μm band because a few pixels are fully occupied by the sun and thus contain all its energy. Moreover, the gain setting of the device is rather high in order to display more details in the radiation distribution. Because it takes 80 s to record one complete image in one spectral band, recordings can only be used on days with a slow-changing cloud distribution.

As delineated in Chapter 3 when discussing the heat balance equation of a surface, the long wave irradiance at the surface of an arbitrarily oriented object is determined by the sky radiance distribution.

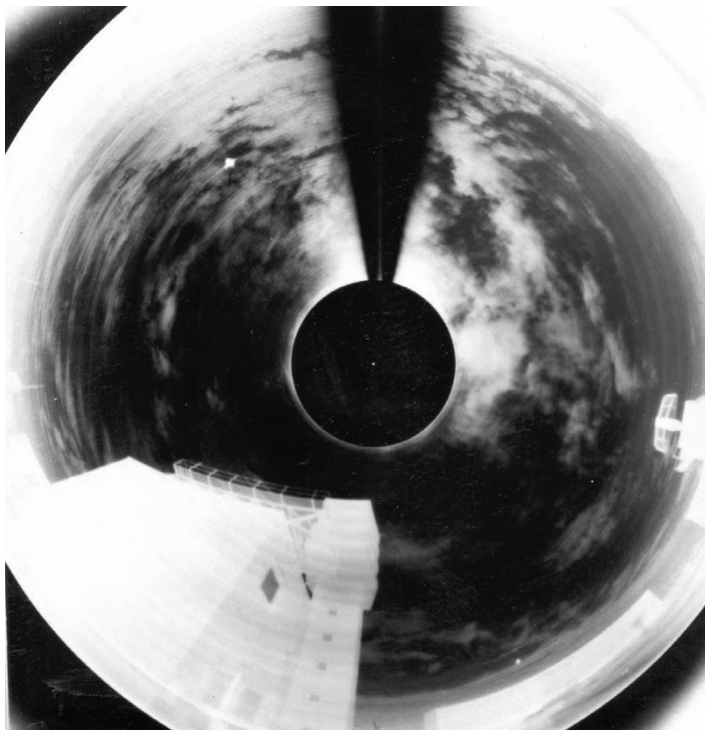


Figure 5.7 SCORPIO 8–12 μm image for a homogeneous cloud layer.

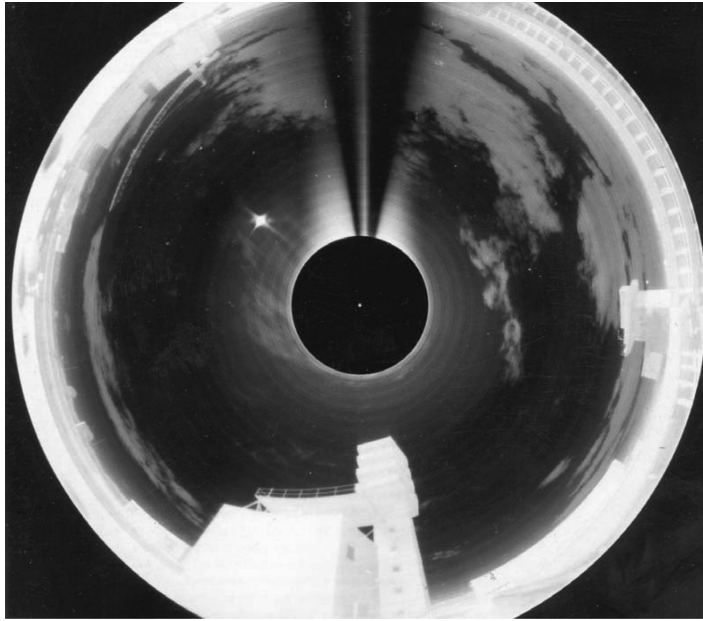


Figure 5.8 SCORPIO 8–12 μm image for a band of clouds in the north.

To investigate the variations of the total sky irradiance at a surface as a function of the sky conditions and radiation distribution over the sky-hemisphere, SCORPIO images were recorded on three different days, comprising a clear, overcast, and partly cloudy day, with a cloud layer in the north sky sector.

Table 5.1 shows the calculated integrated sky irradiance at differently oriented surfaces for these conditions.

The table shows that for clear-sky and overcast conditions, the irradiance on vertical surfaces is about half that on a horizontal surface. This indicates that the sky radiance distribution is independent on azimuth angle, i.e., $E_{sky}(\varphi, \vartheta) = E_{sky}(\vartheta)$. During the clouded situation this is clearly not the case. If, as a best guess, the irradiance on the south-facing surface (facing clear skies) would be taken as half of the irradiance on the horizontal surface, that is, 175 (W m^{-2}), the error would be 25 (W m^{-2}) or 16% relative error. It was shown in

Table 5.1 Calculated sky irradiance using SCORPIO data.

Orientation	Clear sky	Overcast sky	Partly (N) cloudy sky
Horizontal	305	368	350
North	164	186	189
East	167	189	161
South	163	183	150
West	164	185	163

Values in W m^{-2} .

the sensitivity analysis that such an error can lead to a model prediction error of about 2°C.

The broadband atmospheric emission coefficient as a function of elevation and azimuth $\epsilon_a(\varphi, \vartheta)$ can be determined from the measured sky radiance $E(\varphi, \vartheta)$ from

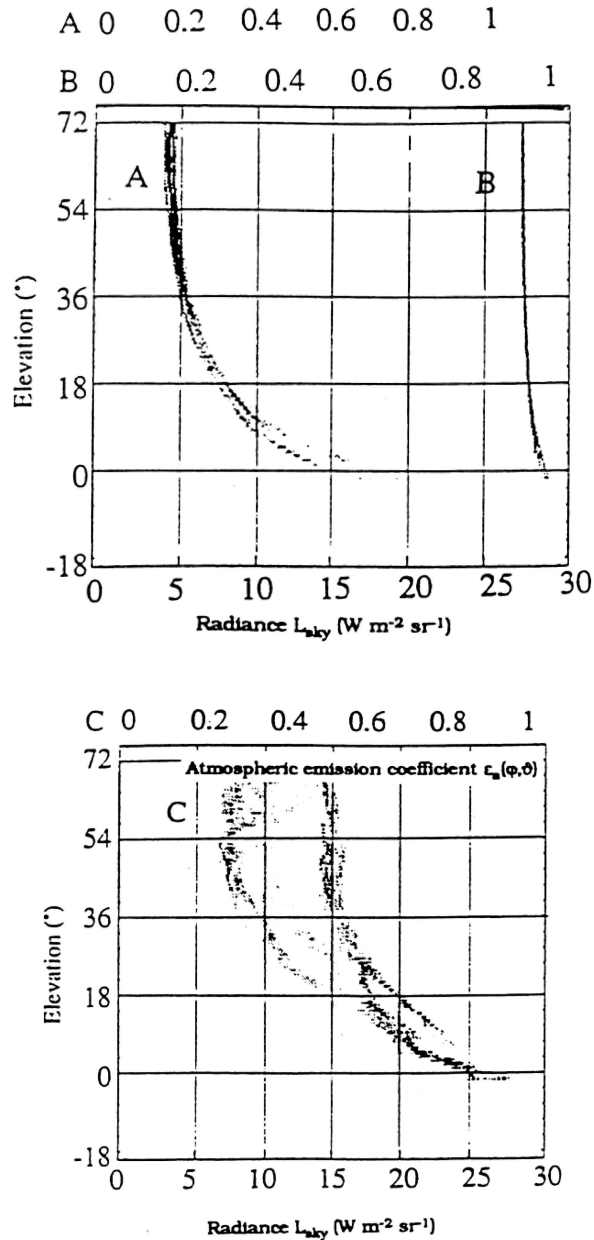


Figure 5.9 Sky radiance distribution and atmospheric emission coefficient for a clear sky (A), an overcast sky (B), and a partly cloudy sky (C).

the sector (φ, ϑ) of the sky-hemisphere, as

$$\varepsilon_a(\varphi, \vartheta) = \frac{F\sigma T_a^4}{E_{sky}(\varphi, \vartheta)} \quad (F \text{ is a geometrical factor}).$$

Figure 5.9 shows $\varepsilon_a(\varphi, \vartheta)$ for a few sample conditions. The top part shows the results for March 3, 1993 (A) and for January 15, 1993 (B). Situation B shows a narrow curve, indicating that the sky radiance is independent on the azimuth angle at a given elevation. In this situation, the radiance is also nearly independent on the elevation angle. This is the typical situation for an overcast sky. In situation A the sky is clear, leading to a very low atmospheric emission coefficient at high elevations (low apparent temperature, typically -60°C in $8-12 \mu\text{m}$).

The bottom part of Fig. 5.9 shows the situation for a partly cloudy sky (case C), leading to a widely scattered radiance distribution for a given elevation angle. The weather conditions during the various situations were

- A Date 03-03-93, time 17:05 (MET), T_a 1°C , RH 80%;
- B Date 15-01-93, time 10:12, T_a 10°C , RH 80%;
- C Date 15-01-93, time 12:46, T_a 11°C , RH 78%.

References

1. S.M. Doss-Hammel, D. Tsintikidis, A.M.J. van Eijk, and G.J. Kunz, *Proceedings of EO STAR: Electro-Optical Signal Transmission and Ranging. Battle-space Atmospheric and Cloud Impacts on Military Operations (BACIMO)*, Monterey CA, USA (2003).
2. P.A.M. Jacobs, "Measurement of long wave sky radiance distribution," *Arch. Met. Geoph. Biocl. Ser.*, B34, 257–265 (1984).

Chapter 6

Infrared Calibration Procedures

For many disciplines within the infrared region, such as sensor development and assessment, camouflage efficiency, or detection probability evaluation and modeling, absolute radiance values (intrinsic apparent or radiometric temperatures) of target and background must be known. Figure 6.1 shows the detection chain again, indicating various calibration steps.

The following calibration types can be distinguished.

- (1) Calibration of the sensor system:
 - (a) A first intermediate step is to relate target and background radiation contrast ΔE_{ap} to the apparent radiation ΔE_{ap}^{det} , which is incident on the detector. This relation is described by the function h as $\Delta E_{ap}^{det} \sim h(\Delta E_{ap})$.
 - (b) In a second step, the detector output voltage, ΔV_{det} , is related to the detector incident radiation by the function f , better known as the system-relative spectral response $R(\lambda)$, as $\Delta V_{det} \sim f(\Delta E_{ap}^{det})$.
- (2) Calibration of the collected data:
 - (a) The final step in a data-acquisition process most frequently is an imaging device (TV screen or computer monitor) in combination with a recording device (tape recorder and/or hard disk). This relation between detector output voltage and the display or recording device, the gray level (G_{image}) is described by the function g as $G_{image} \sim g(\Delta V_{det})$.

For infrared data to be called absolute or calibrated, at least two requirements have to be fulfilled.

- (1) The radiance L or the apparent temperature T_{ap} of any given surface area on the target in the real world must be retrievable from the collected data. So, the relation between a gray level in an image (or the detector voltage of a radiometer) and the intrinsic (i.e., in the target plane) radiation E of a surface area on the target must be known. The physical surface temperature of the target area can be calculated if the emission coefficient is known.
- (2) The geometry of the measurement setup must be known. In other words, the relation between the pixel size in the image or radiometer spot and the actual measurement area on the target, i.e., the projected detector area, must be known. Among others, this implies that accurate sensor-to-target range information is necessary.

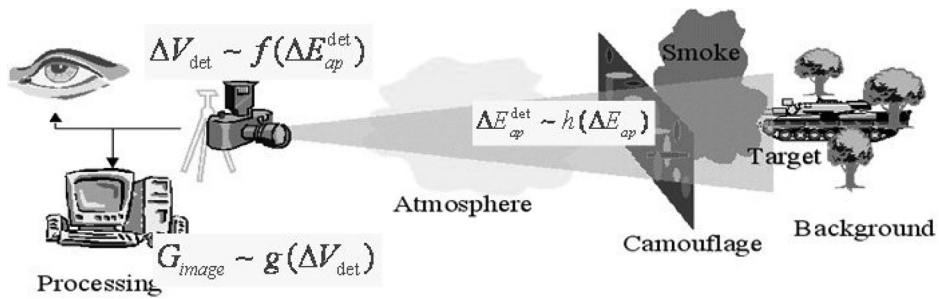


Figure 6.1 Various calibration steps.

It is important that the entire measurement chain is within the calibration loop. This means that, if data are recorded on a videotape, the degradation of the data by the tape recorder (noise, limited bandwidth, linearity, etc.) must be incorporated into the calibration procedure. Preferably, the video signals will be digitized before recording, as this will retain a better signal-to-noise ratio for the stored data. Also, many systems use internal calibration blackbodies that are located behind the front optics; consequently, transmission losses by these optical components (especially the varying influence of dirt) are not incorporated. In this case, external reference blackbodies must also be used.

For calibrated data to turn to *calibrated signatures*, the following supplementary information is needed:

- (1) A description of the measured target (target or background) and a description of its physical condition (exercised, camouflaged, wet, etc.). For a target, this could be its operational-status surface condition, while for a background it could be natural/manmade, color, roughness, or growing stage
- (2) Geographical location, time (UTC), and range to target
- (3) Meteorological conditions (and previous history)
- (4) A complete description of the system (performance) characteristics (including recording/storage medium), such as the spectral response curve, manual or automatic gain setting (the latter is less suitable)

To collect this type of imagery, special arrangements have to be made during the measurements. In the next paragraphs, a list of calibration parameters that have to be known, together with a list of necessary calibration equipment will be presented. Finally, a procedure to collect calibrated signatures¹ is given, elucidated with a practical numerical example.

6.1 Calibration Methodology

The components of the basic setup to collect calibrated signatures can be broken down into four parts:

- (1) IR system + recording facility
- (2) Optical path between target and IR system

- (3) Target characteristics
- (4) Reference blackbodies

The apparent target irradiance E_{ap} is given by Eq. (2.10) as

$$E_{ap} = F(r) \int_{\lambda_0} \left\{ \tau_a(\lambda, r) [\varepsilon_t E(\lambda, T_t) + \rho_l E(\lambda, T_{ae})] + [1 - \tau_a(\lambda, r)] E(\lambda, T_a) \right\} d\lambda.$$

As was explained, $F(r)$ is a factor accounting for the measurement geometry. If the target area completely fills the IFOV, then $F(r)$ is the system IFOV, Ω_s . Consequently, the apparent target radiance L_{ap} is given by

$$L_{ap} = \frac{E_{ap}}{F(r)} = \frac{E_{ap}}{\Omega_s} \quad (\text{W m}^{-2} \text{sr}^{-1}).$$

If nothing is known about the reflected background radiation $\rho_l E(\lambda, T_{ae})$ or the target emissivity is unknown, the target area is taken as a blackbody and the radiance is given by

$$L_{ap} = \int_{\lambda_0} \left\{ \tau_a(\lambda, r) L(\lambda, T_{bb}) + [1 - \tau_a(\lambda, r)] L(\lambda, T_a) \right\} R(\lambda) d\lambda, \quad (6.1)$$

where $\tau_a(\lambda, r)$: atmospheric transmissivity over the optical path
between the imager and the target,
 r : system-to-target range (m),
 $R(\lambda)$: relative system spectral response,
 T_{ap} : apparent target temperature (K),
 T_a : air temperature (K).

The relative system spectral response is a transfer function describing how spectral distributed radiation is transferred through the system. As an example, Fig. 6.2 shows $R(\lambda)$ for the AMBER HS infrared imaging system.

The detector voltage V_{det} , assumed to depend linearly on the radiance L_{ap} for a given gain setting, is then found from

$$V_{det} = gL_{ap} + V_{off}, \quad (6.2)$$

where g : system responsivity (V W^{-1}),
 V_{off} : DC offset (black level) (V).

Since Eq. (6.2) relates the intrinsic target radiance to the detector voltage, it is in fact the equation that has to be solved in the given situation to obtain the calibration coefficients, i.e., determining g and V_{off} . Because Eq. (6.2) contains two unknown variables, at least two independent measurements are required to solve the equation. This means that at least two reference points, preferably blackbodies with known temperatures, must be available. If more system gain settings are to be expected during the measurements, the calibration procedure has to be carried out for each gain setting.

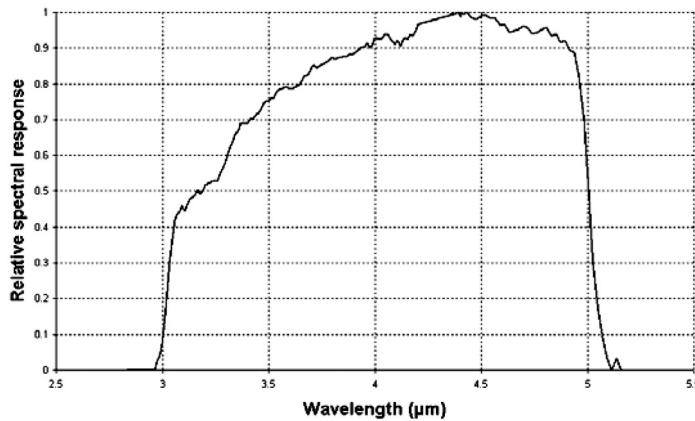


Figure 6.2 Relative spectral response of the AMBER HS infrared imaging system.

Generally, imaging systems can be divided in three categories:

(1) *Single-detector, scanning (imaging) radiometer*

With a scanning mechanism, the instantaneous field of view of a single detector scans the scene of target and background. The detector output is a continuous analog output signal. Often this signal is made TV compatible, in that the voltage levels are converted to gray levels through a black-and-white image on a TV monitor. For such a system, only this single detector must be calibrated. However, single-detector systems are based on obsolete technology.

(2) *Scanning linear array*

A linear array of N vertical detector elements scans the target space, creating N parallel continuous analog output channels. Different scan techniques are possible (serial/parallel), but the detector signals and signal processing, in principle, remain the same. Each detector has its own gain and offset. The complete array, that is, N detectors, have to be calibrated individually.

(3) *Staring 2D focal plane array (FPA)*

The array consists of $N \times M$ detector elements, organized in a square matrix of N rows and M columns. Each detector element has a fixed, staring IFOV and its own gain and offset. In principle, each detector in the matrix should be calibrated individually to be able to obtain quantitative data. In practice, this is hardly achievable. For all these systems, the output is an image in some video format (PAL, NTSC, SECAM) and is recorded in analog or digital format. The final output of the imaging system is a gray (color) scale, producing an image on a TV or computer screen. The gray scale $G(i)$ (i = number of the gray level) is related to the detector output $V_{\text{det}}(i)$ and apparent radiance $L_{\text{ap}}(i)$ by

$$\left. \begin{aligned} L_{\text{ap}}(i) &= aG(i) + L_{\text{off}} \\ G(i) &= \alpha V_{\text{det}}(i) + G_{\text{off}} \end{aligned} \right\}, \quad (6.3)$$

where L_{off} : radiance offset (a constant),
 a : a constant, relating radiance to gray level,
 α : a constant, relating gray level to detector voltage,
 G_{off} : gray level offset (a constant).

The main difference between a non-imaging and an imaging system, if calibration is concerned, is that the end product is a voltage or a gray level, respectively. This implies that a nonimaging system is calibrated for voltage against radiance and an imaging system for gray level against radiance. For nonvarying system parameters, the relations given in Eq. (6.3) are constant. In this case, the coefficients are determined by placing two blackbodies directly in front of the aperture, eliminating atmospheric attenuation [$\tau_a(\lambda, r) = 1$].

The apparent radiance L_A and L_B for the two blackbodies (gray level G_A and G_B , respectively) located directly in front of the aperture and set at temperatures T_A and T_B is solved from Eq. (6.1) as

$$\left. \begin{aligned} L_A &= \int_{\lambda_0} L(\lambda, T_A)R(\lambda)d\lambda = aG_A + L_{off} \\ L_B &= \int_{\lambda_0} L(\lambda, T_B)R(\lambda)d\lambda = aG_B + L_{off} \end{aligned} \right\} \longrightarrow a \text{ and } L_{off}. \quad (6.4)$$

The above assumption that the system parameters are constant in time seldom is valid, especially not when the system is operating under varying outdoor conditions. The consequence is that the entire measurement chain must be calibrated in the field. Especially under varying conditions, calibration should be performed both before and after the experiments.

6.2 Calibration Parameters

As already noted, each detector has to be calibrated. The following discussion outlines the calibration for one single detector. This procedure should be repeated to cover all detectors utilized by a multi-detector imager. The spectral response curve $R(\lambda)$ is a system constant (excluding influences of the front optics) and must be measured once in the laboratory (for instance, with a monochromator). Under normal conditions, $R(\lambda)$ does not change over time.

In a given experimental situation, two more experimental parameters, air temperature T_a and the spectral atmospheric transmissivity $\tau_a(\lambda, r)$, have to be determined:

- The air temperature is easily obtained from a synoptic weather station, which has to be present in any case.
- Direct atmospheric transmission measurements are normally not available during most signature experiments. As discussed previously, the MODTRAN model can be used to calculate the transmission atmospheric coefficient for many conditions.

Finally, at least two blackbody readings are necessary to solve for the calibration coefficients in Eq. (6.3). To increase the level of confidence in the

computation of the calibration curve, preferably more blackbodies (from four to ten) can be used. Also, this offers the opportunity to cover a wider calibration temperature range, by which extended extrapolations can be avoided.

In a practical situation, the main problem in the calibration procedure is the availability of suitable blackbodies. The following considerations must be made:

Blackbody size

- The geometrical resolution on the blackbodies at the given range should be at least twice (but preferably four to five times) the geometrical resolution of the system (IFOV). The system geometrical resolution is determined by the optomechanical characteristics and the electronic bandwidth
- Type of imager (number of detectors)

Blackbody position

- Different/identical range to the target
- Different/same image as the target
- Terrain limitations (line of sight)

Blackbody operation

- Temperature (radiance) stability and uniformity across the spatial extent of the black body
- Weather resistance during long-term outdoor operation
- Power availability, weight and transportability to remote locations
- Condensation problems for temperatures below dew point

The calibration guidelines presented here can be seen as more or less a minimum requirement to obtain calibrated imagery. Depending on the type of measurements and the projected use of the imagery, more specific data can or must be recorded. A full list of possible useful supplementary data would be out of scope here.

A common practical problem is the small size of most commercial blackbodies, which cannot be used at long detection ranges and are normally not designed for long-term outdoor use. Moreover, most of these sources have temperatures above ambient temperature, whereas in some occasions lower temperatures are required (such as with measurements involving low emissivity or specular reflecting surfaces). Simple heating foils or flat radiator plates can be used, but they can only be controlled by heating, not cooling, so the apparent temperature must be monitored continuously.

The best method is to use systems that are controlled both ways, for instance, by regulating the temperature of a liquid coolant flowing through a radiator plate. Such systems can be set to the desired temperature and then left alone.

Figure 6.3 shows blackbodies of 0.5×0.5 m in size, which can be heated and cooled by the use of heat resistors and peltier cooling elements, respectively. These blackbodies cover a temperature range of $T_a - 10^\circ\text{C} < T_{bb} < T_a + 25^\circ\text{C}$.

To calibrate imagery taken at large ranges (especially aerial imagery), large sources of 2×2 m in size, like the one shown in Fig. 6.4, have been made.

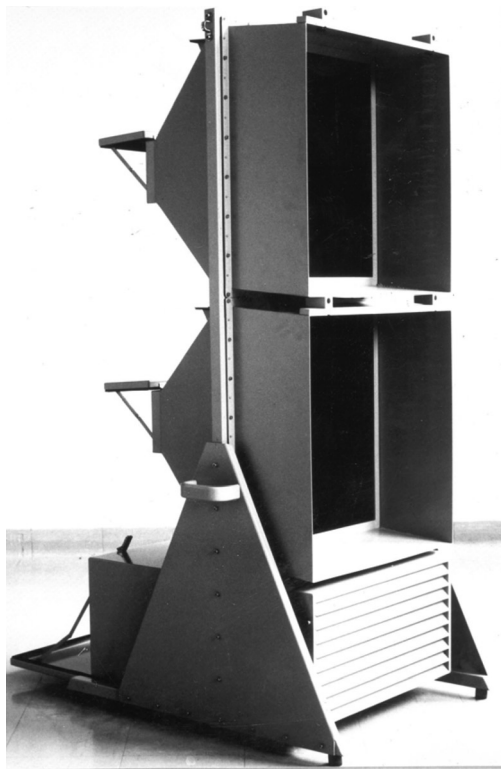


Figure 6.3 Calibration sources 0.5 × 0.5 m in size.

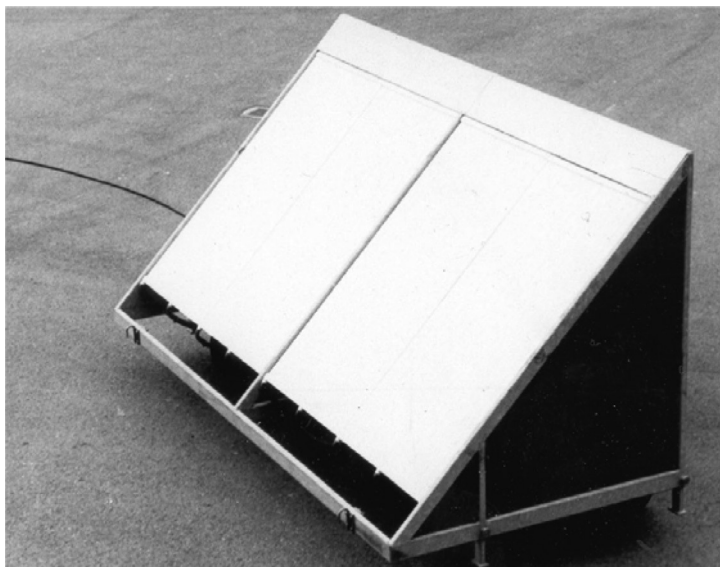


Figure 6.4 Calibration sources 2 × 2 m in size.

This system can maintain preset temperatures in the range of ($T_a - 15^\circ\text{C} < T_{bb} < T_a + 35^\circ\text{C}$). The figure also shows the piping system and electronic controls, which result in a large, heavy construction.

6.3 Calibration Procedures Guidelines

The following procedure describes general guidelines for collecting calibrated imagery. Some special cases, which occur frequently, are discussed.

6.3.1 Blackbodies and target in the same image

Steps to be taken in a calibration experiment:

- (1) The blackbodies are placed at approximately the same bearing and range r as that of the target, so the same spectral atmospheric transmissivity $\tau_a(\lambda, r)$ applies to both optical trajectories, i.e., $\tau_{at}(\lambda, r) \approx \tau_{ab}(\lambda, r) \approx \tau_a(\lambda, r)$. Figure 6.5 shows this situation.
- (2) Select system gain to produce an image without saturation (at least not on the blackbodies).
- (3) In the first step, the apparent radiance L_A and L_B are calculated for the two blackbodies, which are set at temperatures T_A and T_B , using Eq. (6.4):

$$\left. \begin{aligned} L_A &= \int_{\lambda_0} L(\lambda, T_A) R(\lambda) d\lambda \\ L_B &= \int_{\lambda_0} L(\lambda, T_B) R(\lambda) d\lambda \end{aligned} \right\} \longrightarrow L_A \text{ and } L_B. \quad (6.5)$$

- (4) Gain and offset are then calculated from

$$\left. \begin{aligned} L_A &= aG_A + L_{off} \\ L_B &= aG_B + L_{off} \end{aligned} \right\} \longrightarrow a \text{ and } L_{off}. \quad (6.6)$$

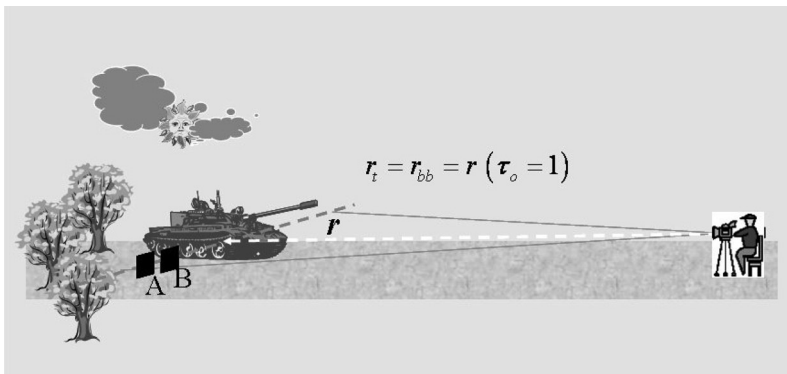


Figure 6.5 Blackbodies and target at the same slant range, bearing, and in the same image.

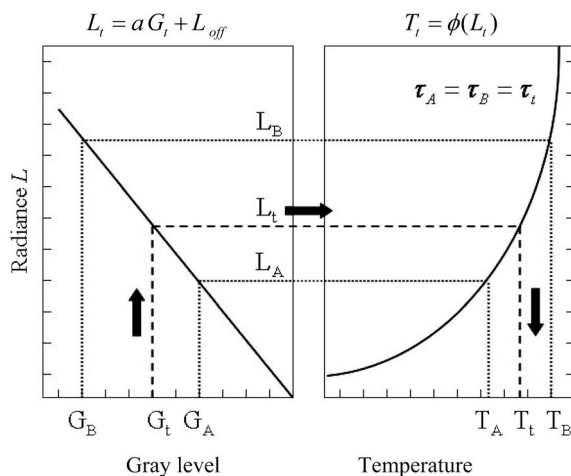


Figure 6.6 Blackbodies and target at the same slant range, bearing, and in the same image, with the radiance as independent variable.

- (5) A gray level on the target G_t can now be converted to a corresponding apparent radiance value. The corresponding apparent target temperature T_t is found from $L_t (= aG_t + L_{off})$ by inversely solving the integral Eq. (6.1) to obtain L_t as

$$L_t = \int_{\lambda_0} \{ \tau_a(\lambda, r)L(\lambda, T_t) + [1 - \tau_a(\lambda, r)]L(\lambda, T_a) \} R(\lambda) d\lambda \longrightarrow T_t. \quad (6.7)$$

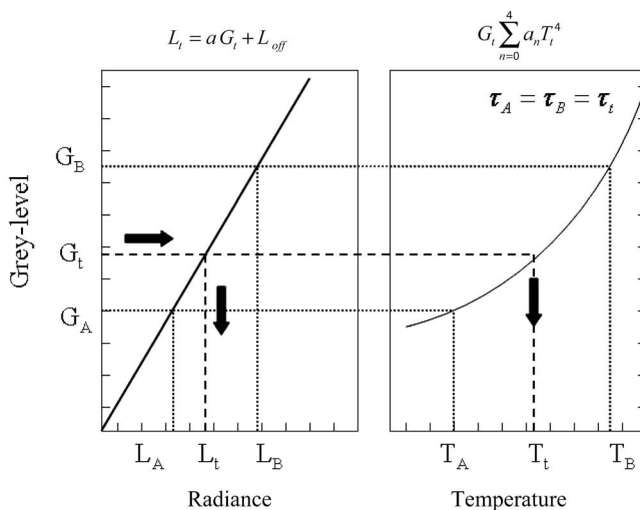


Figure 6.7 Blackbodies and target at the same slant range, bearing, and in the same image, with the gray level as independent variable.

Figure 6.6 shows the graphical representation of this procedure. In this figure, curve B has been found by calculating L for a series of blackbody temperatures [placed at a fixed, constant range $\Rightarrow \tau_a(\lambda, r)$ constant], including the temperatures of the blackbodies used in the image. The left part shows the relation between G and L (Eq. 6.6) and the right part shows the relation between the radiance L and the target temperatures T .

For a system with a variable gain (with fixed discrete steps), each gain setting must be calibrated separately, following the outlined procedure. The practicality of such a task should be considered.

Instead of taking the gray level as an independent variable, the radiance can also be taken as an independent variable, leading to the graph shown in Fig. 6.7.

6.3.2 Blackbodies and target at different ranges

Blackbodies are placed at approximately the same bearing as the target, as shown in Fig. 6.8. The distance between the system and the blackbodies is r_b , and r_t is the distance between the imaging system and the target. The spectral atmospheric system-to-target transmissivity is $\tau_{at}(\lambda, r_t)$ and that for system-to-blackbodies is $\tau_{ab}(\lambda, r_b)$. Select the system gain to produce an image without electronic saturation. The blackbodies may be out of focus, but this is no problem as long as the blackbodies contain enough resolution elements.

First, solve Eqs. (6.1) and (6.6), using the corresponding spectral atmospheric transmissivity for the system-to-blackbody and system-to-target atmospheric path, i.e.,

$$L_A = \int_{\lambda_0} \left\{ \tau_{ab}(\lambda, r_b)L(\lambda, T_A) + [1 - \tau_{ab}(\lambda, r_b)]L(\lambda, T_a) \right\} R(\lambda) d\lambda \quad \text{and} \quad (6.8)$$

$$L_B = \int_{\lambda_0} \left\{ \tau_{ab}(\lambda, r_b)L(\lambda, T_B) + [1 - \tau_{ab}(\lambda, r_b)]L(\lambda, T_a) \right\} R(\lambda) d\lambda.$$

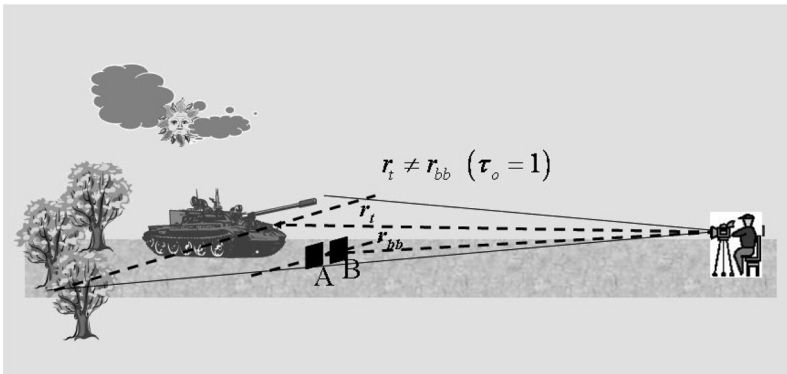


Figure 6.8 Blackbodies and target at different (slant) ranges, but at the same bearing and in the same image.

The calibration coefficients are determined from

$$\left. \begin{aligned} L_A &= aG_A + L_{off} \\ L_B &= aG_B + L_{off} \end{aligned} \right\} \longrightarrow a \quad \text{and} \quad L_{off}. \quad (6.9)$$

A gray level on the target G_t can now be converted to a corresponding apparent radiance value L_t on the target, using $L_t = aG_t + L_{off}$. The corresponding target apparent temperature T_t is found by inversely solving the integral for L . In this case, however, the atmospheric transmissivity $\tau_{at}(\lambda, r_t)$ for the system-to-target optical path is used:

$$L_t = \int_{\lambda_0} \{ \tau_{at}(\lambda, r_t)L(\lambda, T_t) + [1 - \tau_{at}(\lambda, r_t)]L(\lambda, T_a) \} R(\lambda) d\lambda \longrightarrow T_t. \quad (6.10)$$

This procedure is represented graphically in Fig. 6.9. The left part shows the relation between gray level G and apparent radiance Eq. (6.9); the right part, between L and T . The upper curve (τ_{ab}) is created by solving Eq. (6.10) for a series of blackbody temperature settings (including the actual blackbody temperatures). The lower curve (τ_{at}) is also created by using a range of most likely prevailing target temperatures

$$L_t = aG_t + L_{off} \quad T_t = \phi(L_t).$$

6.3.3 Blackbodies and target at different (slant) ranges but at the same bearing and in the same image

This type of measurement is often encountered when dealing with moving targets and when the system is following the target, such as an aircraft or ship passing

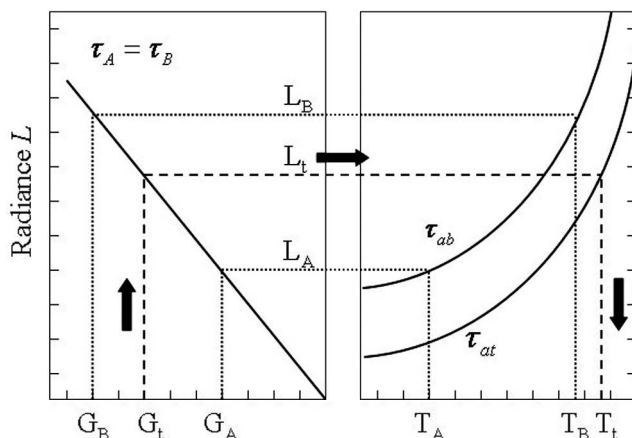


Figure 6.9 Blackbodies and target at different (slant) ranges but at the same bearing and in the same image.

by. Because of the constant change of range to the target (leading to a varying $\tau_{at}(\lambda, r_t) \Rightarrow$ varying apparent radiance), the gain often has to be adjusted. Figure 6.10 shows this situation. For reasons of convenience or because of limited range (for instance, an IR camera following moving targets), the blackbodies are placed directly in front of the aperture, leaving the focus set at infinity.

The calibration coefficients are solved for this situation for all expected gain settings,

$$\left. \begin{aligned} L_A &= \int_{\lambda_0} L(\lambda, T_A)R(\lambda)d\lambda \\ L_B &= \int_{\lambda_0} L(\lambda, T_B)R(\lambda)d\lambda \end{aligned} \right\} L_A \quad \text{and} \quad L_B \left\{ \begin{aligned} L_A &= aG_A + L_{off} \\ L_B &= aG_B + L_{off} \end{aligned} \right\} a \quad \text{and} \quad L_{off}.$$

The target apparent temperature T_t is found by inversely solving the integral for L . In this case, however, the spectral atmospheric transmissivity $\tau_{at}(\lambda, r_t)$ for the system-target optical path must be used:

$$L_t = \int_{\lambda_0} \{ \tau_{at}(\lambda, r_t)L(\lambda, T_t) + [1 - \tau_{at}(\lambda, r_t)]L(\lambda, T_a) \} R(\lambda)d\lambda \rightarrow T_t. \quad (6.11)$$

For one situation, this procedure is represented graphically in Fig. 6.11, showing solutions of Eq. (6.11) for a few different ranges, i.e., for different spectral atmospheric transmissivity. The figure shows that for increasing range, the apparent target temperature decreases, and the gray-level shifts to lower values.

As the target moves, $\tau_{at}(\lambda, r_t)$ is continuously changing (resulting in a varying gain and offset); consequently, Eq. (6.11) must be evaluated for all prevailing situations. Under all circumstances, it is highly desirable to perform the calibration procedure *in situ* and to check it against a third blackbody positioned at a few different ranges and set at different temperatures. With strongly varying conditions, a regular recalculation of the calibration coefficients is highly

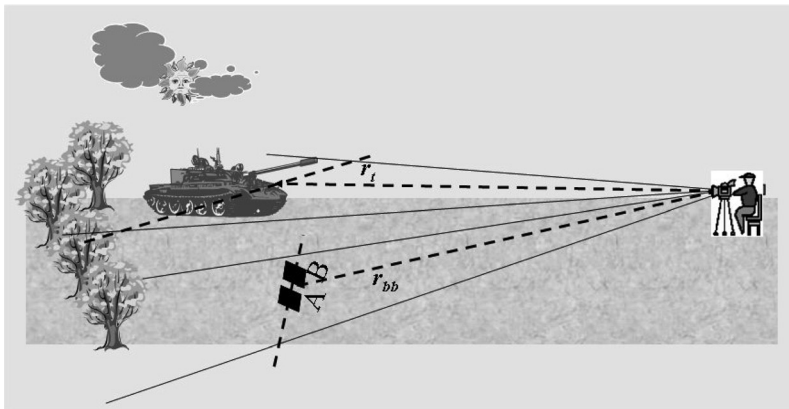


Figure 6.10 Blackbodies and target at different (slant) ranges, bearings, and in different images.

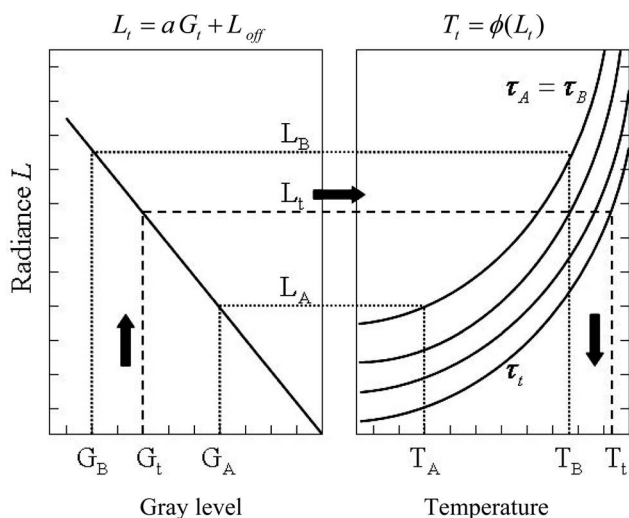


Figure 6.11 Blackbodies and target at different (slant) ranges, bearings, and in different images.

recommended. In any case, recalculation should be performed before and after the measurements.

So far, single-detector imagers have been discussed. For imagers using a linear detector array (N detectors), the outlined procedure must be performed for each detector. In practice, this means each detector in the array must have at least two samples on the blackbodies. For each detector (scan line), the calibration coefficients have to be determined, resulting in N sets of coefficients. Some of these systems use several (M) horizontal scans of the vertical array to produce one image ($N \times M$ scan lines). In that case, the blackbodies have to cover the complete FOV of the imager to calibrate each scan line, resulting in $N \times M$ sets of coefficients. In practice, this can only be done with the blackbodies located directly in front of the aperture.

For imagers using 2D arrays, almost always used as staring arrays, each detector must also be calibrated, and this can only be done by placing the blackbodies, one at a time, directly in front of the aperture. Multi-detector calibration procedures are identical to those outlined in Section 6.1, applied to each individual detector. However, this is practically impossible, because it is not possible to set the gain and offset of each individual detector.

6.4 Practical Example

In the summer of 1988, the NATO group AC243/P4.RSG17 carried out an elaborate, unique field trial,² called IRIS, to collect short-(40 m) and long-range (up to 4 km) calibrated images of 25 targets, including NATO and WP main battle tanks and armored personnel carriers (APCs). All multinational systems

were calibrated in the field, following identical calibration procedures. The results were directly compared in the field and calibrations were repeated if the differences were too large.

The targets were exercised for half an hour, placed on a 60-ton turntable with idling engine as shown in Fig. 6.12, and imagery was collected at every 45-deg angle from two elevation angles (0 and 15 deg). Data were taken in two spectral bands, 3–5 and 8–12 μm , simultaneously and recorded on tape in the form of digital frames of 12-bit temperature dynamic range and also on videotape. A number of reference blackbodies were placed in the field of view.

Weather parameters

The weather station was installed in the direct surroundings of the experimental setup. The location was chosen so that the influence of surrounding obstacles (trees, houses) on sensor operation was minimal. Furthermore, the location was chosen to be representative for the target location weather conditions.

As a supplementary sensor, a pyrgeometer was included in the meteorological station. Data were recorded automatically in digital format on hard disk.

Blackbody positioning

Up to 10 blackbodies (50 \times 50 cm) were placed around the turntable close to the targets, covering a wide range of temperatures. For this case, the calibration parameters are determined following the procedure as outlined in Section 6.3.1. The apparent temperature of the blackbodies was measured every half hour, using a hand-held radiometer kept at close range.

Target conditions

The physical properties (emissivity, solar reflectivity, etc.) and target type, including possible target modifications or upgrades (engine, gear box, bearings compartment heating on/off), were recorded.

The operational condition (engine temperature and engine rpm) and operational history (parking conditions, exercising surface, speed and time) of each target were determined, as was the surface condition of the target (mud/dust covered, wet/dry), each time it was put on the turntable.



Figure 6.12 Turntable measurement facility.

Site conditions

The site is located in Meppen in Germany (52 deg 44' N, 7 deg 20' E). The distance between the IR system and the target on the turntable and also the offset angle in azimuth to the turntable were measured. Due to changing weather conditions, the soil was sometimes dry and then wet again, which can influence the signature of the tracks (mud) or the top part (dust), so this condition was recorded also.

Results for a tank

An example is given for the LEOPARD-I tank. Recording time was at 22:00 LCT (GMT+1 hour) on 7 June 1989. This is the period of late evening to night. This time frame was chosen to avoid solar loading during the measurements, which would have excluded a comparison of different targets. This is also the reason the targets were parked in a garage during daytime.

The turntable was halted at every 22.5-deg rotation to allow for image collection with slow scanning imagers. For instance, the DuDa system (TNO-FEL in-house development) requires four seconds to complete one image.

Imaging system

The experimental imager DuDa features dual-waveband 3–5 and 8–12 μm and 12-bit digital recording. Range target to system is 40 m. IFOV = 1 mrad and a selectable horizontal FOV of 30 or 15 deg vertical FOV = 7 deg. The image is built up of 240×1000 pixels with a geometrical resolution on the target of 5 cm^2 (4.9 cm^2 determined from the blackbody dimensions and the IFOV of the imager). The apparent temperature resolution is 0.1 K per gray level. Figure 6.13 shows the spectral response curves of the DuDa imaging system.

Target conditions

The tank was exercised to operational conditions ($T_{\text{engine}} \cong 90^\circ\text{C}$) and was driven onto the turntable, leaving the engine idling during the measurements. All hatches were closed, with crew members inside the vehicle. The surface was dry and clean.

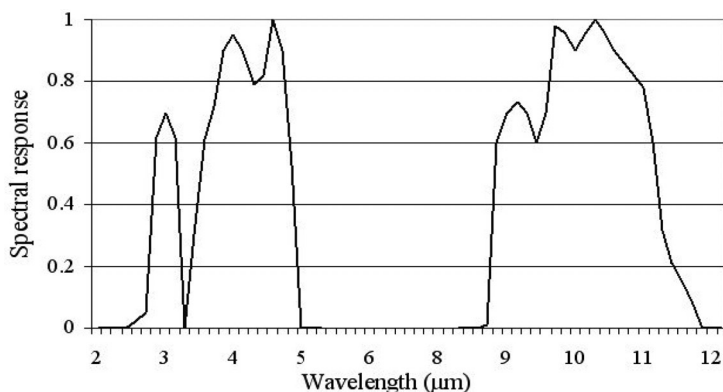


Figure 6.13 Relative spectral response curves of the DuDa system.

Weather conditions

Air temperature	:	10.2°C
Average wind direction	:	200 deg (SSW)
Average wind speed	:	2.5 m s ⁻¹
Visibility	:	8700 m
Relative humidity	:	80%
Local time	:	22:00 hours (night, no solar loading)

Figure 6.14 shows the two images, together with a number of blackbodies to the left and right of the turntable. Viewing aspect angle in elevation $\vartheta = 0$ deg (horizontal) and a viewing angle in azimuth $\varphi = 45$ deg (0 deg front, $\varphi = 90$ deg left-hand side).

The atmospheric transmissivity is calculated with MODTRAN, using the actual weather data. Figure 6.15 shows the calculated spectral atmospheric transmissivity for 3–13 μm . As is to be expected, the atmospheric attenuation for such a short range is quite small.

From the spectral distribution given in Fig. 6.15, the mean atmospheric transmission coefficient in 3–5 μm and 8–12 μm is calculated as $\tau_a(3-5) = 0.92$ and $\tau_a(8-12) = 1.0$.

The blackbodies, shown on the right-hand side of the image (Fig. 6.14), were maintained at temperatures as given below.

$T_1 = 22.0^\circ\text{C}$	$T_2 = 38.0^\circ\text{C}$
$T_3 = 30.0^\circ\text{C}$	$T_4 = 14.0^\circ\text{C}$

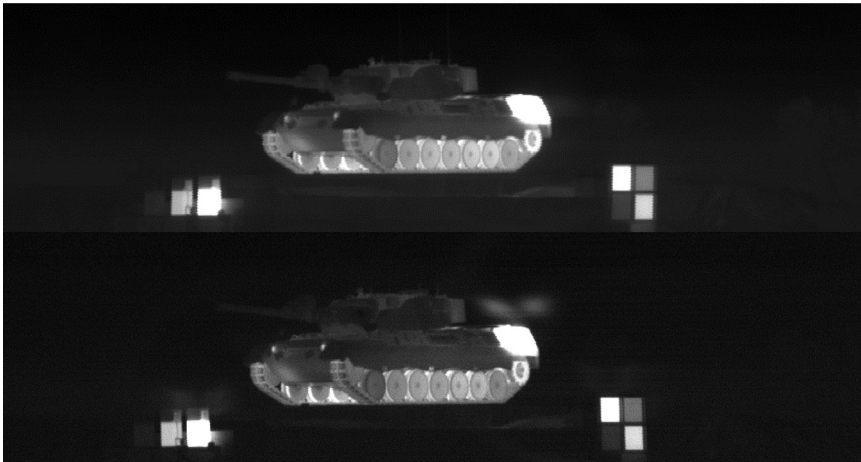


Figure 6.14 An example of a calibrated, high-resolution image from the IRIS trial; top, 8–12 μm ; bottom: 3–5 μm .²

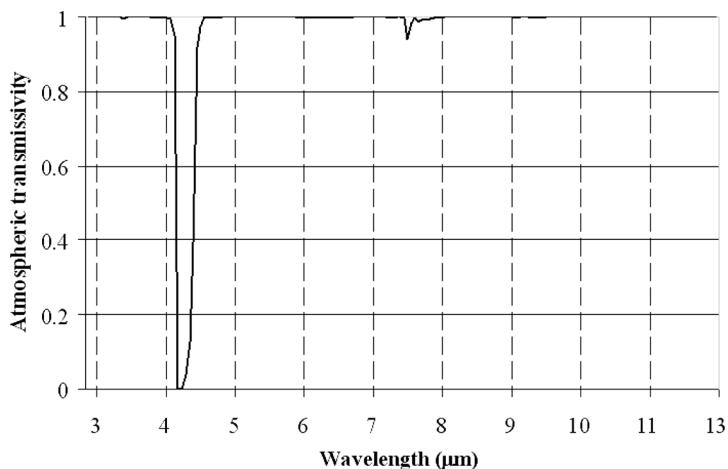


Figure 6.15 Spectral atmospheric transmissivity $\tau_a(\lambda, r)$ for $r = 40$ m.

The corresponding gray levels in 3–5 and 8–12 μm images are:

3 5 μm		8 12 μm	
2095	2272	2142	2320
2174	2035	2048	2063

Now, Eqs. (6.5) and (6.6) can be solved for a and L_{off} , resulting in:

Parameter	3 5 μm	8 12 μm
a	6.5×10^{-3}	3.5×10^{-2}
L_{off}	25.1	124.8

The result of the calibration is expressed in a relation between the gray level G and the intrinsic apparent temperature T_{ap} (i.e., corrected for atmospheric attenuation), as is shown in Eq. (6.7) and Fig. 6.16. Since four blackbodies were available, this relationship between gray level and blackbody temperature is approximated by a fourth-degree polynomial in T_{ap} ,

$$G(T_{ap}) = \sum_{i=0}^4 a_i T_{ap}^i, \text{ where} \tag{6.12}$$

Coefficient	3 5 μm	8 12 μm
a_0	9955.1	3439.7
a_1	108.14	7.14
a_2	0.73455	0.07429
a_3	2.259×10^{-3}	2.555×10^{-4}
a_4	2.659×10^{-6}	1.931×10^{-7}

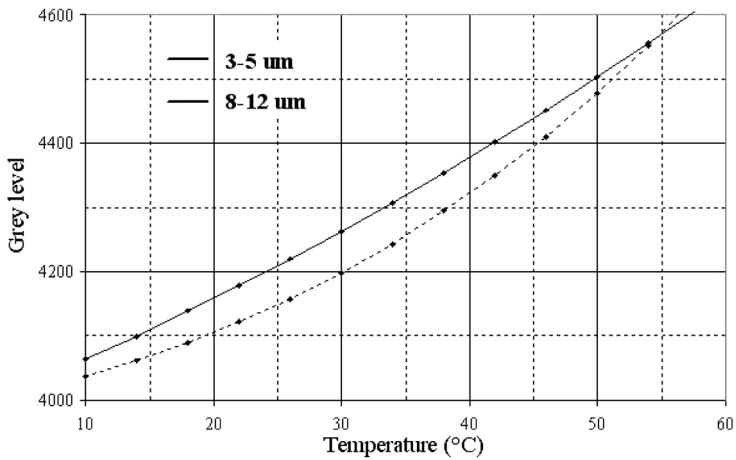


Figure 6.16 DuDa calibration curves.

Finally, Fig. 6.16 shows a combined graphical representation of Eqs. (6.6) and (6.12), directly relating intrinsic target temperature to gray level, using the DuDa image shown in Fig. 6.14 as input.

As an example, the outlined calibration procedure has been applied to a series of images of a T62 tank taken in the 8–12 μm bandwidth during the RSG17 field experiments in Germany. Figure 6.17 shows the starting position of the T62 on the turntable. Images were recorded every 22.5 deg.

For each image, the total radiance of the T62 tank was calculated and converted to a mean temperature, using the calibration curve. The result is



Figure 6.17 T62 placed on the turntable (8–12 μm).

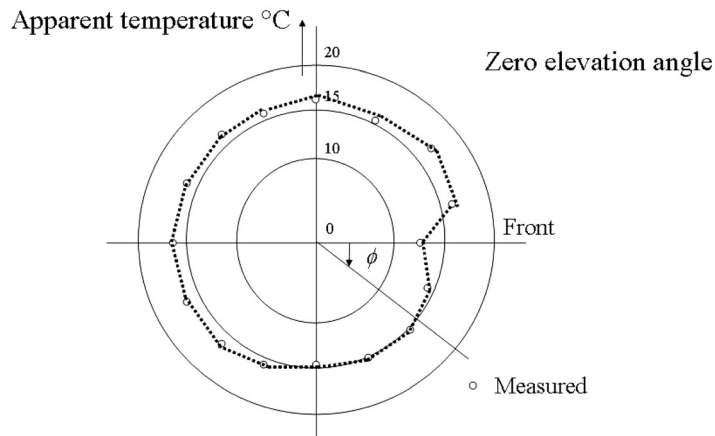


Figure 6.18 Measured temperature polar diagram of a T62 in 8–12 μm .

plotted as a polar diagram in Fig. 6.18 and shows the relationship with calculated temperatures using PRISM.

This international exercise has demonstrated that despite the fact that all participants used the same blackbody reference sources, software, and transmission correction, a spread of 2°C was found in the calibration results of the seven participating nations. This obviously must be caused by an inaccurate measure of system parameters, like the spectral response curve or the digitizing process.

It indeed shows that all parameters that influence the calibration procedure must be accurately known (at least within the desired overall accuracy).

References

1. P. Chevrette, "Calibration procedures for IR signature analysis," *Proceedings of SPIE*, 661 (1986).
2. P.A.M. Jacobs, "NATO AC243/P4.RSG17 on land combat signatures: field trial in Germany," *General Overview of KRC Symposium*, Michigan, Technological University (1989).

Chapter 7

Infrared Signature Characterization

In the previous chapters, parameters related to targets, backgrounds, sensor systems, and atmosphere have been discussed. Information on these parameters must be obtained

- to validate model calculations,
- to determine detection and especially identification clues on the target,
- to train automatic target recognizers (ATR),
- to develop countermeasures,
- for design purposes, and
- as input for simulation models (operational research).

7.1 Target Signatures

Two types of signatures are of interest:

- (1) Signatures taken from close range
This type of signature mainly is used to study the target signature as such, that is, to study the radiance distribution over the target. This type of signature data generally is used to validate the predictions of theoretical models or to develop target signature reduction methods (thermal camouflage). To be able to retrieve intrinsic target data, calibrated images with a high spatial and temperature resolution are needed, preferably taken at close range. Also, a recording of detailed weather information is required.
- (2) Signatures taken from far range
This type of signature is used to study target signatures in relation to background signatures, that is, to investigate the behavior of the target contrast. Signatures can be taken for targets in motion or in static positions. Data often are used in relation to target detection (recognition) and to study the efficiency of thermal camouflage in relation to background clutter. This type of signature need not necessarily be calibrated, because the contrast as such is of main importance.

Both measurements and modeling can be used for signature studies and the best choice depends on the complexity of the problem. Models have the advantage that all kinds of scenarios can be simulated without much trouble, but the results always will contain an unknown, possibly large inaccuracy. For complex geometrical structures, models are not well suited, because the heat-transfer processes are mainly determined by the unknown local conditions at the target facets. The model equations, however, are based on parameters as they are defined in the free airstream.

Measurements have the advantage in that they directly represent the real world. It is, however, extremely time and resource consuming to collect a representative set of target signatures under various weather and target conditions. A sensible mix of modeling and measurements is the best way to characterize IR signatures.

In Chapter 4, it was concluded that two parameters determine the thermal behavior of a surface, i.e., the emission coefficient and the temperature. The next section discusses these two parameters in more detail.

7.1.1 Field measurement of the long wave reflection coefficient

The only way to measure the emissivity of a surface is through a measurement of the radiant emittance of the surface, which was presented in Section 3.1.3 as

$$E_{ap} = \int_{\lambda_0} E(\lambda, T_{ap}) d\lambda \quad \text{or} \quad E_t = \overline{\varepsilon}_t \int_{\lambda_0} E_{bb}(\lambda, T_t) d\lambda. \quad (7.1)$$

The second term in Eq. (7.1) shows that the emission coefficient can be made explicit only if the real surface temperature is known. Rewriting Eq. (7.1) to be explicit in ε_t results in

$$\overline{\varepsilon}_t = \frac{E_t^m}{\int_{\lambda_0} E_{bb}(\lambda, T_t^m) d\lambda} \quad (\text{superscript } m \text{ for measured}). \quad (7.2)$$

For solid materials (that is, having a solid surface), measurement of the surface temperature normally is straightforward and allows the use of Eq. (7.2). However, if the spectral band of the radiometer becomes relatively small, the emittance will be small, especially when the emission coefficient is low. To increase the emittance, it is necessary to heat the material. In cases in which the surface temperature cannot be measured accurately enough or the sample cannot be heated, a different method must be used.

For opaque surfaces, $\rho_l + \varepsilon = 1$ (Section 2.2), which implies that the emission coefficient can be determined from a measurement of the long wave reflection coefficient ρ_l use

$$\rho_l = \frac{E_l^{ref}}{E_l^{in}}, \quad (7.3)$$

where E_l^{in} is the total long wave incident radiation (irradiance) and E_l^{ref} is the total reflected radiation.

Unlike solar radiation, which has a direct (specular) component, long wave (natural) radiation is dominantly diffuse by nature. Natural and many manmade surfaces behave as diffuse reflectors and, to reduce target detectability, great efforts are made to suppress gloss and specular reflection. For this reason the diffuse-diffuse reflection coefficient is of primary importance, meaning “diffuse incident radiation reflected by a diffuse surface.” So, the reflection coefficient in Eq. (7.3) is the diffuse-diffuse reflection coefficient.

Earlier measurements of the reflection coefficient of natural surfaces, exposed to outside atmospheric conditions, were time consuming and cumbersome in execution.⁷ In order to ease this process, a convenient, hand-held system infrared reflectometer was developed at TNO.⁸ The system essentially measures the amount of reflected radiation from a sample surface, illuminated by known IR sources. The practical solution for this principle is shown in Fig. 7.1. The system is a rectangular box whose inside walls have the following functions:

- The bottom surface is the sample surface.
- The four vertical walls are IR specular reflectors.
- The top surface is an IR source and also holds the IR detector.

Radiation from the top surface is directed to the sample surface directly and indirectly via the mirrors; i.e., the sample surface is diffusely illuminated. Reflected radiation goes the opposite direction and diffusely illuminates the top surface, where a detector, located in the center, measures the reflected radiation. In this way the “hemispherical-hemispherical” and “diffuse-diffuse” reflection coefficient is measured. To account for electronic drift (gain and offset), which is hard to avoid when using a DC amplifier under varying environmental conditions, the top surface is configured as a controllable blackbody, switching between two temperatures, T_1 and T_2 .

This is achieved by drilling 16 evenly distributed holes in the top surface. Each hole contains a blackbody and they are arranged in two groups of eight, with one

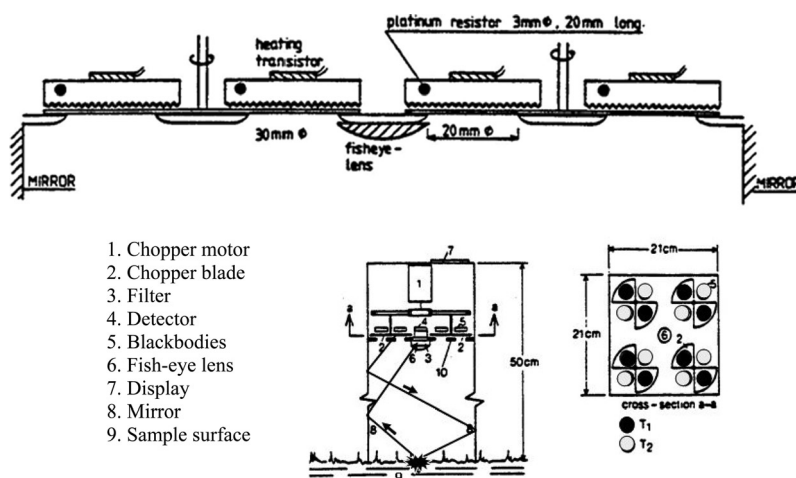


Figure 7.1 Schematic drawings of a hand-held IR reflectometer.

group set at a temperature of $T_1 = 44^\circ\text{C}$ and the other at $T_1 = 67^\circ\text{C}$. The groups are chopped (2 Hz) in such a way that at a given moment, one group is exposed, while the other is covered. At the next chopper position, the second group is exposed, while the first is covered. Figure 7.2 shows a photograph of the complete system and shows this mechanism in detail.

This figure also shows the location of the detector (in the center) and an optional fish-eye lens (IRTRAN II) to correct for radiation incident at small angles. Because of its volume and weight, it can be carried in the field easily and calibration is a simple, straightforward procedure. To calibrate it, the protective cover is installed at the bottom opening. The inside of the cover is provided with household aluminum foil, which approaches a 100% IR reflective surface. In this configuration, a measurement is performed and the readout is adjusted to 100%. If the system is now placed on the sample surface, the display gives an absolute reading of the reflection coefficient. The emission coefficient then simply follows from $\varepsilon = 1 - \rho_L$.

Technical specifications

Detector type	: thermopile (1M Dexter Research Lab)
Spectral response	: from UV to FIR
Filters	: 3–5 μm and 8–12 μm
Sample size	: 16 \times 16 cm
Measurement time	: ± 30 seconds
Accuracy	: $\leq 20\%$ (3 μm) and $\leq 2\%$ (10 μm)
Total height	: 50 cm
Total weight	: ± 15 kg
Spectral curves	: Figure 7.3
Reference surface	: $\pm 99\%$

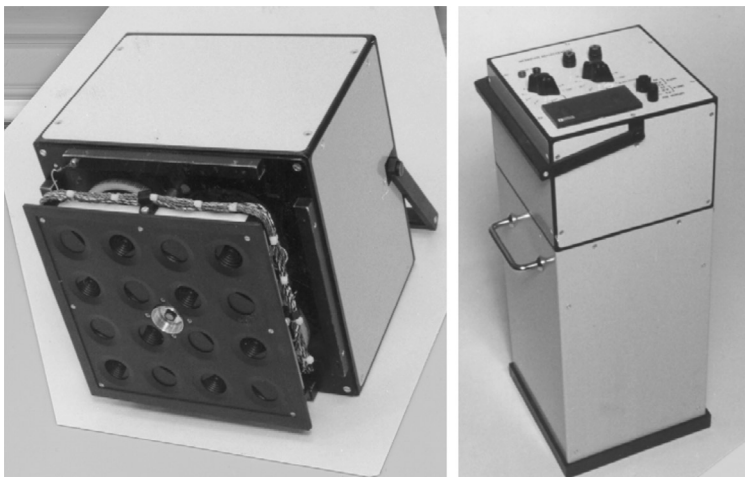


Figure 7.2 Hand-held infrared reflectometer.

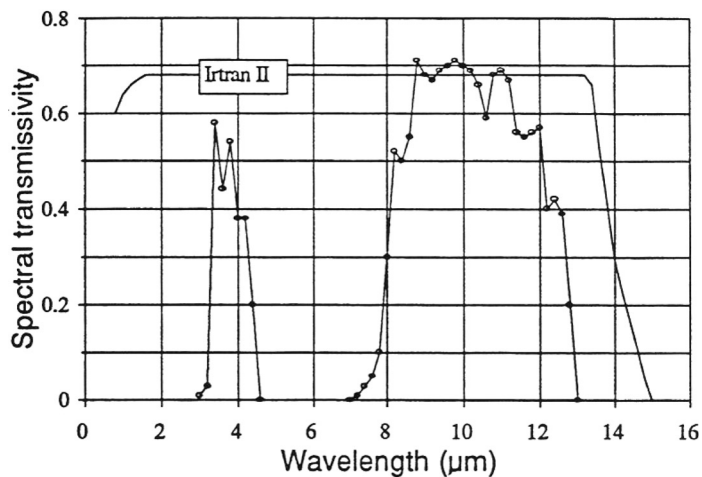


Figure 7.3 Spectral transmissivity of the filters in the infrared reflectometer.

Table 7.1 Reflection coefficient ρ_I for various natural species.

Species	3.0 5.5 μm	8.0 14.0 μm
Maple leaf (top, dry)	0.87	0.92
Grass (meadow)	0.82	0.88
Bark (red oak)	0.90	0.96
Coniferous twigs	0.96	0.97
Corn		0.94
Sugarcane		0.99

Table 7.1 shows the infrared reflection coefficient ρ_I for various species in the spectral region of 3.0–5.5 μm and 8.0–14.0 μm . Note that the sample need not have a smooth surface, but the system allows for quite a degree of roughness.

7.1.2 Measurement of thermal target signatures in the field

Three measurement campaigns will be discussed as examples of IR signature collection efforts.

- (1) CHAR-II experiment in Sardinia in 1994 to collect IR signatures of three different types of targets in a Mediterranean environment.
- (2) IRIS experiments to collect IR signatures of many different main battle tanks (MBT) and armored personnel carriers (APCs). High-resolution signatures at short ranges (turntable) and long-range signatures of mobile targets were recorded.
- (3) HOM experiments to collect multispectral signatures of surface and buried landmines.

7.1.2.1 CHAR-II experiment

After the fall of the Berlin Wall and the change of possible deployment areas into a global coverage, signatures of targets and backgrounds other than in woodland became of interest. In that respect, the CHAR-II experiment was set up in Sardinia in August 1994 to collect IR signatures of targets in and backgrounds of a typical Mediterranean environment. Figure 7.4 shows the sensor layout. The SCORPIO scanner was placed on top of a 7-m-high scaffold. The DuDa camera was placed at the bottom.

Four sets of targets, each comprising a Leopard I tank, a M113 (APC) and a 4-ton truck, were placed in the cardinal directions around the sensor platform. A schematic layout of the experimental setup and some visual images of the target sets are shown in Fig. 7.5. The images clearly show the kinds of backgrounds in the different target-area directions. The terrain is a mixture of bare soil (mostly sand), sparse vegetation, and shrubs. Two calibration blackbodies were placed close to the targets in position 1. Infrared images were taken every half hour for contiguous periods of up to 36 hours. Figure 7.6 shows IR images (DuDa 8–12 μm) of the targets placed in position 1 (SE) in the early morning of 4 August at 02:03 hours and in the early afternoon at 14:01 hours. The targets were exercised to operational temperatures in the evening of 3 August from 19:00–20:00 hours and left untouched for the next 48 hours. Figure 7.6 shows that even after a six-hour cooling period, engine compartments and heavy metal parts are still warm. Lighter materials (toolboxes, tarpaulin), especially those on top of the vehicles, begin to show a negative contrast.

Images such as those shown in Fig. 7.6 are used to study in detail the thermal signatures of targets and backgrounds. With simple image-processing tools, the average apparent temperature of the projected target or background area as



Figure 7.4 CHAR-II experimental setup.

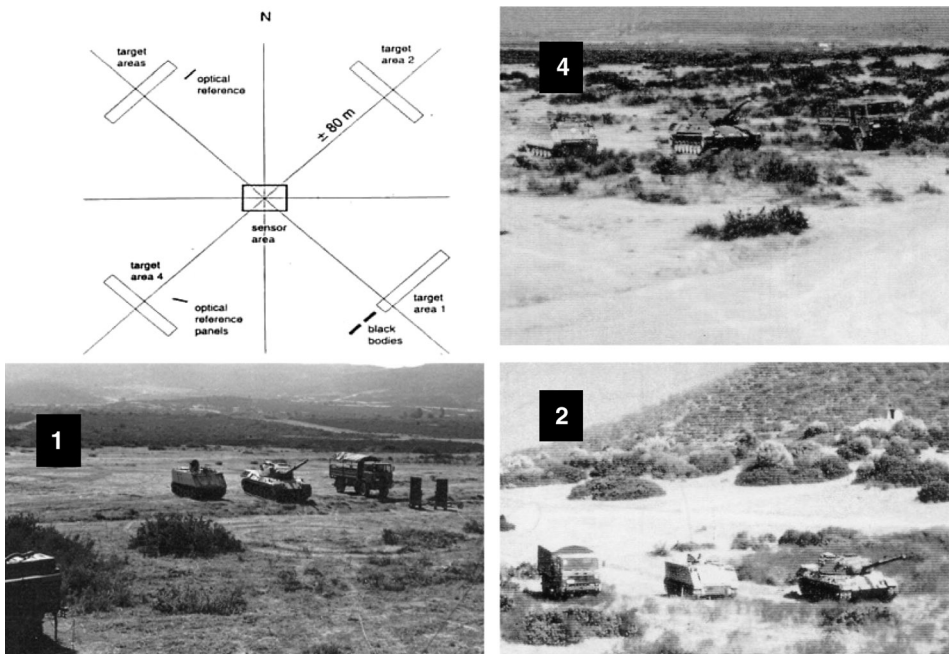


Figure 7.5 CHAR-II instrumentation platform and target positioning.



Figure 7.6 CHAR-II DuDa 8–12 μm images of targets in position 1 (SE) during early night (top) and early afternoon (bottom).

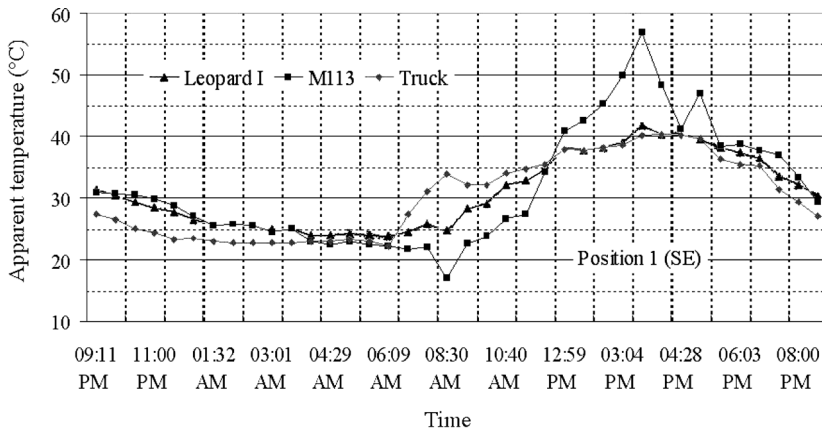


Figure 7.7 Apparent temperatures of various targets observed in SE direction.

imaged in the four directions can be calculated. Figures 7.7 and 7.8 show the resulting apparent target temperature for position 1 (SE) and position 3 (NW). The responses in both directions are quite different in two ways. First, the changing position of the sun creates sunlit and shaded target areas; second, special target features such as the inclined front of the M113 and the tarpaulin cover on the truck have an effect.

Figures 7.9 and 7.10 show the apparent temperature of some background elements as derived from the images in position 1 and 3. At night, the differences are small, but during daytime under sunny conditions the responses in both directions are quite different. Ultimately, the apparent temperature contrast between the targets and the various background elements can be determined.

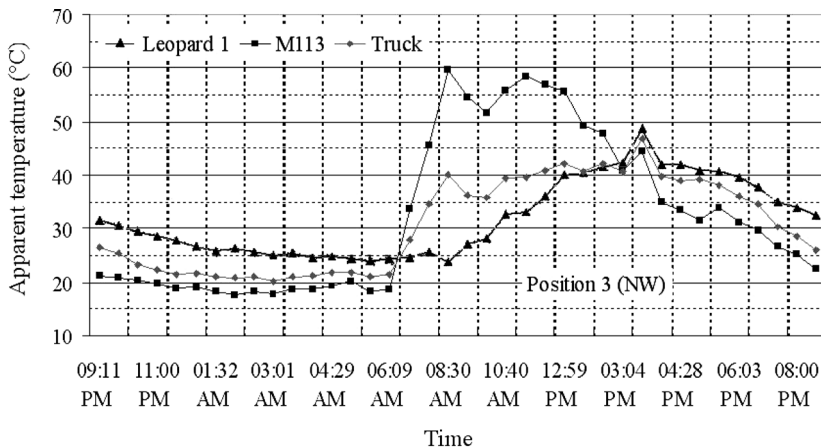


Figure 7.8 Apparent temperatures of various targets observed in NW direction.

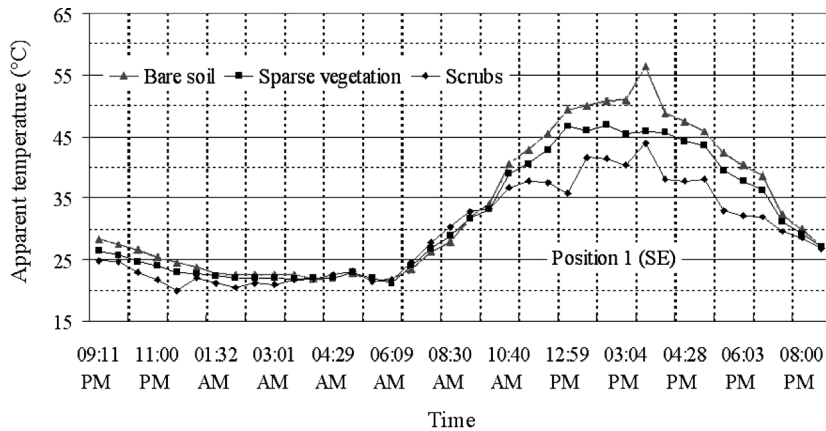


Figure 7.9 Apparent temperatures of various background elements measured in SE direction.

Figures 7.11 and 7.12 show the results for the Leopard I tank. During the cool-down period in the early morning, generally the contrast gradually reduces for both directions from about 5°C to 0°C just before sunrise at about 06:00. After sunrise, the contrast with respect to soil and sparse vegetation behaves quite similarly. But with respect to the shrubs, the contrast in position 3 (NW) is much higher and has a steeper gradient than for the Leopard I in position 1.

It is interesting to note that in a hot, arid region such as Sardinia, the contrast becomes negative for most of the day. This is just the opposite in regions with a moderate climate, such as northwestern Europe. Both figures show that the observed contrast in the infrared, among others, depends on the direction of view, something long known in the visual spectral band.

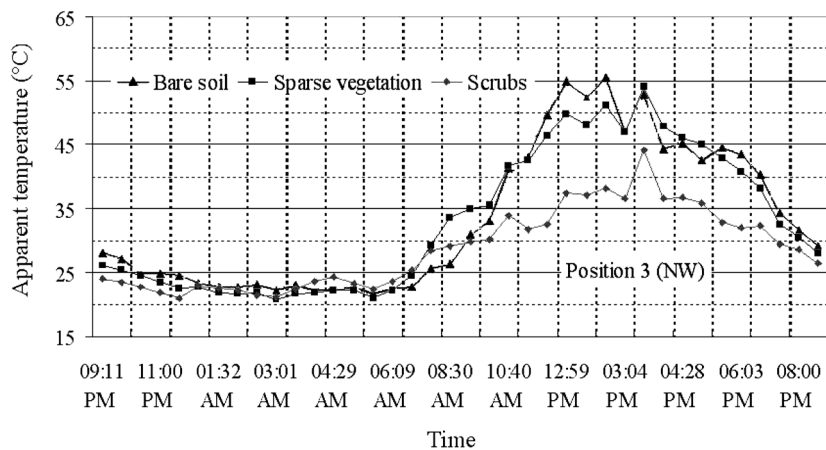


Figure 7.10 Apparent temperatures of various background elements measured in NW direction.

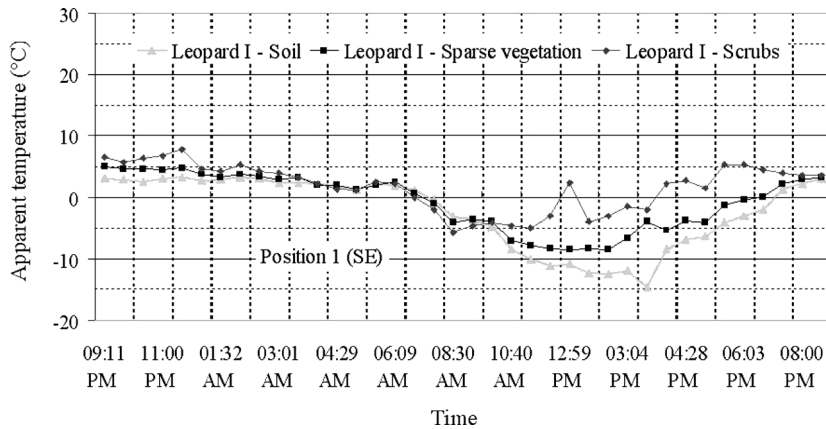


Figure 7.11 Apparent-temperature contrast between the targets and the various background elements in SE direction.

7.1.2.2 IRIS trials

The setup of the turntable measurements to record high-resolution IR signatures of MBTs and APCs was already discussed in Section 6.4. The second part of this trial was held in Münster, Germany, in 1988, and was devoted to recording the IR signatures of moving targets from the ground and from a helicopter platform. The same set of target vehicles used for the turntable measurements took part in this exercise. Since this was an international experiment, carried out by a NATO research group, many nations took the opportunity to bring

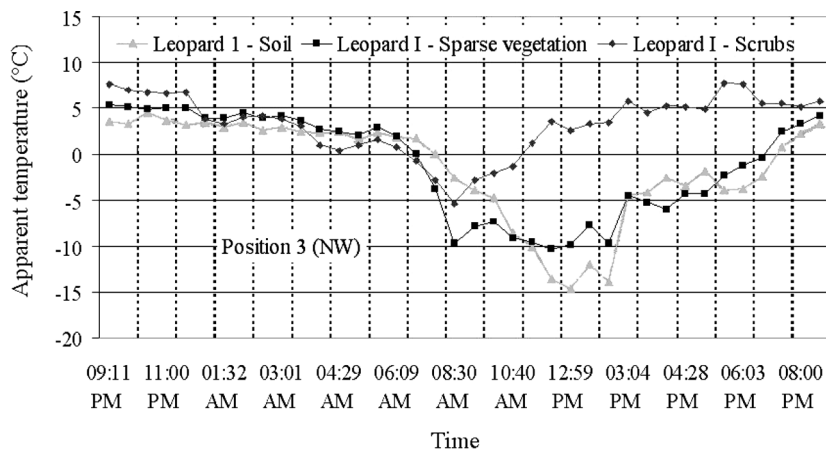


Figure 7.12 Apparent-temperature contrast between the targets and the various background elements in NW direction.



Figure 7.13 Sensor platform.

state-of-the-art IR sensors. During this trial, one of the first FPAs was brought into the field. Figure 7.13 shows the sensor platform setup at the Charlie range in Münster.

The sensors overviewed a range with a free LOS of up to 3 km. Groups of three targets were formed and driven from the far end of the range towards the sensor platform. In order to record all target aspect angles, the target array had to follow a specially designed course. A schematic drawing of this course is shown in Fig. 7.14. Figure 7.18 shows a sample image ($8\text{--}12\ \mu\text{m}$) taken from a videotape of three tanks (frame taken at side aspect of targets) driving a circular pattern at 1 km distance.

Parallel to measurements from the ground, thermal video imagery was collected from a helicopter equipped with a TICM-II FLIR camera ($8\text{--}12\ \mu\text{m}$).

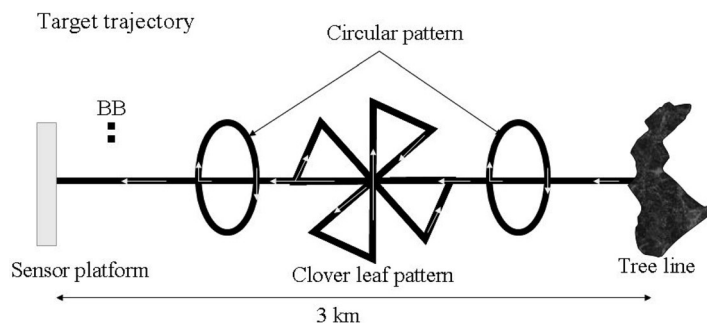


Figure 7.14 Target course.

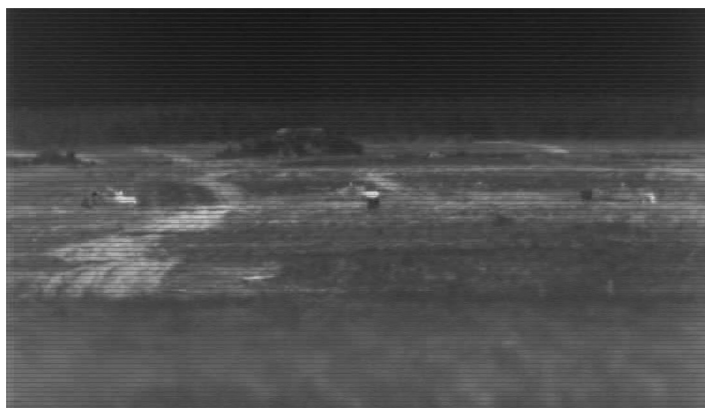


Figure 7.15 Sample image of the IRIS trial (8–12 μm); three targets driving a circular pattern at 1-km distance.

A helicopter provides the flexibility to take images from all directions in a very short time. Figure 7.16 shows a near-top-view image taken from the helicopter of three tanks at close range. This image comes from a video showing the approaching sequence and a full close-up circle of the tanks. Moving vehicles can generate special signatures generated by the moving itself. Figure 7.17 shows a huge dust plume that the driving vehicles generate. Although the topsoil was fairly dry, the plume shows a strong negative signature. Because the tracks move quite a thick layer of soil, more wet (and cooler) subsoil is thrown into the air, which is boosted upwards by the exhaust gases, thereby creating the negative contrast.



Figure 7.16 Close-up image taken from a helicopter with a TICM-II camera (8–12 μm).

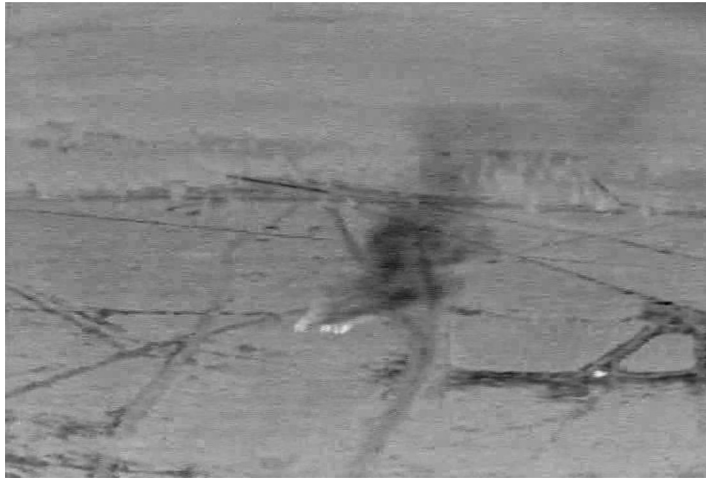


Figure 7.17 Dust plume generated by driving tanks.

7.1.2.3 *Land mine detection experiments*

In connection with humanitarian de-mining, dedicated sensor systems to detect surface and buried land mines are developed, improved, and tested. In parallel, an outdoor test facility¹⁵ has been established to measure multispectral signatures of many types of land mines under controlled soil conditions (Fig. 7.18). The test



Figure 7.18 Test bed to measure multispectral signatures of surface and buried land mines.

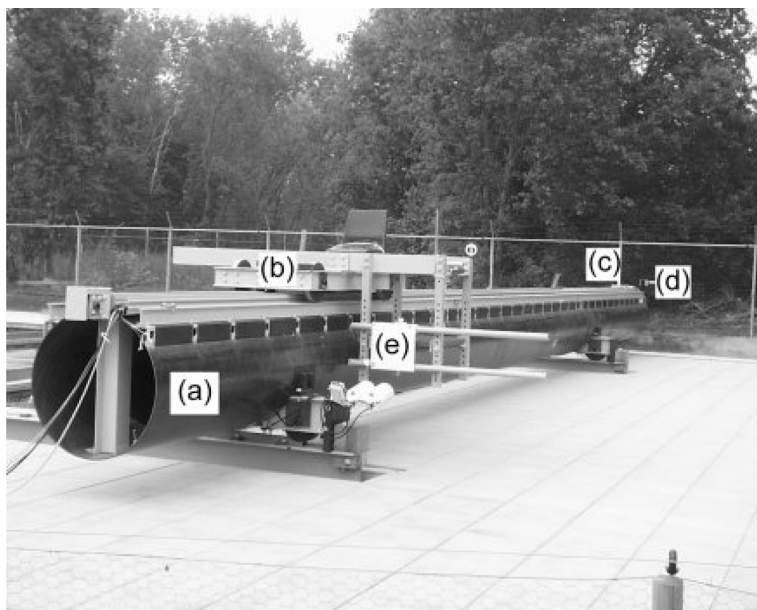


Figure 7.19 Instrumentation platform. (a) polyester tube (b) sensor platform (c) electric motor (d) laser range finder (e) metal detector.

facility entails six test lanes of 30 m² each (10-m long and 3-m wide), filled with different types of soil.

The groundwater level of each lane can be regulated separately. The temperature of the soil at various depths and the test mines are monitored continuously. The instrumentation platform is shown in Fig. 7.19. Next to cameras covering

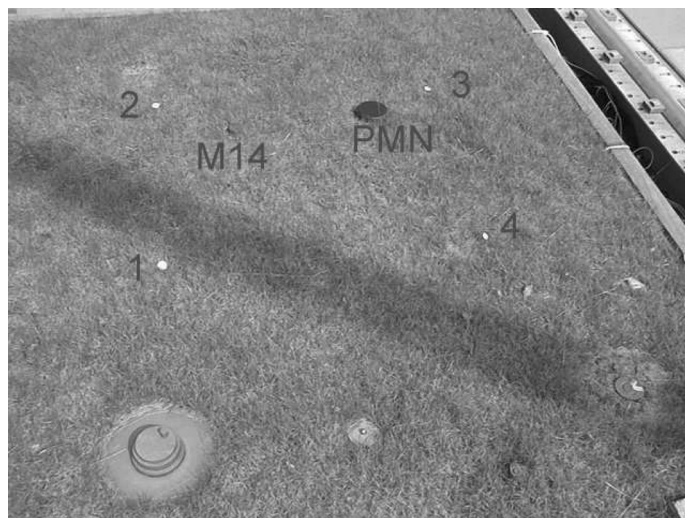


Figure 7.20 Configuration of surface and buried mines in the test bed.

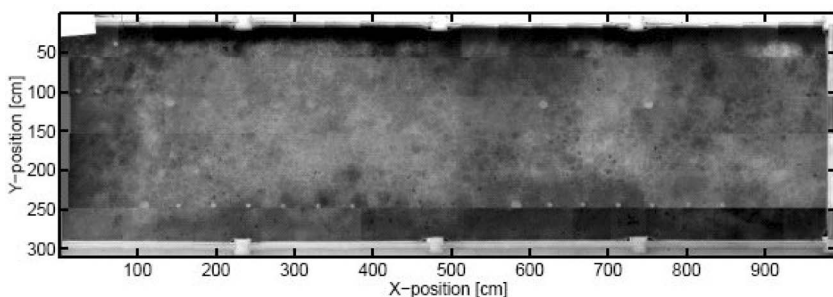


Figure 7.21 Sample top view IR image (Radiance HS 3–5 μm) of the mine test bed.

the IR bands, a ground-penetrating radar (GPR) and a metal detector were used.¹⁸ Various types of mines were placed on and buried in the different lanes.

Figure 7.20 shows an example of the layout of some surface and buried mines on a grass area in the test bed. The IR camera (Radiance HS 3–5 μm) on the instrumentation platform is run over the test bed six times to cover the total width of the test bed. During each run, images are taken in such a way that contiguous series of images are created. As an example, Fig. 7.21 shows the composed mosaic of such series, taken during a sunny afternoon in August 2002.

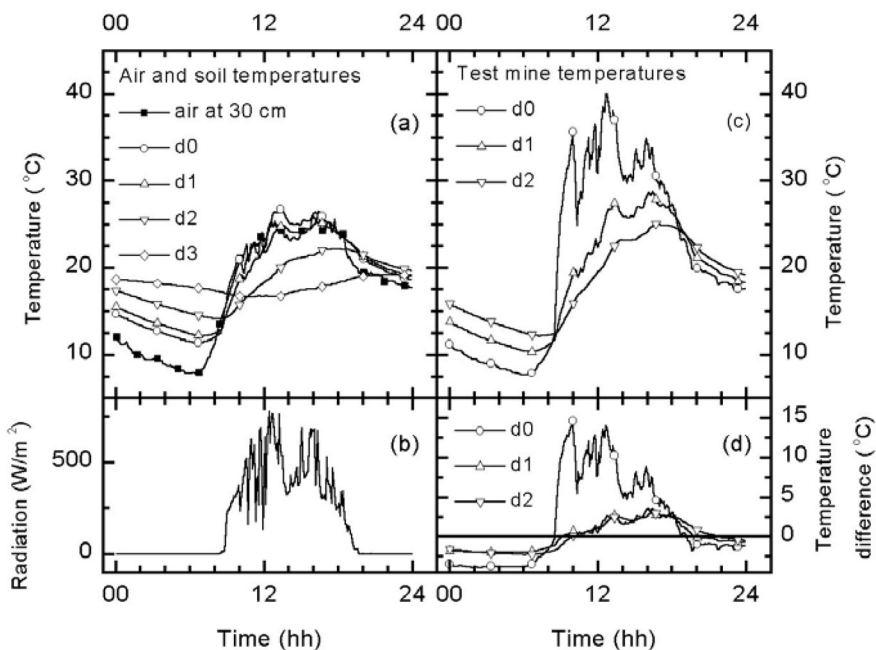


Figure 7.22 Sample of data recordings. Temperatures are given at four different depths: d_0 = surface, d_1 = 2.5 cm, d_2 = 10 cm and d_3 = 30 cm below the surface. Global irradiance is given in (b). (c) shows the temperature of an AP mine buried at various depths. (d) shows the temperature difference between the mines and the soil measured at the same depth.

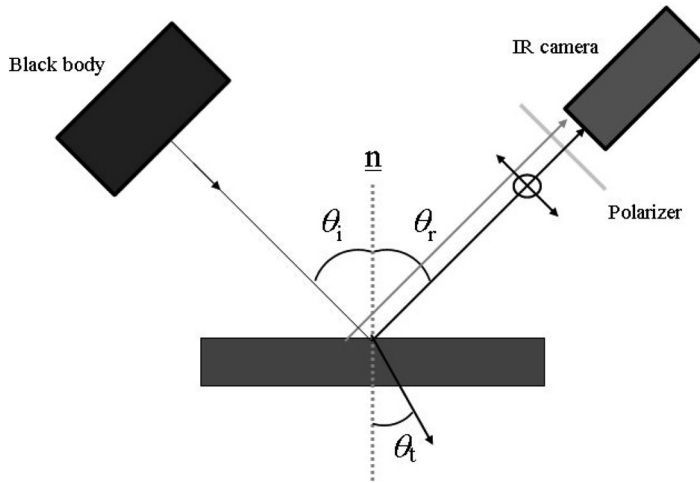


Figure 7.23 Detection of reflected polarized IR radiation.

Images like those in Fig. 7.21 were taken at regular intervals for longer periods of time to monitor the thermal behavior of the mines over time. Weather conditions and supplementary data, such as soil temperatures and water level, were recorded in parallel. Since the exact location of the mines was known, apparent temperatures of the mines could be determined from the IR images. Finally, graphs as shown in Fig. 7.22 are produced to present a compact view of the relevant parameters.



Figure 7.24 Collection of surface mines in a grassy area.

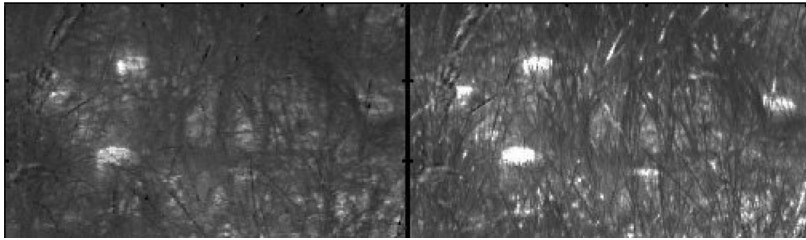


Figure 7.25 Left image taken with the Radiance HS (3–5 μm) camera with the polarizer at 0 deg; right image with polarizer at 180 deg.

To enhance the detection probability, a camera system was added to measure the degree of polarization of reflected infrared radiation by the surface mines.^{19,20} Although emitted thermal radiation itself is not polarized, reflected long wave radiation may be, depending on the reflective surface. The essential part of such a system is the polarizer (Fig. 7.23). The principle is the same as that used in sunglasses to reduce glare from highly reflective surfaces.

Figure 7.24 shows an image of a collection of surface mines in a grass area. Figure 7.25 shows two thermal images (Radiance HS, 3–5 μm) with the polarizer at 0 and 180 deg, respectively, clearly demonstrating the effect of polarization.

7.1.3 IR target modeling

As shown in Chapter 4, models are excellent tools with which to study the relative influence of parameters that determine the surface temperature of an object. This type of model strongly depends on the physical description of the heat and radiation transfer processes in the object and at the atmospheric-surface boundary. Many models of various types of military targets exist,^{1,2} but also civil installations such as buildings and power plants have been modeled. In essence, they all solve the same heat balance equation and only differ in the complexity of the mathematical representation of the target geometry (by polygons or facets). Because of today's CAD/CAM design capabilities, the geometry of the target often is available in some numerical format. Examples including T62 tanks and land mines will be discussed.

7.1.3.1 T62 tank

The thermal model PRISM³ is used to calculate thermal signatures. This model was developed by the Keweenaw Research Center at Michigan Technological University and is applied to a T62 tank. Data were taken from a field trial,⁴ where the T62 was put on a turntable for signature measurements. To avoid directional-dependent target heating by solar irradiance, the measurements were carried out at night. The targets were parked in hangars during daytime to create identical starting conditions for all targets. Consequently, the calculations do not incorporate solar load. In addition to external parameters, the model includes internal

heat flows, such as engine and compartment heating, exhaust gases, and friction-related heat losses.

Model input

Input data are taken from the field trial in Meppen in Germany.

Location : 52 deg 44'N, 7 deg 20' E
Local time : 21:30 hours (night, no solar loading)

Viewing aspect angle in elevation angle $\vartheta = 0$ deg (horizontal) and 16 azimuth angles φ at 22.5-deg increments (0 deg front, $\varphi = 90$ -deg left-hand side).

Weather conditions

Air temperature : 10.2°C
Dew-point temperature : 9.0°C
Average wind direction : 200 deg
Average wind speed : 2.5 m s⁻¹
Relative humidity : 80%
Visibility : 8700 m

Target conditions

T62 exercised to operational conditions
Idling engine during the turntable measurements
Initial target temperature is 15.2°C
All 115 facets used in the model have been given an average emission coefficient of $\varepsilon = 0.94$.

Measurement system

DuDa imager 8–12 μ m
Spectral response curve of the DuDa shown in Fig. 6.13
12-bit recording on 9-track CCT

Model output

Since the PRISM model contains a full 3D representation of a T62, an IR image of an arbitrary viewing angle can be calculated. As an example, Fig. 7.26 shows the calculated image of a T62 tank for (ϑ, φ) = (10 deg, 135 deg), using input data given in the previous section. An optical blur function has been applied to generate a more realistic picture.

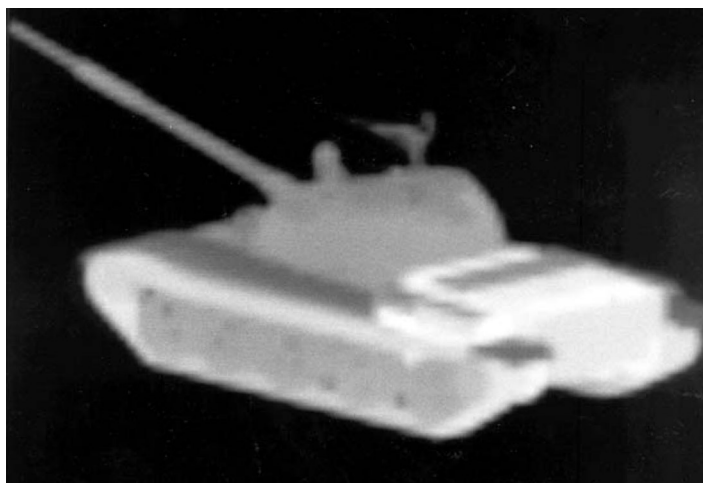


Figure 7.26 Calculated image of a T62 in 8–12 μm for $(\vartheta, \varphi) = (10 \text{ deg}, 135 \text{ deg})$.

Temperature statistics

Figures 7.27 through 7.29 show examples of the calculated apparent temperature histograms for $\varphi = 0 \text{ deg}, 180 \text{ deg},$ and 270 deg ($\vartheta = 0 \text{ deg}$ in both cases) in comparison with the histograms derived from the recorded images in the field. For all aspect angles, the maximum temperature has a shift of 3–4°C between measurements and calculations. The limited number of target facets used in the calculations to speed up processing time might cause this. But nonetheless, this type of histogram gives a good impression of the temperature dynamics of the vehicle and in general supports efforts to reduce target signatures.

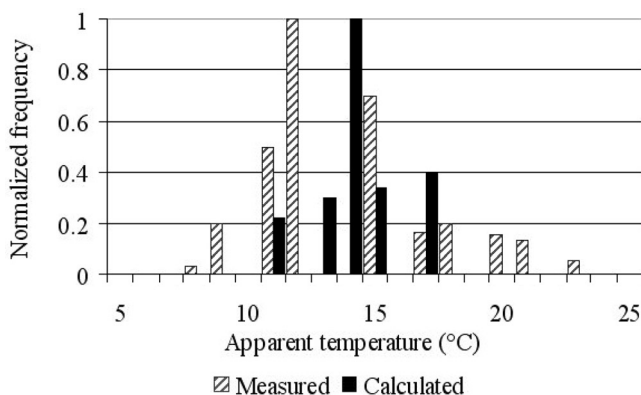


Figure 7.27 Calculated and measured histogram for $\varphi = 0^\circ$ and $\vartheta = 0^\circ$.

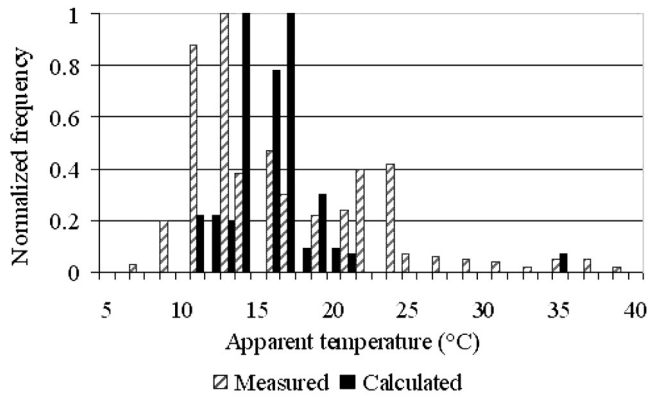


Figure 7.28 Calculated and measured histogram for $\varphi = 180^\circ$ and $\vartheta = 0^\circ$.

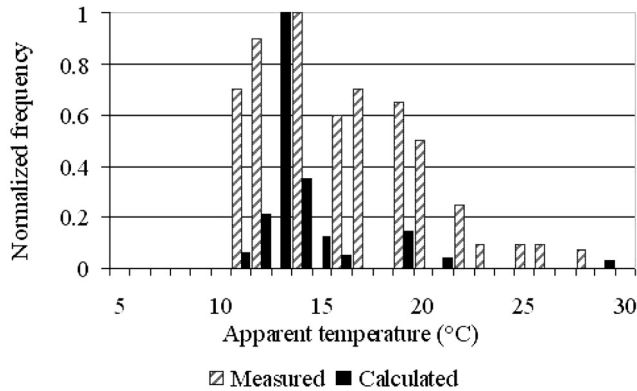


Figure 7.29 Calculated and measured histogram for $\varphi = 270$ deg and $\vartheta = 0$ deg.

Polar diagram

Figure 7.30 shows a polar diagram comparing calculated and measured apparent temperatures of the T62 tank, using images taken on the turntable at zero degrees elevation.

In spite of the fact that the temperature distribution over the tank is rather different for measurements and calculations, the average temperature (averaged over the total target area, viewed from a given aspect angle) shows a surprisingly strong agreement.

7.1.3.2 Land mines

Numerical models were used to support the interpretation of the measured data of the land mine detection program (cf. Section 7.1.2.3). In Chapter 4, the impli-

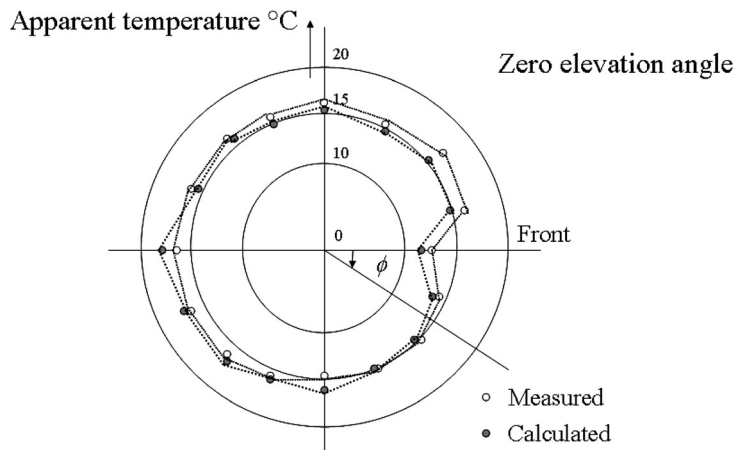


Figure 7.30 Calculated and measured polar temperature diagram of a T62 tank for $\vartheta = 0$ deg.

cations of thermal modeling were discussed using a simple and more complicated model. The model used to calculate the thermal behavior of a cylindrical mine of finite thickness is somewhere in between. The parameters required to perform the calculations, however, are the same.

A 2.5D model of an antipersonnel (AP) mine buried in a sandy soil was developed using the FEMLAB¹⁷ software package. The model involves a mine of type PMN (diameter, 117 mm \varnothing , height, 48 mm, and weight, 669 g), which is buried 1 cm below the surface. The mine is a replica made of materials with physical properties close to the real values.¹⁵ Figure 7.31 shows the various components of this type of AP mine.

Figure 7.32 shows the geometrical layout (cross section with the ordinate as vertical circle symmetry axis) used for the model calculations. It also shows the mesh generated by FEMLAB, which is used for the calculations. The soil is subdivided into two layers, a 4-cm top layer of dry sand and a 46-cm sublayer of moist sand.

The following conditions have been used:

- Three mines and mine positions (C35, C38 and C49). The temperature of the sand surface above the mine was determined from the IR images. The mines were buried 1 cm below surface. The mine temperature is compared with the temperature of a patch of undisturbed sand 20 cm away.
- A continuous period of almost 36 hours of data recordings of 8–9 μm images (24–26 July 2001), taken from the sand lane. Figure 7.33 shows a snapshot of the mine test bed, indicating the location of the mines under investigation.
- Material and electro-optical (EO) properties of the mines were taken from the literature.¹⁵
- The material properties of the sand were determined by a parameter-optimization process, using the measured temperatures of the undisturbed

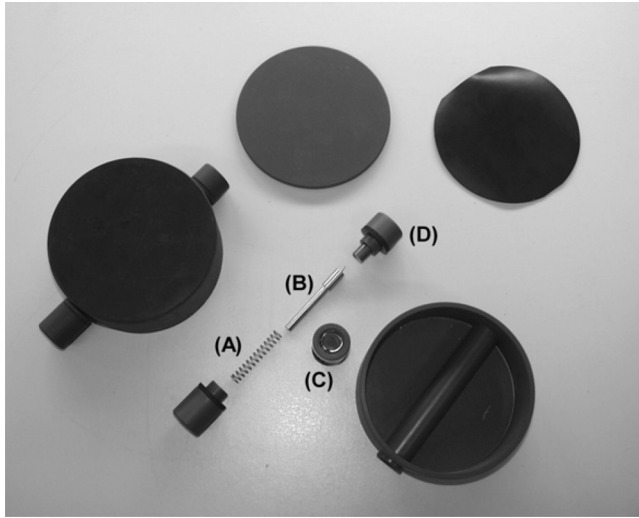


Figure 7.31 AP mine (type PMN) used for thermal modeling purposes.

sand at different depths together with the measured meteorological parameters. In this optimization process, the sand was modeled in two layers with independent parameters.

Figure 7.35 shows the results in graphical form of the calculations at 17:00 hours (local time) on 24 July for the mine and the surrounding sand. The graph clearly

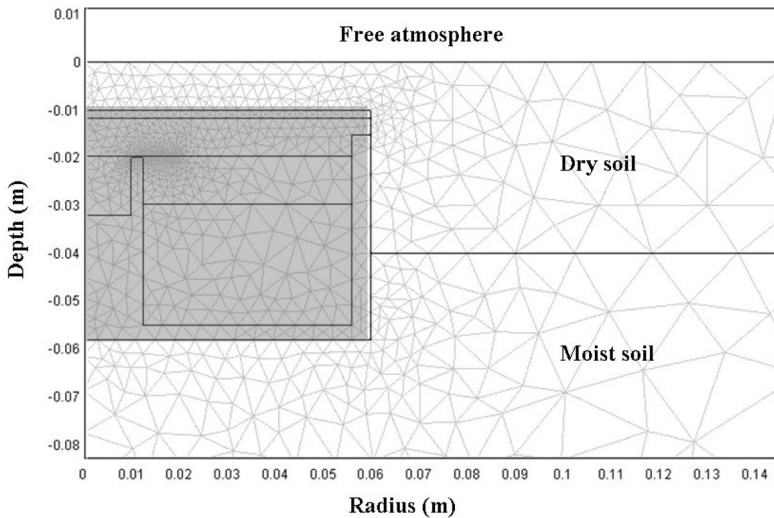


Figure 7.32 Geometrical model layout with computational mesh.

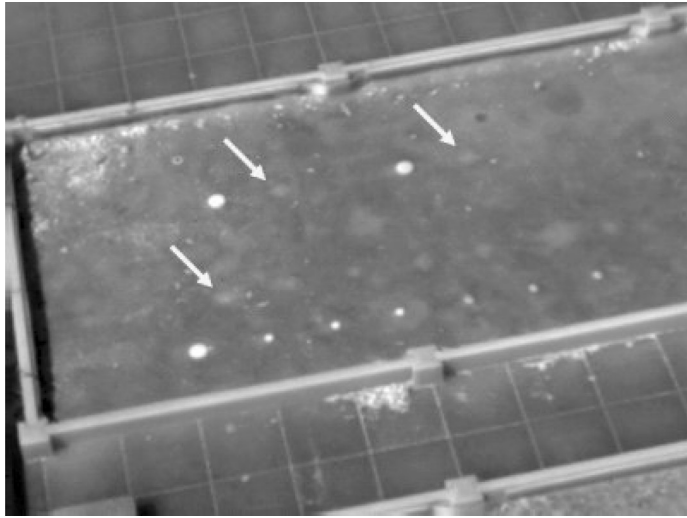


Figure 7.33 IR image (QWIP 8–9 μm) of the mine test bed. The arrows refer to the location of the mines under investigation.

shows a difference in surface temperature (the top sand layer) between the location of the mine and the undisturbed sand at 16 cm distance.

Figure 7.35 shows the measured and calculated real temperature contrast between the sand above the mines and the surrounding sand. Real temperatures of the sand have been estimated from the IR images, knowing the camera's spectral range and the best-guess emissivity of the sand. The figure shows that

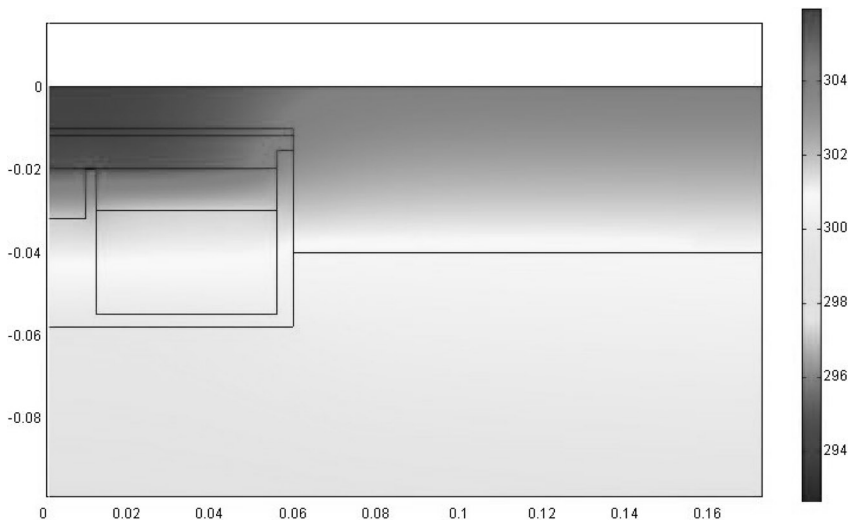


Figure 7.34 Graphical presentation of model temperature calculations.

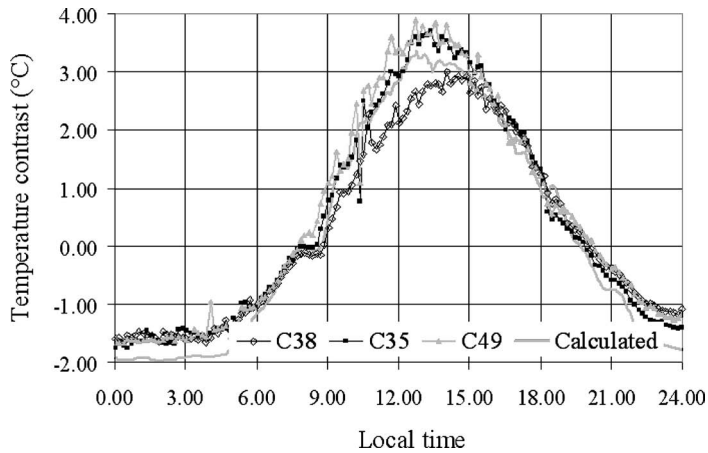


Figure 7.35 Measured temperature contrast of three buried AP mines with the surrounding sand in comparison with calculated values.

the measured temperature variations among the three mine locations are relatively small. The highest probability for detecting a mine occurs when the temperature contrast is the highest (in the absolute sense) and the lowest when the contrast is minimal (at the crossover). Judging the output of the model in that sense shows:

- The predicted time of contrast inversion (crossover) is correct within half an hour.
- The predicted positive contrast follows the measurements quite well and the predicted maximum coincides with the measured temperatures.
- The predicted negative contrast is too low, but the trend follows the measured curves well.

7.2 IR Background Characterization

The detection of a target in relation to its background is determined by both the radiance (temperature) contrast and the background clutter. The lack of background information often is treated as of little importance by assuming that the apparent temperature of vegetation is about ambient air temperature. This attitude may be one of the reasons that little effort has been put into this area and that, consequently, so little is known about the thermal behavior of backgrounds. Often, background signatures are collected as a byproduct of other signature measurements.

Figure 7.36 shows the measured apparent temperatures of coniferous and deciduous trees at various geographical orientations in relation to the air temperature for an August day. The measurements clearly show that, especially at midday, the differences are remarkable; and although at night they become smaller, the

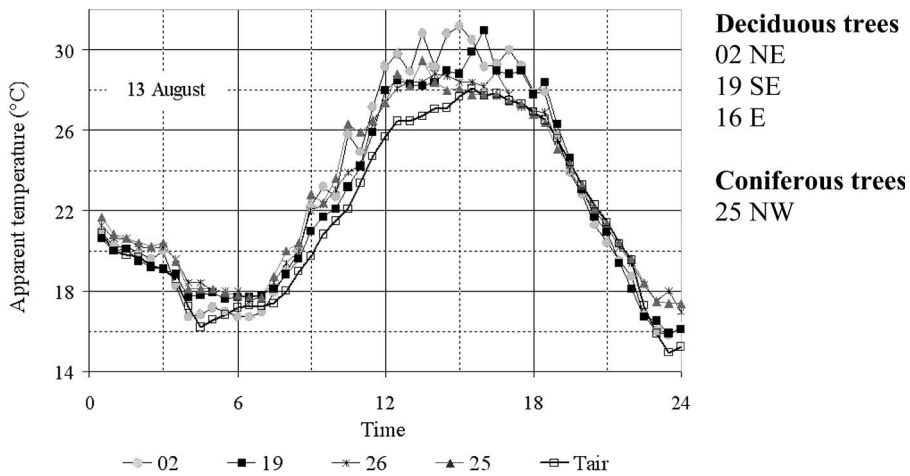


Figure 7.36 Comparison between the air temperature and the apparent temperature of variously oriented tree lines during a summer day.

differences still are large in terms of detection criteria. Also, because of differences in the heat capacity of different background elements, each element shows a specific time lag with the air temperature.

Even in winter, when most of nature is dormant, temperature differences among various backgrounds may differ considerably. Figure 7.38 shows a winter day at midnight when the sky is becoming very clear and temperatures plummet. It is interesting to see that the various background elements all react differently to this radiation cooling effect. Then, when clouds appear later during the day, temperatures increase again and temperature differences between the various background elements decrease.

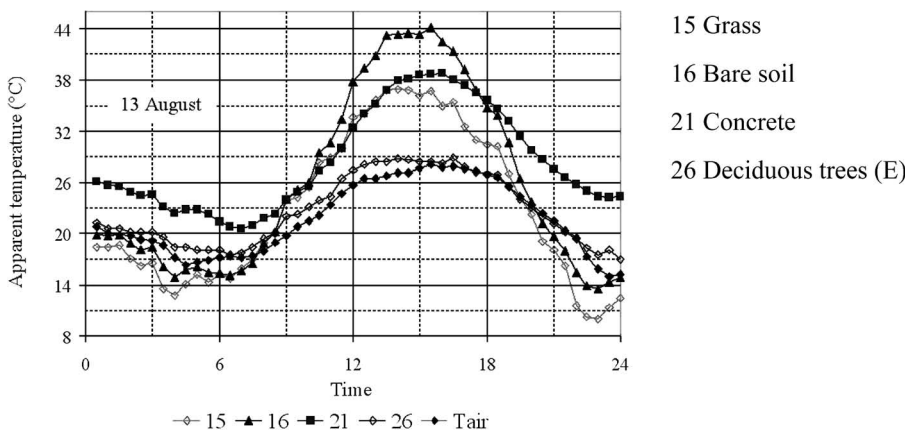


Figure 7.37 Comparison between the air temperature and the apparent temperature of a variety of background elements during a summer day.

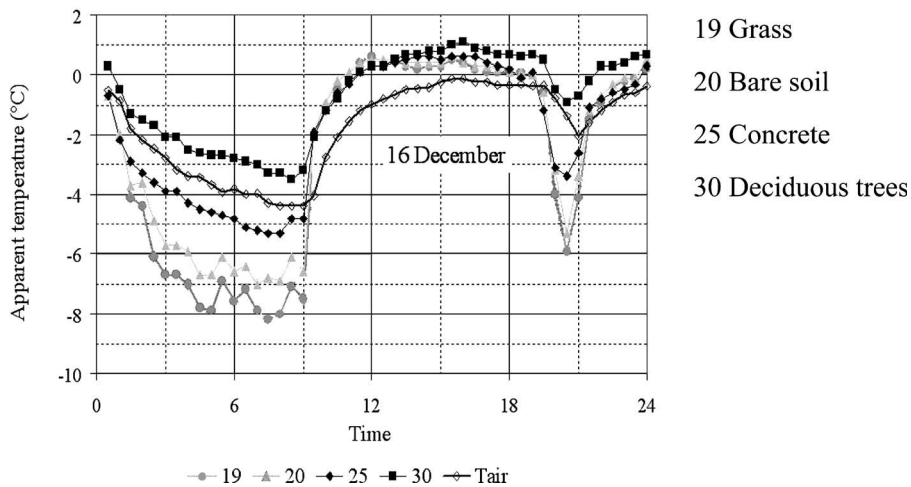


Figure 7.38 Comparison between the air temperature and the apparent temperature of a variety of background elements during a winter day.

The data presented in Figs. 7.36 through 7.38 are not exceptional. They show that in most cases, the air temperature is not representative for the background temperature. Therefore, more information on the thermal behavior of backgrounds is needed, which commonly is obtained through direct measurements and/or modeling efforts.

As a first step, theoretical models can be used to study the thermal behavior of backgrounds, but, as explained in Section 4.3, the mathematical description of the surface roughness elements (ploughed earth, grass, corn field) is cumbersome. Even if this is done in a realistic way, it is hard to define physical parameters like the solar absorption coefficient and the emission coefficient. These parameters are crucial, because it is unrealistic to work with physical temperatures of vegetated surfaces and apparent temperatures must be used instead.

The most difficult job after having defined a model is to validate it with measurements. For this, first the physical properties have to be measured *in situ* at regular intervals, because they can change all the time. Second, systematic measurements of the apparent temperature have to be performed, with a relatively small time scale (≤ 15 min) and over a long measurement period (≥ 1 year). This is required to obtain statistically relevant results.

A second approach to studying the thermal behavior of backgrounds is to take measurements as the starting point. Data can be used to develop empirical models, which can be based on statistical or correlation techniques or on a curve fit of the data to theoretical equations, like the heat balance equation. As was the case for the target signatures, a sensible mix of theory and experiment will lead to an optimal result that is feasible for practical application. The remainder of this chapter will deal with the physical characterization of background elements and discuss radiometric measurements of such elements. Finally, examples of data analyses will be given.

Most parameters of individual constituents of a background element, such as branches, single leaves, stalks, etc., can be determined with existing techniques or laboratory instruments. Small samples of these elements, such as the reflection coefficient,⁵ which can be determined in nearly any part of the electromagnetic spectrum (in this context, shortwave and long wave) are readily measured in the laboratory. Also, parameters such as heat conductivity, heat capacity, etc., can be measured if the physical constitution is not changed during the measurement (e.g., evaporation of bound water).

In the field, however, the physical properties of a background element are not those of the individual components, but are determined by the distribution of these components in space. The optical properties especially are sensitive to the nature of this distribution. This implies that the optical properties have to be measured in the field without disturbing this distribution too much. It also implies that values of similar background elements cannot be used, because while the name may be the same, the geometrical structure might be completely different.

7.2.1 Field measurement of the shortwave reflection coefficient

The reflectance ρ is defined as the ratio of the reflected radiant flux to the total incident solar flux (direct and diffuse). Most natural surfaces reflect solar radiation as a combination of direct and diffuse radiation. The reflected flux can only be determined from the integration of the measured bidirectional reflection coefficient $\rho(\vartheta, \varphi)$ over the sky-hemisphere. A practical problem is that the solar incident angle is changing continuously, so measurements must be done in a very short time. To obtain a representative measure, the sampling area can become quite large for rough, non-uniform layers (a square meter or more), which can result in large optics and heavy, bulky equipment.⁶

To simplify the measurement, an artificial light source can be used as with the following prototype instrument. Detector and light source are mounted on two independently moving bars. The detector and light source can be positioned along the bars (Fig. 7.39). The detector position is denoted by (ϑ_d, φ_d) and the source position by (ϑ_s, φ_s) , while $\rho(\vartheta_s, \varphi_s, \vartheta_d, \varphi_d)$ denotes the reflection coefficient for this setting. This construction offers the possibility of positioning the detector and the light source at any point on an imaginary hemisphere. The sample size is 10×10 cm, which keeps the system reasonably compact and portable. However, because of this size, only fairly uniform rough layers can be allowed. The light source is a commercially available quartz-tungsten-halogen lamp (Oriol, QTH 6332), which is projected as a parallel beam (width 9 cm) onto the sample. To suppress background radiation, the source is mechanically chopped (200 Hz). The reflected, modulated beam of light is measured by a photodiode detector (Siemens, TP60). The detector output is amplified with an AC-coupled amplifier synchronized with the beam-modulation frequency.

Figure 7.40 shows the spectral source emittance $E(\lambda)$ and the system spectral response $R(\lambda)$. The system is calibrated with two reference reflectors. One surface is a 100% directional reflecting mirror (no diffuse reflection); the other a 100%

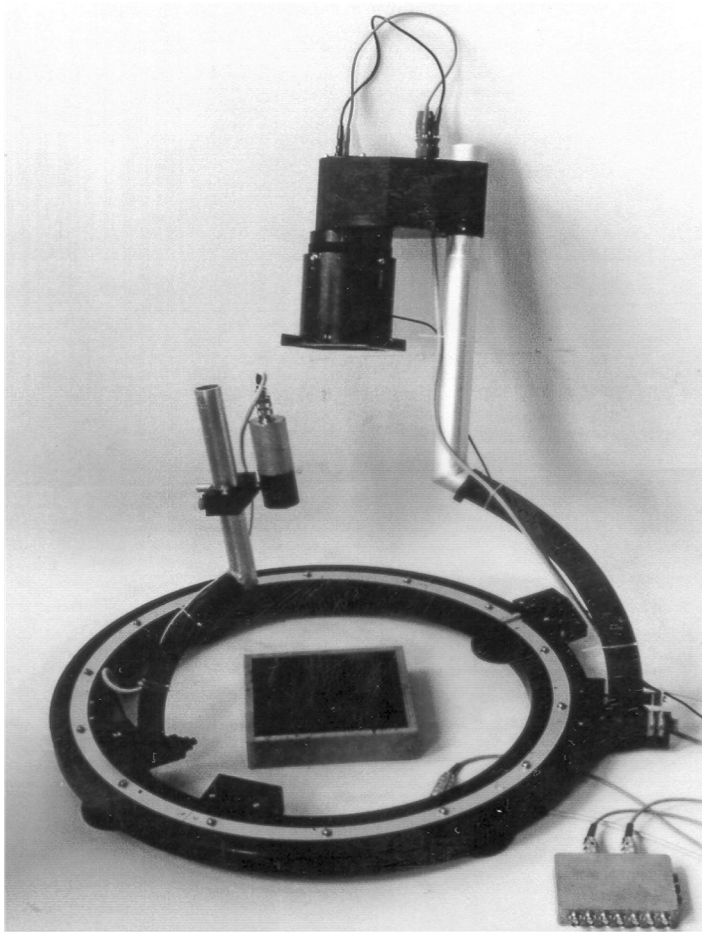


Figure 7.39 Measurement of the bidirectional shortwave reflection coefficient.

diffuse reflecting surface, also used as a white standard (magnesium oxide, MgO , or barium sulfate, BaSO_4). Figure 7.41 shows, as an example, the bidirectional reflection coefficient, expressed in equireflection lines, for a sample of grass, where the lamp is always located at a fixed position ($\vartheta_s = 90$ deg, $\varphi_s = 0$ deg) straight above the grass, e.g., $\rho(\vartheta_d, \varphi_d, 90$ deg, 0 deg).

The detector was varied in azimuth with increments of 30 over 360 deg and the elevation was alternated between 30 and 60 deg. Values in between are found by weighted nonlinear interpolation.

The directional-hemispherical reflection coefficient $\rho(90$ deg, 0 deg) for this situation is found by integrating the bidirectional reflection coefficient $\rho(\vartheta_d, \varphi_d, 90$ deg, 0 deg) over the half hemisphere as

$$\rho(90^\circ, 0^\circ) = \frac{1}{2\pi} \int_0^{2\pi} d\varphi_d \int_0^{\pi/2} \rho(\vartheta_d, \varphi_d, 90^\circ, 0^\circ) \cos(\vartheta_d) d\vartheta_d.$$

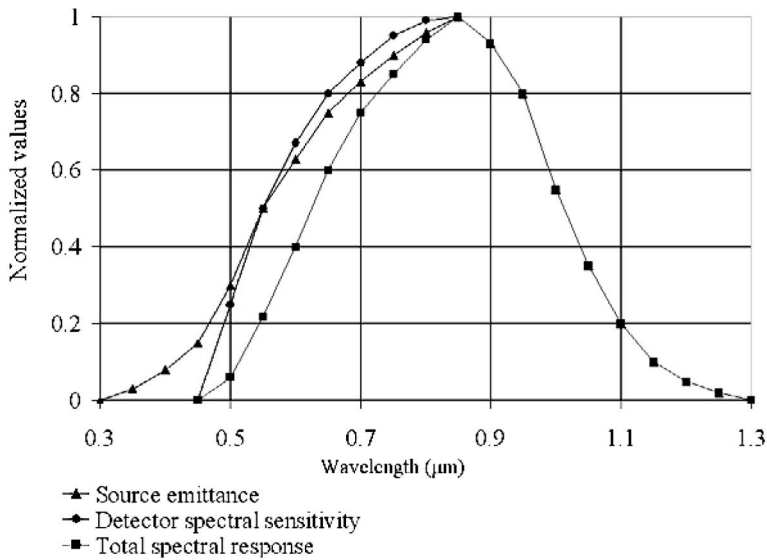


Figure 7.40 Normalized spectral source emittance $E(\lambda)$ and spectral system response $R(\lambda)$.

A computer reads the detector voltage and, using previously stored calibration results, directly converts to a reflection coefficient. The source and detector are still positioned by hand, but in the final design this will be done automatically. It then will be possible to have the computer position the lamp and the detector and, as a result, the computer can perform the complete measurement automatically and autonomously. Also in the final design, the spectral range must be extended from 1.3 μm to 3.0 μm to comply with the international standard for solar radiation.

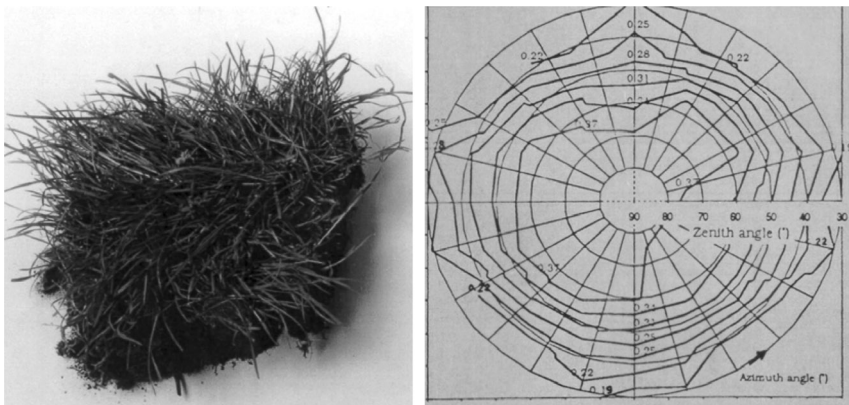


Figure 7.41 Bidirectional reflection coefficient $\rho(\vartheta_{dr}, \varphi_{dr}, 90 \text{ deg}, 0 \text{ deg})$ for a grass sample.

7.2.2 Measurement of background apparent temperatures

Measurements have the advantage over model calculations in that the desired quantity, i.e., the apparent emittance E_{ap} (or T_{ap}), of a background element is measured directly in relation to the prevailing weather conditions. Under outdoor conditions, measured radiation properties of manmade and natural elements can respond quite quickly to changes in weather conditions (for instance, reflected radiation can change dramatically in a matter of minutes because of a change of sky conditions). To gain an understanding of the thermal behavior of the various background elements, radiation measurements of these elements should be carried out with a small time step and systematically over long periods, preferably covering all seasons. Such measurements have been reported,^{9,16} but no profound analyses have been made yet and the measurement location was quite specific, in that it was a rather small open area in a forest. This circumstance may have created very specific local weather and environmental conditions.

Next to measuring the apparent temperature and weather conditions, a number of parameters, such as geographical orientation, height, emission coefficient, and solar reflection coefficient (as in Section 4.3), describing the physical characteristics and condition of the background element, have to be measured.

In order to collect apparent temperatures of various background elements over longer periods of time (implying a large variety of weather conditions), measurements should be automated and equipment should withstand long-term outdoor operation. TNO developed such a radiometer along the following design and operational requirements.

- (1) Because IR imagers usually make use of 3–5 μm and/or 8–12 μm spectral regions, background analyses have to be done in both spectral windows.
- (2) Optical alignment of both channels must give an exact overlay of both measured background areas. Only reflective optics was used because this is relatively inexpensive and simple. The instantaneous field of view was chosen 1×1 deg to cover a reasonable background area at short ranges (spot diameter of $\cong 85$ cm at 10 m distance).
- (3) Experience shows that as soon as an instrument is placed in an outdoor environment, extra precautions must be taken to guarantee undisturbed, reliable operation. Apart from using adequate materials and a watertight (and condensation-free) design, special arrangements have to be taken to compensate for electronic drift. This is best done by an internal calibration procedure.
- (4) To achieve sufficient temperature sensitivity, both measurement channels (3–5 μm and 8–12 μm) must have a noise equivalent temperature difference (NETD) of better than 0.03 K and an overall absolute measurement accuracy better than 0.2 K.
- (5) Because measurements of a number of different background elements are taken repeatedly, repositioning accuracy of the radiometer must be better than 0.1 deg in azimuth and elevation.

- (6) Since the system will be used in isolated areas, it must be able to run unattended for a number of weeks with no manpower requirements. Data handling and system control are completely autonomous and include error-trap routines to recover from errors, such as a power failure. As an option, the system is remotely accessible by wireless communication to enable data download and error-report transmission.

This system, which is called CARABAS (CALibrated RADiometer for BACK-ground Studies), will be discussed next.

7.2.2.1 CARABAS measurement system configuration

For reasons of flexibility and handling, the control/data registration unit is physically separated from the sensor unit of the CARABAS system.¹⁰ The sensor-head assembly (with pre-amplifiers) and the (x,y,z) -motion unit are placed on a tripod. A computer is used to program the coordinates of the measurement locations into the system, control the measurement sequence, execute the calibration procedure, and store the calculated apparent temperatures on hard disk. Figure 7.42 shows the sensor head including the (x, y, z) -motion unit, which was also developed in-house. For aiming and documentation purposes, a small CCD-TV camera (Fig. 7.43) can be mounted on top of the sensor head. The camera is bore sighted with the IR channels so it can also be used to select and program the desired measurement areas.

Sensor unit

Figure 7.44 shows a photograph of the sensor-head interior. Figure 7.45 shows the schematic drawings of the top view, explaining the different components as displayed in the photograph. The size of the sensor unit is $40 \times 25 \times 20$ cm ($l \times w \times h$).



Figure 7.42 CARABAS sensor head.



Figure 7.43 CARABAS sensor head with CCD-TV camera.

Scanning mechanism

The heart of the sensor head is a rotating flat mirror at a 45-deg angle to the optical axis (Figs. 7.45 and 7.46). This double-sided mirror is rotated and holds a fixed position for one second at every 90-deg rotation, thus taking four discrete positions per revolution. In this way, two optical channels are created having exactly the same optical axis and scanning four positions per revolution.

A continuously running dc motor in combination with a Maltese cross cog-wheel creates the movement of the mirror. With this method, the motor life is

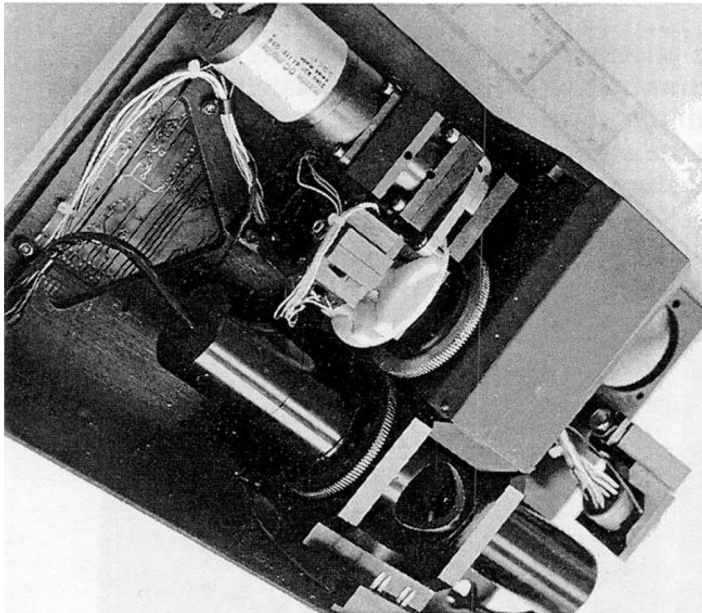


Figure 7.44 Photograph of the sensor head.

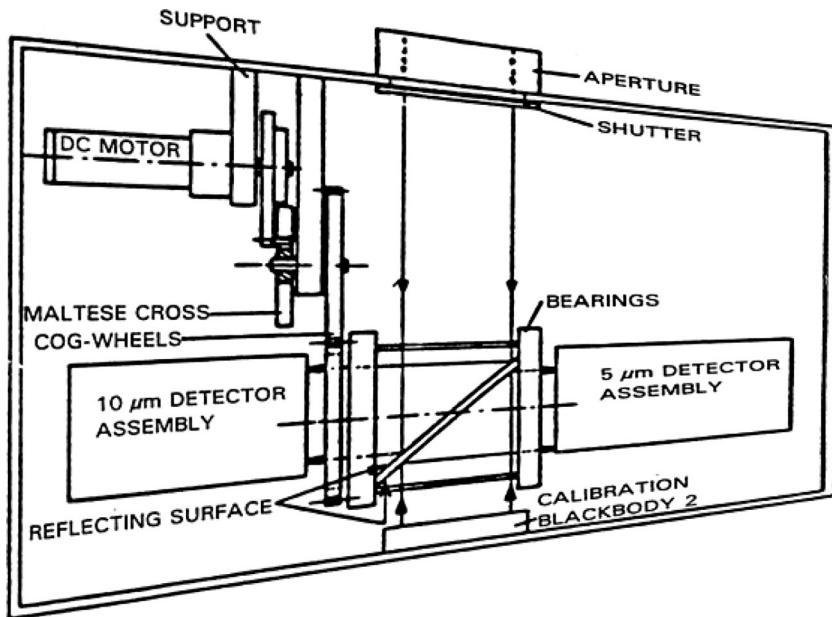


Figure 7.45 Schematic drawing of the top view of the sensor head.

increased considerably because it avoids the need for an almost continuous on/off switching to create the discontinuous mirror movement. But much more important is the fact that the mirror takes exactly the same four positions at every revolution. These four positions are chosen as the perpendicular projection of the optical path on the four walls of the sensor housing. One position is used to perform the actual

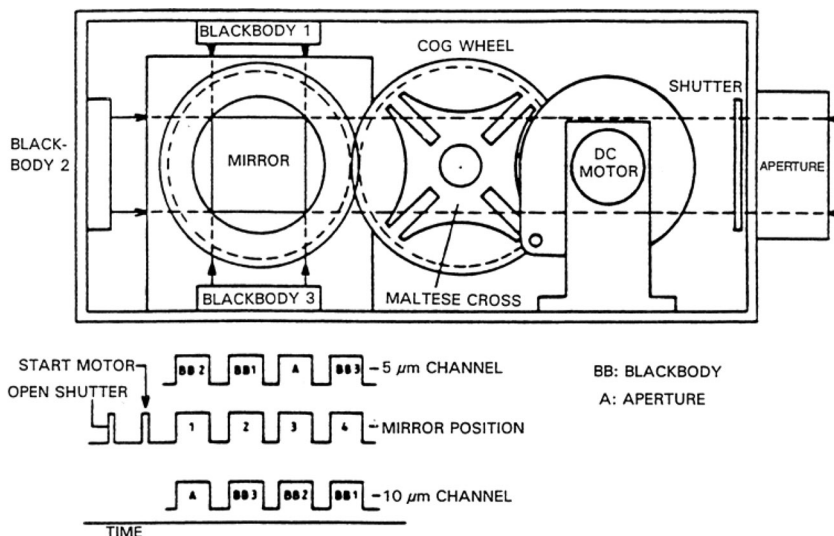


Figure 7.46 The mirror's driving mechanism and timing sequence.

measurement; the other three are used for calibration purposes. Figure 7.46 also shows the driving mechanism for the mirror and includes the timing sequence for both measurement channels during a complete revolution of the scan mirror. In both channels, a thermopile detector (Laser Optronic type 5M) is used as the sensitive element. Radiation entering through the aperture is reflected from the scan mirror and focused on the detector by Cassegrain optics. The combination of this detector type and the chosen optics results in a field of view of 1×1 deg.

Calibration procedure

To calibrate the system, three blackbody reference sources are placed against the inside wall of the housing at the three remaining measurement positions. The temperature $T_{cal}(i)$ ($i = 1, 2, 3$) of the blackbodies is set and maintained at respectively T_h , $T_h + 3^\circ\text{C}$, and $T_h + 9^\circ\text{C}$, where T_h is the temperature of the rear part of the sensor housing, which normally will be close to ambient air temperature. Just below the surface, a platinum resistor (P_t100) controls the blackbody temperature and measures the actual blackbody surface temperature. Together with the detector readings of the blackbodies $V_{cal}(i)$, the calibration parameters a and b are determined from a least square curve fit from

$$E_{cal}(i) = \int_{\lambda_o} R(\lambda) E_{bb}[\lambda, T_{cal}(i)] d\lambda = aV_{cal}(i) + b \quad (\text{W m}^{-2}), \quad (7.4)$$

where

- $E_{cal}(i)$: irradiance from the blackbody (W m^{-2}),
- $E_{bb}[\lambda, T_{cal}(i)]$: blackbody spectral emittance ($\text{W m}^{-2} \mu\text{m}^{-1}$),
- $T_{cal}(i)$: blackbody temperature (K),
- $V_{cal}(i)$: detector voltage (V),
- $R(\lambda)$: system relative spectral response (Fig. 7.47),
- (a, b) : regression coefficients.

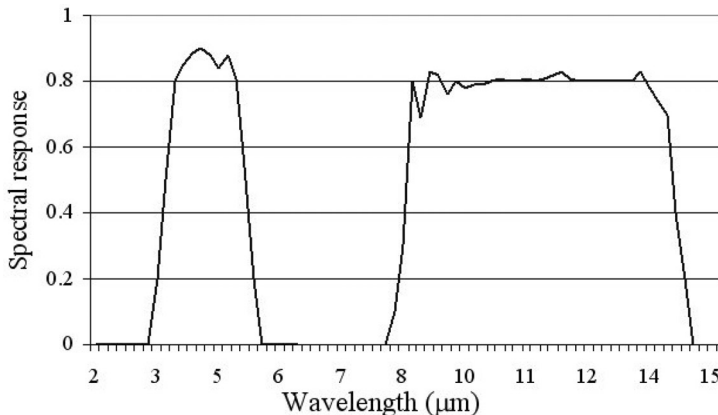


Figure 7.47 Spectral response curve for both CARABAS windows.

The linear relation between the incoming energy and the detector reading is assumed to hold for the limited operating-temperature range. The calibration curve of the detector voltage against detector irradiance confirms this assumption.

The apparent temperature $T_{ap}(X)$ of the unknown surface X , reading a voltage $V(X)$, is found by solving $T_{ap}(X)$ from the implicit equation,

$$aV(X) + b = \int_{\lambda_0} R(\lambda) E[\lambda, T_{ap}(X)] d\lambda \implies T_{ap}(X). \quad (7.5)$$

This way, detector voltages are directly converted to temperatures after each measurement cycle and stored on hard disk. Since only reflective optics is used and no optical components such as a front lens or a protective window are added in the optical path when performing the actual measurement, the calibration in theory is perfect.

As a consequence of the limited calibration temperature range of 9°C , however, the measurement accuracy decreases with increasing temperature offset to this range. The maximum accuracy is maintained if the temperature of the background element is within the temperature range of $(T_h - 10) < T_{ap}(X) < (T_h + 25)^\circ\text{C}$. This is the case for most natural background elements under most environmental conditions. In the standby position, the aperture is covered by a shutter to avoid dust and insects entering the sensor head. In this situation, the internal blackbodies remain switched on to enable a direct start and keep the inside air temperature above the dew-point temperature, to avoid condensation.

System performance

Table 7.2 summarizes the most important system parameters.

Table 7.2 System performance parameters.

System parameter	Window I* (3 5 μm)	Window II (8 12 μm)
NETD measured at 20°C	< 0.04	< 0.002
IFOV (deg)	1×1	1×1
Temperature accuracy ($^\circ\text{C}$)	< 0.2	< 0.1
Positioning accuracy (deg)	< 0.1	< 0.1
Positioning precision (deg)	< 0.1	< 0.1
Total measurement time per position	4 s	
Operational temperature range ($^\circ\text{C}$)	$(T_h - 10) < T_{ax} < (T_h + 25)$	

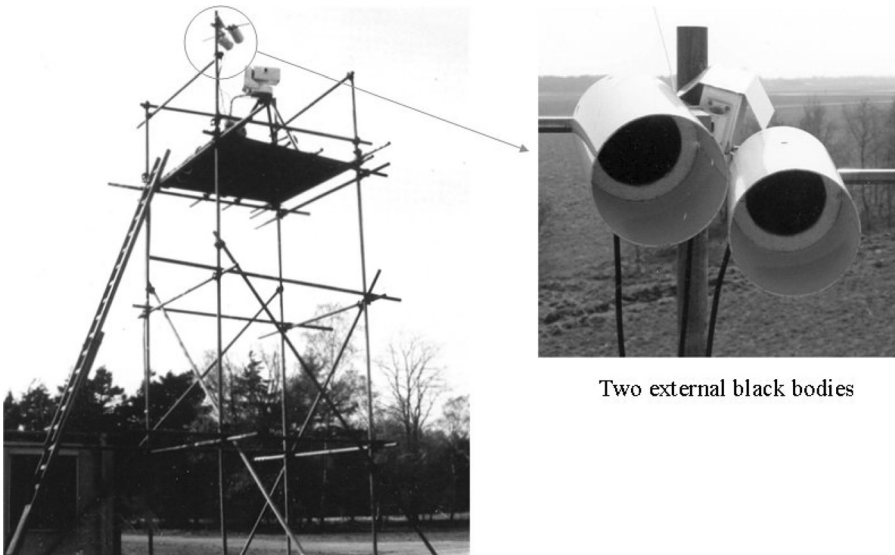
*Spectral curves given in Figure 7.47.

Outdoor testing and field installation

Together with a synoptic weather station, supplemented with a pyrgeometer and a rain gauge, the system was installed on the air force base in Gilze Rijen, located in the south of the Netherlands. To cover a wide range of different background elements, the CARABAS was placed on an elevated platform about 7 m in height. Figure 7.48 shows the CARABAS system in position and Fig. 7.49 gives an aerial overview of the experimental site, showing the various types of background.

In operation, the system autonomously and automatically scans all preselected measurement positions every preset time interval by retrieving the coordinates from memory. After completing the scan, the detector readings are converted to apparent temperatures and stored on hard disk. Two external blackbody reference sources, positioned at 1 m from the aperture, are incorporated in the measurement cycle to check system performance continuously (Fig. 7.48).

Next to the recordings of the apparent temperatures and the accompanying weather conditions, the physical characteristics of each element have to be recorded as well. A descriptor like “grass” or “concrete” is rather meaningless, because such a subjective expression does not say anything about the physical properties. To demonstrate this, apparent temperatures ($8\text{--}12\ \mu\text{m}$) of two different patches of grass are shown in Fig. 7.50. The grass in position 1 contained a fair amount of dried-out grass, while the grass in position 15 looked green and healthy. The grass in both patches was quite long. The figure shows the apparent temperature for both areas on 28 June and, although both are called simply “grass,” noticeable differences can be observed. The grass was cut on 29 June and Fig. 7.50 also shows the apparent temperatures on 30 June. This time, both curves are quite similar. During night conditions, differences are less pronounced.



Two external black bodies

Figure 7.48 Positioning of the CARABAS system at Gilze Rijen Air Force Base.



Figure 7.49 Aerial photograph of the experimental site.

However, for practical reasons, these subject descriptors will be used throughout the remainder of this tutorial. In Section 4.3, several parameters were derived that have a major influence on the apparent temperature, and therefore preferably should be measured. Here, a problem arises in that a sensible compromise has to be found between the number of required parameters, the effort (and possibility) required to measure them, and practical considerations like the availability of suitable measuring equipment and the complexity of database handling (time and memory). Other parameters, for instance the emission coefficient of a tree, simply cannot be measured. A set of descriptors that provides a good or at least adequate physical description of a background element must be defined.

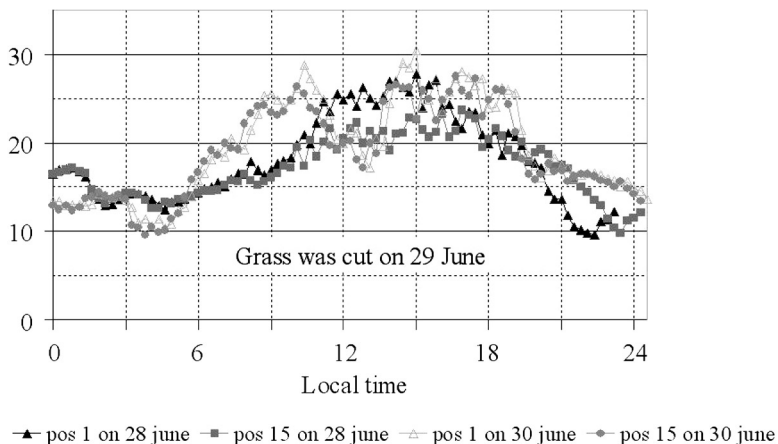


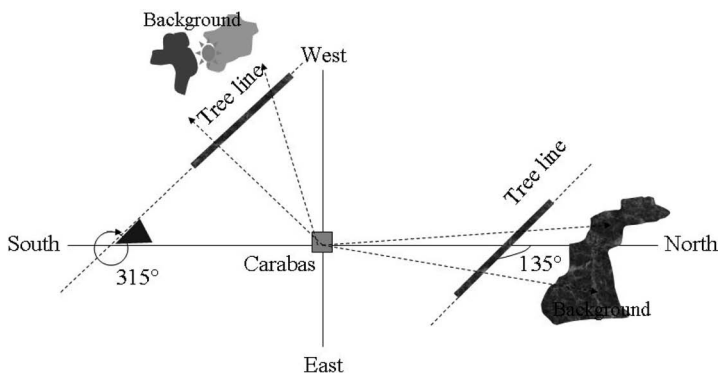
Figure 7.50 Apparent temperature of two grass areas, before and after cutting.

Table 7.3 Example of an element information table for 13 August 1990.

Parameter	Position 1	Position 2
x Coordinate	2.0	1.5
y Coordinate	0.3	1.0
Element description	Grass	Deciduous trees
Condition	Partly dead	Fresh green leaves
Elevation angle	0 deg	90 deg
Azimuth angle	90 deg	300 deg
Height	0.08 m	5 m
Emission coefficient	0.86	0.90
Range to CARABAS	20 m	30 m
Background of the element		
Description	n.a.	Coniferous trees
Condition	n.a.	Healthy

During the CARABAS experiments, the IR reflectometer as described in Section 7.1.1 was used where possible. It is unfortunate that, because a practical field measuring system was missing, the solar absorptivity could not be measured. Table 7.3 shows an example of an element information table for 13 August 1990.

In view of the directional effects introduced by the element bearings and some of the weather parameters, it is important to register from what direction the temperature is measured. Table 7.4 shows how the different angles, which relate the CARABAS measuring direction, principal directions and element bearings, are defined. For reasons of simplicity, but even more because of the lack of measuring equipment, a relatively small, simple set of parameters was defined. The last two descriptors in Table 7.3, describing what is located behind the element, are included because the apparent temperature can be influenced by the transparency of the element (deciduous trees in winter, for example). In that case, the apparent

Table 7.4 Angle conventions to define element orientation.

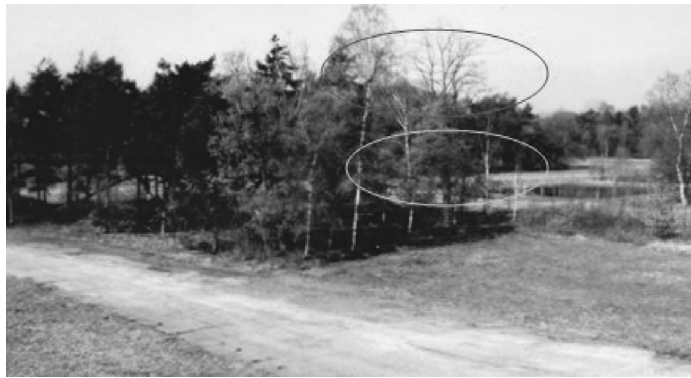


Figure 7.51 Example of different backgrounds for a tree line.

temperature with a blue sky background differs considerably from the case in which the background is another tree line, as is shown in Fig. 7.51.

7.2.2.2 Practical examples

After successful testing under various weather conditions for several months, the CARABAS was set to collect background data systematically in April 1990. Data of 25 background elements has been collected for more than a year, taken every 15 minutes, 24 hours per day. Field operation was checked every measurement cycle with the two external blackbodies, indicating accuracy for both channels of better than 0.2 K over a full year. This impressive figure can be completely credited to the internal calibration. The calibration procedure also compensates automatically for the degrading performance of optical components and electronic drift. From the year of data, only two weeks are missing because of a system breakdown caused by a bird that had managed to slip in—with fatal consequences. Table 7.5 gives an example of the format of the data as it has been stored on disk.

Table 7.5 Database example of collected background data.

Date 13-08-1990	Description			Elevation horizontal			AZIMUTH 315 deg			
	T_3	T_8	T_a	RH	Q_g	Q_p	v	Φ_v	PR	p
Time	(°C)	(°C)	(°C)	(%)	(W m ⁻²)	(W m ⁻²)	(m s ⁻¹)	(deg)	(mm)	(hPa)
00:30	18.7	19.5	20.6	83.3	0.0	392	2.2	27.7	0.0	1011.5
00:45	18.6	19.0	20.3	86.7	0.0	398	1.3	32.4	0.0	1011.3
01:00	18.0	18.7	19.9	89.2	0.0	391	1.5	28.6	0.0	1011.2
01:15	18.1	19.0	19.8	91.3	0.0	393	1.6	16.5	0.0	1011.0

The following elements were measured:

- (1) Various types of grass at 200 deg and 340 deg, including cutting,
- (2) Deciduous trees at 50, 90, 100, 220, 290, and 340 deg, 2–7 m in height, having different types of backgrounds at ranges of 20–50 m,
- (3) Coniferous trees at 350 deg, 4 m height at 100 m,
- (4) Agricultural field at 190 deg (seasonal plant growing),
- (5) Bare soil at 200 deg (rough surface),
- (6) Concrete at 90 deg azimuth,
- (7) Various camouflage materials.

In the summer of 1990, the following elements were added:

- (8) Water surface (small pond, 1 m depth),
- (9) Up and downhill slopes (bare soil and grassy).

7.3 Background temperature statistics

Experimental data, like those collected at Gilze Rijen AFB, are mainly applied in the following two situations.

(1) To study the thermal behavior of backgrounds

This ranges from studies of the temporal thermal behavior during specific terrain and weather conditions to the formulation of empirical background models. In the latter case, a description of the apparent temperature of the background in relation to measured weather and environmental parameters is the ultimate goal.

(2) To relate thermal background behavior to target thermal signatures

In almost all situations, this type of research is related to target detection/recognition. On the one hand, sensors are optimized to find (detect) specific targets in specific backgrounds. On the other hand, countermeasures are optimized to delay or prevent target detection. For both efforts, detailed information on target and background signatures is required. An example was shown in Figs. 7.11 and 7.12, in which measured apparent temperatures of various targets are shown in relation to the measured apparent temperature envelope of the background.

An extensive discussion of both types of studies goes beyond the purpose of this text. It is neither possible nor practical to give a complete treatment here of all the given types of analysis, using a full year of data. Therefore, illustrative examples of the different analysis techniques will be discussed, applied to a limited data set that includes a summer and a fall/winter period. A full analysis will not change the fundamental approach discussed here.

The temperature distributions of various elements over a given period of time are analyzed for the following situations:

- (1) 25 July–19 August 1990
- (2) 1–30 December 1990

7.3.1 Background temperature distributions

The following figures show apparent temperature histograms of various background elements. The variance of the distribution is calculated as a root mean square (rms), as

$$\text{rms} = \frac{1}{N} \sqrt{\sum_{i=1}^N (T_i - T_m)^2} \quad (\text{K}), \quad (7.6)$$

where $T_m = \frac{1}{N} \sum_{i=1}^N T_i$ (K).

Figure 7.52 shows the temperature histograms of two grass areas (position 1 and 15 from the CARABAS database) during daytime for the month of June. For both distributions, the mean temperature, T_m , and the rms are calculated as 20.2°C and 18.4°C, and 4.5°C and 3.7°C, respectively. These figures indicate that there is no significant difference between the two distributions.

However, on a smaller time scale the behavior is quite different (Fig. 7.50), except when freshly cut. Figure 7.53 shows the histogram for the grass area at position 1 for June and August.

The figure shows a completely different behavior, with a long, warm tail for August. Figure 7.54 shows a graph comparing the temperature distribution of grass (position 15), concrete, and deciduous trees (position 26) for the period 25 July to 19 August. The figure shows that the grass is consistently colder than the concrete and mostly warmer except for cooler periods. Figure 7.55 shows the distribution for the same elements during December. As expected during winter, many background elements show similar temperature behavior because they behave as dead material. Exceptions are elements with a large heat capacity, such as concrete and asphalt. These bodies store large amounts of heat in

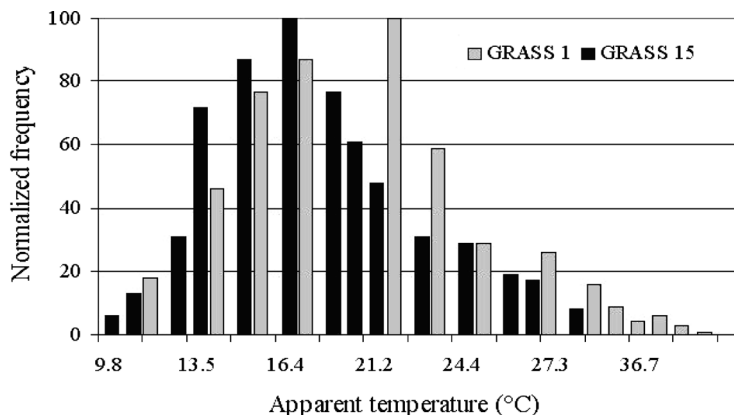


Figure 7.52 Temperature histogram of two different grass areas during daytime in June.

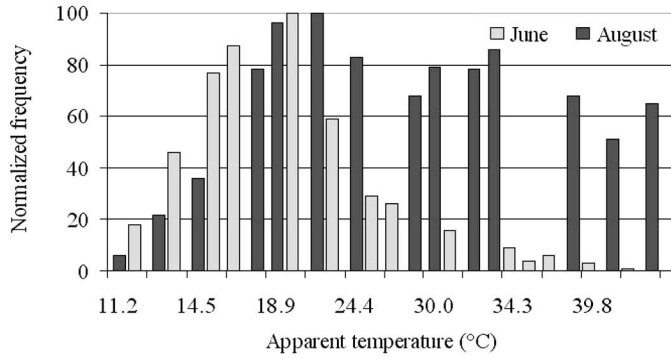


Figure 7.53 Temperature histogram of the same grass area during day time in June and August.

summer and release it very slowly during the fall. Conversely, in the winter, cold penetrates deeply into these bodies and is released slowly during spring. As a result, these types of surfaces are relatively warmer during the fall and colder during spring than material with less heat capacity (such as trees and vegetation).

Figure 7.56 shows a comparison of the same background elements during night for the summer period of 25 July to 19 August. As discussed, concrete accumulates much heat and does not cool down at night. In the situation shown, deciduous trees are warmer than grass, which is typical in summer. Warm air is trapped in and under the canopy during daytime, while the grass area is exposed

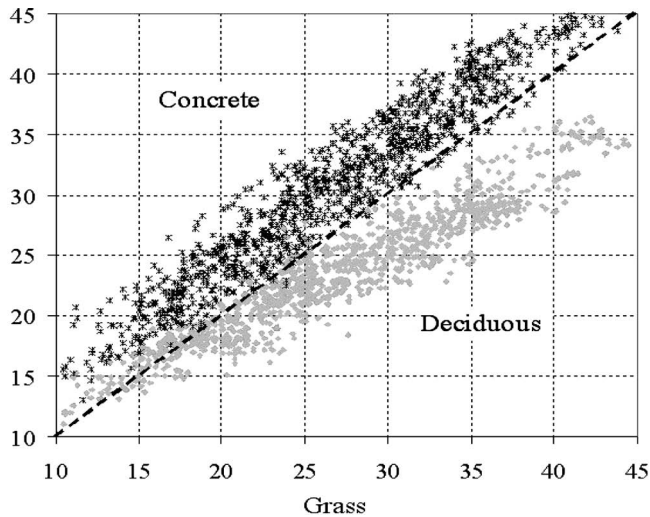


Figure 7.54 Comparison of the temperature distribution of grass (position 15), concrete, and deciduous trees (position 26) in daytime for the period 25 July to 19 August.

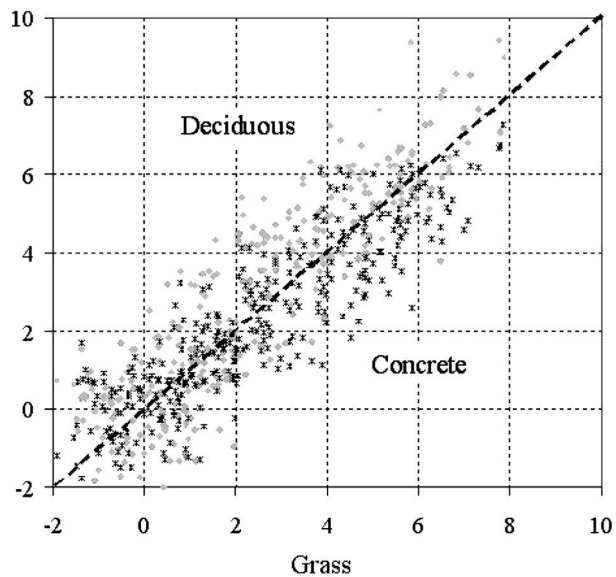


Figure 7.55 Comparison of the temperature distribution of grass (position 19), concrete, and deciduous trees (position 30) in daytime for the period 1 to 30 December.

to a clear cold sky, resulting in radiation cooling. The effect of radiation cooling was earlier shown in Fig. 7.38.

Table 7.6 shows some sample temperature statistics (mean temperature and variance [rms]) of various background elements.

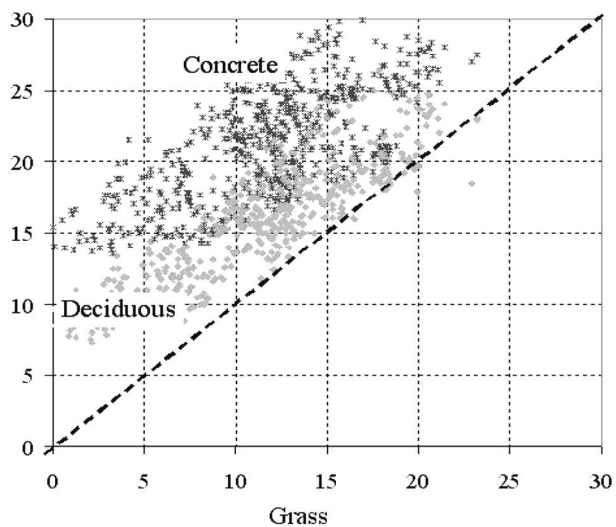


Figure 7.56 Comparison of the temperature distribution of grass (position 15), concrete, and deciduous trees (position 26) at night for the period 25 July to 19 August.

Table 7.6 Sample temperature statistics of some background elements.

Time period	November		August			
	Day		Night		Day	
	T_m	σ	T_m	σ	T_m	σ
Trees (S)	7.1	3.6	15.2	3.8	22.5	5.7
Trees (N)	6.6	3.8	15.1	3.9	22.9	5.5
Grass	7.0	3.8	12.1	5.1	23.7	7.3
Bare soil	6.6	3.7	13.3	4.6	26.9	9.7
Concrete	5.9	3.7	19.3	3.8	27.4	7.1

T_m and σ in degrees Celsius. Total number of 768 contributing data points.

In relation to target thermal signatures, it is interesting to know the temperature contrasts that prevail in a background during a given time period. The percentage of time γ for which the temperature contrast ΔT between two background elements is smaller than a given contrast, ΔT_o , is calculated from

$$\gamma = \frac{(\Delta T || \Delta T| \leq \Delta T_o)}{N} \times 100\%.$$

Tables 7.7 and 7.8 show sample calculations for γ in both spectral regions for the summer and winter period used earlier. The pre-selected contrast ΔT_o has been set to 1, 2, and 5°C during day as well as night. Table 7.8 again shows that during winter, the contrast values are moderate. Expressed in a percentage of time, the wintertime contrasts are within $\pm 2^\circ\text{C}$ almost 90% of time, that is, 31 of 35 days! The tables also show that the differences between the two wavelength bands are small. For small values of ΔT_o this is different, because ΔT_o is of the same order of magnitude as the variance.

Table 7.7 Temperature-contrast statistics during the summer period.

Contrast	3 5 μm									
	Day					Night				
	Statistics		γ (%)			Statistics		γ (%)		
	ΔT_m	σ	1°C	2°C	5°C	ΔT_m	σ	1°C	2°C	5°C
Grass soil	1.0	1.8	44	69	98	0.1	1.9	61	88	96
Grass concrete	2.7	3.1	17	33	77	7.5	3.0	2	5	23
Trees grass*	4.4	3.9	14	26	57	2.2	2.1	14	35	94
			8 12 μm							
Grass soil	0.3	1.7	54	76	99	0.0	1.7	79	94	96
Grass concrete	1.0	3.6	21	39	82	5.9	3.3	12	16	37
Trees grass*	5.0	4.1	14	26	53	2.0	1.9	28	45	97

*Sunlit, south facing tree line.

Table 7.8 Temperature-contrast statistics γ during the winter period.

3-5 μm										
Contrast	Day					Night				
	Statistics		γ (%)			Statistics		γ (%)		
	ΔT_m	σ	1°C	2°C	5°C	ΔT_m	σ	1°C	2°C	5°C
Grass soil	0.1	1.1	63	92	100	0.1	1.3	57	88	100
Grass concrete	0.3	1.3	59	88	100	0.5	1.7	48	78	99
Trees grass*	0.4	1.2	59	91	100	1.0	1.6	43	64	100
8-12 μm										
Grass soil	0.3	0.6	92	92	100	0.0	0.6	96	99	100
Grass concrete	0.9	1.1	62	62	100	0.0	1.1	68	94	100
Trees grass*	0.2	0.4	97	97	100	0.6	0.7	82	89	100

*Sunlit, south facing tree line.

7.3.2 Statistical temperature differences between 3-5 μm and 8-12 μm

In the discussion of which spectral band, 3-5 or 8-12 μm , can best be used to detect targets in woodland terrain, it is interesting to check the CARABAS database. Figure 7.57 shows a comparison for concrete during days in summer.

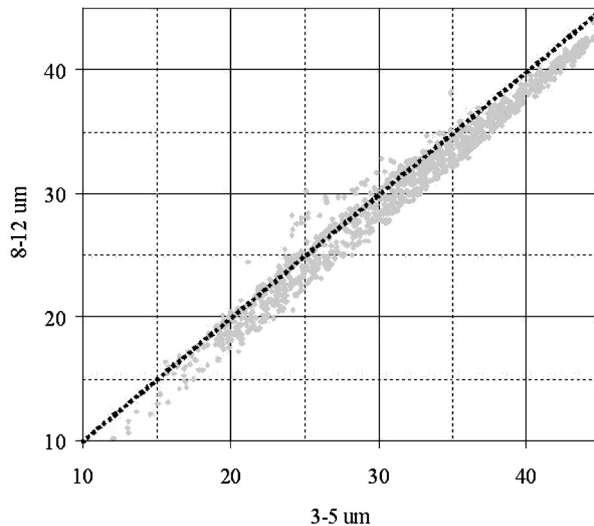


Figure 7.57 Apparent temperature of concrete in 3-5 and 8-12 μm during days in the summer.

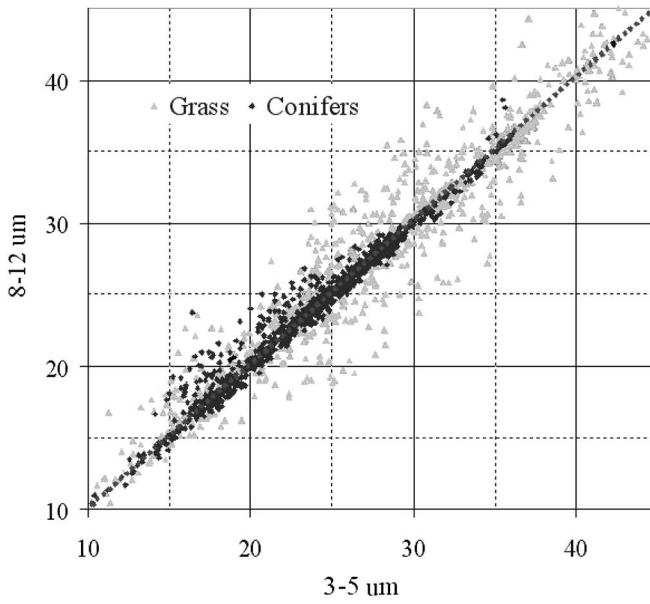


Figure 7.58 Apparent temperature of grass and conifers in 3–5 and 8–12 μm during days in the summer period.

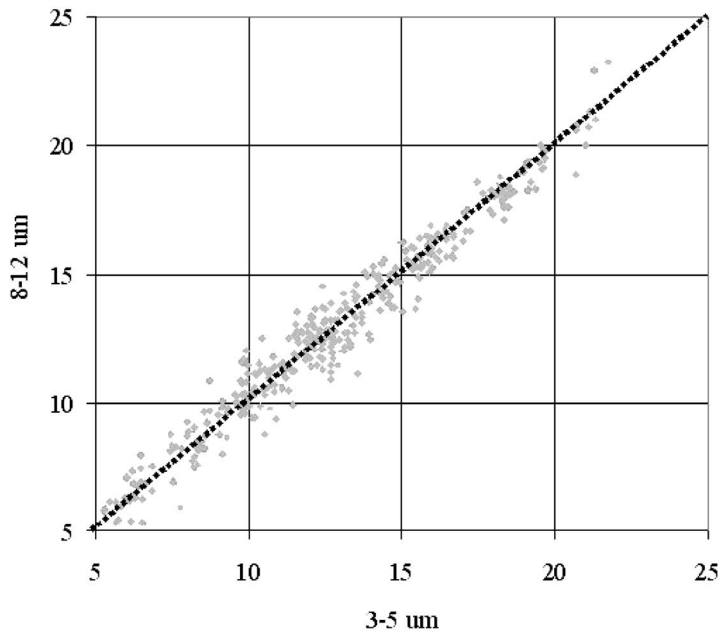


Figure 7.59 Apparent temperature of grass in 3–5 and 8–12 μm during night time in summer.

Table 7.9 Comparison of the mean temperature (degrees C) in 3–5 and 8–12 μm .

August									
Time period	Night				Day time				
	$T_m(3\ 5)$	σ	$T_m(8\ 12)$	σ	$T_m(3\ 5)$	σ	$T_m(8\ 12)$	σ	
Grass	10.9	4.2	12.1	5.1	23.3	7.3	23.7	7.3	
Concrete					28.4	7.4	27.4	7.1	

T_m and σ in degrees C. Total of 768 contributing data points.

The apparent temperature difference in the two wavelength bands is defined as $\Delta T = T_m(3-5\ \mu\text{m}) - T_m(8-12\ \mu\text{m})$. Apparent temperatures in 3–5 μm are slightly, but not significantly, higher. Figure 7.58 shows a comparison of the apparent temperature of grass and conifers during days in the summer. Figure 7.59 shows this comparison for grass during summer nights. As before, there are some scattered but no systematic differences.

Table 7.9 shows the mean temperature and the variance for both spectral regions. The results again indicate that no significant difference exists for the given situations. A more extensive analysis showed a similar trend, but did not lead to an unequivocal conclusion. If this conclusion holds, this means that a possible benefit of using 3–5 μm is determined mainly by target signatures and to a much lesser extent by background signatures.

7.3.3 Background temperature curve fitting

Curve fitting is a way to represent measured data by a small set of regression coefficients instead of using the database itself. The best fit is produced using parameters that have a major direct influence on the data to be fitted. Two examples are

- (a) The behavior of the (apparent) temperature $T_{ap}(X, t)$ of an element X is enforced by environmental conditions in combination with the physical properties of the element. Since the weather is the driving mechanism for the temperature of an element, a first attempt can be a straightforward linear fit of the apparent temperature with meteorological parameters M , as

$$T_{ap}(X, t) = \sum_i a_i M_i(t). \quad (7.7)$$

- (b) One step further is to fit temperature data directly to known theoretical expressions for the various heat-exchange mechanisms $Q_i(X, t)$, as in

$$T_{ap}(X, t) = \sum_i b_i Q_i(X, t). \quad (7.8)$$

7.3.3.1 Radiometer data

It is important to note that the choice of X implicitly determines a number of physical parameters. The choice of X is not only made by name, like grass, but also includes the choice of a number of physical parameters. For instance, the choice could be:

- A horizontal patch of grass
- $0.8 < \varepsilon < 0.95$
- $10 < h < 20$ cm
- $8 < \lambda < 12$ μm

The influence of different meteorological parameters on the apparent temperature of a surface can be determined by theoretical model calculations, as shown in Chapter 4. The influence of a parameter depends on the type of surface and may change from weather type to weather type. The general order of importance is solar irradiance, air temperature, long wave sky irradiance, and wind speed. For vertical surfaces, the wind direction may become important, too. The influence of atmospheric pressure is negligible.

Lemche¹¹ has tested many curve-fit equations (models), starting with one and increasing to 17 parameters. The latter model, called FULL, includes parameters to differentiate between day/night and actual month. For each model, the quality of the fit (correlation coefficient R^2) and the standard deviation, σ , were calculated. The FULL model gave the best results over the four seasons and almost always achieved $R^2 > 0.95$. The optimum between R^2 and the practical number of parameters was found by the equation

$$T_{ap}(X, t) = a_o + a_1 Q_s(X, t) + a_2 Q_p(X, t) + a_3 T_a(X, t) + a_4 v(X, t),$$

where Q_s : solar irradiance,
 Q_p : sky irradiance,
 T_a : air temperature,
 v : wind speed.

Surprisingly, the dependence on wind speed was found to be quite weak.

Since much more is known about the heat exchange processes involved, it is more interesting to establish a curve-fit method directly relating the apparent temperature to these processes. To write Eq. (7.8) more explicitly, the terms in the heat balance equation are linearized in T by the following approach. The starting point is the heat balance equation (neglecting latent heat exchange) for the top layer of a background element, written as

$$\alpha_s E_g + \alpha_l E_p - \varepsilon \sigma T^4 - h(T - T_a) + \lambda \left(\frac{\partial T}{\partial z} \right)_{z=0} = 0, \quad (7.9)$$

where α_s : absorption coefficient for shortwave radiation,
 α_l : absorption coefficient for long wave radiation,
 σ : Stefan-Boltzmann constant,

- E_g : global irradiance (solarimeter output),
 E_p : long wave down welling radiation (pyrgeometer output),
 h : convective heat transfer coefficient,
 T_a : air temperature,
 T : element temperature,
 λ : heat conductivity,
 z : linear dimension.

Rewriting $\alpha_l E_p$ in Eq. (7.9),

$$\alpha_l E_p = \varepsilon(f_1 \varepsilon_a \sigma T_a^4 + f_2 E_t),$$

- where ε : element emission coefficient,
 f_1, f_2 : view factors,
 ε_a : atmospheric emission coefficient,
 E_t : emittance of the surrounding terrain;

and setting

$$\lambda \left(\frac{\partial T}{\partial z} \right)_{z=0} = \frac{\lambda}{d} (T_c - T) = D(T_c - T)$$

with T_c : constant temperature at $z = d$,

$$D: \frac{\lambda}{d}$$

leads to

$$\alpha_s E_g + \varepsilon f_2 E_t + \varepsilon \sigma (f_1 \varepsilon_a T^4 - T^4) - hT + hT_a + D(T_c - T) = 0. \quad (7.10)$$

Linearize the term $-\varepsilon \sigma (T^4 - \beta T_a^4)$ in Eq. (7.10), with $\beta = (f_1 \varepsilon_a) \neq 1$, as

$$-\varepsilon \sigma (T^3 + \beta^{0.25} T^2 T_a + \beta^{0.5} T T_a^2 + \beta^{0.75} T_a^3) (T - \beta^{0.25} T_a). \quad (7.11)$$

If T and T_a are of the same order of magnitude, then Eq. (7.11) converts to

$$-\varepsilon \sigma T_m^3 (T - \beta^{0.25} T_a) \left(\frac{1 - \beta}{1 - \beta^{0.25}} \right) = \gamma (T - \beta^{0.25} T_a), \quad (7.12)$$

where $T_m = \frac{(T + T_a)}{2}$.

The error introduced by Eq. (7.12) is less than 2% for $270 < (T, T_a) < 315$ K. Rewriting Eq. (7.11) using Eq. (7.12) leads to

$$\alpha_s E_g + \gamma \beta^{0.25} T_a + hT_a - (h + D - \gamma)T + DT_c + \varepsilon f_2 E_t = 0. \quad (7.13)$$

Simplifying further by assuming that $h \ll D$ and $\gamma \ll D$ leads to

$$c_1 E_g + c_2 \varepsilon_a^{0.25} T_a + hT_a + \delta = T \quad (\delta = DT_c + \varepsilon f_2 E_t = \text{constant}). \quad (7.14)$$

If $\varepsilon \cong 1$, then $T \cong T_{ap}$ and Eq. (7.14) converts to

$$T_{ap} = c_1 E_g + c_2 \varepsilon_a^{0.25} T_a + hT_a + \delta. \quad (7.15)$$

Breaking down Eq. (7.15) further to contain only weather parameters, using

$$h = c_4 v^n,$$

where v : wind speed,
 n : ranges from 0.6 to 0.8,

and

$$\varepsilon_a = p + q\sqrt{e},$$

where e : atmospheric water vapor pressure,
 $p \cong 0.6$ and $q \cong 0.06$.

Evaluate $\varepsilon_a^{0.25}$ in Eq. (7.15) by applying the following series expansion twice:

$$(1+x)^{0.5} = \left(1 + \frac{x}{2} - \frac{x^2}{8} + \dots\right), \quad \text{with } x < 1.$$

Neglecting quadratic and higher-power terms leads to

$$\varepsilon_a^{0.25} = \left(p + q\sqrt{e}\right)^{0.25} \cong p^{0.25} \left(1 + \frac{q\sqrt{e}}{4p}\right). \quad (7.16)$$

The truncation error is less than 2% for $10 < e < 30$ hPa.

Substituting Eq. (7.16) in Eq. (7.15) results in the final expression for T_{ap} , as

$$T_{ap} = a_1 E_g + a_2 T_a + a_3 T_a \sqrt{e} + a_4 T_a v^n + a_5. \quad (7.17)$$

Water vapor pressure can be expressed in terms of directly measured weather parameters, such as the absolute humidity, χ (g m^{-3}) and/or the relative humidity, by using the functional relations

$$\chi = \frac{217 e}{T_a} \quad \text{and} \quad \text{RH} = \frac{e}{e_s}.$$

The saturation vapor pressure, e_s , can be approximated (error <2%) by

$$e_s = 1.831 \times 10^{-9} T_a \exp(0.06 T_a) \quad (\text{hPa}).$$

The beauty of this simple theoretical approach is given by the fact that the apparent temperature is expressed in four basic (synoptic) weather parameters. The coefficients in Eq. (7.17) are determined for each element during a certain period of time and for the desired weather conditions within that time frame. As an example, the regression coefficients in Eq. (7.17) are determined for a south-facing deciduous tree line from a least square fit of the experimental data during daytime for the period of 25 July to 19 August. The no-rain condition is the only limitation for the weather conditions, and temperature data are taken in the 3–5 μm spectral region. The quality of the fit is determined by the rms value (7.6).

Analyses are performed separately for night and day. Figure 7.60 shows the results for day as a comparison between the measured and predicted apparent temperatures using the regression coefficients found for the entire period of 15 July to 19 August. Also, the curve is shown for the predicted temperature for

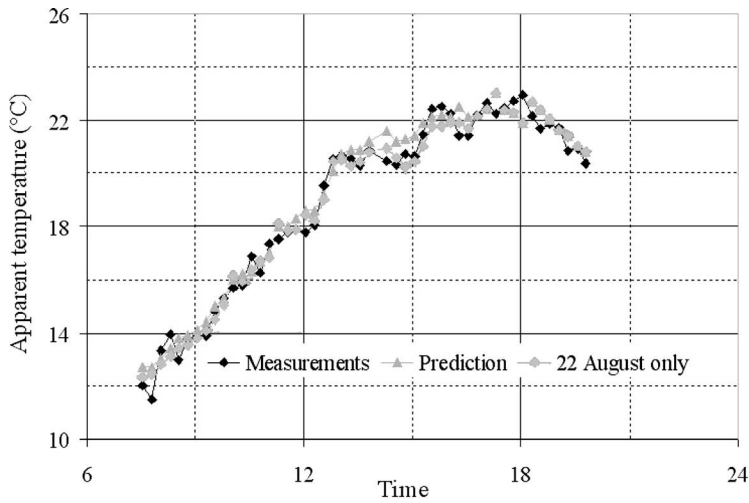


Figure 7.60 Measured and predicted temperatures of deciduous trees during day time using regression coefficients for the entire period of 25 July to 19 August. Also, the curve is shown for the predicted values using the regression coefficients derived for the single day of 22 August.

22 August using the regression coefficients that employ input data only from 22 August. The figure shows an excellent correlation between measurements and predicted values. Figure 7.61 shows the apparent temperature of the same tree line at night. It is emphasized that the curve fit, i.e., the regression coefficients, are based on average input conditions over the selected time period. Therefore, when applied

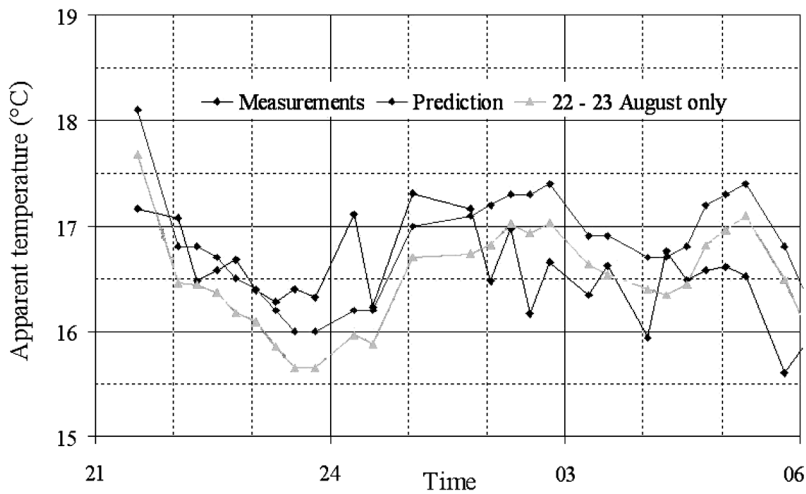


Figure 7.61 Measured and predicted temperatures of deciduous trees during night time using regression coefficients for the period of 25 July to 19 August. Also, the curve is shown for the predicted values using the regression coefficients of 22 August.

to actual weather conditions, which contain moments of relatively large, fast changes, the fit is less accurate. This is especially true with partly broken skies in combination with high solar loading or during night with variable wind speed and direction in combination with “light” (little thermal mass) surfaces.

Figure 7.61 shows this effect in the fluctuating behavior of the measured data, while the predicted curves are more flattened. For surfaces with a high thermal mass, the actual surface temperature is, so to speak, out of phase with actual weather conditions. Take, for instance, the situation in which the sun disappears behind a cloud, reducing irradiance from 800 to 300 W m^{-2} (all other parameters are assumed to be constant). It will take more than an hour for the surface temperature to fall to a value corresponding to, or in phase with, the new situation. As pointed out earlier, this type of surface also accumulates large amounts of energy during summer, which will slowly and continuously raise the temperature. This increase temperature cannot be related to the actual weather conditions, but is determined by the weather history. Figure 7.62 shows this effect, presenting the temperature curve for concrete during daytime on 22 August. When using the entire period of 25 July to 19 August to determine the regression coefficients, the predicted temperatures are too high, but the curve follows the curve of the measured temperatures quite well. This is also demonstrated in Fig. 7.63, showing a comparison between the histograms of the measured and predicted temperatures during daytime for the period of 25 July to 19 August.

The distributions are quite similar, with some larger differences at the warm and cool ends. These are caused by days that completely deviate from the general weather picture during the considered time period.

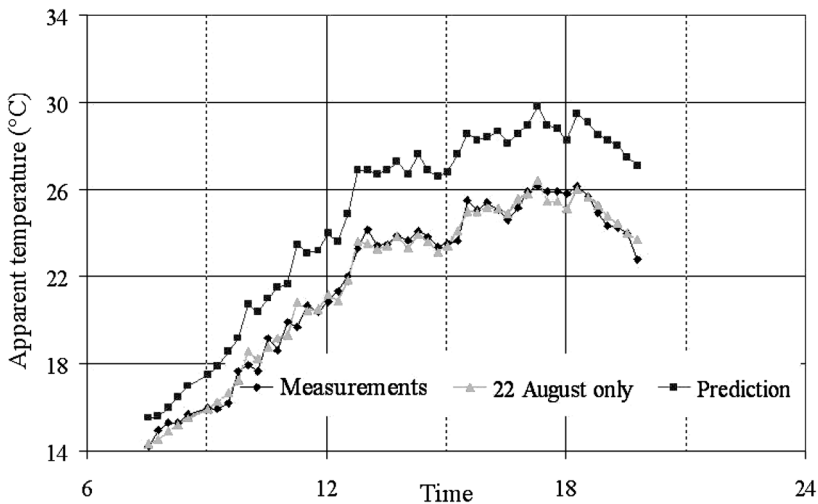


Figure 7.62 Measured and predicted temperatures of concrete during day time, using regression coefficients for the entire period of 25 July to 19 August. Also, the curve is shown for the predicted values using the regression coefficients derived for the single day of 22 August.

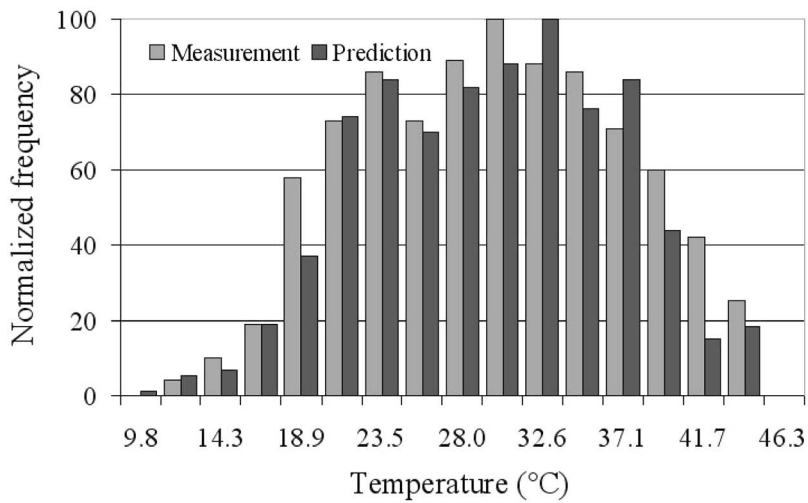


Figure 7.63 Measured and predicted temperature histograms of concrete during day time between 25 July and 19 August.

Figure 7.64 shows the measured and predicted temperatures of concrete at night for the same time period. Again, the predicted temperatures are too high, but the trend follows the measured temperature curve quite well.

At night, thermal behavior is usually driven by sky radiation (in absence of the dominant solar loading in daytime). This effect is strongest for horizontal surfaces with relatively small heat capacity. Figure 7.66 shows the measured and predicted temperatures of grass at night for the period of 25 July to 19 August. Figure 7.66

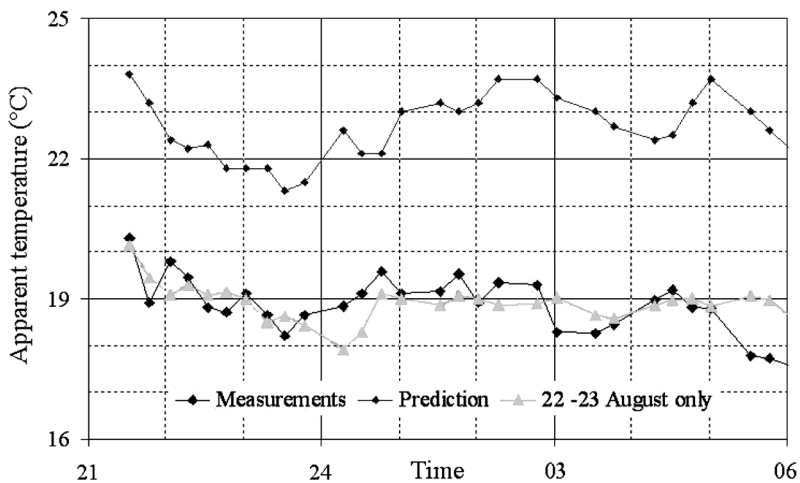


Figure 7.64 Measured and predicted temperatures of concrete at night, using regression coefficients for the entire period of 25 July to 19 August. Also, the curve is shown for the predicted values using the regression coefficients derived for the single day of 22 August.

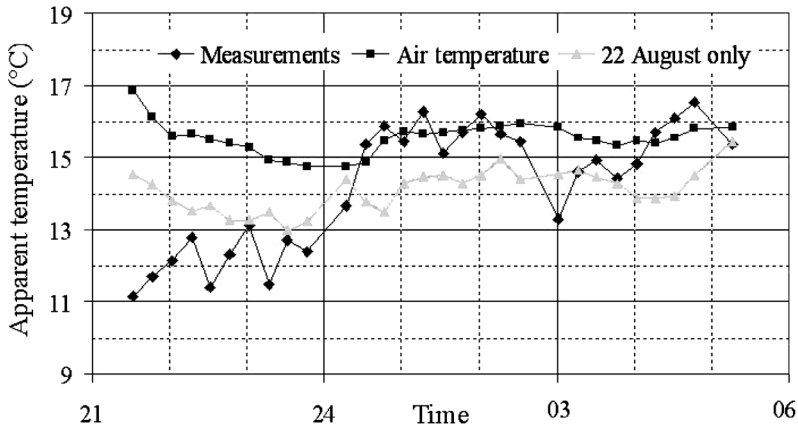


Figure 7.65 Measured and predicted temperatures of grass at night on 22 August, using regression coefficients for the entire period of 25 July to 19 August. The ambient air temperature is shown for comparison.

shows the long wave sky irradiance (pyrgeometer) during the night of 22–23 August. This figure shows clear sky in the evening of 22 August, followed by a period of increasing cloudiness in the early morning of 23 August. Figure 7.65 shows that the apparent temperature of grass drops below air temperature during clear sky (and calm wind) conditions, increasing from 12 to 16°C as the clouds come in. The slope of the sky irradiance and the apparent temperature of the grass are more or less identical.

Figure 7.65 shows a moderate response of the predicted temperature to the rather large change in sky irradiance as shown in Fig. 7.66. Figure 7.67 explains this. It shows the nighttime sky irradiance for the period of 25 July to 19 August, along with the mean values for the entire period and for the night of 22 August. The figure shows that the sky irradiance on 22 August is unique compared with the entire period that is unusually high. The consequence is that the regression coefficients are too small, because the sky irradiance during the entire period is lower.

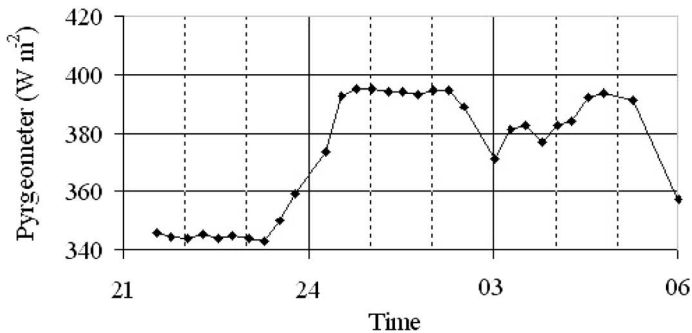


Figure 7.66 Long wave sky irradiance during the night of 22–23 August.

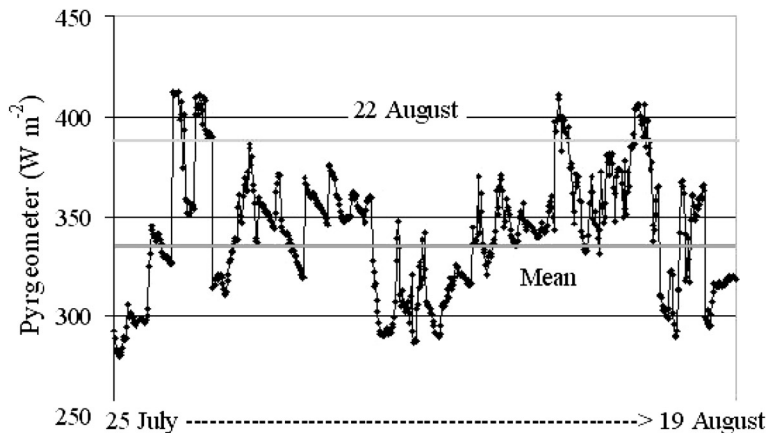


Figure 7.67 Sky irradiance during night for the entire period of 25 July to 19 August, along with the mean values for the entire period and for the night of 22 August.

This analysis is just one example to show the application of the curve-fit procedure and is by no means complete. Generally, this technique works quite well for normal weather periods. Moreover, it was shown that the apparent temperature of natural elements may stay close to the ambient air temperature, but with increasing thermal mass there is an increasing divergence. This also is the case under more extreme weather conditions, such as clear night skies or high solar load under low wind conditions. Hence, extra caution has to be taken when using the curve-fit procedure.

The influence of the various input time frames was analyzed but not discussed here. It appeared to be marginal, giving good results for curve-fit periods of up to five weeks. This means that all background-element apparent temperature data can be represented with five regression coefficients without too much loss of accuracy. It is to be expected that, especially during spring and fall, when nature changes rapidly in a short time, the semi-empirical relation breaks down much sooner. This semi-empirical approach also has been used successfully to describe the apparent temperatures of desert backgrounds.

7.3.3.2 Images

Thermal characteristics of natural backgrounds are normally determined by

- (a) objects found in the background, i.e., trees, roads, houses, targets, grass, hills, etc.,
- (b) electro-optical properties (reflectance, emittance, and transmittance) of objects,
- (c) meteorological conditions, and
- (d) season and time of day.

In general, spatial information in an image, determined by parameters such as location, size, and orientation of natural elements, within a given background does not vary much. For this reason, the spatial distribution in that particular background scene will only change slowly with time. This is in contrast with the change of temporal (multispectral) radiation levels in the background scene, which may vary on a small time scale.^{11–13} Therefore, the temporal changes will largely determine the thermal dynamics in the scene.

In previous sections, a background was characterized by describing the thermal behavior of the individual background elements. Similarly, the thermal dynamics in a background scene can be described by applying the same curve-fit technique to each pixel in the image (Fig. 7.68). This can be done straightforwardly, i.e., without knowing what kind of element a pixel represents, or by image segmentation, i.e., identifying similar background clusters. Having determined the regression coefficients for each pixel, a thermal image of this geometrically fixed scene can be generated for any given weather conditions provided these conditions fall within the time frame in which the curve fit holds.

In an image sequence, each pixel in the sequence corresponds to a timeline of observed apparent temperatures of a particular background element or object. Equation (7.17) is applied to the timeline of each pixel, generating a set of five regression coefficients. Hence, each pixel is treated as a separate background element and its apparent-temperature timeline is represented by these five regression coefficients.

This procedure will be demonstrated for a set of desert background images, which was collected along with the weather parameters required for the curve-fit procedure. Figures 7.69 through 7.71 give an impression of the experimental setup during the PLUTO campaign, held in the Negev desert in Israel on 23–24 June 1996.

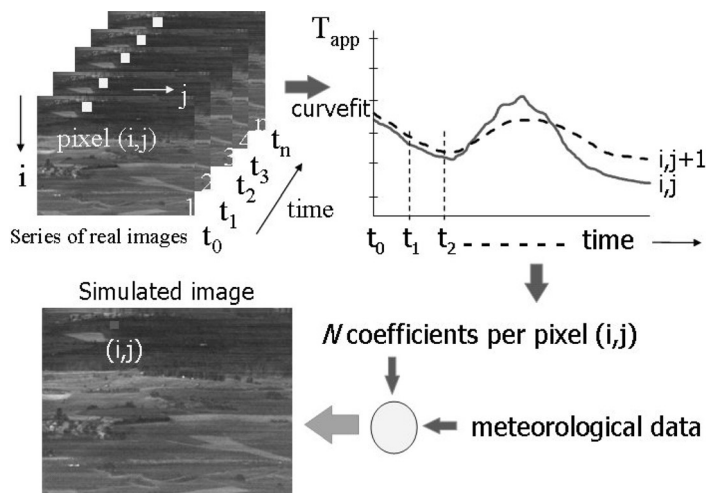


Figure 7.68 Curve-fit procedure applied to thermal images.



Figure 7.69 Experimental setup on the edge of a mountain.

Cameras, calibration blackbodies and weather station were set up on the edge of a mountain, allowing a nice view on a mountain ridge, a dry riverbed (wadi), and a gravel road. Special precautions had to be taken to shield all equipment from the intense solar loading occurring in a desert environment. Many were improvised and needed constant attention because of strong winds. The weather station was complemented with a visibility sensor to monitor clouds of fine dust particles, which occur quite frequently in a desert. Figure 7.72 shows a view of the background under investigation, incorporating the mountain ridge, the wadi, and the gravel road. Several visual and infrared reference panels were placed alongside the road. Figure 7.73 shows the weather station setup, which in this case was supplemented with a visibility sensor.



Figure 7.70 Measurement setup with SCORPIO (Section 5.2) on top of scaffold and the DuDa imager (Section 6.4) to the left under a party tent.



Figure 7.71 Visual and infrared (DuDa 8–12 μm) image of the calibration setup. Blackbodies are placed inside the van to shield from solar irradiance.

Figure 7.74 shows the weather data on 24 June, which were used for the curve-fit calculations. With an ambient air temperature up to 40°C during early afternoon, relative humidity up to 30–40% at night and 0% during the afternoon, 24 June was a windy day with thermal-wind speeds up to 30 km h^{-1} . Also noticeable was the decrease of the long wave sky irradiance in the afternoon.

Figure 7.75 shows a measured thermal image (8–12 μm), taken at noon. Salient feature is the relatively cold gravel road, which probably is caused by the strong wind and the clear skies.

Images taken from 06:30 to 16:00 hours (local time) on 24 June were used as input for the curve-fit calculations. Figure 7.76 shows the calculated image at noon



Figure 7.72 Image of the background under investigation. A series of visual and infrared reference panels is visible in the mid-left part of the image.

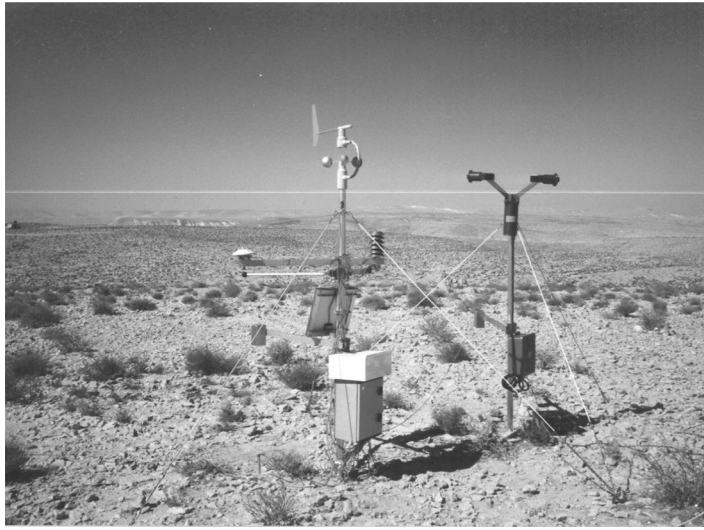


Figure 7.73 Weather station, including a visibility sensor to the right.

as an example, while Fig. 7.77 shows an image of a straightforward subtraction of the calculated and measured images.

A better way to express the quality of the curve fit is through the rms value, calculated as

$$rms_{i,j} = \sqrt{\frac{1}{N} \sum_{k=1}^N (T_{i,j}^m - T_{i,j}^c)^2},$$

with $T_{i,j}^m$ and $T_{i,j}^c$ the measured and calculated apparent temperature of pixel (i, j) , respectively.

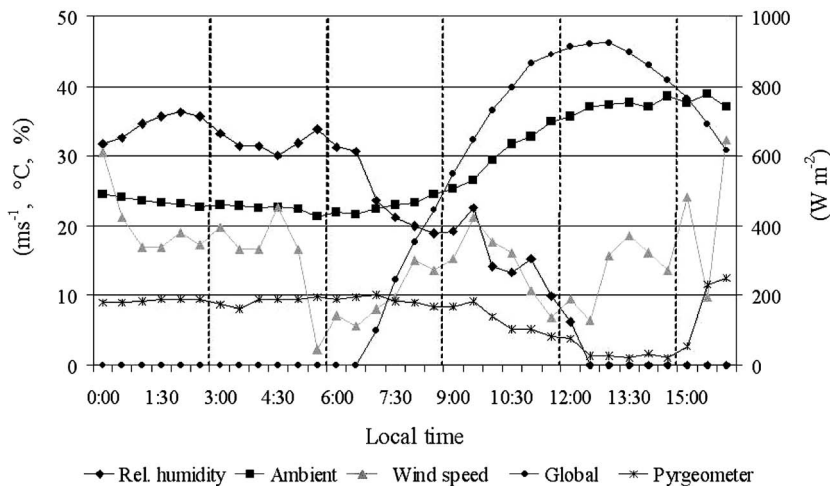


Figure 7.74 Weather data on 24 June 1996 during PLUTO experiments.



Figure 7.75 Measured thermal image (8–12 μm) of the background scene at noon on 24 June.



Figure 7.76 Calculated thermal image at noon (8–12 μm) on 24 June.

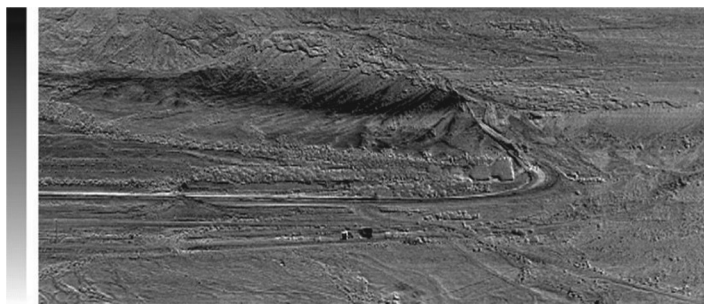


Figure 7.77 Subtraction of calculated and measured image at noon on 24 June. Temperature scale black = -3°C and white = $+3^{\circ}\text{C}$.



Figure 7.78 rms scale: black = 0°C and white = 3°C.

7.3.4 Pros and cons

In summary, the pros and cons of empirical modeling can be formulated in general terms as follows:

Pros

- Direct measurement of the desired quantity, i.e., the apparent emittance (temperature).
- Complex structures can be handled easily.
- Quick data retrieval.
- Easy to generate images under different weather conditions (but within the valid weather range).

Cons

- The need for specific, sometimes expensive measurement equipment.
- Very long measurement periods.
- Describe only one moment (short period) in time.
- Results are limited to climate and geographical zone where data was recorded.

References

1. K. Johnson et al., "Utilization of a multiple mode thermal contrast model in an infrared tactical decision aid," *Proceedings Of The 1988 KRC Symposium On Ground Vehicle Signatures* (1989).
2. W.K. Suttie, "The use of a finite domain code in thermal signature prediction," *Proceedings Of The 1989 KRC Symposium On Ground Vehicle Signatures* (1990).

3. T. Gonda et al., "PRISM model of the T62 using the faceted region editor (FRED), Phase I," *Proceedings Of The 1989 KRC Symposium On Ground Vehicle Signatures* (1990).
4. G. Miosga et al., "RSG17 Joint Trials test plan," (1988).
5. F. Grum and G.W. Luckey, "Optical sphere paint and a working standard of reflectance," *Appl. Opt.*, 7(11) (1968).
6. N.J.J. Bunnik and W. Verhoef, "The spectral directional reflectance of agricultural crops, measurements on wheat and grass canopy," *NIWARS publication no. 23* (1974).
7. K. Schurer, "A method for measuring infrared emissivities of near-black surfaces at ambient temperatures," *Infrared Physics*, 16(1976).
8. A.N. de Jong, "Description of an infrared reflectometer," *TNO publication PHL-1982-25* (1982).
9. A.E. Krusinger, "An empirical surface temperature model," *US Army Corps of Engineers ETL* (1988).
10. P.A.M. Jacobs, "CARABAS, A programmable scanning radiometer for the characterization of backgrounds in the thermal infrared," *Int. J. of Remote Sensing*, 13(15), pp. 2865–2871 (1992).
11. V. Lemche, "IR radiation from camouflage materials and backgrounds," *DDRE N-16* (1992).
12. N. Ben-Yosef and K. Wilner, "Temporal behaviour of thermal images," *Applied Optics*, 24(2), p. 284 (1985).
13. N. Ben-Yosef, K. Wilner, I. Fuchs, S. Simhony, and M. Abitbol, "Natural terrain infrared radiance statistics: daily variations," *Applied Optics*, 24(23), p. 4167 (1985).
14. J.R. Maxwell, "Statistical analysis of selected terrain and water background measurements data," *Environmental Research Institute of Michigan, Report 132300-1-f* (1979).
15. W. de Jong et al., "Sophisticated test facility to detect land mines," *Proceedings of SPIE*, 3710, pp. 1409–1418 (1999).
16. E. Strømman et al., "An automatic station for measurement of meteorological parameters and thermal signatures," *FFI-Rapport-2001/05402*.
17. FEMLAB modeling guide, COMSOL AB, Version 4.0 (January 2004).
18. J.G.M. Schavemaker, E. den Breejen, F. Cremer, K. Schutte, and K.W. Benoist. "Depth fusion for anti-personnel land mine detection," *Proceedings of SPIE*, 4394, pp. 1071–1081 (2001).
19. F. Cremer, W. de Jong, and K. Schutte. "Infrared polarization measurements and modeling applied to surface laid antipersonnel land mines," *Optical Engineering*, 41(5), pp. 1021–1032 (2002).
20. F. Cremer, "Polarimetric infrared and sensor fusion for the detection of land mines," The Hague; ISBN 90-5986-032-2 (2003).

Chapter 8

Signature Management

Signature management is a problem area where target and background signatures come together. To prevent targets from being detected or recognized at an early stage (far range), target signatures can be manipulated in such a way that the target adapts better to the local surroundings. With the large spectral range at which modern sensor systems can operate, signature management needs to be effective in all these spectral bands simultaneously. This often leads to contradicting material requirements.

To be effective, generally two conditions must be fulfilled:

(1) Temperature similarity

Signature management has to shift the range of apparent temperatures on the target within, or at least close to, the temperature envelope of the background. The level of temperature similarity depends on the desired degree of protection, that is, for detection, recognition, or identification. In the detection phase, the target normally is no more than a warm/cold spot in the background, while in the recognition and identification phases, more target details are required. For detection, for instance, measures should emphasize the adjustment of the average target signature (temperature similarity) combined with shape distortion.

(2) Spatial similarity

To prevent target recognition and identification, measures must not only create temperature similarity but also portray detailed geometrical similarity with the background. This spatial similarity must be such that the resulting temperature distribution over the target is similar to that of the background. This means that a pattern has to be created on the target that fits into the background. In this case, it is not so much the local background, but a much larger portion of the field of view that determines the detectability (and eventually recognition) of the target.

In this textbook, mainly temperature similarity will be discussed. The first step is to determine whether a target has a signature problem in relation to the background of its operational environment.

8.1 Target and Background Signature Analysis

Today, personnel and equipment can be deployed in any part of the world. Where in the Cold War era, woodland was the predominant background type, deserts and,

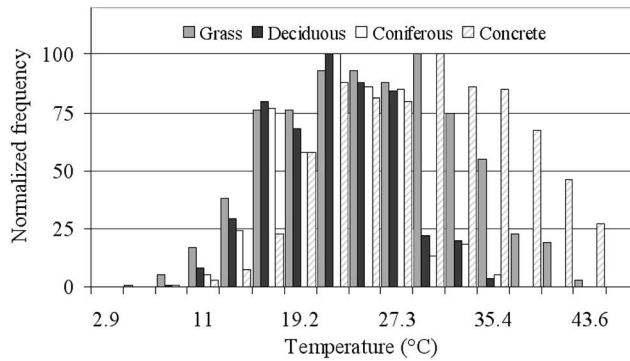


Figure 8.1 Temperature statistics of various background elements during summertime.

even more important, urban areas have become battlegrounds today and in the future. This implies that these backgrounds have to be studied first in order to map their behavior in the spectral bands of interest. Since it is impossible to do this for long periods in all most likely crisis locations, representative measurements have to do the job. Even that is a major task! The PLUTO experiments discussed in Section 7.3.3.2 can be mentioned as an example, as can the CARABAS measurements described in Section 7.2.2. Figure 8.1 shows the temperature statistics of some background elements during daytime in the summer as measured with the CARABAS system.

Most of the time, databases to do this type of statistical analysis are not available and investigations are often limited to a worst-case scenario. Figure 8.2 shows some extreme temperatures (worst cases) of some background elements.

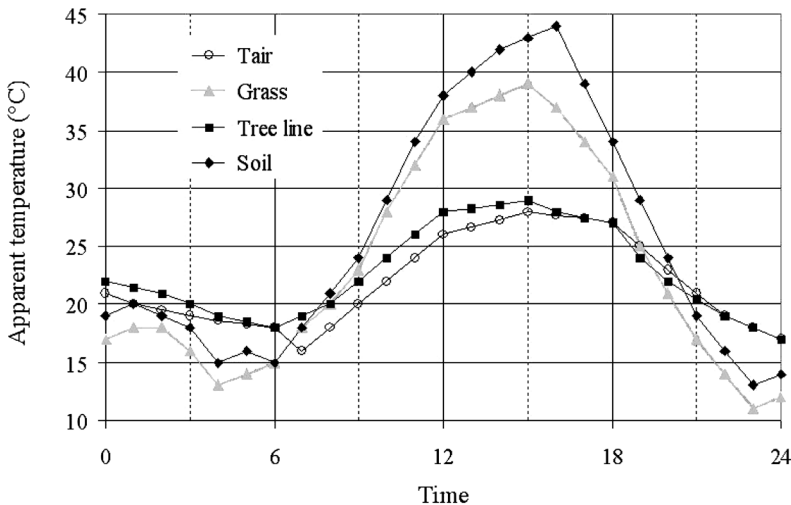


Figure 8.2 Measured apparent temperatures of some background elements during a sunny summer day.

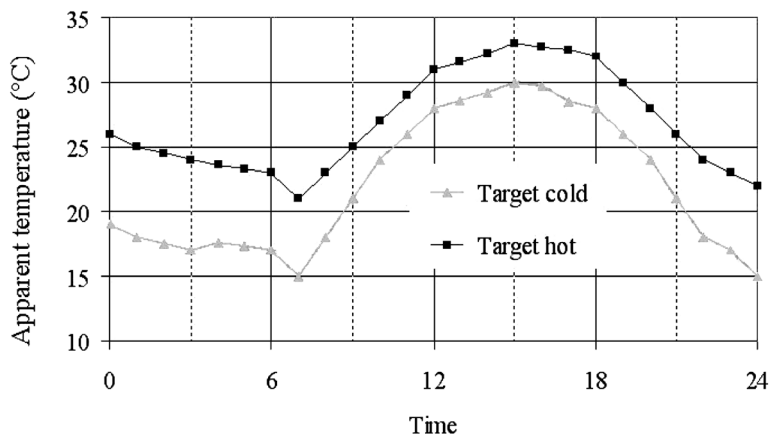


Figure 8.3 Calculated apparent temperature of an exercised (hot) and cold target.

Today's target models are accurate and detailed enough to calculate signatures in various spectral bands, as shown for a T62 in Section 7.1.3. The effects of design and material properties on the thermal signature can be determined quite easily. It becomes a more complicated story if comparisons of modeled targets and real backgrounds are necessary. Theoretical models (simulations) of natural backgrounds are not yet good enough to be used for this type of evaluation. Figure 8.3 shows calculated apparent temperatures of a target, using the weather conditions prevailing during the background measurements shown in Fig. 8.2. Figure 8.4 shows the apparent temperature contrast of the hot and cold target against the grass and the tree line. What does this mean?

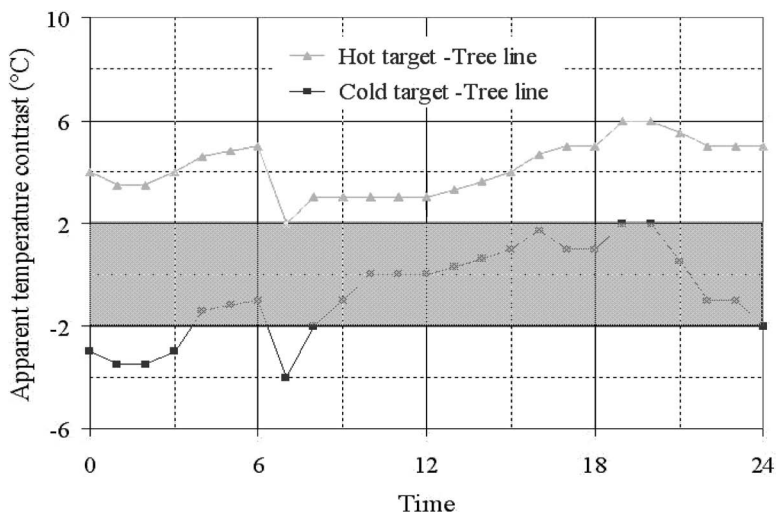


Figure 8.4 Apparent temperature contrast between a cold and exercised target and a natural tree line. Shaded area is good camouflage.

Over the many years of international cooperation on signature management, a rule of thumb emerged: “An absolute contrast of less than 2°C is good camouflage.” The shaded area in Fig. 8.4 represents the time periods of good camouflage. The figure shows typical behavior for a moderate climate zone (such as northwest Europe) in that exercised targets in general show up as too warm during day and night when examined against a tree line. At night, the exercised target is still too hot, while the cold target falls largely within the absolute 2°C temperature band. In a desert environment, which often lacks vegetation and trees, targets generally show a negative apparent temperature contrast.

This again emphasizes the need to investigate target and background signatures together, as one entity. Figure 8.5 shows a number of target modifications as the first step to reducing the visible and thermal signature of the target. In this case, the intended operational background is obviously wood land. The first action is to reduce hot-spot radiation, such as the exhaust grid and wheel train. Figure 8.6 shows thermal images ($8\text{--}12\ \mu\text{m}$) before and after treatment. The figure shows that shielding the exhaust grid did more harm than good. Because the screen did not fit properly to the hull, hot exhaust gases heated up the area around the screen. Also, because the exhaust gases were redirected upwards, the back side of the turret was heated up.

The visual color pattern is made out of paint with reduced emissivity in the infrared spectral band. The effects of this low-emissivity paint (LEP) are clearly noticeable on the thermal image as a mixture of dark and gray shades over the target. However, caution must be taken when using LEPs. Because the LEP



Figure 8.5 Target modifications to reduce the visible and infrared signature.

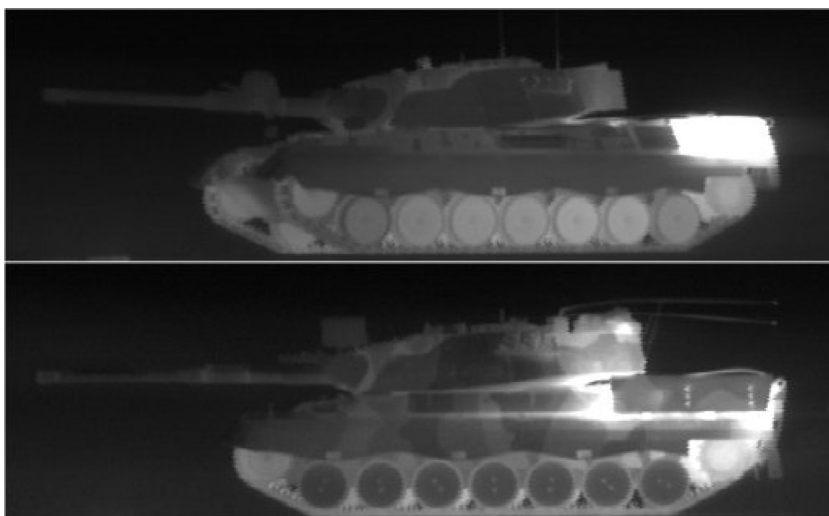


Figure 8.6 Thermal image (8–12 μm) before and after treatment.

principle is mainly based on reflection of cold-sky radiation, its effect in a thermal image strongly depends on sky condition in combination with the location and orientation of the LEP surface.

Figure 8.7 shows the effects of low emissivity (blank steel) on the hangar door on the rear deck of a frigate. Because of the reflection of solar radiation in 3–5 μm , the door shows up as a bright area. At the same time, the door has a strong negative contrast in 8–12 μm .

This example not only shows the effect of low emissivity, but also indicates that IR signatures depend greatly on the spectral band under consideration. What is good in one spectral band may be completely wrong in another. Before using paints and other materials to control thermal signatures of targets, the thermal response of these materials should be investigated. In a first step, the



Figure 8.7 IR signature of hangar door on the rear deck of a frigate.

EO and thermal material properties can be measured in the laboratory. Next, the thermal behavior of the material can be tested in a controlled climate room, equipped with a simulated sun (xenon lamp), simulated cold sky (cooled plate) and generated wind flow (fan). It may be clear that this is a special facility that does not exist in everyone's back yard. The Forschungsinstitut für Optik in Germany, for instance, has built a large climate-controlled room in order to pre-select materials. Samples (1×1 m) can be exposed to solar radiation (xenon source), various wind speeds, and cold-sky radiation. The real weather in the outside world is something else; but this type of information allows a first judgment of the material's potential. Additionally, outdoor measurements over longer periods, as for the characterization of thermal background behavior, should be taken.

8.2 Thermal Signatures of Materials

For this reason, various camouflage materials were included in the CARABAS experiments detailed in Section 7.2.2. Figure 8.8 shows various types of materials laid directly on the grass, except for the camouflage net (#13), which was stretched over the grass at a height of about 25 cm.

Figure 8.9 shows the apparent temperature statistics ($3\text{--}5\ \mu\text{m}$) of the surrounding grass in comparison with a canvas-type material (#11) and the camouflage net. The analyzing period is daytime, 25 July–19 August. The canvas material is too warm and is widely spread, but the camouflage net works quite well. That is, the apparent temperature of the net statistically looks like that of grass. Figure 8.10 shows a comparison between the same nets and a coniferous tree line.

It shows that in this case the canvas material compared to the tree line is far too hot.



Figure 8.8 Some camouflage materials laid out during the CARABAS experiments.

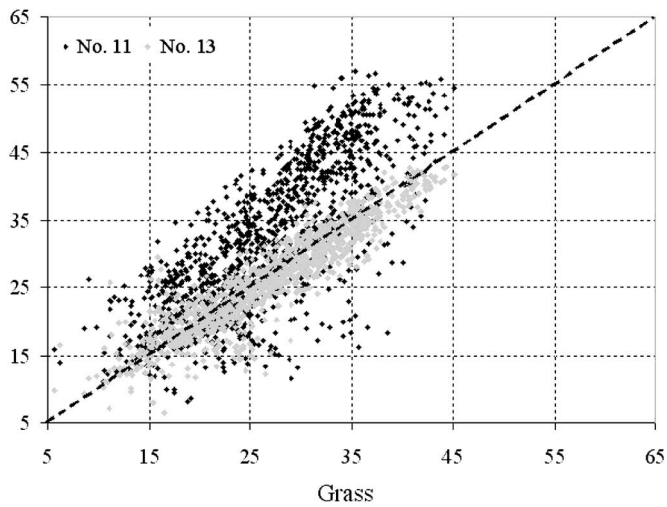


Figure 8.9 Apparent temperature statistics (3–5 μm) of grass and the camouflage nets in location 11 and 13 (Fig. 8.8), from daytime 25 July–19 August.

Compared to the tree line, the camouflage net shows more spreading, but it is quite evenly distributed on the low and high side. This analysis demonstrates two things:

- (1) To have more control over the thermal signature of the camouflage material, deploy it in such a way that is not touching any other surface. This will minimize the influence of these surfaces on the thermal signature of the material.

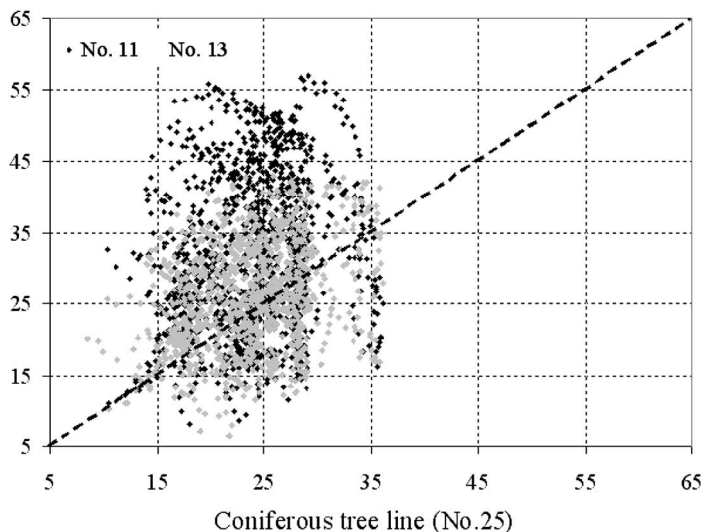


Figure 8.10 Apparent temperature statistics (3–5 μm) of a coniferous tree line and the camouflage nets in location 11 and 13 (Fig. 8.8), from daytime 25 July–19 August.

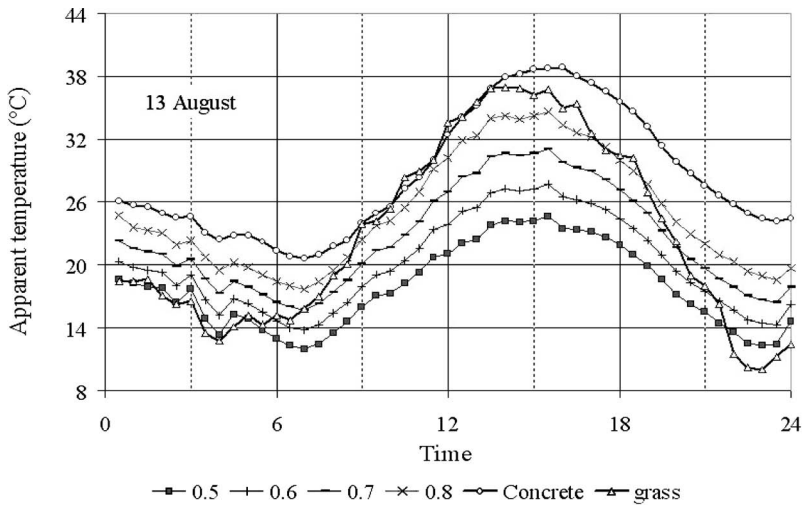


Figure 8.11 Calculated apparent temperatures of a horizontal concrete surface with different emission coefficients for 13 August (Fig. 8.12).

- (2) Deploy the material geometrically in such a way that it optimally mimics the predominant background geometry. In other words, don't place the material horizontally if the background has predominantly vertical structures, such as trees and walls.

Also, models can be used to test prototype camouflage materials and optimize their performance. Models can be used especially to determine the effect of material properties on the apparent temperature. With this kind of analysis, the original situation is compared with the camouflaged one and consequently the models predict relative performance, which may be more meaningful than absolute values. Models, therefore, are a quick and effective way to test the camouflaging potential of a material. Figure 8.11 shows the calculated apparent temperature (8–12 μm) of a concrete surface for a variety of emission coefficients on 13 August, using the model described in Chapter 4. Since sky conditions determine the effects of low emissivity, the pyrgeometer data for this day are incorporated in Fig. 8.12.

The sky irradiance varies moderately during the chosen time period. Figure 8.11 shows that, if LEP is used on concrete to have it look like grass, the emission coefficient should be something like 0.5 at night and 0.8–0.9 during daytime. Under clear sky conditions, this effect might become much worse, as is shown. Figure 8.13 during a winter night under clearing conditions (Fig. 8.14). In the early morning situation, the low emission coefficients result in much-too-low apparent temperatures. As was discussed in Chapter 4, calculations can easily be performed on simple geometries, like LEP on concrete or any other solid with a well-defined surface structure and physical properties. Camouflage materials applied in a practical and realistic way, however, have very irregular

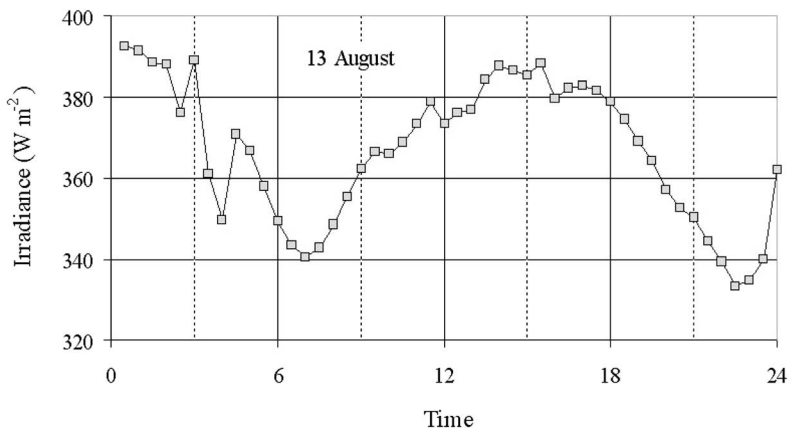


Figure 8.12 Pyrgeometer data for 13 August.

shapes and, for net materials, transparency strongly depends on deployment. As in the thermal background characterization problem, first principles models are not so practical in this case, either.

Having said that, first principles models actually can be used for simple camouflage net configurations, as in the case of straightened horizontal and vertical nets (Fig. 8.15). A number of radiometers are placed over the net to measure the apparent temperature at various angles. Weather data are collected with a small portable weather station. The net is straightened over a wooden back panel

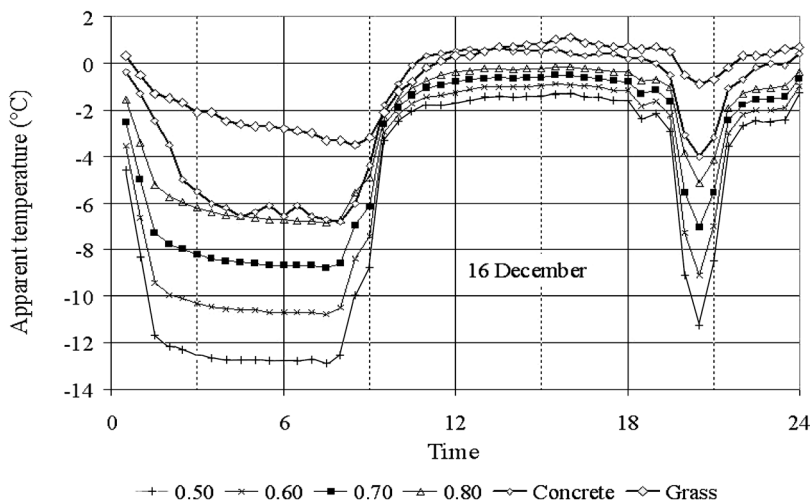


Figure 8.13 Pyrgeometer data and calculated apparent temperatures of a horizontal concrete surface with different emission coefficients during a clearing night sky.

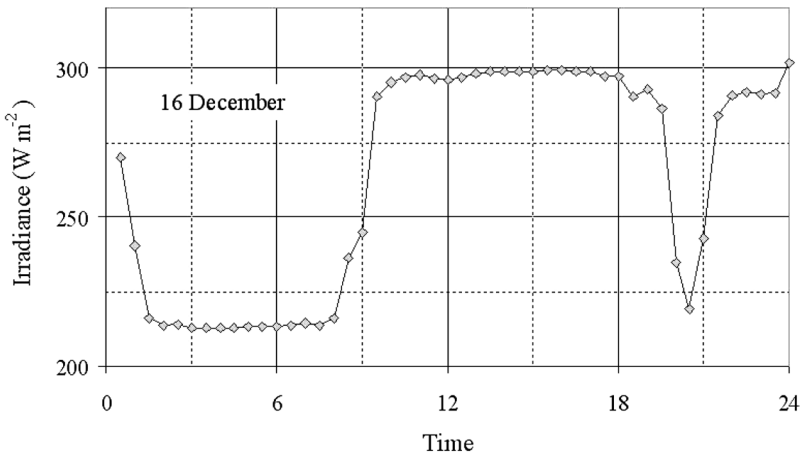


Figure 8.14 Pyrgometer data for 16 December.

($\epsilon \cong 1$) at about 50 cm distance. The physical temperature of the back panel is also measured. The net is a flat 2D net, which looks very much like marquisette.

In the model, a solid sheet of material containing rows and columns of holes represents the net. The material is built up of two layers, which allows the use of different EO and physical parameters for both sides. The model is similar to that discussed in Chapter 4, but in this case two atmospheric boundaries are used instead of one. Figure 8.16 shows a comparison between calculated and measured apparent temperatures of the horizontally positioned camouflage net. Net characteristics can be varied in order to find an optimal signature match (in temperature only) with the intended operational background.

Figure 8.17 shows a prototype camouflage net that was tested during the CHAR experiments in Sardinia.¹ The figure shows that, although the color setting and pattern generally fit quite well in a Mediterranean background, the



Figure 8.15 Measurement setup of camouflage net to collect input data for net model.

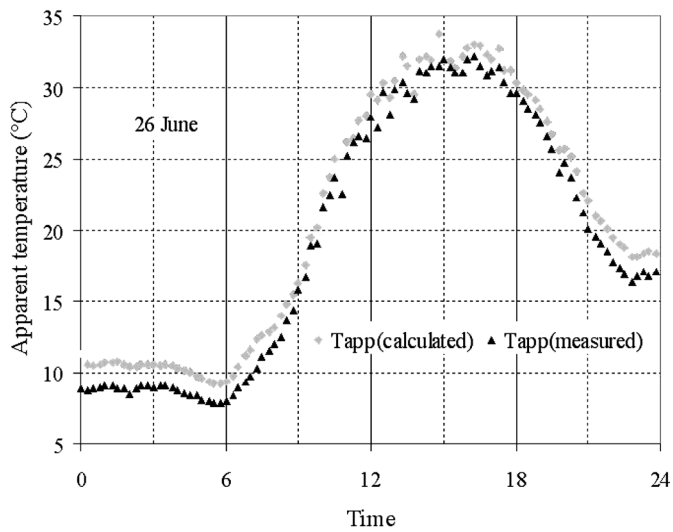


Figure 8.16 Comparison between calculated and measured apparent temperatures of the horizontally positioned camouflage net (Fig. 8.15).

local background determines its performance. Figure 8.18 shows IR images of the same scene and indicates a good thermal match with the local background. Despite that, the “give-away” of the net is its unnatural tent shape, which stands out against the hot (white) sand background.



Figure 8.17 Testing of prototype camouflage nets during the CHAR experiments in Sardinia.

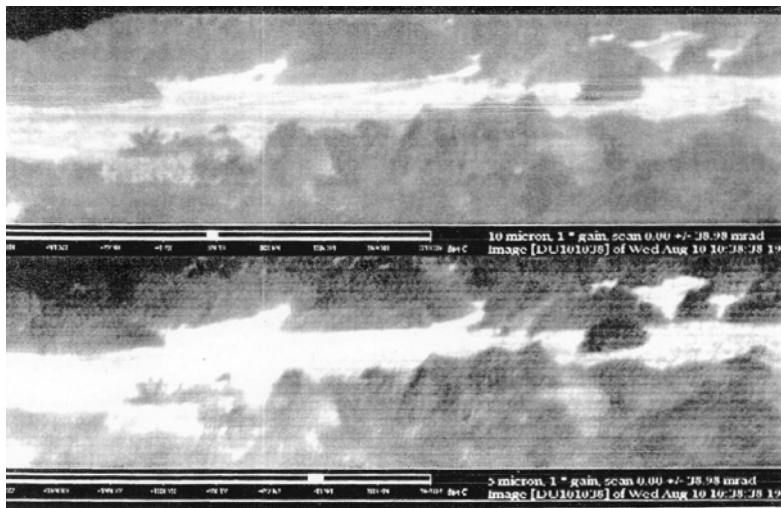


Figure 8.18 IR images of a prototype camouflage net (Fig. 8.17).

8.3 Mobile Camouflage Systems

Because of the high mobility of today's operations and the heavy workload, little time is available to properly camouflage assets. The first step to reduce signatures is proper target design. However, operational and performance requirements dictate that generic and target-specific signatures are inevitable. This situation can be improved by adding permanent camouflage measures to the target that stay in place when driving, although this mobile camouflage system (MCS) cannot be optimal. A former NATO research group (SCI-005) investigated the feasibility of an MCS on a number of mobile platforms.² Since most mobile platforms operate in a driving pattern involving short and longer halts, signature reduction was optimized for these three situations.

Figure 8.19 shows the basic configuration of a Canadian Forces COYOTE vehicle, together with the developmental measures for the three situations. The permanent measures are based on vehicular thermal signatures under various conditions. Various materials are used to treat hot spots, which are distributed over the geometry of the vehicle. In order not to "drive off materials" or damage the hull, a safe distance between the bottom line of the MCS and the ground must be maintained. The top row in Fig. 8.20 shows infrared (8–12 μm) images of the bare and MCS-treated vehicle shortly after stopping. This figure shows the heat leakage through conduction and radiation from the shielded, externally placed muffler to adjacent parts. The wheels (or tracks) are among the hottest parts of a vehicle and remain so for long periods after stopping.

This was the impetus for providing a thermal cover for the lower part of the vehicle when making a short halt (Fig. 8.19). While driving, this cover (a special camouflage net) is rolled up and carried alongside the vehicle. When



Figure 8.19 MCS applied to the Canadian COYOTE. Original (top left), permanent measures (top right), short halt (bottom left), and longer halt (bottom right). (Courtesy Canadian Forces.)

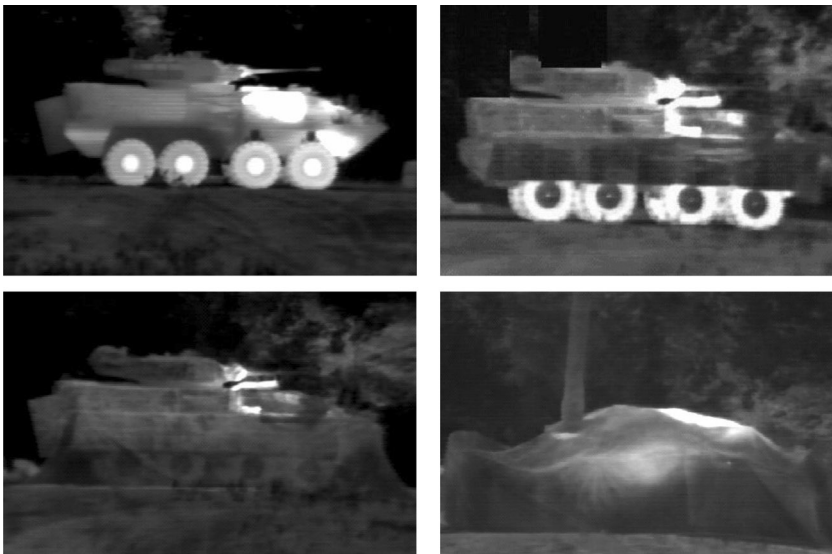


Figure 8.20 MCS applied to the Canadian COYOTE. Early evening, 8–12 μm infrared images (Agema1000). Original (top left), permanent measures (top right), short halt (bottom left), and longer halt (bottom right). (Courtesy Canadian Forces.)

Table 8.1 Camouflage efficiency of the MCS in the visual and 8–12 μm spectral bands.

	% Reduction in detection range		
	Permanent	Short halt	Long halt
Day (visual)	20	38	66
Night (thermal)	32	72	25*

*Warm exhaust gases trapped under the camouflage net.

stopped, the cover is released, stretched out over the lower part of the vehicle, and simply pegged to the ground. In a final form, this could be an automated system that can be deployed and retracted by the push of a button. The lower left part in Figs. 8.19 and 8.20 show the effect of the short-halt measure in the visible and infrared, respectively.

For longer halts, traditional camouflage can be applied, covering most of the vehicle. Care must be taken not to trap hot exhaust gases under the net, thereby creating a big hot spot as shown in Fig. 8.20. Using photo- and video-simulation techniques, the effect of the various measures is determined and expressed in terms of a reduction of the detection range. Table 8.1 shows an overview of the results.

8.4 Thermal Camouflage of Personnel

Applying special materials to human beings to control the radiation budget of the outer clothing layer is a sensitive business. First, care must be taken not to cause too much human discomfort, which can be difficult considering that the comfortable temperature range is $37 \pm 3^\circ\text{C}$. Second, clothing should not hinder the performance of military personnel. In practice, a soldier in action carries a lot of gear and even in the best suitable clothing, comfort levels are often pushed to and over the limits. At rest, a person generates about 100–200 W of heat, which is dissipated to the environment by sweating, which creates warm, moist air. For a fully packed soldier in action, this can amount to up to 1–2 kW. Because of this heat production, a person's apparent temperature contrast with a woodland background generally is positive. Naked and exposed skin (face and hands), but also areas where clothing is pressed to the body (shoulders) are especially critical. The main problem thus is to prevent this internally generated heat from warming up the outer clothing layers. But, the heat has to go somewhere!

The heat balance equation (4.3) is a good starting point to find principal means to transport energy (heat): radiation, convection, conduction and condensation/evaporation.

(1) Radiation

The absorption coefficient for shortwave radiation can be lowered. This will lead to contrast enhancement in the visible, but reduces the rise of the temperature. The emission coefficient for long wave radiation can be

lowered (for example, with LEP). This will have in principle no effect on the visible contrast. While the amount of emitted radiation is reduced, the reflection of the thermal radiation of the surrounding background is increased. Whether this will reduce or enhance the apparent thermal contrast strongly depends on the situation. Either way, reducing the emission coefficient means less radiation is emitted and the person inside might become uncomfortable.

(2) Convection

Natural convection is enhanced by increasing the effective exchange area and/or the friction velocity [cf. Eq. (4.12)]. Figure 8.21 shows an example of these measures in the form of a large number of textile strips. Care must be taken not to completely insulate the inside and to leave enough ventilation to transfer body heat. The figure also demonstrates that such a suit limits freedom of movement and can only be used for special purposes, such as for snipers.

Forced convection through active ventilation can be used to enhance the transfer of warm, moist air away from the body. Arranging a system of semi-permeable tubes as a separation layer between the body and the outer clothing layer is one way to accomplish this (schematics shown in



Figure 8.21 Enhanced natural convection.

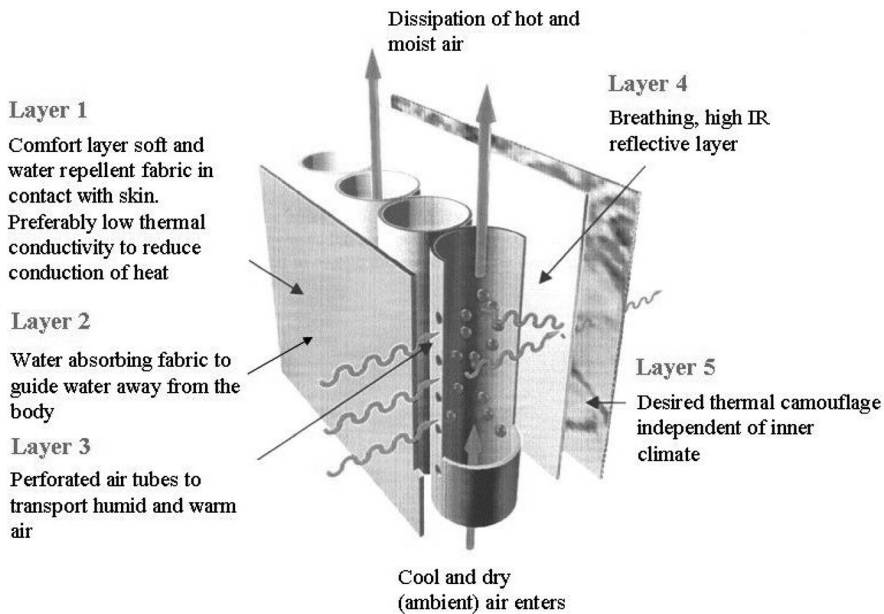


Figure 8.22 Forced convection by active ventilation.

Fig. 8.22). It is important to maintain comfort levels. Too much ventilation will cool the skin to uncomfortable levels.

(3) Conduction

Conduction of heat to and from the body is reduced by using multiple textile layers. The air gap between layers provides heat resistance and maintains a certain temperature difference. Thus, with many layers the temperature is reduced through a number of discrete temperature steps. Nomads have used this principle for centuries to reduce to acceptable levels hot desert temperatures of over 50°C . When carrying gear, these layers are pressed together and this effect is largely lost. Spacer materials can be used to avoid this and to maintain the gap even under pressure. Figure 8.23 shows an experimental suit that has an internal metal wire frame to maintain a 10-cm air gap between the textile and the body. As one can imagine, this is not practical for military operations but could, for instance, be used by firefighters.

(4) Condensation/Evaporation

When moist air condenses, heat is released to the environment, while with evaporation heat is withdrawn from the environment. The human body utilizes this mechanism to cool down by evaporating sweat. Since some form of liquid is required to generate cooling by evaporation, it is not practical in use. But the principle was demonstrated successfully in a hot, desert-like environment on a pre-wetted overgarment.

A variety of experimental thermal suits based on these heat-exchange mechanisms (single or in combination) were tested during an experiment³ in 2002 in



Figure 8.23 Suit with reduced heat conduction, created by a 10-cm air space.

the Marnewaard in The Netherlands. Figure 8.24 shows a line-up of the various thermal suits against a tree line. The funny colors emphasize the thermal (and not the visible) character of the experiment. A standard in service NL battle dress (far right) was included as a reference.



Figure 8.24 Experimental thermal suits during the Marnewaard experiments.

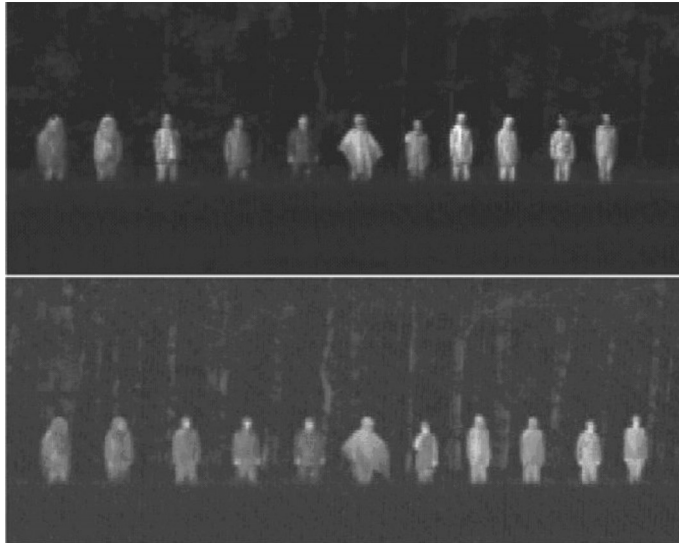


Figure 8.25 Thermal image ($3\text{--}5\ \mu\text{m}$) of the various suits while in the sun (top) and during overcast conditions (bottom).

Figure 8.25 shows a sample thermal image ($3\text{--}5\ \mu\text{m}$) of the various suits under sunny and overcast conditions. The suits show a mix of responses to the environmental conditions, but the thermal reduction compared to the reference is marginally better or considerably worse.

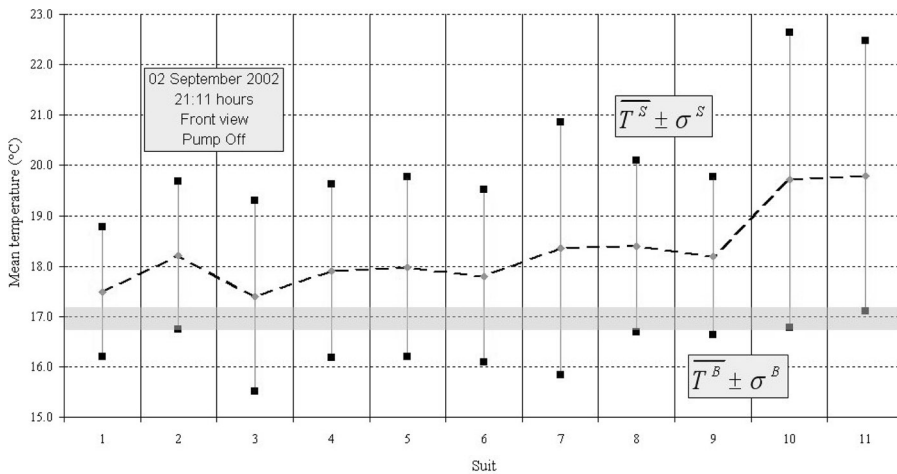


Figure 8.26 Comparison of the mean apparent temperature in $3\text{--}5\ \mu\text{m}$ for all suits with the mean apparent temperature of the background. The bars denote the temperature variance $\pm\sigma^S$ of each suit. The gray area is the temperature variance $\pm\sigma^B$ of the background.

_____ To compare the thermal behavior of the suits, the average apparent temperature $\overline{T^S}$ was calculated for a rectangular square on the chest of each suit, as was the temperature variance, $\pm\sigma^S$ within the rectangle. Figure 8.26 shows the result. This figure also shows the average background temperature, $\overline{T^B}$ and temperature variance $\pm\sigma^B$. It clearly shows that the average temperatures of all the suits are well above the temperature envelope of the background. So, there is lots of work to do.

References

1. G. Hübner, "Camouflage hardware for hot arid regions," *Trial CHAR 2, Sardinia, Report AC/243(CCD)TR/7* (1994).
2. NATO RTO-TM-019, "Integrated camouflage for mobile weapons systems—an effectiveness evaluation," *Report AC/323(SCI-005)TP/30* (1999).
3. NATO RTO-TM-SCI-096, "Multispectral camouflage for the soldier system," *Report AC/323(SCI-096)TP/79* (2004).

Index

- absolute atmospheric humidity, 51
- acceleration of gravity, 47
- active systems, 1
- active ventilation, 175
- apparent emittance, 11
- apparent radiation contrast, 14
- apparent target radiance, 81
- apparent temperature, 11
- atmospheric boundary, 29
- atmospheric emission coefficient, 46, 77
- atmospheric propagation, 12
- atmospheric transmissivity, 12
- atmospheric visibility, 70

- background elements, 123
- bidirectional reflection, 125
- blackbody, 7
- blackbody operation, 84
- blackbody position, 84
- blackbody size, 84

- calibrated signatures, 80
- calibration curves, 96
- calibration guidelines, 84
- calibration procedure, 81
- calibration sources, 85
- camouflage, 164
- camouflage efficiency, 174
- camouflage materials, 166
- camouflage net, 170
- camouflage of personnel, 174
- CARABAS system, 129
- CHAR-II experiment, 103
- cloud base temperature, 46
- cloud emittance, 46
- cloud radiation, 43

- coefficient of thermal expansion
 - of air, 47
- cold-sky radiation, 165
- color pattern, 164
- comfort levels, 174
- conditional stability, 57
- convective heat exchange, 47
- COYOTE, 172
- cumulative error, 63
- curve fitting, 145
- curve-fit method, 146

- degree of cloud cover, 46
- density of air, 50
- density of water, 32
- desert background, 154
- detector voltage, 81, 133
- dew-point temperature, 52
- direct component, 41
- diffuse irradiance, 41

- element bearings, 136
- emission coefficient ϵ , 10, 44
- emittance, 9
- energy conservation, 30
- energy transfer, 30
- environmental temperature, 11
- environmental variations, 24
- EOSTAR, 70
- exhaust gases, 110
- extended target, 23

- field trial, 91
- finite differences, 55
- finite-difference method, 54
- first-principle models, 54
- focal plane array, 20

- forced convection, 48
- free convection, 48
- friction velocity, 50

- Grashof number, 47
- gray bodies, 10
- gray level offset, 83

- heat capacity, 32
- heat flow, 31
- heat flux, 31
- heat transfer coefficient, 48
- heat-balance equation, 35
- HOM experiments, 103
- hydraulic conductivity, 32
- hyperspectral imaging, 4

- image sequence, 154
- imaging systems, 20, 82
- infrared detector, 19
- infrared reflectometer, 101
- initial condition, 57
- instantaneous field of view, 22
- intrinsic, 12
- IR background characterization, 122
- IR target modeling, 115
- IRIS, 91
- IRIS experiments, 103
- irradiance, 7

- Julian day, 41

- Kelvin, 11
- kinematic viscosity, 47
- Kirchhoff, 7

- laminar, 47
- Lambert's cosine law, 10
- land mine detection, 111, 119
- latent heat, 51
- latent heat of vaporization, 51
- Leopard I tank, 104
- LIDAR, 2
- line spread function, 74
- long-wave sky irradiance, 45
- long wave reflection coefficient, 11
- long wave spectral reflectivity, 11
- low-emissivity paint, 164

- M113 (APC), 104
- Maltese cross, 130

- materials properties, 25
- mean reflection coefficient, 40
- mobile camouflage system, 172
- MODTRAN, 18, 70
- moisture content, 32
- moisture flow, 32
- Monin-Obukhov similarity, 49

- NEI, 21
- noise equivalent temperature difference, 74
- nonlinear transport coefficients, 32

- passive systems, 18
- physical characterization, 29
- physical description, 135
- pixels, 20
- Planck, 8
- point target, 22
- polar diagram, 97
- polarizer, 115
- porous materials, 32
- principal directions, 136
- PRISM, 115
- properties of soils, 34
- pyrgeometer, 70
- pyrheliometer, 41, 71

- Radar, 1
- radiance, 10
- radiance offset, 83
- radiant exitance, 8
- radiant flux, 7
- radiant flux density, 7
- radiant intensity, 9
- radiation contrast, 18
- radiometer, 19
- rain gauge, 71
- range, 13
- relative error, 63
- relative humidity, 52
- relative system spectral response, 81
- Reynolds number, 47
- Richardson number, 49
- roughness length, 50

- SAR, 2
- saturation deficit, 52
- saturation vapor pressure, 52, 148
- SCORPIO, 73

- sensitivity analysis, 60
- signature management, 161
- sky irradiance, 72, 152
- sky radiance distribution, 75
- solar absorption coefficient, 36
- solar constant, 41
- solar incident angle, 41
- solar radiation, 41
- solarimeter, 41, 70
- spatial similarity, 161
- specific enthalpy, 32
- specific heat, 31
- specific mass, 31
- spectral absorptivity, 7
- spectral diversity, 25
- spectral emissivity, 8
- spectral radiometer, 4
- state diagram, 53
- Stefan-Boltzmann constant, 9
- sun azimuth angle, 41
- sun elevation angle, 41
- surface emittance, 47
- synoptic, 70
- system responsivity, 81
- T62 tank, 115
- target detection, 17
- target conditions, 24
- target radiance, 81
- target signatures, 99
- temperature contrasts, 142
- temperature histograms, 117, 139
- temperature prediction, 57
- temperature similarity, 161
- temperature statistics, 117
- temperature-contrast statistics, 143
- test bed, 113
- thermal background behavior, 138
- thermal conductivity, 31
- thermal diffusivity, 31
- thermal suits, 177
- thermopile, 102
- TICM-II FLIR, 109
- turbulent, 47
- visibility sensor, 70
- von Kármán constant, 50
- water vapor pressure, 45
- weather parameters, 69
- weather station, 157
- Wien's displacement law, 9
- wind sensor, 71
- zero displacement level, 50



Pieter A.M. Jacobs is a senior scientist working for the Electro-Optics group at TNO, located in The Hague, The Netherlands. The laboratory in The Hague is part of the Defence, Security, and Safety Organization, which is the main contractor for the Dutch Ministry of Defence. Over a period of more than 30 years he has become an expert on thermal sensor systems and countermeasures. He holds a master degree from the University of Eindhoven and a Ph.D. in physics from the

University of Wageningen. As the Dutch representative in many national and international (NATO) research projects he is well informed on the state of the art in his area of expertise. He has presented his work during many conferences and symposia over the years. This Tutorial Text tries to summarize his experiences, without going too much into theoretical details, but instead focusing on practical issues.